A MEASUREMENT OF THE $\bar{p}p \to \overline{\Lambda}\Lambda$ AND $\bar{p}p \to \overline{\Sigma}^0\Lambda + c.c.$ REACTIONS AT 1.726 GeV/c.

BY

REX L. TAYLOE

B.S., Purdue University, 1986
M.S., University of Illinois, 1987

THESIS

Submitted in partial fulfillment of the requirements
for the degree of Doctor of Philosophy in Physics
in the Graduate College of the
University of Illinois at Urbana-Champaign, 1995

Urbana, Illinois

UNIVERSITY OF ILLINOIS AT URBANA-CHAMPAIGN

THE GRADUATE COLLEGE

MARCH 1995

WE HEREBY RECOMMEND THAT THE THESIS BY

REX L. TAYLOE

ENTITLED A MEASUREMENT OF THE $\bar{p}p \to \bar{\Lambda}\Lambda$ AND $\bar{p}p \to \bar{\Sigma}^0\Lambda$ + c.c.

REACTIONS AT 1.726 GeV/c

BE ACCEPTED IN PARTIAL FULFILLMENT OF THE REQUIREMENTS FOR

THE DEGREE OF DOCTOR OF PHILOSOPHY

Director of Thesis Research

Head of Department

Committee on Final Examination†

Chairperson

M.K. Brussel

Peter G. Debrunner

Jochen Wambach

† Required for doctor's degree but not for master's

O-517

A MEASUREMENT OF THE $\bar{p}p \rightarrow \overline{\Lambda}\Lambda$ AND $\bar{p}p \rightarrow \overline{\Sigma}^0\Lambda + c.c.$ REACTIONS AT 1.726 GeV/c.

Rex L. Tayloe, Ph.D.
Department of Physics
University of Illinois at Urbana-Champaign, 1995
David W. Hertzog, Advisor

The reactions $\bar{p}p \rightarrow \overline{\Lambda}\Lambda$ and $\bar{p}p \rightarrow \overline{\Sigma}^0\Lambda + c.c.$ were investigated at an average antiproton momentum of 1.726 ± 0.001 GeV/c using the Low Energy Antiproton Ring (LEAR) at CERN. Total and differential cross sections, hyperon polarizations, and spin correlation coefficients were measured for these strangeness production reactions. Emphasis was placed on a comparison of the data from the $\bar{p}p \rightarrow \overline{\Lambda}\Lambda$ reaction with that measured for the $\bar{p}p \rightarrow \overline{\Sigma}^0\Lambda + c.c.$ reaction. A comparison of these complementary channels provides insight into the dynamics of strangeness production.

Acknowledgements

The work described in this thesis was supported by the National Science Foundation under Grants NSF PHY 86-10493, NSF PHY 89-21146, and NSF PHY 93-10871.

I owe many thanks to my thesis advisor David Hertzog. His enthusiastic support and assistance have kept me on track during the arduous process of completing this project. I also thank him for providing me the opportunity to travel to CERN, FNAL, BNL, and to conferences that has allowed me to meet, work with, and learn from a host other physicists on many projects. I think that I leave the University of Illinois as a well trained and educated physicist; this would not have been possible without the efforts of David Hertzog.

I would also like to thank Bob Eisenstein as an additional advisor and collaborator. His discussions about PS185 physics, suggestions for improving this thesis, and help with all aspects of the PS185 experiment have greatly strengthened the final product of this effort.

The PS185 collaboration has been an enjoyable group to work and associate with during my time as a graduate student. My trips to CERN were rewarding, productive, and fun due, in no small part, to the folks of this collaboration. In particular, I thank Roland von Frankenberg, Staffan Ohlsson, Brian Quinn for teaching me about physics and the PS185 experiment.

I thank the staff of the LEAR facility at CERN for providing the high-quality source of antiprotons without which this experiment would have not been possible.

I heartily thank all of the members of our medium energy physics group at the

U of I. Sarah Hughes and Paul Reimer worked long and hard on the preparation and execution of this experiment and provided help with the analysis. Philip Harris helped to write and managed the monte carlo program that was crucial in extracting the final results. I thank Tim Jones for reading and commenting on this thesis and for politely and intently listening to my tirades about the data analysis.

I also would like to thank Rob Timmermans for patient discussions about the theoretical aspects of PS185 during his visit to Illinois, at conferences, and via E-mail.

I owe many thanks to the staff of the University of Illinois Nuclear Physics Lab. Without the work of Jim Gabbard and Kyle Gerlach on the construction and design of the calorimeter, it could never have been built. The assistance of Penny Sigler and Gaylon Reeves was crucial in getting people and equipment to and from CERN and in finishing this thesis. Most of all, I would like to thank Milco Moushmof for his thousands of hours of heartfelt and conscientious work weaving fibers, lead, and glue to build the calorimeter.

Thanks are due to all of the graduate students at the Nuclear Physics Lab. One could always find enthusiastic help in solving a LaTeX, statistics, or computer problem at any time of day or night. In particular I would like to thank fellow graduate student, officemate, and friend Bruce Macgibbon for making my tenure at NPL a load of fun.

Finally I would like to thank my Mom and Dad. Their influence has given me the self-confidence and fortitude necessary to succeed in the pursuit of those things that are important.

The PS185 Collaboration

G. Franklin, B. Quinn, R. Schumacher, V. Zeps

Carnegie-Mellon University

N. Hamann

CERN

W. Eyrich, M. Kirsch, R. Kraft, F. Stinzing, H. Wirth

Universität Erlangen

P. Birien, H. Fischer, J. Franz, E. Rössle, H. Schmitt, R. Todenhagen, H.J. Urban

Universität Freiburg

R.A. Eisenstein, P. Harris, D. Hertzog, S. Hughes, P. Reimer, R. Tayloe

University of Illinois

R. Bröders, G. Decker, R.v. Frankenberg, K. Kilian, W. Oelert, K. Röhrich,

T. Sefzick, G. Sehl, M. Ziolkowsky

IKP-KFA Jülich

P.D. Barnes

LAMPF

T. Johansson, S. Ohlsson

Uppsala University

W.H. Breunlich, R. Geyer

IMEP-ÖAW, Vienna

Say what some poets will, Nature is not so much her own ever-sweet interpreter, as the mere supplier of that cunning alphabet ...

— Herman Melville, Moby-Dick

The whole secret of the study of nature lies in learning how to use one's eyes.

— George Sand, Nouvelles Lettres d'un Voyageur

Contents

List of Tables

List of Figures

Chapter 1

Introduction

The first $\bar{p}p \rightarrow \overline{\Lambda}\Lambda$, $\bar{p}p \rightarrow \overline{\Sigma}^0\Lambda$, and $\bar{p}p \rightarrow \overline{\Lambda}\Sigma^0$ reactions were observed in 1960 by J. Button et al. [1,2] using the new 72-inch hydrogen bubble chamber at the Bevatron in Berkeley, California. At this time, the field of particle physics was still in its adolescence. A consistent scheme of mesons and baryons and the incorporation of the idea of "strange" particles had only recently been proposed [1]. The particle-antiparticle symmetry, as suggested by the Dirac equation, was in the process of verification with the discovery of the antiproton, antineutron, and antilambda [3-6] just several years prior (also at the Berkeley Bevatron). An intricate yet enticingly symmetric picture of particle physics was beginning to emerge. The force that binds these particles and mediates their interactions, the "strong" nuclear force, was the subject of much inquiry. Button and colleagues, through the production of hyperon-antihyperon pairs in antiproton-proton collisions, hoped to provide answers to some of the questions, from the long list, about the strong nuclear force.

Almost 25 years later and 7000 miles away the PS185 collaboration continues to work on the same list of questions. Although many have been answered, many more remain. As observed by the philosopher Heraclitus in the early stages of science, "Nature is wont to hide herself." Using the LEAR antiproton facility at CERN in Geneva, Switzerland and with modern detection techniques, approximately four orders of magnitude more $\bar{p}p \rightarrow \overline{\Lambda}\Lambda$, $\bar{p}p \rightarrow \overline{\Sigma}^0\Lambda$, and $\bar{p}p \rightarrow \overline{\Lambda}\Sigma^0$ events have been

collected and analyzed since that first bubble chamber experiment at Berkeley. The large number of events and the accuracy with which they are measured have allowed more and more of the subtle aspects of the strong nuclear force, through hyperon-antihyperon production, to be brought to light.

This work reports on a subset of the extensive PS185 experimental effort: an investigation of the reactions $\bar{p}p \rightarrow \overline{\Lambda}\Lambda$, $\bar{p}p \rightarrow \overline{\Sigma}^0\Lambda$, and $\bar{p}p \rightarrow \overline{\Lambda}\Sigma^0$ at an incident antiproton momentum of 1.729 Gev/c. Special emphasis is placed on the study of $\bar{p}p \rightarrow \overline{\Sigma}^0\Lambda$ and $\bar{p}p \rightarrow \overline{\Lambda}\Sigma^0$, two lesser-known channels, to enable a thorough comparison with the similar and well-measured $\bar{p}p \rightarrow \overline{\Lambda}\Lambda$ channel. In this introductory chapter, the physics background and the motivation of the experiment is elaborated. Previous results of others and the PS185 experiment are presented and some interpretations of these results are given. It concludes with an overview of the challenges involved with a measurement of the $\bar{p}p \rightarrow \overline{\Sigma}^0\Lambda$ and $\bar{p}p \rightarrow \overline{\Lambda}\Sigma^0$ channels and the solutions implemented to meet them.

1.1 Resolving the Hadrons

As the correct picture of the nucleus developed in the 1930's, it was noticed that a new type of force must be responsible for the interaction of nucleons. This force must be strong enough to hold a nucleus together against the electromagnetic repulsion between the charged protons and of finite range as the force is not seen at distances much beyond a nucleon radius. In 1935 Yukawa proposed that a particle mediates the strong nuclear force as the photon does for the electromagnetic force [7]. Its mass would be that as calculated from the range of the nuclear force (≈ 1 fm $= 10^{-15}$ m) and the uncertainty principle. This yielded ≈ 200 MeV/c^2 for the mass of the Yukawa particle. And indeed, the pion was discovered in 1947 and assigned (too simplistically, it turned out) to be this particle, the quantum of the strong nuclear force.

In the years following, a plethora of particles interacting via the strong nuclear

force were discovered. These particles, the hadrons, come in two varieties: the integral-spin mesons and the half-integral-spin baryons. The proton and neutron had been known for some time and a triplet of pions was eventually identified. The experimentalists also came across a new class of hadrons, the "strange" particles. These particles are distinguished by a larger mass than their ordinary meson and baryon counterparts and by their multiple patterns of delayed decay. Once the complication of multiple decays was understood and the experimental mass resolution became sufficiently precise, the K mesons and the Λ and Σ hyperons[1] emerged.

Along with these developments, a regularity of particle-antiparticle symmetry was surfacing. The positron was discovered in 1932 by Anderson [8], confirming the prediction of the Dirac equation, that there should exist a particle with the same mass and opposite charge as that of the electron. With the discoveries of the antiproton, antineutron, and antilambda, it appeared that this symmetry would hold for the baryons as well. This was perhaps surprising since the measurement of the magnetic moment of the proton and neutron was not as predicted by the Dirac theory. Also, why was the baryon-antibaryon symmetry not seen in macroscopic observations? Where are the antimatter galaxies?

Even with these hints that the hadrons were more complicated than recognized, a model proposed by Gell-Mann and Ne'eman [9] was fairly successful in explaining (or at least categorizing) the observed properties of these particles. In this model, the "eightfold way", the SU(2) isospin symmetry that was observed in the strong interaction, was incorporated into the larger symmetry of SU(3). The isospin multiplets were grouped into octets or into multiplets that could be made by combinations of the octets with each octet or multiplet containing particles of the same spin and parity. The spin-$\frac{1}{2}$ baryon and antibaryon octets and the spin-0 meson octet are diagrammed

[1]The term *hyperon* was introduced as a name for the new baryons that were larger in mass than the familar neutron and proton. Today it has come to denote a baryon with at least one quark that is not a u or a d.

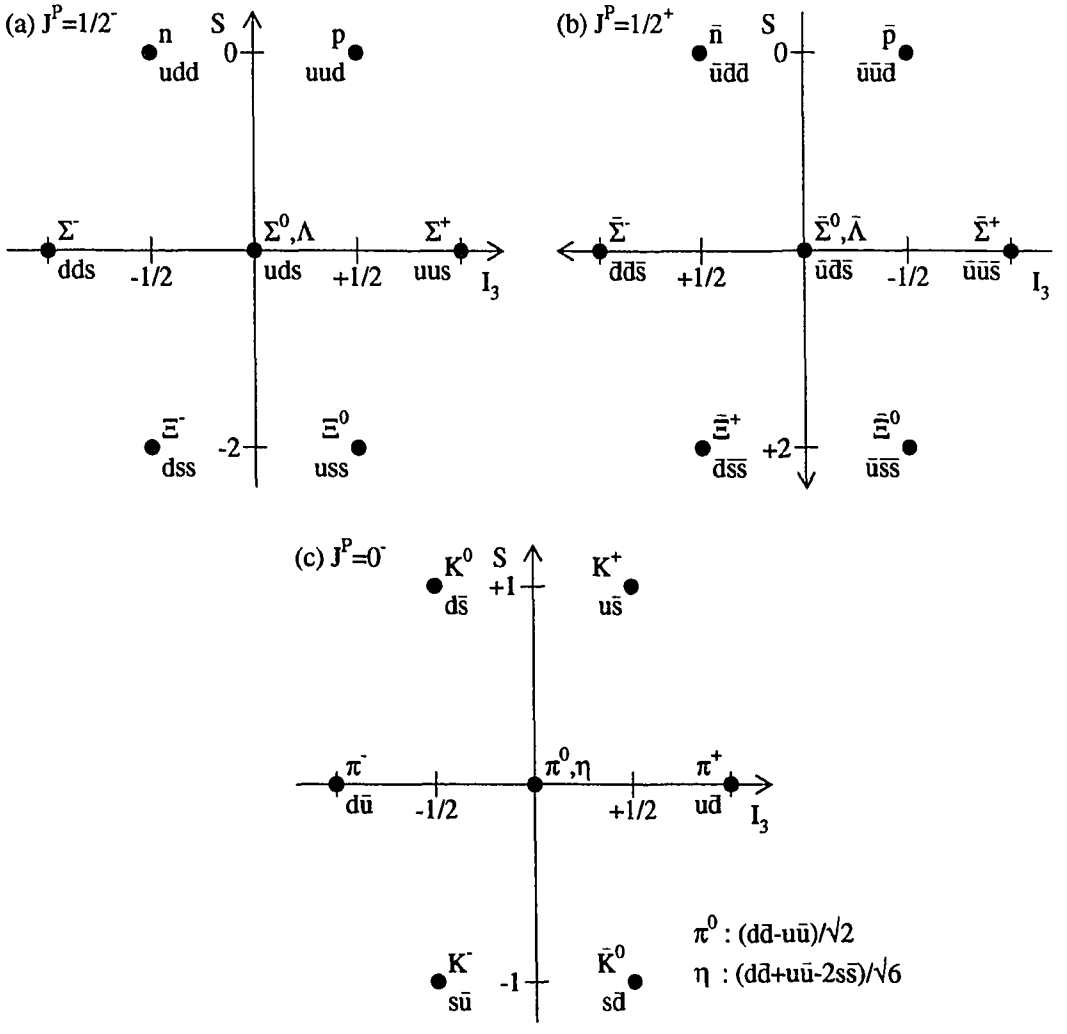

Figure 1.1: The (a) $J^P = \frac{1}{2}^-$ baryon, (b) $J^P = \frac{1}{2}^+$ antibaryon octets, and the (c) $J^P = 0^-$ meson octet. The strangeness is plotted on the vertical axes and the third component of isospin on the horizontal. The quark assignments are noted along with the name of each hadron state.

in Fig. 1.1. The particles of the other multiplets where gradually incorporated into this scheme. In fact, many of the particles were predicted to exist before they were seen in the laboratory; the most notable example is the $S = -3$ Ω^-.

While this model was adequate to organize the particles into various multiplets, it fell short in explanatory power. Why did these particles organize themselves into

this elaborate scheme of multiplets? A remarkable breakthrough occurred when Gell-Mann and, independently, Zweig proposed [10] that hadrons are constructed of smaller constituents, the quarks. The hadron multiplet scheme could be constructed with combinations of three quarks: the up (u), down (d), and strange (s). The u and d quarks together form a strangeness-zero isospin doublet and the s quark is an isosinglet with strangeness -1. The u quark is assigned a charge (in units of the proton charge) $+2/3$ and the d and s, a charge of $-1/3$. The baryons (antibaryons) are constructed with SU(3) combinations of the three quarks (antiquarks) and the mesons, a quark-antiquark pair.

The reality of quarks as objects and not as only theoretical constructs was accepted with skepticism at first as a free quark had never been observed. The arguments were later strengthened with the results of deep-inelastic scattering experiments and through the production of mesons containing the heavier charm (c), bottom (b) , and top (t) quarks[2] that showed that hadrons are well explained with quark constituents.

In the years following the quark hypothesis, many advances have been made, in both theory and experiment, to bring together the modern picture of particle physics into what is now called the "standard model" [11]. In this picture there are three families of quarks and leptons. The leptons — the electron, muon, tau, and their neutrino partners — do not interact strongly and are handled successfully with the electroweak theory. The interactions of quarks are dominated by the strong force which has been quantified with the theory of quantum chromodynamics (QCD).

In QCD the quark interactions are mediated via the exchange of a massless spin-1 particle known as the gluon. In addition to charge, the quarks carry a quantum number called "color" which takes on one of three values, called (somewhat whimsically) red, green, and blue. The gluons couple to color, analogous to the way the photon

[2]The CDF collaboration at Fermilab reports, as of this writing, strong evidence for the hitherto undiscovered t quark.

couples to charge in the electromagnetic interaction. Only color singlet combinations of quarks can appear as physical particles in this theory, thus accounting for the experimental fact that single quarks, not bound inside a hadron, are not observed.

The color interactions are modeled in a manner similar to the electromagnetic interaction in precision theory of quantum electrodynamics (QED), with the substitution of the strong coupling constant α_s for $\alpha = \frac{1}{137}$ of QED. However, unlike QED, due to the non-Abelian nature of the gluonic interactions, α_s decreases with decreasing distances. Thus, QCD exhibits "asymptotic freedom"; the quark-quark interaction essentially vanishes for small distances where they behave as if they are free, non-interacting particles. This allows QCD to be used as a quantitative calculational tool for high momentum transfers (short distances) with perturbation techniques as is done for QED. And indeed, for processes where the relevant momentum transfers are large, the strong coupling becomes small[3] and the observables for these processes are calculable with precision.

When quarks are separated by large distances, the interaction strength increases without limit, much like a harmonic oscillator. This behavior is referred to as "confinement. Thus, calculations in the lower energy regime are non-perturbative and present an almost intractable problem. Although progress is being made, for example, through the use of lattice techniques, the present understanding relies mainly on semi-phenomenological models. The majority of the successful low-energy models of hadron interactions use meson-exchange techniques to explain the observables. These techniques are not entirely different than those proposed by Yukawa over 50 years ago! Where are the quarks and gluons? Ultimately, the interactions of hadrons must be able to be incorporated into the scheme of QCD through the interactions of the basic constituents: the quarks and gluons.

[3]The current best estimate for α_s at the Z mass (91.2 GeV/c^2) obtained from a fit to the results of various experiments is $\alpha_s(M_Z) = 0.117 \pm 0.005$[12].

1.2 Antiproton-Proton Reactions at Low Energies

Antiproton-proton reactions are interesting because of the large number of complementary reaction channels available in which to study the interactions of quarks and gluons. A data set may be obtained that spans a continuous spectrum of the reaction mechanisms. For example, some of the possible reactions include $\overline{p}p \rightarrow \overline{p}p$ (elastic scattering), $\overline{p}p \rightarrow \overline{n}n$ (charge exchange), $\overline{p}p \rightarrow \pi\pi, \pi\pi\pi$ (non-strange meson production), $\overline{p}p \rightarrow \overline{Y}Y$ (strange baryon production), and $\overline{p}p \rightarrow \overline{K}K$ (strange meson production). These reactions, and other similar ones, each provide a slightly different focus on the strong-interaction reaction mechanisms.

By conducting these investigations at low energies (around a few GeV) it is hoped to gather greater understanding of the strong interaction in this energy region. That is, at interaction distance scales on the order of the hadron size. The LEAR facility at CERN provides a low energy antiproton source of unprecedented quality. The purity, intensity, and precision of the antiproton beam of momentum 0.1–2.0 GeV/c allows the observables in the above-mentioned reaction channels to be precisely measured, thereby enabling a solid program of low-energy strong-interaction studies.

1.3 The PS185 Experiment

The PS185 experiment was initiated in the early 1980's with the goal of studying the strong interaction by investigating strange quark production via a precise and complete measurement of the exclusive hyperon production reactions $\overline{p}p \rightarrow \overline{Y}Y$ near threshold. Here $\overline{Y}Y$ is one of the final states $\overline{\Lambda}\Lambda$, $\overline{\Sigma}^0\Lambda$, $\overline{\Lambda}\Sigma^0$, $\overline{\Sigma}^-\Sigma^+$, or $\overline{\Sigma}^+\Sigma^-$. The program began with the $\overline{p}p \rightarrow \overline{\Lambda}\Lambda$ channel and has recently become more complete by providing measurements from the other channels.

Strangeness production in these channels near their respective reaction thresholds is particularly attractive for a host of reasons. As is evident from the name, strangeness production involves production of strange quarks, more specifically, an

$\bar{s}s$ quark pair. Because of the larger mass of the s quark (as compared to the u and d), the production of an $\bar{s}s$ quark pair requires a large momentum transfer all the way down to reaction threshold. Therefore, these reactions should be sensitive to the strong interaction effects from the shorter-range end of the nuclear distance scale. Near threshold, due to the angular momentum "centrifugal" barrier in the final state, only the lower angular momentum values need be included. This allows for an easier interpretation of the data using a partial wave analysis.

The reactions to the $\overline{Y}Y$ states $\overline{\Lambda}\Lambda$, $\overline{\Sigma}^0\Lambda$, and $\overline{\Lambda}\Sigma^0$ have an additional advantage due to the Λ hyperons in the final state. Since they decay via the weak interaction, the lifetimes are relatively long and the decay products exhibit an angular asymmetry due to the parity-nonconserving nature of this interaction. The long lifetimes allow for an unmistakable signature of these reactions in the detector which ensures a virtually zero-background measurement. The angular asymmetry enables the polarizations of the hyperons in the final state and their spin-correlations to be determined without the need for double scattering. These spin observables, along with the differential cross sections, constitute a very complete data set that sheds light on the strength, range, and spin dynamics of the strong interaction.

1.4 A New Channel: $\bar{p}p \to \overline{\Sigma}^0\Lambda + c.c.$

Before beginning a discussion of the merits of this measurement, a few words about notation are necessary. Although a hyperon Y, in a strict sense, is a baryon with at least one s (or heavier) quark, the reaction shorthand $\bar{p}p \to \overline{Y}Y$ is used throughout this document as notation for the three channels of interest here: $\bar{p}p \to \overline{\Lambda}\Lambda$, $\bar{p}p \to \overline{\Sigma}^0\Lambda$, and $\bar{p}p \to \overline{\Lambda}\Sigma^0$. Also, the shorthand notation $\bar{p}p \to \overline{\Sigma}^0\Lambda + c.c.$ is used to indicate the $\bar{p}p \to \overline{\Sigma}^0\Lambda$ and $\bar{p}p \to \overline{\Lambda}\Sigma^0$ channels together. This is a common practice as they are charge conjugate channels and the charge conjugation symmetry of the strong interaction implies strict constraints among the observables as is explained in

(a)

hyperon	Λ	Σ^0
mass (GeV/c^2)	1.1157	1.1926
J^P	$\frac{1}{2}^-$	$\frac{1}{2}^-$
strangeness	-1	-1
isospin	0	1

(b)

reaction	$\overline{p}p \to \overline{\Lambda}\Lambda$	$\overline{p}p \to \overline{\Sigma}^0\Lambda + c.c.$
total c.m. energy (GeV)	2.231	2.308
$\overline{p}$ lab energy (GeV)	1.715	1.900
$\overline{p}$ lab momentum (GeV/c)	1.435	1.653
momentum transfer (GeV/c)	0.603	0.672

Table 1.1: Parameters of (a) the Λ and Σ^0 hyperons and of (b) the $\overline{p}p \to \overline{\Lambda}\Lambda$ and $\overline{p}p \to \overline{\Sigma}^0\Lambda$ reaction kinematics at threshold.

Chapter 2. For this reason, these two channels are usually considered as one and called the $\overline{p}p \to \overline{\Sigma}^0\Lambda$ + c.c. channel. Any exceptions to these conventions are noted.

A measurement of the reaction $\overline{p}p \to \overline{\Sigma}^0\Lambda + c.c.$ and subsequent comparison with $\overline{p}p \to \overline{\Lambda}\Lambda$ is interesting due to the similarity between the Λ and Σ^0 hyperons and therefore between the dynamics of the two reactions $\overline{p}p \to \overline{\Sigma}^0\Lambda + c.c.$ and $\overline{p}p \to \overline{\Lambda}\Lambda$. The relevant parameters of the Λ and Σ^0 hyperons and of the $\overline{p}p \to \overline{\Lambda}\Lambda$ and $\overline{p}p \to \overline{\Sigma}^0\Lambda$ + c.c. reactions near threshold are shown in Table 1.1. As can be seen from this table, the kinematic parameters are very similar; the major difference is that of isospin.

A quark line diagram of the $\overline{p}p \to \overline{Y}Y$ reaction is shown in Fig. 1.2(a). In this simple quark picture, the u and d quarks of the isosinglet Λ are in an isospin-zero, spin-zero ($I = S = 0$) state; thus, the s quark carries all of the spin of the Λ. This is in contrast to the isospin-1 Σ^0 where the u and d are paired in an $I = S = 1$ state and share the total spin with the s quark. Therefore a measurement of the $\overline{\Lambda}\Lambda$ spin state

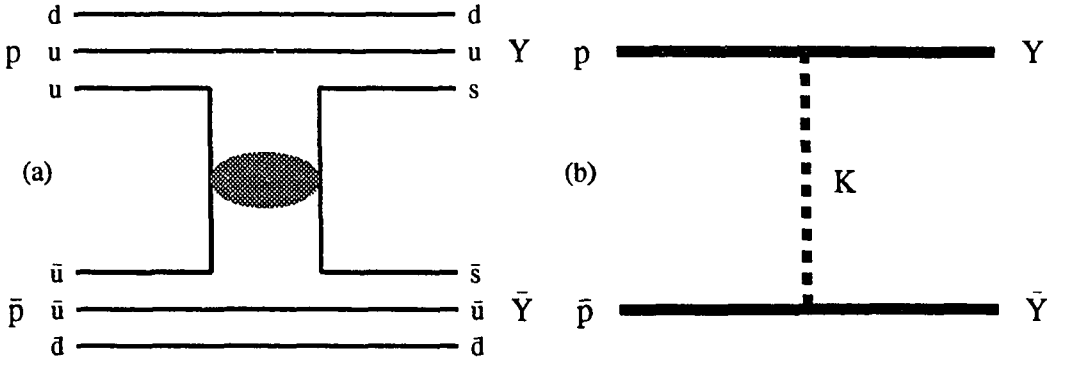

Figure 1.2: Two ways to view the $\overline{p}p \rightarrow \overline{Y}Y$ reaction: (a) a quark line diagram and (b) a kaon-exchange diagram.

yields the spin state of the $\overline{s}s$ system while a measurement of the $\overline{\Sigma}^0\Lambda$ spin state yields spin information about the $\overline{s}s$ pair combined with the "spectator" u and d quarks. The study of these complementary channels can help to zero in on the quark pair creation mechanisms. Of course, these arguments are naive in that they are based on a non-relativistic quark model and neglect any interactions in the $\overline{\Lambda}\Lambda$ final state. Another way to state the above would be that the $\overline{p}p \rightarrow \overline{\Sigma}^0\Lambda + c.c.$ reaction takes place through different spin-isospin channels. The study of $\overline{p}p \rightarrow \overline{\Sigma}^0\Lambda + c.c.$ and comparison with $\overline{p}p \rightarrow \overline{\Lambda}\Lambda$ should yield information on the isospin dependence of the reaction mechanisms.

An alternative way to view the $\overline{p}p \rightarrow \overline{Y}Y$ reaction is through meson exchange depicted schematically in Fig. 1.2(b). In this framework, strangeness is created via the exchange of kaons; the $K(494)$, the $K^*(892)$, and the $K_2^*(1430)$ are most commonly considered. In the language of the meson-exchange formalism, a comparison of $\overline{p}p \rightarrow \overline{\Sigma}^0\Lambda + c.c.$ with $\overline{p}p \rightarrow \overline{\Lambda}\Lambda$ is interesting due to the different meson-nucleon coupling constants involved in the two reactions. The SU(3) (and SU(6)) symmetry relations predict that the coupling to the K^* is stronger in $\overline{p}p \rightarrow \overline{\Sigma}^0\Lambda + c.c.$ than in $\overline{p}p \rightarrow \overline{\Lambda}\Lambda$. Thus, the $\overline{p}p \rightarrow \overline{\Sigma}^0\Lambda + c.c.$ reaction is more sensitive to the shorter-range K^* exchange and should provide a good test of the meson-exchange approach to hyperon

production.

It is tempting to state that a comparison of $\bar{p}p \rightarrow \overline{\Sigma}^0\Lambda + c.c.$ with $\bar{p}p \rightarrow \overline{\Lambda}\Lambda$ will help to distinguish between the quark and meson-exchange pictures represented in Fig. 1.2, but this is probably an overly optimistic viewpoint. Meson exchange approaches have achieved much success in explaining the data, are based on firm theoretical ground, and cannot be labeled "incorrect". However, these systems must ultimately be able to be described in terms of the basic constituents, the quarks and gluons. Providing high-precision observables for the $\bar{p}p \rightarrow \overline{\Sigma}^0\Lambda + c.c.$ and $\bar{p}p \rightarrow \overline{\Lambda}\Lambda$ reactions, it is hoped, will advance understanding on all fronts. This is the goal of the measurement described here.

1.5 The Existing Data

Before proceeding with the new measurement it is instructive to examine the existing $\bar{p}p \rightarrow \overline{\Lambda}\Lambda$ and $\bar{p}p \rightarrow \overline{\Sigma}^0\Lambda + c.c.$ data reported by PS185 and by other experiments to summarize what has been learned.

1.5.1 Pre-PS185 $\bar{p}p \rightarrow \overline{Y}Y$ Data

Before the commencement of the PS185 experiment, there were approximately 10 experiments with measurements of the $\bar{p}p \rightarrow \overline{\Lambda}\Lambda$ and $\bar{p}p \rightarrow \overline{\Sigma}^0\Lambda + c.c.$ channels with antiproton momenta[4] from 6.0 GeV/c down to 1.5 GeV/c. The majority of these were bubble chamber experiments [2,13–21]. The results suffered from low statistical precision, especially near threshold where the reaction cross sections are decreasing rapidly. The other experiments using more modern detectors [22,23] were carried out at momenta far from reaction threshold. The highest precision experiment near threshold [20] produced a $\bar{p}p \rightarrow \overline{\Lambda}\Lambda$ cross section at 1.5 GeV/c with 25% errors. This same experiment reported polarization data but for momenta integrated over the

[4]It is conventional with these experiments to use the incident antiproton lab momentum as the determining kinematic variable.

range 1.5–2.0 GeV/c. For $\bar{p}p \rightarrow \overline{\Sigma}^0\Lambda + c.c.$, the one experiment that concentrated in the near-threshold momentum region yielded only total cross section results with approximately 25% errors.

1.5.2 PS185 $\bar{p}p \rightarrow \overline{\Lambda}\Lambda$ Data

The PS185 collaboration has thoroughly mapped out the $\bar{p}p \rightarrow \overline{\Lambda}\Lambda$ reaction near threshold [24–30] with differential cross section, polarization, and spin-correlation coefficient results. Approximately 10^5 $\bar{p}p \rightarrow \overline{\Lambda}\Lambda$ events have been collected and analyzed, producing high precision data with which to investigate the inner workings of this system. The total cross section values measured for the $\bar{p}p \rightarrow \overline{\Lambda}\Lambda$ reaction by PS185 and previous experiments in the near-threshold momentum region are plotted in Fig. 1.3. Note that the $\bar{p}p \rightarrow \overline{\Lambda}\Lambda$ reaction has indeed been well measured with high precision by PS185 all the way down to reaction threshold.

The corresponding differential cross sections measured by PS185 are shown in Fig. 1.4. The antiproton lab momentum and the excess energy ε, where $\varepsilon = \sqrt{s} - 2m_\Lambda$ is the kinetic energy available to the final state hyperons, are tabulated on each plot. The most striking feature of these data is the forward peaking that persists all the way down to reaction threshold. The polarization values of the Λ hyperons in the reaction $\bar{p}p \rightarrow \overline{\Lambda}\Lambda$ are shown in Fig. 1.5. These data show a sizeable hyperon polarization throughout the momentum range with an indication of a zero crossing that begins at low-momenta in the backward $\cos\theta^*$ region and moves forward with increasing momentum.

The higher momentum data sets also allowed the extraction of a full set of spin correlation coefficients. A quantity derived from these, the *singlet fraction*, is shown as a function of momentum in Fig. 1.6. The singlet fraction is a measure of the average spin state of the final-state hyperon pair; a value of 1 (0) indicates pure singlet (triplet) production and a value of $\frac{1}{4}$ is expected for uncorrelated production. As is clearly seen in this plot, the data show that the final-state $\overline{\Lambda}\Lambda$ are produced

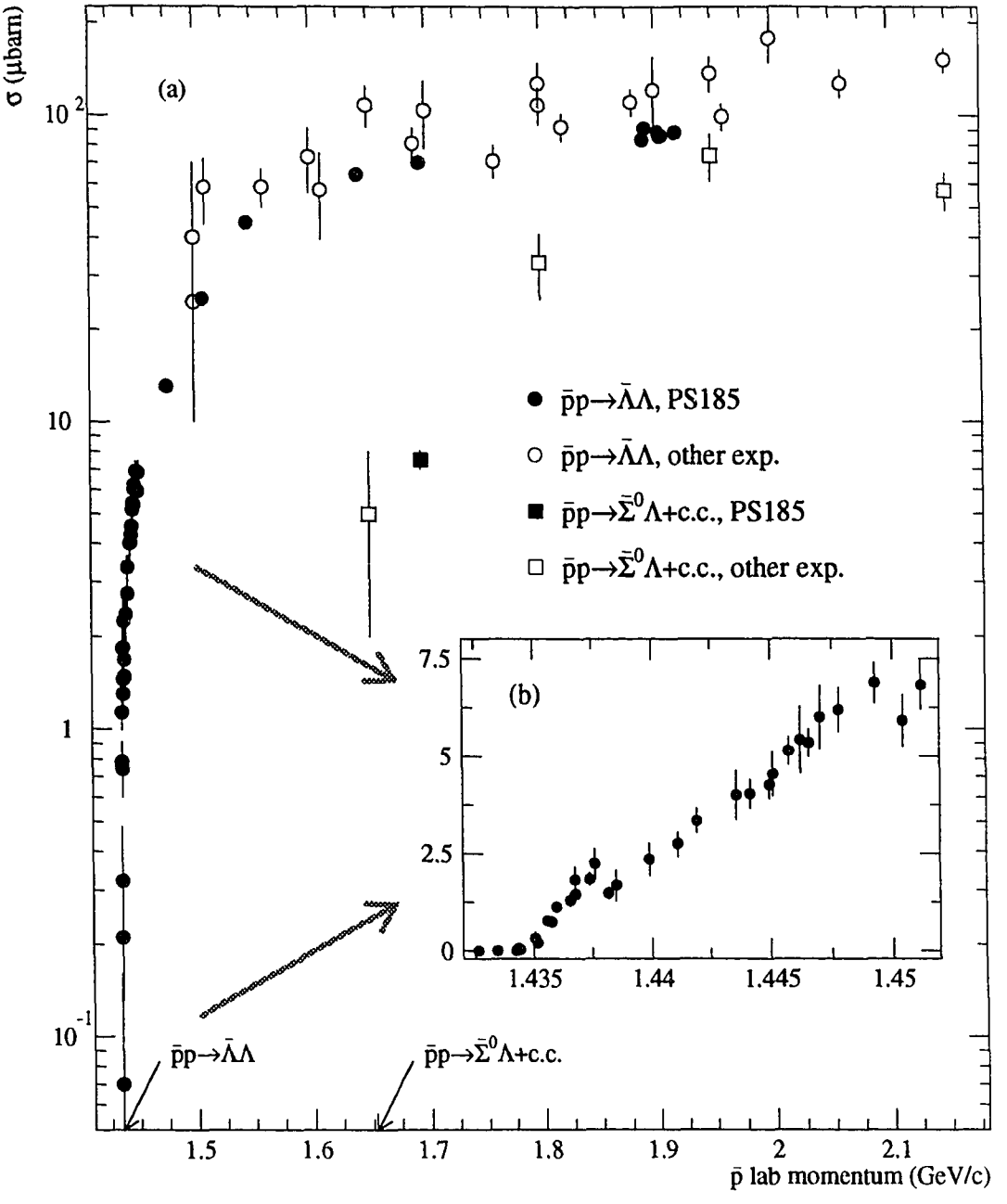

Figure 1.3: The (a) total cross sections for the reactions $\overline{p}p \rightarrow \overline{\Lambda}\Lambda$ and $\overline{p}p \rightarrow \overline{\Sigma}^0\Lambda + c.c.$ as measured by the PS185 experiment and others in the region near reaction threshold and (b) total cross sections for the reaction $\overline{p}p \rightarrow \overline{\Lambda}\Lambda$ within a smaller momentum range around threshold and with a linear scale. The arrows on the momentum axis point out the reaction thresholds.

almost exclusively in a spin triplet state.

1.5.3 PS185 $\bar{p}p \to \overline{\Sigma}^0\Lambda + c.c.$ Data

Previous to this work, the reaction $\bar{p}p \to \overline{\Sigma}^0\Lambda + c.c.$ has been measured by PS185 [31], but at only one momentum point and with less-than-optimum statistics. The total cross section result is shown in Fig. 1.3 along with the $\bar{p}p \to \overline{\Lambda}\Lambda$ data and other measurements of $\bar{p}p \to \overline{\Sigma}^0\Lambda + c.c.$. The differential cross section at 1.695 GeV/c is shown in Fig. 1.7(a). As in the $\bar{p}p \to \overline{\Lambda}\Lambda$ channel, this data shows a strong forward-peaked differential cross section. The limited statistical precision of this measurement did not allow for a precise determination of the hyperon polarizations, as can be seen from Figs. 1.7(b) and 1.7(c). No extraction of the spin correlation coefficients was possible.

1.6 What Has Been Learned?

The high-quality $\bar{p}p \to \overline{\Lambda}\Lambda$ data presented by PS185 has lead to considerable advances in understanding the dynamics of strangeness production in this channel. The most striking feature – the forward-peaking of the differential cross section data – indicate that this is a highly peripheral process. It is perhaps surprising that this behavior persists down to near threshold where the final-state hyperons in the c.m. system leave the interaction region with only a few MeV of kinetic energy. In fact, much can be learned by examining the data in the context of scattering from an absorbing (black) disk.

In the black disk model [32, 33], the differential cross section, as a function of the four-momentum transfer (squared) t, should have the form e^{-bt}, where b is the radius of the disk. As can be seen from the plots in Fig. 1.4 the data is fairly well described in the forward region with an exponential form. If fit to this form, b takes on the value of about 9 GeV^{-2} and is fairly independent of the momentum. This

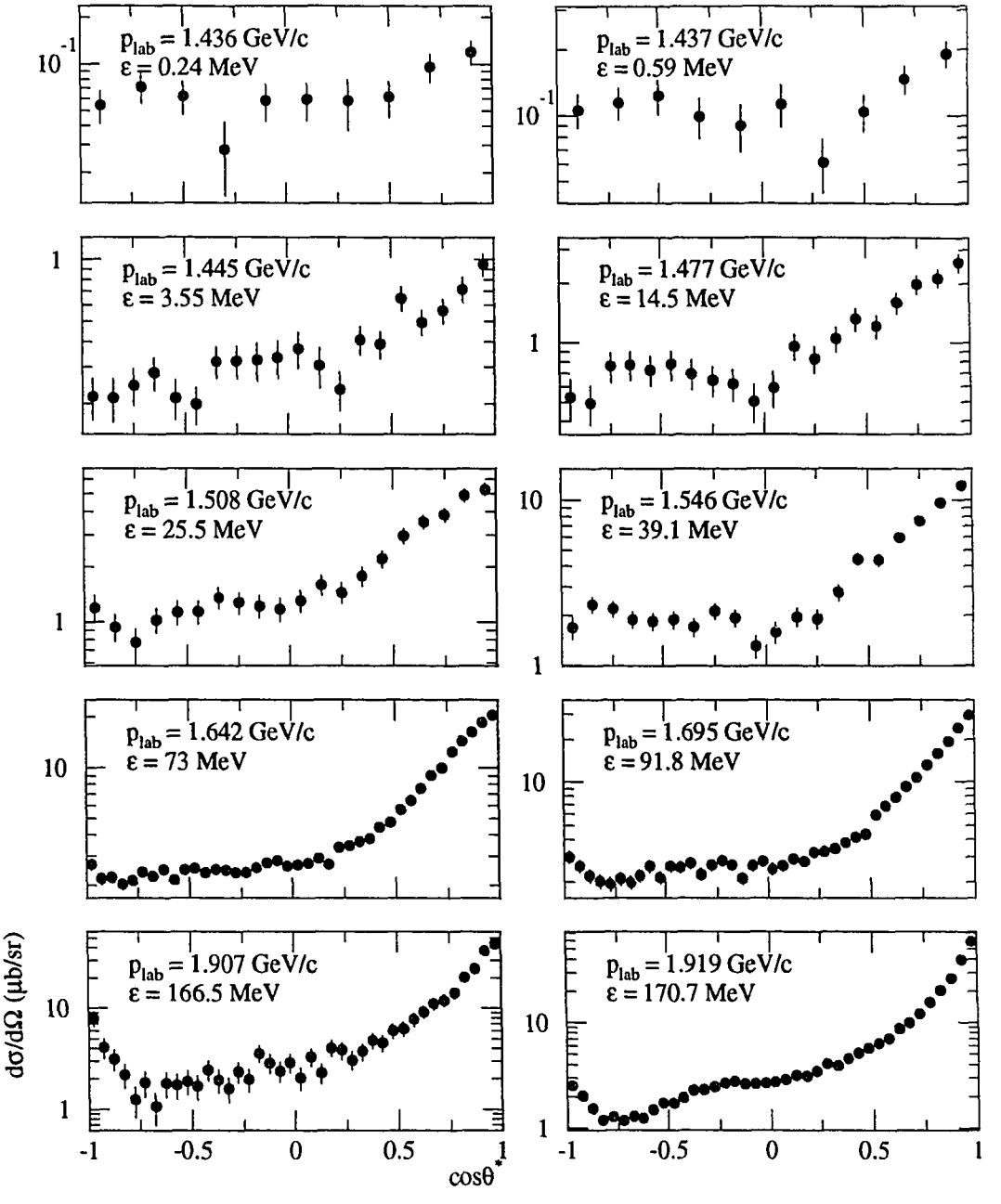

Figure 1.4: Differential cross sections as a function of the cosine of the c.m. scattering angle, $\cos\theta^*$, for the $\overline{p}p \rightarrow \overline{\Lambda}\Lambda$ reaction for a range of momenta near reaction threshold. The antiproton momenta and excess energy values are tabulated on each plot.

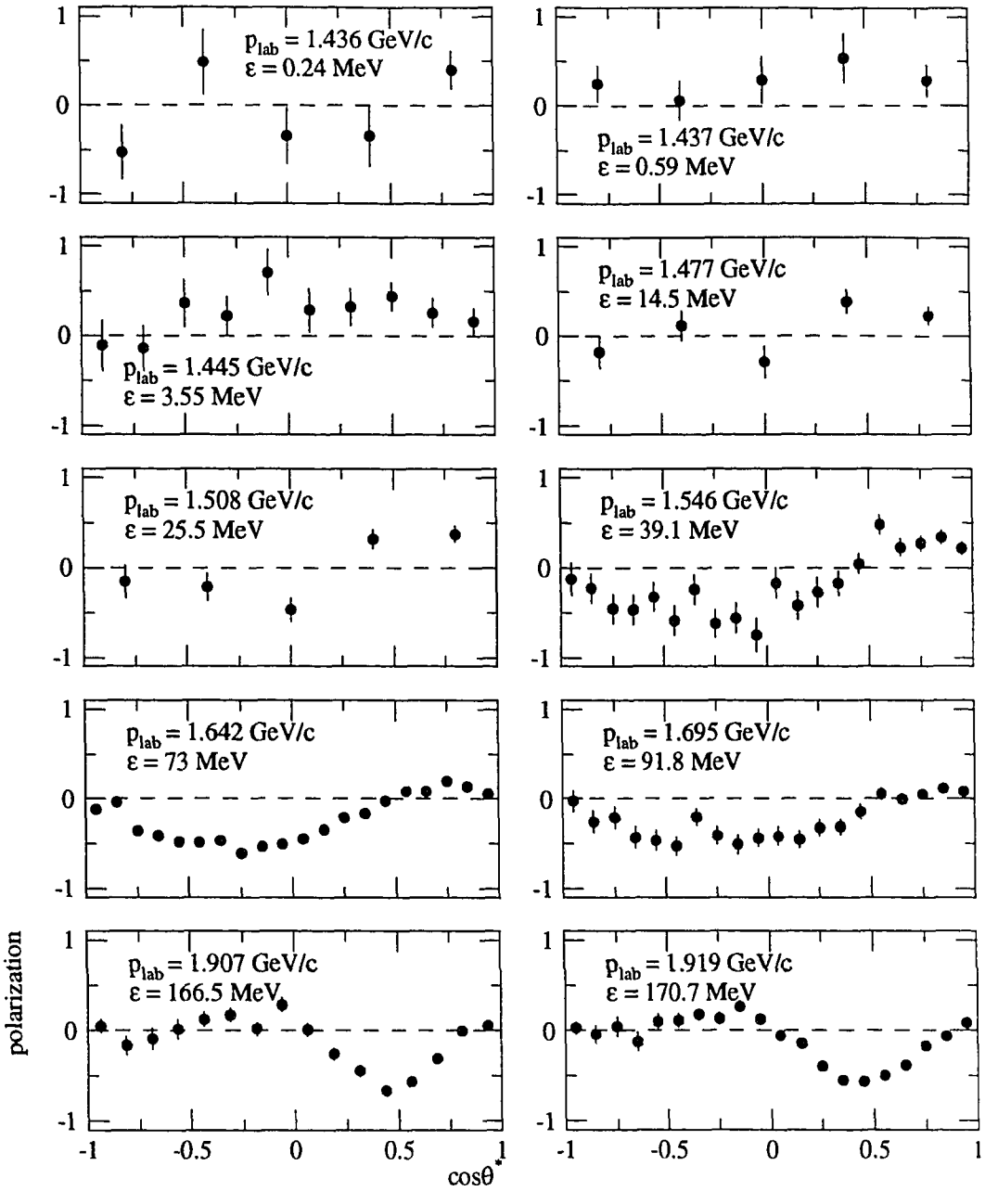

Figure 1.5: Average Λ and $\overline{\Lambda}$ polarization values in the $\bar{p}p \rightarrow \overline{\Lambda}\Lambda$ reaction for a range of momenta near reaction threshold. The antiproton momenta and excess energy values are tabulated on each plot and correspond to those in Fig. 1.4.

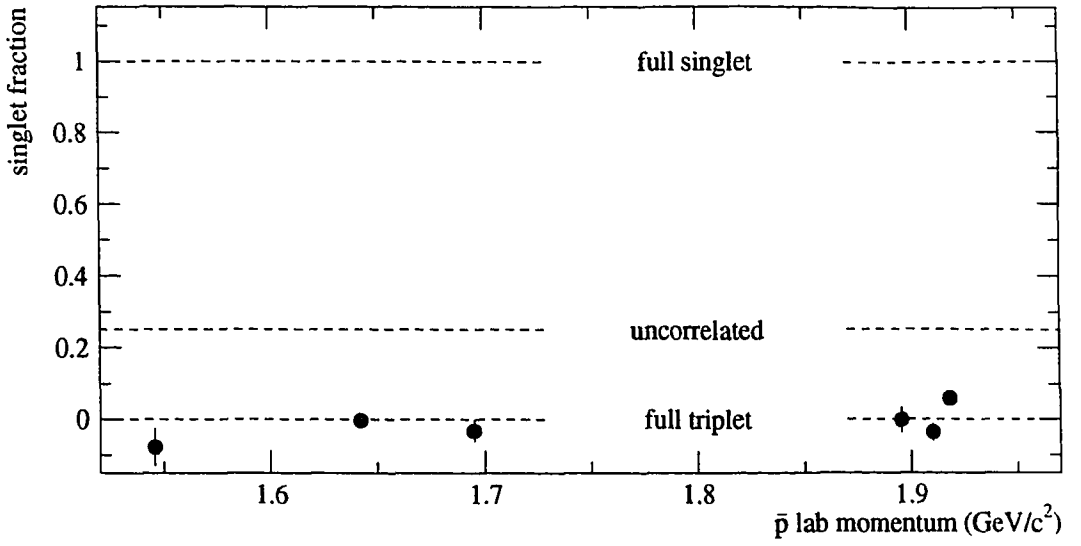

Figure 1.6: Singlet fraction for the $\overline{p}p \rightarrow \overline{\Lambda}\Lambda$ reaction. The dashed lines show the expected values for three different $\overline{\Lambda}\Lambda$ spin configurations.

corresponds to a disk radius ($R = 2\hbar c\sqrt{b}$) of approximately 1.2 fm. The fact that the data are fairly well described with this simple model is most probably due to the strong effects of annihilation. More central $\overline{p}p$ collisions couple to other channels such as multi-pion production. It is interesting to note that this model describes other reactions involving strange particles such as $\pi^- p \rightarrow K^0\Lambda$ and $K^- p \rightarrow \pi^0\Lambda$ with similar values for b [32]. In terms of a partial-wave decomposition, the forward peaking is described by a relatively large contribution from the higher partial waves due to the absorption of the small-impact-parameter low partial waves. This is also seen in the total cross section data as both S and P waves are needed to describe the threshold behavior.

However, a simple scattering model such as a black disk falls short in explaining the behavior of polarization data. Although, it is interesting to note that the polarization zero-crossing that is present in the $\overline{p}p \rightarrow \overline{\Lambda}\Lambda$ polarization data occurs at the same value of $\cos\theta^*$ as the slope change in the differential cross section data. This

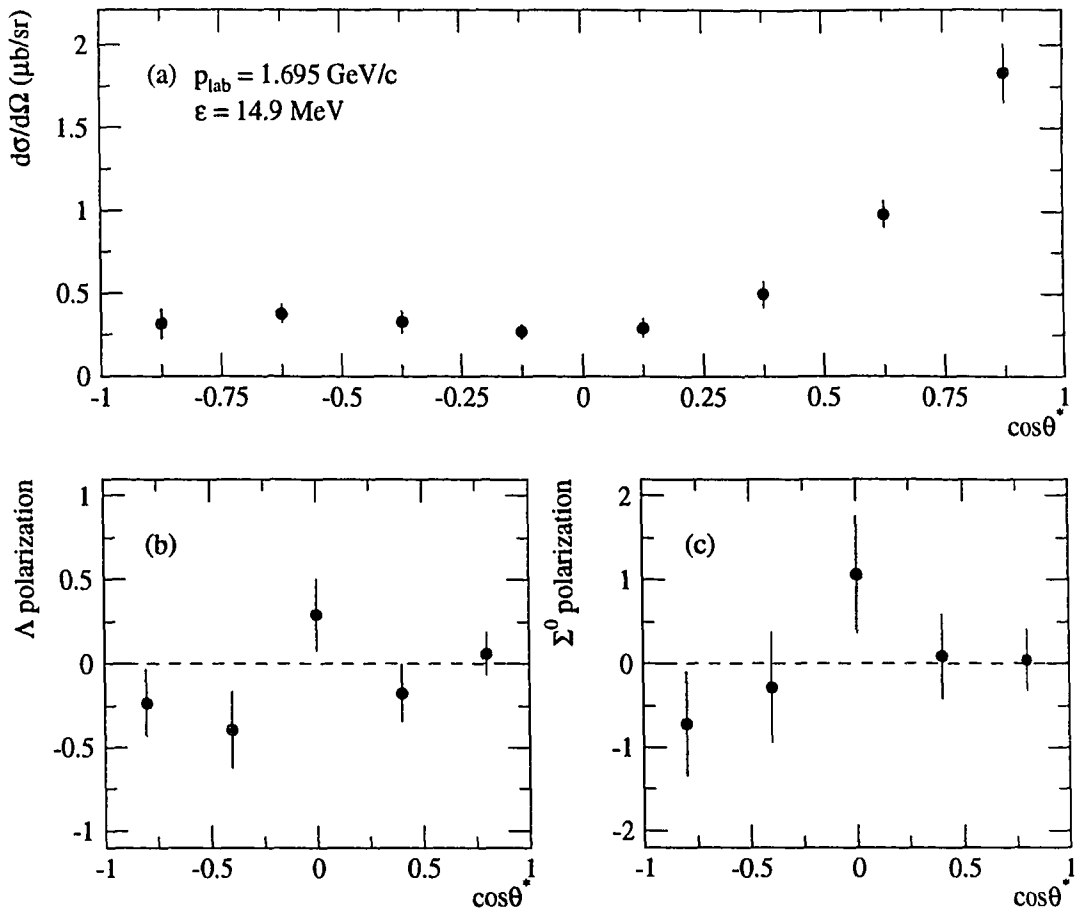

Figure 1.7: The (a) differential cross section, (b) Λ polarization, and (c) Σ^0 polarization for the $\bar{p}p \rightarrow \overline{\Sigma}^0\Lambda + c.c.$ reaction at an antiproton momentum of 1.695 GeV/c.

can be seen by examining Figs. 1.4 and 1.5 together. This correlation is observed in other hadron scattering processes and may be related to the distance scale of the interaction [34,35]. In terms of partial waves, the angular behavior of the polarization data (as well as the spin correlation coefficients) sets constraints amongst the amplitudes that allow conclusions about the nature of the forces involved [36]. This is discussed further in Chapter 3. The singlet fraction data shows that the reaction produces the $\overline{\Lambda}\Lambda$ pair in a spin triplet state throughout the entire momentum range

investigated by PS185. This is such a fundamental feature that it has come to be considered a dynamical selection rule [37] and is an indication of the presence of a strong tensor force.

The lone PS185 $\bar{p}p \rightarrow \overline{\Sigma}^0\Lambda + c.c.$ measurement shows a differential cross section with forward peaking similar in shape to those of $\bar{p}p \rightarrow \overline{\Lambda}\Lambda$. When plotted as a function of t and fit to the black disk form e^{-bt}, the resulting value for b is approximately 14 GeV^{-2}, somewhat larger than in the $\bar{p}p \rightarrow \overline{\Lambda}\Lambda$ channel. This corresponds to a black disk radius of about 1.5 fm, perhaps evidence for stronger absorption in this channel. Unfortunately, the statistical errors on the polarizations from this data set allow no significant conclusions to be reached.

1.7 A Measurement of $\bar{p}p \rightarrow \overline{\Sigma}^0\Lambda + c.c.$ and $\bar{p}p \rightarrow \overline{\Lambda}\Lambda$

The somewhat incomplete data set on $\bar{p}p \rightarrow \overline{\Sigma}^0\Lambda + c.c.$ leaves many questions about this channel unanswered. Does this reaction exhibit the same peripheralism down to threshold as does $\bar{p}p \rightarrow \overline{\Lambda}\Lambda$? Is the polarization structure the same? And, what will the singlet fraction show? These are the questions that the PS185 collaboration set out to answer with the expansion of the $\bar{p}p \rightarrow \overline{Y}Y$ program to include the $\bar{p}p \rightarrow \overline{\Sigma}^0\Lambda +$ *c.c.* channel. The goal was to investigate this new strangeness production channel in the near-threshold region with as high precision as was achieved for $\bar{p}p \rightarrow \overline{\Lambda}\Lambda$.

This task was not just a simple extension of the $\bar{p}p \rightarrow \overline{\Lambda}\Lambda$ program. The reactions $\bar{p}p \rightarrow \overline{\Sigma}^0\Lambda + c.c.$ and $\bar{p}p \rightarrow \overline{\Lambda}\Lambda$ are topologically very similar: they look much alike in the detector. And, since the beam momentum threshold for $\bar{p}p \rightarrow \overline{\Lambda}\Lambda$ is around 200 MeV/c lower than for $\bar{p}p \rightarrow \overline{\Sigma}^0\Lambda + c.c.$, the cross section of $\bar{p}p \rightarrow \overline{\Lambda}\Lambda$ is relatively large in the momentum region where the $\bar{p}p \rightarrow \overline{\Sigma}^0\Lambda + c.c.$ reaction is near threshold and has a small cross section. This results in the potential for a background from $\bar{p}p \rightarrow \overline{\Lambda}\Lambda$ contaminating the $\bar{p}p \rightarrow \overline{\Sigma}^0\Lambda + c.c.$ measurement. A more subtle, yet equally detrimental, problem is the possibility of misidentifying a $\bar{p}p \rightarrow \overline{\Sigma}^0\Lambda$ event

as a $\bar{p}p \rightarrow \overline{\Lambda}\Sigma^0$ and vice versa. Although the observables of these reactions are equivalent, according to charge conjugation symmetry, as is discussed in Chapter 2, a misidentification of this type can distort the angular distributions.

To reduce the effects of these problems, the PS185 detector was upgraded with two new detector components. These new components increased the kinematic resolution of the apparatus, thus allowing a measurement of $\bar{p}p \rightarrow \overline{\Sigma}^0\Lambda + c.c.$ with quality approaching that of the $\bar{p}p \rightarrow \overline{\Lambda}\Lambda$ channel. A set of silicon microstrips installed immediately upstream of the target enabled a precise measurement of the incident antiproton so that the intial state kinematics could be more tightly constrained. Also, a lead/scintillating-fiber calorimeter was added to the apparatus to allow the detection of the Σ^0-decay photon which further constrains the reaction kinematics.

In addition to the hardware improvements to the PS185 detector, significant additions to the analysis software were implemented. Even though the misidentification problems discussed above were mitigated through the use of the new detectors, they still remained at a level where corrections were needed. This was achieved with a new and elaborate detector-simulation program and reaction misidentification correction methods. Together, they improved the analysis chain in order to produce results with satisfactory systematic errors.

The $\bar{p}p \rightarrow \overline{\Sigma}^0\Lambda + c.c.$-dedicated runs occurred in November 1989 and April 1990 at six different antiproton momentum settings in the $\bar{p}p \rightarrow \overline{\Sigma}^0\Lambda + c.c.$ threshold region corresponding to excess energy values from 40 down to 0 MeV. Although the descriptions of the theory, experiment, and analysis techniques are relevant for all of the data collected in these runs, the final results reported here are for only one of the six points, at an antiproton momentum of 1.729 GeV/c. As the analysis of the $\bar{p}p \rightarrow \overline{\Lambda}\Lambda$ channel is very similar to that of $\bar{p}p \rightarrow \overline{\Sigma}^0\Lambda + c.c.$ and it is present in the data collected, the analysis and results from this channel are reported in parallel with that of $\bar{p}p \rightarrow \overline{\Sigma}^0\Lambda + c.c.$.

Following this introductory chapter is Chapter 2 which describes the physics ob-

servables, the constraints imposed on them by the strong interaction symmetries, and how these observables are extracted from the data. Chapter 3 contains a discussion of the theory and summaries of a few of the "state-of-the-art" models constructed to explain the PS185 $\bar{p}p \to \overline{Y}Y$ data. In Chapter 4 the topology of the $\bar{p}p \to \overline{\Lambda}\Lambda$ and $\bar{p}p \to \overline{\Sigma}^0\Lambda + c.c.$ reactions is explained and the PS185 detector which was designed to reconstruct these reactions is described. Chapter 5 details the process of taking the experimental data from raw detector information to final results for the total and differential cross sections and Chapter 6 explains the procedure to extract the spin observables. Then, in Chapter 7, the results are presented and their meaning interpreted. Chapter 8 concludes the report with a summary and look to the future.

Chapter 2

Observables

An experimental study of $\overline{Y}Y$ production must include a report of what is seen through the lens of the strong-interaction "microscope". This is accomplished though the use of the $\overline{p}p \to \overline{Y}Y$ observables, which quantify, in well-defined and conventional terms, what is seen in the $\overline{p}p \to \overline{\Lambda}\Lambda$ and $\overline{p}p \to \overline{\Sigma}^0\Lambda + c.c.$ reactions. In this chapter, the observables and necessary framework are explained. The constraints on the observables imposed by the symmetries of the interaction are explained and catalogued. The density matrix formalism is then introduced and utilized to analyze the hyperon decays and to obtain the $\overline{p}p \to \overline{Y}Y$ spin observables in terms of the reconstructed antiproton and proton momentum vectors.

2.1 Definitions of the Observables

2.1.1 Cross Section

The cross section σ for a reaction is defined as the reaction rate per unit incident flux per target particle [33]. As implied by the name, a cross section has dimensions of area and is usually reported in units of barns (1 barn = $10^{-28}\mathrm{m}^2$). In a classical sense, it represents the scattering area per target particle (for a specific reaction channel) seen by the incident particle. When measured in the experiment, it is calculated via $\sigma = N/\int \mathcal{L}\,dt$, where N is the number of events for a reaction that occurred and $\int \mathcal{L}\,dt$ is the luminosity (beam flux per target particle) integrated over the running

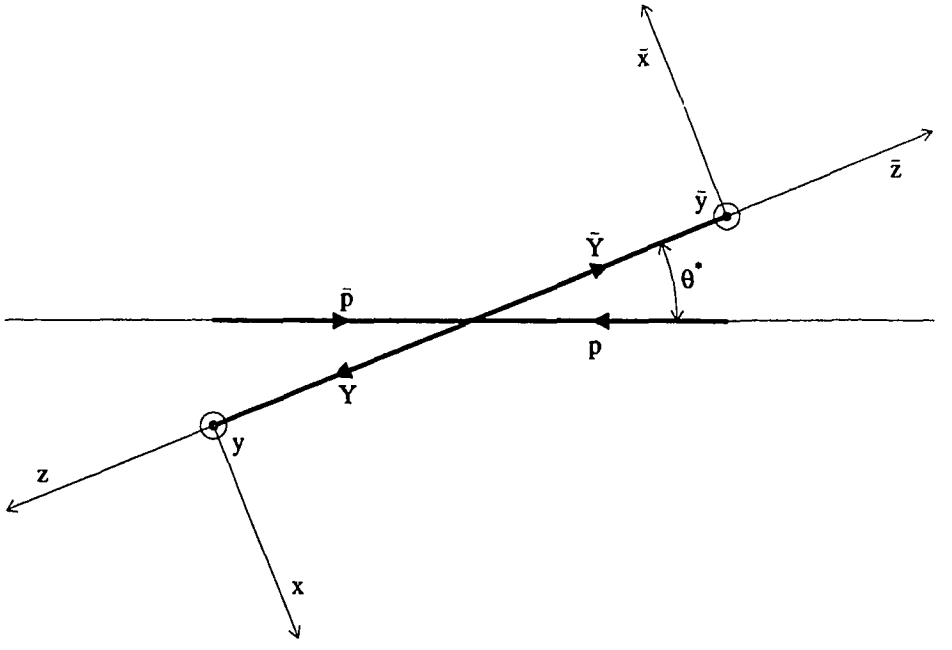

Figure 2.1: A diagram of the $\bar{p}p \rightarrow \overline{Y}Y$ reaction in the center of momentum (c.m.) system illustrating the production angle θ^* and the two coordinate systems used for the spin observable measurements. The reaction is contained in the $\bar{x}\bar{z}$, xz planes and the $\bar{y}$ and y axes are directed out of the plane of the page.

time of the experiment.

The differential cross section $d\sigma/d\Omega$ is the cross section per unit solid angle. It is not a Lorentz-invariant quantity and must be quoted in a specific reference frame. All differential cross sections reported in this work are the values in the center of momentum (c.m.) frame. Due to the azimuthal symmetry of the collision geometry, $d\sigma/d\Omega$ is completely specified (at a fixed collision energy) by the c.m. production angle θ^*. This is the angle, in the c.m. frame, between the initial-state antiproton and the final-state *antiparticle*, as diagramed in Fig. 2.1. The angle θ^* is the $\bar{p} - \overline{\Lambda}$ angle for the $\bar{p}p \rightarrow \overline{\Lambda}\Lambda$ and $\bar{p}p \rightarrow \overline{\Lambda}\Sigma^0$ channels and the $\bar{p} - \overline{\Sigma}^0$ angle for $\bar{p}p \rightarrow \overline{\Sigma}^0\Lambda$. This particular choice is the most sensible due to the constraints imposed by charge conjugation symmetry.

2.1.2 Polarization

The vector polarization $\mathbf{P} = (P_x, P_y, P_z)$ of a particle is defined as the expectation value of the spin operator $\mathbf{J} = (J_x, J_y, J_z)$ normalized to have a maximum magnitude of 1:

$$\mathbf{P} = \frac{\langle \mathbf{J} \rangle}{j}, \tag{2.1}$$

where j is the spin of the particle [32]. This definition is restricted to the particle rest frame since the operator $\mathbf{J}$ depends on the selection of the axis of quantization and it is problematic to make this selection for relativistic particles.

The coordinate systems that are used to define the polarization and spin correlation coefficients are illustrated in Fig. 2.1. These two systems, one for the $\overline{Y}$ and one for the Y, are fixed to the rest frame of each particle. The $\bar{z}$ and z axes are along the direction of motion of the respective hyperon and the $\bar{y}$ and y axes are normal to the production plane along a vector given by $\mathbf{p}_{\overline{p}} \times \mathbf{p}_{\overline{Y}}$ where $\mathbf{p}_{\overline{p}}$ and $\mathbf{p}_{\overline{Y}}$ are the momentum vectors of the $\overline{p}$ and $\overline{Y}$. The $\bar{x}$ and x axes are then fixed by requirement that the coordinate systems are right-handed and orthogonal. In the remainder of this chapter, the "bar" notation on the axes of the $\overline{Y}$ system is dropped; this causes no ambiguity since the $\overline{Y}$ (Y) is always measured with respect to the $\bar{x}\bar{y}\bar{z}$ (xyz) system.

These coordinate definitions are quite natural when using the helicity formalism [38,39]. The helicity of a particle is unchanged by a Lorentz transformation along the direction of motion, so the helicity states correspond to the rest frame spin states calculated for the axes shown in Fig. 2.1. This allows for simple calculation of the spin observables, defined in the individual particle rest frames, using helicity states, calculated in the c.m. system.

2.1.3 Spin Correlation Coefficients

The spin correlation coefficients C_{ij} quantify the correlations between the spin projection i of particle 1 and the spin projection j of particle 2. They are defined:

$$C_{ij} = \frac{\langle J_i^{(1)} J_j^{(2)} \rangle}{j_1 j_2}. \tag{2.2}$$

The C_{ij} have maximum magnitude of 1 and the convention is to label the antiparticle (index i) as particle 1. For example, the spin correlation coefficient C_{xy}, applied to the $\overline{Y}Y$ system, is a measure of the correlation between the x projection of the $\overline{Y}$ spin with the y projection of the Y spin. Note that, with the choice of coordinate systems as shown in Fig. 2.1, there will be a sign difference for C_{xx}, C_{zz}, C_{xz}, and C_{zx} when compared to a measurement where the same orientation of coordinate systems are used for both the $\overline{Y}$ and Y.

An additional quantity reported is the singlet fraction S. It is the expectation value of the singlet operator $\hat{S}$:

$$S = \langle \hat{S} \rangle = \frac{1}{4} \langle 1 - \mathbf{J}^{(1)} \cdot \mathbf{J}^{(2)} \rangle. \tag{2.3}$$

And, in terms of the C_{ij}, the singlet fraction is

$$S = \frac{1}{4}(1 + C_{xx} - C_{yy} + C_{zz}). \tag{2.4}$$

The singlet fraction is a measure of the $\overline{Y}Y$ combined spin state and is constrained by $0 \leq S \leq 1$. For the $\overline{Y}Y$ system in a pure spin singlet state, $S = 1$, and for a pure spin triplet, $S = 0$. A system with completely uncorrelated spins would yield $S = \frac{1}{4}$.

2.2 C and P Symmetries

The assumption of invariance of the strong interaction under the parity (P) and charge-conjugation (C) transformations, along with rotational symmetry at $\theta^* = 0$ and π, imposes a number of constraints between the observables of the three $\overline{p}p \rightarrow$

$\overline{Y}Y$ channels [39]. These constraints may then be used to reduce the number of independent observables and to check that the experimental data follows the correct behavior.

The assumption of C invariance of the strong interaction implies that the differential cross section at a given θ^* for a reaction and its charge conjugate will be equal. This adds no restrictions for the charge self-conjugate $\overline{p}p \to \overline{\Lambda}\Lambda$ reaction. However, for $\overline{p}p \to \overline{\Sigma}^0\Lambda$ and $\overline{p}p \to \overline{\Lambda}\Sigma^0$, this yields the constraint, for all θ^*,

$$\frac{d\sigma}{d\Omega}(\overline{\Sigma}^0\Lambda) = \frac{d\sigma}{d\Omega}(\overline{\Lambda}\Sigma^0). \tag{2.5}$$

This, of course, implies that

$$\sigma(\overline{\Sigma}^0\Lambda) = \sigma(\overline{\Lambda}\Sigma^0). \tag{2.6}$$

The notation indicating each reaction channel in these and the following equations has been shortened by writing explicitly only the final state hyperons.

Invariance under C also requires that the polarization of the antihyperon produced at a c.m. angle θ in one reaction is equal to that of the hyperon produced at $\pi - \theta$ in the charge conjugate reaction. And since θ^* is defined with respect to the *antihyperon* in all reaction channels, the following constraints are imposed on the polarizations for all θ^*:

$$\mathbf{P}_{\overline{\Lambda}}(\overline{\Lambda}\Lambda) = \mathbf{P}_{\Lambda}(\overline{\Lambda}\Lambda), \tag{2.7}$$

$$\mathbf{P}_{\overline{\Sigma}^0}(\overline{\Sigma}^0\Lambda) = \mathbf{P}_{\Sigma^0}(\overline{\Lambda}\Sigma^0), \tag{2.8}$$

$$\mathbf{P}_{\overline{\Lambda}}(\overline{\Lambda}\Sigma^0) = \mathbf{P}_{\Lambda}(\overline{\Sigma}^0\Lambda). \tag{2.9}$$

The same arguments lead to the conclusion that the spin correlation coefficient C_{ij} for a reaction is equal to C_{ji} for the charge-conjugate reaction. This results in the constraints,

$$C_{ij}(\overline{\Lambda}\Lambda) = C_{ji}(\overline{\Lambda}\Lambda), \tag{2.10}$$

$$C_{ij}(\overline{\Sigma}^0\Lambda) = C_{ji}(\overline{\Lambda}\Sigma^0). \tag{2.11}$$

The assumption of P invariance in the strong interaction, along with the fact that the initial-state $\overline{p}p$ system is unpolarized, implies that there can be no polarization of the final-state hyperons in the production (xz) plane:

$$P_{x,\overline{Y}} = P_{z,\overline{Y}} = P_{x,Y} = P_{z,Y} = 0. \tag{2.12}$$

Only P_y is physically allowed to be non-zero. This is equivalent to the well-known rule that the polarization must be normal to the production plane. These assumptions also yield the conclusion that the spin correlation coefficients between the direction normal $(\hat{y})$ to the production plane and those coplanar ($\hat{x}$ and $\hat{z}$) must be zero:

$$C_{xy} = C_{yx} = C_{yz} = C_{zy} = 0, \tag{2.13}$$

for all three $\overline{p}p \to \overline{Y}Y$ reaction channels.

At $\theta^* = 0$ and π the production plane is ill-defined, so there must be a symmetry between the x and y directions. This implies, along with P conservation, that for $\theta^* = 0$ and π

$$P_{y,\overline{Y}} = P_{y,Y} = 0, \tag{2.14}$$

$$C_{xz} = C_{zx} = 0, \tag{2.15}$$

$$C_{xx} = -C_{yy}. \tag{2.16}$$

Again, these constraints are for all three $\overline{p}p \to \overline{Y}Y$ channels. The relative -1 in the last equation arises because of the choice of coordinate systems (the x axes have a different relative orientation compared to the y axes in the $\overline{Y}$ and Y systems, see Fig. 2.1).

The constraint on the $\overline{p}p \to \overline{\Sigma}^0\Lambda$ and $\overline{p}p \to \overline{\Lambda}\Sigma^0$ differential cross sections (Eq. 2.5) is imposed, after examining the channels separately, by averaging the values for these two channels to obtain one $\overline{p}p \to \overline{\Sigma}^0\Lambda + c.c.$ differential cross section as the reported observable. The constraint equations for the spin observables, Eqs. 2.7–2.13, leave

five independent quantities for $\overline{p}p \to \overline{\Lambda}\Lambda$ that contain the spin state information of the system: $P_{y,\Lambda}$, C_{xx}, C_{yy}, C_{zz}, and C_{xz}. For the charge conjugate channels $\overline{p}p \to \overline{\Sigma}^0\Lambda$ and $\overline{p}p \to \overline{\Lambda}\Sigma^0$ combined, seven spin observables are needed: $P_{y,\Sigma}$, $P_{y,\Lambda}$, C_{xx}, C_{yy}, C_{zz}, C_{xz}, and $C_{zx,}$. This reduction, which is due to the constraints imposed by the C and P symmetries is exploited in the final data analysis by averaging the spin observables that are required to be equal. The constraints on the spin observables at $\theta^* = 0$ and π (Eqs. 2.14–2.16) are used to verify that the measured quantities are consistent with the required symmetries.

2.3 Density Matrix Formalism

The density matrix formalism allows for a convenient description of systems that are a mixed ensemble of spin states such as a beam of antiprotons or a collection of hyperons [32,40]. It provides a convenient way to calculate the $\overline{Y}Y$ observables, to analyze the hyperon decays and to relate the angular distributions of the decay products in terms of the $\overline{Y}Y$ spin observables.

2.3.1 Definition

A mixed ensemble may be described as a mixture of states $|\psi_i\rangle$ each with a fractional weight w_i. The average of an observable A over this ensemble is [40]

$$\langle A \rangle = \sum_i w_i \langle \psi_i | A | \psi_i \rangle. \tag{2.17}$$

This can be rewritten using sums over a general set of basis states $|\chi\rangle$:

$$\langle A \rangle = \sum_i w_i \sum_{\chi'} \sum_{\chi''} \langle \psi_i | \chi' \rangle \langle \chi' | A | \chi'' \rangle \langle \chi'' | \psi_i \rangle \tag{2.18}$$

$$= \sum_{\chi'} \sum_{\chi''} \left(\sum_i w_i \langle \chi'' | \psi_i \rangle \langle \psi_i | \chi' \rangle \right) \langle \chi' | A | \chi'' \rangle. \tag{2.19}$$

Then, defining the density matrix ρ with elements

$$\langle \chi' | \rho | \chi'' \rangle = \sum_i w_i \langle \chi'' | \psi_i \rangle \langle \psi_i | \chi' \rangle, \tag{2.20}$$

and using the matrix representation of A ($\langle\chi'|A|\chi''\rangle$), the ensemble average of A may be written in the simple form,

$$\langle A\rangle = \mathrm{Tr}\rho A. \tag{2.21}$$

This is a powerful relation: the states of the system are completely described by the density matrix ρ, the matrices ρ and A can be evaluated using any convenient basis, and the ensemble average of an observable is found by simply taking the trace of a product of matrices.

In Eq. 2.21 it is assumed that ρ is normalized such that $\mathrm{Tr}\rho = 1$. This is easily realized if the state probabilities w_i satisfy $\sum w_i = 1$. Another common approach is to choose the normalization such that $\mathrm{Tr}\rho$ is equal to a constant such as the differential cross section. In this case, Eq. 2.21 is slightly modified:

$$\langle A\rangle = \frac{\mathrm{Tr}\rho A}{\mathrm{Tr}\rho}. \tag{2.22}$$

Applying this formalism to describe the spin states of a system yields several useful relations. Using the density matrix, the vector polarization can be expressed as

$$\mathbf{P} = \frac{\langle \mathbf{J}\rangle}{j} = \frac{\mathrm{Tr}\rho\mathbf{J}}{j}. \tag{2.23}$$

If the system is a spin-$\frac{1}{2}$ particle, the matrix representation of $\mathbf{J}$ is $\frac{1}{2}\boldsymbol{\sigma}$, where $\boldsymbol{\sigma}$ is the vector of Pauli matrices, and the polarization can be written in the simple form,

$$\mathbf{P} = \mathrm{Tr}\rho\boldsymbol{\sigma}. \tag{2.24}$$

Conversely, the spin-$\frac{1}{2}$ density matrix can be written in terms of the polarization, the Pauli matrices, and the identity matrix $\mathcal{I}$:

$$\rho = \frac{1}{2}(\mathcal{I} + \mathbf{P}\cdot\boldsymbol{\sigma}). \tag{2.25}$$

These relations are used in the following sections to determine the density matrices and polarizations of the particles in the $\overline{Y}Y$ decay chain.

2.3.2 The Density Matrix for the $\overline{p}p \rightarrow \overline{Y}Y$ Reaction

The density matrix formalism introduced above and applied to a spin-$\frac{1}{2}$ particle can be extended to describe a system of two spin-$\frac{1}{2}$ particles such as the initial-state $\overline{p}p$ and final-state $\overline{Y}Y$ systems. The (4×4) density matrix for the initial-state $\overline{p}p$ system, since the beam and target are prepared in an uncorrelated manner, can be written as an outer product in a separable form [41],

$$\rho_{\overline{p}p} = \frac{1}{4}(\mathcal{I}^{\overline{p}} + \boldsymbol{\sigma}^{\overline{p}} \cdot \mathbf{P}_{\overline{p}}) \otimes (\mathcal{I}^{p} + \boldsymbol{\sigma}^{p} \cdot \mathbf{P}_{p}). \tag{2.26}$$

And since, for the PS185 experiment, both beam and target are unpolarized, this expression reduces to

$$\rho_{\overline{p}p} = \frac{1}{4}(\mathcal{I}^{\overline{p}} \otimes \mathcal{I}^{p}), \tag{2.27}$$

which is just $\frac{1}{4}$ times the 4×4 identity matrix. The normalization has been chosen such that $\mathrm{Tr}\rho_{\overline{p}p} = 1$.

For the final-state $\overline{Y}Y$ system, because of the production mechanism, the density matrix can not be written in a separable form. Instead, it is expressed as

$$\rho_{\overline{Y}Y} = \frac{\mathcal{R}}{4}\left(\mathcal{I}^{\overline{Y}} \otimes \mathcal{I}^{Y} + \mathbf{P}_{\overline{Y}} \cdot \boldsymbol{\sigma}^{\overline{Y}} \otimes \mathcal{I}^{Y} + \mathcal{I}^{\overline{Y}} \otimes \boldsymbol{\sigma}^{Y} \cdot \mathbf{P}_{Y} + \sum_{i,j=1}^{3} C_{ij}(\sigma_i^{\overline{Y}} \otimes \sigma_j^{Y})\right) \tag{2.28}$$

$$= \frac{\mathcal{R}}{4}\sum_{\mu,\nu=0}^{3} C_{\mu\nu}(\sigma_\mu^{\overline{Y}} \otimes \sigma_\nu^{Y}), \tag{2.29}$$

where the $\mathbf{P}_{\overline{Y}}$, $\mathbf{P}_{Y}$, and C_{ij} are the antihyperon, hyperon polarizations and spin-correlation coefficients. The $\sigma_\mu^{\overline{Y}} \otimes \sigma_\nu^{Y}$ are the 16 independent Hermitian matrices formed by the outer products of the 2×2 identity matrix (σ_0) and the three Pauli matrices ($\sigma_{i=1,3}$) [41,42]. The $C_{\mu\nu}$ are elements of a combined spin observables matrix with $C_{00} = 1$, $C_{i0} = P_{i,\overline{Y}}$, $C_{0j} = P_{j,Y}$, and the remaining $C_{\mu\nu}$ are the spin correlation coefficients C_{ij}. It is important to remember that, most generally, $\rho_{\overline{Y}Y}$ and the spin observables are functions of the the c.m. scattering angle θ^*. The normalization of $\rho_{\overline{Y}Y}$ has been chosen such that $\mathrm{Tr}\rho_{\overline{Y}Y} = \mathcal{R}$ and may be conveniently identified with

the differential cross section. Equation 2.29 is particularly handy since it contains a complete description of the spin states of the $\overline{Y}Y$ system in a compact form. The $\overline{Y}Y$ observables, in terms of the $\overline{Y}Y$ density matrix, are now easily calculated from the relations:

$$\mathcal{R} = \mathrm{Tr}(\rho_{\overline{Y}Y}), \tag{2.30}$$

$$\mathbf{P}_{\overline{Y}} = \frac{1}{\mathcal{R}}\mathrm{Tr}(\rho_{\overline{Y}Y}\boldsymbol{\sigma}^{\overline{Y}}), \tag{2.31}$$

$$\mathbf{P}_{Y} = \frac{1}{\mathcal{R}}\mathrm{Tr}(\rho_{\overline{Y}Y}\boldsymbol{\sigma}^{Y}), \tag{2.32}$$

$$C_{ij} = \frac{1}{\mathcal{R}}\mathrm{Tr}(\rho_{\overline{Y}Y}\sigma_i^{\overline{Y}} \otimes \sigma_j^{Y}). \tag{2.33}$$

The density matrix formalism also allows for a convenient way to describe the $\overline{p}p \rightarrow \overline{Y}Y$ transition. The final-state density matrix $\rho_{\overline{Y}Y}$ is obtained by operating on the initial-state density matrix $\rho_{\overline{p}p}$ with a (4×4) transition matrix $T(\theta^*)$ [41]:

$$\rho_{\overline{Y}Y} = T(\theta^*)\rho_{\overline{p}p}T(\theta^*)^\dagger. \tag{2.34}$$

The transition matrix contains all the information about the dynamics of the $\overline{p}p \rightarrow \overline{Y}Y$ reaction; each element quantifies the connection between the initial and final spin-states. Of course, the density matrix formalism does not prescribe how to calculate the elements of the transition matrix; that requires a model of the $\overline{p}p \rightarrow \overline{Y}Y$ reaction dynamics. But, once $T(\theta^*)$ is prescribed it is a relatively simple procedure to calculate the $\overline{Y}Y$ spin density matrix and then the $\overline{Y}Y$ observables. For example, starting with Eq. 2.30, the differential cross section can be calculated using the expressions developed for the density matrices:

$$\mathcal{R} = \frac{d\sigma}{d\Omega}(\theta^*) = \mathrm{Tr}(\rho_{\overline{Y}Y}) \tag{2.35}$$

$$= \mathrm{Tr}(T(\theta^*)\rho_{\overline{p}p}T(\theta^*)^\dagger) \tag{2.36}$$

$$= \frac{1}{4}\mathrm{Tr}(T(\theta^*)T(\theta^*)^\dagger). \tag{2.37}$$

And, the $\overline{Y}Y$ spin observables may be calculated in a similar fashion.

The expressions derived above relate the observables to $\rho_{\overline{Y}Y}$, and $\rho_{\overline{Y}Y}$ to the transition matrix $T(\theta^*)$. They allow a straightforward calculation of the observables from a theory that quantifies $T(\theta^*)$ and, conversely, allow constraints on $T(\theta^*)$ based on the measured values of the observables. The use of the density matrix formalism will be continued in the next sections to show how $\rho_{\overline{Y}Y}$ and the $\overline{Y}Y$ observables are obtained from the information gathered in the experiment.

2.4 Hyperon Decays

The Λ and $\overline{\Lambda}$ hyperons decay via the parity-violating weak interaction. The Λ decays 64% of the time through $\Lambda \to p\pi^-$ and the $\overline{\Lambda}$, through $\overline{\Lambda} \to \overline{p}\pi^+$ with the same branching fraction. The angular distribution of the decay products displays an asymmetry that is proportional to the polarization of the parent hyperon. A measurement of this asymmetry yields the Λ, $\overline{\Lambda}$ polarizations. The $\overline{p}p \to \overline{\Lambda}\Sigma^0$ and $\overline{p}p \to \overline{\Sigma}^0\Lambda$ reactions have the added complication of a Σ^0 ($\overline{\Sigma}^0$) in the final state which decays via the electromagnetic interaction to a Λ ($\overline{\Lambda}$) and a γ. The effect of this decay can be quantified and the relation between the polarizations of the parent Σ^0 and daughter Λ can be derived. Then the measurement of the daughter Λ decay angular asymmetry can be used to determine the polarization of the Σ^0. The density matrix formalism is used to describe these decays and derive the expressions that relate the measured angular distributions of the decay protons and antiprotons to the spin observables for the $\overline{p}p \to \overline{Y}Y$ reactions. Only the hyperon decays are examined explicitly. The antihyperon decays proceed analogously; any important differences are noted.

2.4.1 The $\Sigma^0 \to \Lambda\gamma$ Decay

The density matrix of the daughter Λ ($J = \frac{1}{2}$) from the Σ^0 ($J = \frac{1}{2}$) decay is calculated from the Σ^0 density matrix:

$$\rho_\Lambda = T_{\Sigma^0}\rho_{\Sigma^0}T^\dagger_{\Sigma^0}, \tag{2.38}$$

where T_{Σ^0} is the (2×2) transition matrix that describes the electromagnetic decay of the Σ^0. With the choice of helicity states as the basis, the elements of T_{Σ^0} are products of a Wigner $\mathcal{D}$ function and a decay matrix element g_μ:

$$T_{\Sigma^0,\mu m} = \frac{g_\mu}{\sqrt{2\pi}} \mathcal{D}^{\frac{1}{2}*}_{m,-\mu}(\phi, \theta, -\phi), \tag{2.39}$$

where θ and ϕ are the usual angles describing the Λ direction in the rest frame of the Σ^0 with the coordinate system as shown in Fig. 2.1. The phase convention used in this expression is that of Jacob and Wick [38]. The index m labels the Σ^0 rest frame spin states and μ labels the Λ helicity states. The $-\mu$ subscript of the $\mathcal{D}$ function arises because the Λ helicity, which determines the ordering of the elements in ρ_Λ, has the opposite sign from that of the total helicity, which determines the transition amplitude, since the γ carries helicity ± 1. In this expression, the $\mathcal{D}$ function takes care of the angular dependence and the g_μ represent the amplitude for the decay Λ to be emitted with helicity μ. Because the electromagnetic interaction conserves parity, the two helicity amplitudes must be equal: $g_{+\frac{1}{2}} = g_{-\frac{1}{2}} = g$.

Inserting the individual $\mathcal{D}$ functions and writing each element explicitly yields

$$T_{\Sigma^0} = \frac{g}{\sqrt{2\pi}} \begin{bmatrix} -e^{i\phi} \sin\frac{\theta}{2} & \cos\frac{\theta}{2} \\ \cos\frac{\theta}{2} & e^{-i\phi} \sin\frac{\theta}{2} \end{bmatrix}. \tag{2.40}$$

The density matrix of the Σ^0 can be written as in Eq. 2.25,

$$\rho_{\Sigma^0} = \frac{1}{2}(\mathcal{I} + \mathbf{P}_{\Sigma^0} \cdot \boldsymbol{\sigma}), \tag{2.41}$$

where $\mathbf{P}_{\Sigma^0}$ is the vector polarization of the Σ^0. Using these expressions for ρ_{Σ^0} and T_{Σ^0}, the density matrix of the decay Λ is easily determined. Calculating the angular distribution of the Λ in the Σ^0 frame yields

$$I(\theta, \phi) = \mathrm{Tr}(\rho_\Lambda) = \mathrm{Tr}(T_{\Sigma^0} \rho_{\Sigma^0} T^\dagger_{\Sigma^0}) = \frac{g}{4\pi}. \tag{2.42}$$

This result shows that the distribution of the decay Λ is isotropic in the Σ^0 rest frame and that this is true regardless of the Σ^0 polarization.

The polarization components of the Λ in its rest frame are given by

$$P_{i,\Lambda} = \frac{\mathrm{Tr}(\rho_\Lambda \sigma_i)}{\mathrm{Tr}(\rho_\Lambda)} = \frac{\mathrm{Tr}(T_{\Sigma^0}\rho_{\Sigma^0}T_{\Sigma^0}^\dagger \sigma_i)}{\mathrm{Tr}(T_{\Sigma^0}\rho_{\Sigma^0}T_{\Sigma^0}^\dagger)}. \tag{2.43}$$

Which, after the necessary accounting, yields

$$P_{x,\Lambda} = (\cos^2\frac{\theta}{2} - \cos 2\phi \sin^2\frac{\theta}{2})P_{x,\Sigma^0} - (\sin 2\phi \sin^2\frac{\theta}{2})P_{y,\Sigma^0} - (\cos\phi \sin\theta)P_{z,\Sigma^0}, \tag{2.44}$$

$$P_{y,\Lambda} = (\sin 2\phi \sin^2\frac{\theta}{2})P_{x,\Sigma^0} - (\cos^2\frac{\theta}{2} - \cos 2\phi \sin^2\frac{\theta}{2})P_{y,\Sigma^0} + (\sin\phi \sin\theta)P_{z,\Sigma^0}, \tag{2.45}$$

$$P_{z,\Lambda} = -(\cos\phi \sin\theta)P_{x,\Sigma^0} - (\sin\phi \sin\theta)P_{y,\Sigma^0} - (\cos\theta)P_{z,\Sigma^0}, \tag{2.46}$$

$$= -\mathbf{P}_{\Sigma^0} \cdot \hat{p}_\Lambda, \tag{2.47}$$

where $\hat{p}_\Lambda$ is the decay Λ direction vector in the Σ^0 rest frame. The coordinate system for these expressions has the z axis along the direction of motion of the Λ and the x and y axes determined by an Euler rotation of the parent-Σ^0 system with angles $(\phi, \theta, -\phi)$. These expressions quantify how the polarization of the Σ^0 is passed to the decay Λ.

2.4.2 The $\Lambda \to p\pi$ Decay

The next step is to determine the angular distribution of the Λ-decay proton as a function of the Λ polarization. Proceeding as for the Σ^0 decay, the density matrix of the daughter proton from the Λ decay is given by

$$\rho_p = T_\Lambda \rho_\Lambda T_\Lambda^\dagger, \tag{2.48}$$

where T_Λ is the transition matrix for the weak decay of the Λ. Again the choice is made to represent ρ_p in terms of helicity states. With this choice, the elements of the transition matrix are

$$T_{\Lambda,\mu m} = \frac{f_\mu}{\sqrt{2\pi}} \mathcal{D}^{\frac{1}{2}*}_{m,\mu}(\phi, \theta, -\phi), \tag{2.49}$$

with m and μ labeling the Λ and p states respectively.

The weak interaction is not invariant under the parity operation. Therefore, it is not possible to equate the two matrix elements $f_{+\frac{1}{2}}$ and $f_{-\frac{1}{2}}$ as was done for the Σ^0 decay. Inserting the $\mathcal{D}$ functions yields

$$T_\Lambda = \frac{1}{\sqrt{2\pi}} \begin{bmatrix} f_+ \cos\frac{\theta}{2} & f_+ e^{-i\phi} \sin\frac{\theta}{2} \\ -f_- e^{i\phi} \sin\frac{\theta}{2} & f_- \cos\frac{\theta}{2} \end{bmatrix}, \tag{2.50}$$

with the shortened notation f_+ and f_- replacing $f_{+\frac{1}{2}}$ and $f_{-\frac{1}{2}}$.

The angular distribution of the decay proton in the Λ rest frame is obtained using $\rho_\Lambda = \frac{1}{2}(\mathcal{I} + \mathbf{P}_\Lambda \cdot \boldsymbol{\sigma})$ and taking the trace of ρ_p:

$$\begin{aligned} I(\theta,\phi) &= \frac{f_+^2 + f_-^2}{4\pi}(1 + \alpha(P_{x,\Lambda}\cos\phi\sin\theta + P_{y,\Lambda}\sin\phi\sin\theta + P_{z,\Lambda}\cos\theta)) \\ &= \frac{f_+^2 + f_-^2}{4\pi}(1 + \alpha \mathbf{P}_\Lambda \cdot \hat{p}_p). \end{aligned} \tag{2.51}$$

Here $\hat{p}_p$ is the direction vector of the proton in the Λ rest frame and

$$\alpha = \frac{(f_+^2 - f_-^2)}{(f_+^2 + f_-^2)} \tag{2.52}$$

is the $\Lambda \rightarrow p\pi$ decay parameter.

The corresponding parameter for the $\overline{\Lambda}$ decay, $\overline{\alpha}$, is required by CP conservation to satisfy $\overline{\alpha} = -\alpha$. This has been investigated in previous work of the PS185 experiment [43] with no evidence for CP violation found. The level of CP violation is expected to be small, for example, the quantity $A = (\alpha + \overline{\alpha})/(\alpha - \overline{\alpha})$ is expected to be $\approx 10^{-4}$ in the Kobayashi-Maskawa model [44, 45]. Even if A was on the order of that allowed by the Particle Data Group average value of -0.03 ± 0.06 [12], the effect of this ($\approx 3\%$) on the polarization measurements of this work would be negligible given the statistical errors. So, for the analysis of this data, the Λ and $\overline{\Lambda}$ weak-decay parameter assignments [12],

$$\alpha = -\overline{\alpha} = 0.642 \pm 0.013 \tag{2.53}$$

are used.

2.5 The $\overline{p}p$ Angular Distributions and Spin Observables

The formalism developed in the previous sections to calculate the polarization and angular distributions for *single* Σ^0 and Λ decays can now be used to determine the combined angular distribution of the detected antiproton and proton as a function of the spin observables. The combined density matrix of the detected antiproton and proton, $\rho^{(\mathrm{d})}_{\overline{p}p}$, may be written in terms of the original $\overline{Y}Y$ density matrix and the electromagnetic and weak decay transition matrices introduced above. Starting with Eq. 2.29 for the general $\overline{Y}Y$ density matrix and applying the transition matrices for each decay yields the following equations for the detected $\overline{p}p$ density matrices for each $\overline{Y}Y$ reaction:

$$\rho^{(\mathrm{d})}_{\overline{p}p,\overline{\Lambda}\Lambda} = \frac{\mathcal{R}_{\overline{\Lambda}\Lambda}}{4}\sum_{\mu\nu} C_{\mu\nu,\overline{\Lambda}\Lambda}\left(T_{\overline{\Lambda}}\sigma^{\overline{\Lambda}}_{\mu}T^{\dagger}_{\overline{\Lambda}}\right)\otimes\left(T_{\Lambda}\sigma^{\Lambda}_{\nu}T^{\dagger}_{\Lambda}\right), \tag{2.54}$$

$$\rho^{(\mathrm{d})}_{\overline{p}p,\overline{\Sigma}^0\Lambda} = \frac{\mathcal{R}_{\overline{\Sigma}^0\Lambda}}{4}\sum_{\mu\nu} C_{\mu\nu,\overline{\Sigma}^0\Lambda}\left(T_{\overline{\Lambda}}T_{\overline{\Sigma}^0}\sigma^{\overline{\Sigma}^0}_{\mu}T^{\dagger}_{\overline{\Sigma}^0}T^{\dagger}_{\overline{\Lambda}}\right)\otimes\left(T_{\Lambda}\sigma^{\Lambda}_{\nu}T^{\dagger}_{\Lambda}\right), \tag{2.55}$$

$$\rho^{(\mathrm{d})}_{\overline{p}p,\overline{\Lambda}\Sigma^0} = \frac{\mathcal{R}_{\overline{\Lambda}\Sigma^0}}{4}\sum_{\mu\nu} C_{\mu\nu,\overline{\Lambda}\Sigma^0}\left(T_{\overline{\Lambda}}\sigma^{\overline{\Lambda}}_{\mu}T^{\dagger}_{\overline{\Lambda}}\right)\otimes\left(T_{\Lambda}T_{\Sigma^0}\sigma^{\Sigma^0}_{\nu}T^{\dagger}_{\Sigma^0}T^{\dagger}_{\Lambda}\right). \tag{2.56}$$

The combined angular distribution of the detected antiproton and proton for each $\overline{Y}Y$ channel is found by taking the trace of each of these density matrices. For the $\overline{p}p \to \overline{\Sigma}^0\Lambda$ ($\overline{p}p \to \overline{\Lambda}\Sigma^0$) channel, an average over the azimuthal angle of the decay $\bar{p}$ (p) in the $\overline{\Lambda}$ (Λ) rest frame is included, as this variable is not distinguished in the experiment.

This leads to the following distributions:

$$I_{\overline{p}p,\overline{\Lambda}\Lambda}(\hat{p}_{\overline{p}},\hat{p}_p) = \frac{\mathcal{R}_{\overline{\Lambda}\Lambda}}{16\pi^2}\left[1+\overline{\alpha}\mathbf{P}_{\overline{\Lambda}}\cdot\hat{p}_{\overline{p}}+\alpha\mathbf{P}_{\Lambda}\cdot\hat{p}_p+\overline{\alpha}\alpha\sum_{i,j}C_{ij}p_{\overline{p},i}p_{p,j}\right], \tag{2.57}$$

$$I_{\overline{p}p,\overline{\Sigma}^0\Lambda}(\hat{p}_{\overline{p}},\hat{p}_p,\hat{p}_{\overline{\Lambda}}) = \frac{\mathcal{R}_{\overline{\Sigma}^0\Lambda}}{64\pi^3}\left[1-\overline{\alpha}(\mathbf{P}_{\overline{\Sigma}^0}\cdot\hat{p}_{\overline{\Lambda}})(\hat{p}_{\overline{\Lambda}}\cdot\hat{p}_{\overline{p}})+\alpha\mathbf{P}_{\Lambda}\cdot\hat{p}_p-\overline{\alpha}\alpha(\hat{p}_{\overline{\Lambda}}\cdot\hat{p}_{\overline{p}})\sum_{i,j}C_{ij}p_{\overline{\Lambda},i}p_{p,j}\right], \tag{2.58}$$

$$I_{\overline{p}p,\overline{\Lambda}\Sigma^0}(\hat{p}_{\overline{p}},\hat{p}_p,\hat{p}_\Lambda) =$$
$$\frac{\mathcal{R}_{\overline{\Lambda}\Sigma^0}}{64\pi^3}\left[1+\overline{\alpha}\mathbf{P}_{\overline{\Lambda}}\cdot\hat{p}_{\overline{p}}-\alpha(\mathbf{P}_{\Sigma^0}\cdot\hat{p}_\Lambda)(\hat{p}_\Lambda\cdot\hat{p}_p)-\overline{\alpha}\alpha(\hat{p}_\Lambda\cdot\hat{p}_p)\sum_{i,j}C_{ij}p_{\overline{p},i}p_{\Lambda,j}\right], \quad (2.59)$$

where the $\hat{p}$ are the direction vectors of the decay particles as measured in the *parent particle rest frame.* For brevity of notation, the reaction channel index on the spin observables has been dropped. The normalization has been changed slightly so that an integration over all particle directions yields the differential cross section $\mathcal{R}_{\overline{Y}Y}$.

The $\overline{p}p$ distributions may be simplified further, with some loss of information, by integrating over all Σ^0-decay Λ directions. This corresponds to the distributions seen in the detector if the direction of the Σ^0-decay Λ is not distinguished in the experiment. This step is somewhat complicated for a real experimental situation with finite detector acceptance as is explained in Chapter 6. Performing this integral yields distributions for the $\overline{p}p \to \overline{\Sigma}^0\Lambda + c.c.$ channels of the same form as for $\overline{p}p \to \overline{\Lambda}\Lambda$ with an additional factor of $-\frac{1}{3}$ due to the dilution effect of the Σ^0 decay. The integrated distributions are

$$I_{\overline{p}p,\overline{\Sigma}^0\Lambda}(\hat{p}_{\overline{p}},\hat{p}_p) = \frac{\mathcal{R}_{\overline{\Sigma}^0\Lambda}}{16\pi^2}\left[1-\frac{1}{3}\overline{\alpha}\mathbf{P}_{\overline{\Sigma}^0}\cdot\hat{p}_{\overline{p}}+\alpha\mathbf{P}_\Lambda\cdot\hat{p}_p-\frac{1}{3}\overline{\alpha}\alpha\sum_{i,j}C_{ij}p_{\overline{p},i}p_{p,j}\right], \quad (2.60)$$

$$I_{\overline{p}p,\overline{\Lambda}\Sigma^0}(\hat{p}_{\overline{p}},\hat{p}_p) = \frac{\mathcal{R}_{\overline{\Lambda}\Sigma^0}}{16\pi^2}\left[1+\overline{\alpha}\mathbf{P}_{\overline{\Lambda}}\cdot\hat{p}_{\overline{p}}-\frac{1}{3}\alpha\mathbf{P}_{\Sigma^0}\cdot\hat{p}_p-\frac{1}{3}\overline{\alpha}\alpha\sum_{i,j}C_{ij}p_{\overline{p},i}p_{p,j}\right]. \quad (2.61)$$

Equations 2.57-2.61 quantify the dependence of the $\overline{p}p$ angular distributions on spin observables. Using these, the spin observables for each $\overline{Y}Y$ channel may be extracted from the experimentally measured antiproton and proton angular distributions. These relations are used as the starting point to obtain the spin observables in the analysis of Chapter 6.

Chapter 3

Theoretical Models of $\overline{p}p \rightarrow \overline{Y}Y$

Any measurement of a physical phenomenon such as the $\overline{p}p \rightarrow \overline{Y}Y$ process begs for a microscopic theory that explains what is observed. The theory of the strong interactions of quarks and gluons, QCD, is at present not able to be used to analyze this process in the near-threshold energy region. For this reason, the explanations are mostly provided through models, ranging from more to less phenomenological. The goal of the PS185 experiment is to facilitate the development of these models by providing an accurate and complete data set on the $\overline{p}p \rightarrow \overline{Y}Y$ reactions. It is hoped that the models proposed can eventually be unified and understood with an encompassing theory of the interactions of quarks and gluons.

In this chapter, the PS185 data set is summarized and a short history of the development of the models created to address this data set is given. After a few preliminaries, three of the more recent theoretical efforts are described in some detail in order to provide a view into the workings of the models. The chapter is concluded with an exposition of what is expected in the relatively new $\overline{p}p \rightarrow \overline{\Sigma}^0\Lambda + c.c.$ channel.

3.1 The PS185 Data Set

The PS185 experiment has provided a voluminous data set which constrains and guides the theoretical efforts to explain the $\overline{p}p \rightarrow \overline{Y}Y$ process. As of this writing, PS185 has reported over 650 data points for the $\overline{p}p \rightarrow \overline{\Lambda}\Lambda$ reaction, consisting of

differential cross sections, hyperon polarizations, and spin correlation coefficients. Work towards the goal of completing a similar collection for the $\overline{p}p \rightarrow \overline{\Sigma}^0\Lambda + c.c.$, $\overline{p}p \rightarrow \overline{\Sigma}^-\Sigma^+$, and $\overline{p}p \rightarrow \overline{\Sigma}^+\Sigma^-$ reactions is progressing. As is easily imagined, the task of providing an adequate model to account for all of this data is a significant challenge.

The majority of the published theoretical work has been inspired by and directed toward the $\overline{p}p \rightarrow \overline{\Lambda}\Lambda$ data. The dominant features of this data which must be addressed by a successful model are:

- the energy dependence of the total cross section near threshold;
- the strong forward peaking of the differential cross section down to very near threshold;
- the substantial hyperon polarization, also down to near threshold, with its characteristic angular dependence; and
- the $\overline{\Lambda}\Lambda$ singlet fraction which indicates, for all momenta measured by PS185, that the $\overline{\Lambda}\Lambda$ pair is produced almost exclusively in a triplet spin state.

The data from the $\overline{p}p \rightarrow \overline{\Sigma}^0\Lambda + c.c.$ reaction at 1.695 GeV/c antiproton momentum, also indicates a forward peaking in the differential cross section but unfortunately allows little to be concluded about the behavior of the spin observables. A summary fraction of this data is displayed in Chapter 1, Figures 1.3–1.7. These features, including the behavior of the spin observables, must be accounted for in a complete and correct theoretical model of the $\overline{p}p \rightarrow \overline{Y}Y$ process.

3.2 Historical Background

Many models have been proposed to explain the $\overline{p}p \rightarrow \overline{Y}Y$ reaction [46–76]. Most of the groups involved in the construction of these are well-versed in work on other

nucleon-nucleon (NN) and antinucleon-nucleon ($\overline{N}N$) scattering processes in this low-energy ($\approx$ 1 GeV) region. The $\overline{p}p \rightarrow \overline{\Lambda}\Lambda$ data provides an opportunity to extend their expertise to encompass strangeness production. The symmetries of the strong interaction make this a natural extension. However, due to various complications that arise and the symmetries that are broken (such as SU(3)), it is a challenging project.

The first models of $\overline{p}p \rightarrow \overline{\Lambda}\Lambda$ were proposed before the inception of PS185, stimulated by the results of various bubble chamber experiments in the 3–7 GeV/c momentum region. These works [46,47] used Regge-pole theory and included the $K^*(892)$ and/or the $K_2^*(1430)$ as the dominant trajectories (the $K(494)$ was deemed negligible) to describe the existing data adequately. In 1985, spurred on by the forthcoming PS185 results, Tabakin and Eisenstein [41] developed a meson exchange approach using Born approximation methods and accounting for initial and final state effects. They came to the conclusion that K, K^*, and K_2^* exchanges are important to consider and that the spin observables are extremely sensitive to the nature of these meson exchanges. In this light, they (correctly) predicted that a forward peaking of the differential cross section would exist down to threshold and the polarization and spin correlations would remain sizeable.

An alternative approach, also stimulated by the expected PS185 data, was proposed by Genz and Tatur [48] in 1984. They considered the various $\overline{p}p \rightarrow \overline{Y}Y$ processes from a quark-pair annihilation perspective. Assuming that the annihilation of a $\overline{u}u$ or $\overline{d}d$ quark pair and subsequent creation of a $\overline{s}s$ quark pair proceeds through one gluon exchange, they worked out the $\overline{p}p \rightarrow \overline{Y}Y$ cross section ratios using spin, flavor, and color symmetries. These results were in reasonable agreement with the current data and obtained (by construction) the triplet dominance in the $\overline{p}p \rightarrow \overline{\Lambda}\Lambda$ channel. However, this model did not address the shape of the differential cross sections and it yielded zero polarization for all $\overline{p}p \rightarrow \overline{Y}Y$ channels: results of the overly simplistic nature of the model.

The publication of the PS185 $\overline{p}p \to \overline{\Lambda}\Lambda$ results from various momenta near reaction threshold during the last 10 years has inspired many more theoretical works [36,49–77]. The complexity of the models has increased, not surprisingly, in proportion to the size of the data set — a necessary consequence of the completeness and accuracy of the data and of the subtle and intricate nature of the strong-interaction processes involved. The majority of these models use a meson exchange mechanism for the creation of the strangeness in the final state [49–60]. Many others consider quark-based mechanisms of the "$^3S_1$" and/or "$^3P_0$" variety [61–69]. Additional approaches include models utilizing near-threshold P-wave enhancements [70, 72], quark-diquark mechanisms [73,74], more phenomenological zero-range [75] or scattering-length [76] approximations, and even Regge-pole theory [77] (an extrapolation down to threshold of an earlier work [47]).

3.3 Preliminaries

Before diving into the details of the some of the $\overline{p}p \to \overline{Y}Y$ models, it is instructive to examine some aspects of the formalism and the application of selection rules on the $\overline{p}p \to \overline{Y}Y$ process.

The helicity basis that was introduced and utilized in Chapter 2, while convenient to analyze hyperon decays and to quantify the reaction spin observables, is less convenient to use to calculate the $\overline{p}p \to \overline{Y}Y$ transition amplitudes. Plane-wave helicity states are not eigenstates of parity or angular momentum and so do not allow the easy application of these symmetries. To circumvent this problem, the most common approach is to use two-particle basis states that are eigenstates of spin, orbital, and total angular momentum — the LS states — with labels $^{2S+1}L_J$. These states may then be transformed back to helicity states for the calculation of observables via the unitary transformation that links the two bases.

The symmetry of the strong interaction under the parity (P) and charge-

conjugation (C) operations allows the derivation of selection rules for the participating LS states in the $\overline{p}p \rightarrow \overline{Y}Y$ transition. The parity of a $\overline{p}p$ or $\overline{Y}Y$ pair in an LS state is

$$P = (-1)^{L+1} \tag{3.1}$$

with the extra $+1$ arising in the exponent due to the opposite intrinsic parity of fermion and antifermion. The conservation of P implies that only transitions between initial and final LS states with $\Delta L = 0, 2, 4, \ldots$ are allowed. The further application of angular momentum conservation limits these to transitions with $\Delta L = 0, 2$. For the $\overline{p}p \rightarrow \overline{\Lambda}\Lambda$ reaction the invariance of the strong interaction under C may also be applied. For $\overline{p}p \rightarrow \overline{\Sigma}^0\Lambda$ or $\overline{p}p \rightarrow \overline{\Lambda}\Sigma^0$, the final state is not an eigenstate of C and this selection rule is not applicable. The C-parity value for the $\overline{p}p$ or $\overline{\Lambda}\Lambda$ states is

$$C = (-1)^{L+S}. \tag{3.2}$$

This has the effect that, for the $\overline{p}p \rightarrow \overline{\Lambda}\Lambda$ reaction, there must be no change in total spin from the initial to final states. The allowed transitions between initial and final LS states in $\overline{p}p \rightarrow \overline{\Lambda}\Lambda$ and $\overline{p}p \rightarrow \overline{\Sigma}^0\Lambda + c.c.$ for $J \leq 2$ are summarized in Table 3.1.

The $\overline{\Lambda}\Lambda$ state has isospin 0 while the $\overline{\Sigma}^0\Lambda$ and $\overline{\Lambda}\Sigma^0$ states are of isospin 1. This fact, together with the assumption of isospin invariance of the transition, implies that the $\overline{p}p \rightarrow \overline{\Lambda}\Lambda$ reaction occurs through the $I = 0$ channel and $\overline{p}p \rightarrow \overline{\Sigma}^0\Lambda + c.c.$ via $I = 1$. Although usually buried in the formalism, this symmetry is a feature of the model transition mechanisms.

The convenience of the LS basis of states to analyze a reaction near threshold is due to the "centrifugal barrier". The LS basis radial matrix elements, using the Born approximation, have the form

$$\langle L_f|T|L_i\rangle \propto \int_0^\infty j_{L_f}(q_f r)V(r)j_{L_i}(q_i r)r^2 dr, \tag{3.3}$$

where the j_L are the spherical Bessel functions and the q, L are the c.m. momenta and orbital angular momentum values for the initial and final states. The limiting

initial state	final state	
$\overline{p}p$	$\overline{\Lambda}\Lambda$, $\overline{\Lambda}\Sigma^0 + c.c.$	$\overline{\Lambda}\Sigma^0 + c.c.$ only
${}^1S_0$	${}^1S_0$	
${}^1P_1$	${}^1P_1$	${}^3P_1$
${}^1D_2$	${}^1D_2$	${}^3D_2$
${}^1F_3$	${}^1F_3$	${}^3F_3$
${}^3P_0$	${}^3P_0$	
${}^3S_1$	${}^3S_1, {}^3D_1$	
${}^3P_1$	${}^3P_1$	${}^1P_1$
${}^3D_1$	${}^3D_1, {}^3S_1$	
${}^3P_2$	${}^3P_2, {}^3F_2$	
${}^3D_2$	${}^3D_2$	${}^1D_2$
${}^3F_2$	${}^3F_2, {}^3P_2$	

Table 3.1: Allowed partial wave transitions for the $\overline{p}p \rightarrow \overline{\Lambda}\Lambda$ and $\overline{p}p \rightarrow \overline{\Sigma}^0\Lambda + c.c.$ reactions for $J \leq 2$. The first column contains the initial state partial wave, the second column contains the allowed final states common to both $\overline{p}p \rightarrow \overline{\Lambda}\Lambda$ and $\overline{p}p \rightarrow \overline{\Sigma}^0\Lambda + c.c.$, and the third column contains the additional final states allowed in $\overline{p}p \rightarrow \overline{\Sigma}^0\Lambda + c.c.$ only. The state notation is ${}^{2S+1}L_J$.

form of the Bessel functions for small qr values is $(qr)^L/((2L+1)!!)$. This remains small for values of $qr < \sqrt{L(L+1)}$. Since the potential V(r) is of finite range, the matrix elements are negligible for sufficiently large values of L. This provides a cutoff which allows for a truncated basis of LS states, thereby limiting the number of LS transitions that need to be considered in the analysis of the process.

The transitions from Table 3.1 that connect initial and final states of different L values merit further examination. The most common potential forms, central and spin-orbit, do not connect states of different L values. If these transitions are observed, it is evidence for a different type of potential form, the tensor. The tensor operator connects states of different L and allows only triplet-to-triplet transitions.

This is worth noting when examining the $\bar{p}p \rightarrow \overline{\Lambda}\Lambda$ singlet-fraction data.

3.4 The Models

In the following subsections, three models of the $\bar{p}p \rightarrow \overline{Y}Y$ reaction are examined in some detail. These works constitute an important subset of the calculations that have been proposed over the years. These specific examples have been chosen because they have been published fairly recently and therefore address the largest portion of the PS185 data. They are also somewhat orthogonal in their methods; thereby, in examining these models, a representative sample of approaches is surveyed.

3.4.1 The Tabakin, Eisenstein, and Lu Amplitude Analysis

Tabakin, Eisenstein, and Lu [36] have performed a reasonably model-independent amplitude analysis followed by the application of a scattering length approximation. Using these "tried-and-true" techniques, they take a step back and determine the behavior of the $\bar{p}p \rightarrow \overline{\Lambda}\Lambda$ observables expected simply because it is a strongly absorptive reaction taking place near threshold. The observables are derived in terms of partial wave amplitudes and compared to the data. Various conclusions are then drawn about the nature of the reaction mechanisms that are consistent with the data. Also, the methods used in this analysis provide an excellent introduction to the fundamental aspects of the $\bar{p}p \rightarrow \overline{Y}Y$ reaction; thus making this work a good place to begin this survey.

The calculation is started by expressing the transition matrix that describes the dynamics of the $\bar{p}p \rightarrow \overline{\Lambda}\Lambda$ process using the helicity basis [38]. For reasons described in the previous section, the calculation is then transformed from this basis to the LS basis via a unitary transformation. The resulting LS amplitudes reflect the constraints of angular momentum, parity, and charge conjugation invariance in that only amplitudes of the allowed transitions shown in Table 3.1 appear.

The observables are then obtained using density matrix methods as is shown in Chapter 2, Eqs. 2.30–2.33. This results in expressions for all the observables — differential cross sections, polarizations, and spin-correlation coefficients — as functions of an infinite sum of bilinear products of LS amplitudes. In these expressions, all of the angular dependence is contained in products of Wigner $\mathcal{D}$ functions. Using the properties of these functions, the angular dependence is then simplified so that all the observables may be described as sums of Legendre polynomials,

$$\sum_L a_L P_L(\cos\theta^*), \tag{3.4}$$

or of associated Legendre polynomials

$$\sum_L b_L P_L^1(\cos\theta^*), \tag{3.5}$$

with the coefficients a_L and b_L given by products of LS amplitudes, and θ^* as the c.m. scattering angle.

The next step of the calculation involves choosing a limited set of partial-wave amplitudes for the subsequent analysis. Near threshold, due to the centrifugal barrier, it is expected that the transition proceeds through only a few low-L partial waves. This assumption restricts the calculation to only a few LS states with $J \leq 1$ plus the $^3P_2$ state (to include all P waves). This allows contributions from seven LS states, two singlet— $^1S_0$ and $^1P_1$ — and five triplet — $^3P_0$,$^3S_1$,$^3D_1$,$^3P_1$, and $^3P_2$. As can be seen from Table 3.1, only the $^3S_1$ and $^3D_1$ states feed off-diagonal transitions. Including these transitions yields nine total partial-wave amplitudes.

The PS185 data was fit using the forms in Eqs. 3.4 and 3.5 and the fit values of the a_L and b_L coefficients were compared to the equations involving the truncated set of LS amplitudes. The $\overline{p}p \rightarrow \overline{\Lambda}\Lambda$ data from threshold up to an antiproton momentum of 1.695 GeV/c (corresponding to $\approx$ 92 MeV excess energy) were considered. It is dubious whether it was appropriate to fit this highest momentum point with this small set of amplitudes but, with this in mind, they proceeded. This fitting exercise,

while not able to constrain each amplitude individually, allowed for the extraction of information about the relative sizes and phase relationships of the competing amplitudes.

The fits to the differential cross section, polarization, and spin correlation coefficients revealed several points. First it was assumed, in light of the singlet fraction measurements, that the singlet amplitudes may be safely neglected. The shape of the differential cross sections and, in particular, the forward peaking was attributed to an interference between S- and P-wave amplitudes which, naturally, means that both of these terms must be present. This data also indicates significant ${}^3P_2$ contributions as well as some ${}^3D_1$. The behavior of the polarization data, especially the location of the central node with momentum, indicates that there is a contribution from S waves and that there is most probably a difference in magnitude and phase — a *splitting* — between the different P waves. An examination of the spin-correlation data served to add additional support to these conclusions.

In the procedure described above, the authors assumed no energy dependence of the amplitudes; the fits at each momentum were independent. To gain further insight into the behavior of the data, they introduced a scattering length approximation [78]. This approximation dictates a momentum dependence of each partial-wave amplitude $\mathcal{T}_{SLJ}$:

$$\mathcal{T}_{SLJ} = \mathcal{A}_{SLJ} q^L, \tag{3.6}$$

with $\mathcal{A}_{SLJ}$ as a complex, energy-independent scattering-length and q as the final c.m. momentum. The differential cross section and polarization data for the six momenta nearest threshold (the data at 1.695 MeV/c were omitted) were fit simultaneously with seven amplitudes of this form. The singlet amplitudes were again assumed to be negligible.

The amplitudes calculated from the seven complex fit scattering-lengths are shown in the conventional, unitless, S-matrix form in Fig. 3.1 as an Argand diagram. The

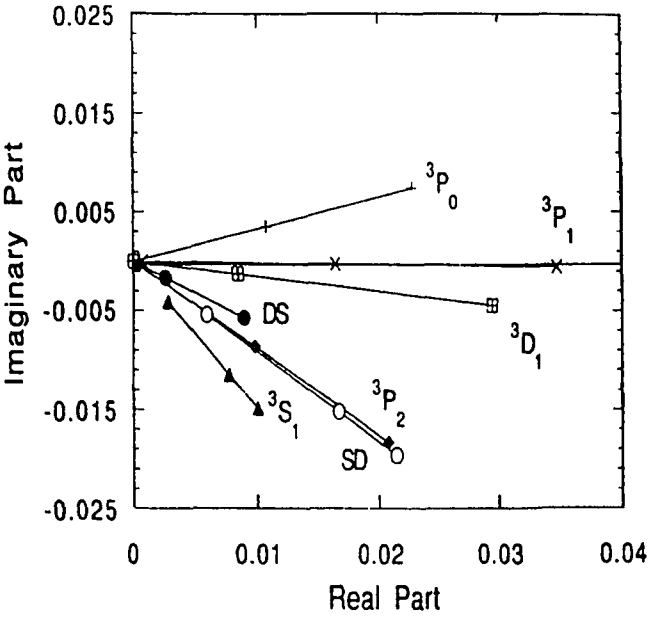

Figure 3.1: An Argand diagram of the unitless amplitudes resulting from the complex scattering length fit of Tabakin, Eisenstein, and Lu [36]. The amplitudes marked SD and DS refer to the $\overline{p}p(^3D_1) \rightarrow \overline{\Lambda}\Lambda(^3S_1)$ and $\overline{p}p(^3S_1) \rightarrow \overline{\Lambda}\Lambda(^3D_1)$ transitions respectively. The markers indicate the values of each amplitude at 1.436, 1.477, and 1.546 GeV/c.

fit was of reasonable quality with a reduced χ^2 of 1.75. Along with this presentation of the fit amplitudes, several important characteristics were noted. Among these were: the $^3S_1$ and $D \rightarrow S$ amplitudes are substantial at the lowest momenta while the others are very small; the $D \rightarrow S$ amplitude is actually the larger of the two, indicating the presence of a tensor force even near threshold; the P and D amplitudes increase rapidly with momentum; and the P amplitudes display a large splitting.

These conclusions constrain the dynamical models that may be constructed to explain the $\overline{p}p \rightarrow \overline{Y}Y$ system. The fact that the S-wave amplitude is not negligible serves to limit the amount of annihilation in the $\overline{p}p$ system. It was also noted that the presence of *only* $^3S_1$ and $^3P_0$ amplitudes is ruled out, therefore any quark-based model

constructed must be able to generate more than just these waves in the $\overline{p}p \rightarrow \overline{\Lambda}\Lambda$ system. The P-wave splitting is interesting in that it arises in the presence of $\mathbf{L} \cdot \mathbf{S}$ and/or tensor forces which are generated, in a meson-exchange model, from the exchange of vector mesons.

3.4.2 Meson Exchange vs. Quark-Based Calculations

In the next two subsections, two different dynamical models of the $\overline{p}p \rightarrow \overline{\Lambda}\Lambda$ reaction are described. These models are representative "state-of-the-art" calculations and illustrate the dichotomy of approaches that has evolved over the years. The calculation of the Nijmegen group, involving kaon exchange in the t-channel, represents the more conventional side of the division. The calculation of the Washington-Colorado (WC) group, involving gluonic-type exchanges is a good example of the more modern, but less developed, opposite side of the division. A simple diagram illustrating the two approaches is shown in Fig. 1.2. Of course these are not the only ways to approach the problem, as other models have been proposed, but these, in some form, have come to be recognized as the most fundamental and successful.

It is naive to hope that one type of model can be labeled "right" and the other "wrong" for certainly both quark-gluon and meson processes play a role. If an antiproton and proton come within 1 fm of one another, surely the quarks and antiquarks are able to interact. And on the other hand, if the meson-exchange potentials are significant at ranges greater than 1 fm, the mesons also must play a role. A more correct way to phrase the question would be to ask if one approach is more appropriate than the other to describe the $\overline{p}p \rightarrow \overline{Y}Y$ process in the PS185 energy regime or does one model stress a less important degree of freedom at the expense of the more salient.

Both approaches divide the problem up in a similar fashion, however each part are is handled differently. The three parts of the problem are: the initial-state interaction, the reaction mechanism, and the final-state interaction. Both agree that

all three of these must be addressed, with emphasis on the latter two, are important in reproducing the experimental results.

3.4.3 The Nijmegen Meson-Exchange Model

The Nijmegen group is an excellent example of a group with a long history of work on NN, $\overline{N}N$, and YN scattering processes. The work described here [42,37] draws on this expertise to produce an elaborate meson-exchange model that describes the data well.

To account correctly for the strong annihilation in the initial and final state in the presence of many open reaction channels, the Nijmegen group uses a coupled-channels approach. This is accomplished by solving the Schrödinger equation in channel space. For a partial wave with angular momentum J, this matrix equation is written,

$$\left[\frac{d^2}{dr^2} - \frac{L^2}{r^2} - U^J + k^2\right] \Phi^J(r) = 0. \tag{3.7}$$

In this equation, $U^J = \sqrt{2m}V^J\sqrt{2m}$, where V^J is the matrix of coupled-channels potentials and k, m, and L^2 are diagonal matrices containing the momenta, reduced masses, and $L(L+1)$ values. All baryon channels below 2.0 GeV/c antiproton momentum are considered: $\bar{p}p$, $\overline{n}n$, $\overline{\Lambda}\Lambda$, $\overline{\Lambda}\Sigma^0 + c.c.$, and three charged-$\Sigma$ channels.

The coupled-channels potential matrix V^J was determined in a manner analogous to that used for the Nijmegen soft-core one-boson-exchange nucleon-nucleon and hyperon-nucleon potential [79,80] with the proper C-parity transforms to change from nucleons to antinucleons. The mesons considered included the $J^{PC} = 0^{-+}$ pseudoscalars, the $J^{PC} = 1^{--}$ vectors, the $J^{PC} = 0^{++}$ scalars, and the $J^{PC} = 2^{++}$ tensors. The momentum-space potentials were calculated using a set of meson-baryon Feynman rules assuming SU(3) flavor symmetry for the baryon-meson couplings. Gaussian form factors were used at the vertices with a cutoff mass set to the value determined from their previous NN work. These potentials were then Fourier-transformed into

configuration-space to yield V^J. The elements of V^J contain no free parameters. The resulting potential for the $\overline{p}p \rightarrow \overline{\Lambda}\Lambda$ channel shows a very strong tensor force from the coherence of the K and K^* exchanges. This is in contrast to the spin-spin part of the potential where these mesons add deconstructively.

Within these potentials only two-body baryonic channels were considered. The authors consider this to be an adequate model for the long-range part of the interaction. To take care of the complicated short-range interaction where the annihilation couples to many mesonic channels and where quark-gluon degrees of freedom are perhaps important, a phenomenological P-matrix formalism [81] is used. The P matrix relates the inner to outer region physics by setting a (logarithmic derivative) boundary condition for the solution to the channel-space Schrödinger equation (Eq. 3.7) at a distance b from the origin:

$$P = b\left(\frac{d\Phi}{dr}\Phi^{-1}\right)_{r=b}. \tag{3.8}$$

The distance b was determined to be best set to 1.2 fm and the parameters of the P matrix were set with a fit to the data, as explained below.

With the potential matrix set and the P matrix parameterized, Eq. 3.7 was solved numerically for each partial wave with $J \leq J_{\max}$ and matched with the P matrix at $r = b$. Then the scattering matrix was determined from the solution matrix and the observables were calculated.

This model was then used to fit the PS185 $\overline{p}p \rightarrow \overline{\Lambda}\Lambda$ data including differential cross sections, polarizations, and spin correlation coefficients at six different antiproton momenta (practically the same set as was used for the Tabakin, Eisenstein, and Lu analysis described above). In total, this amounted to 157 data points (seven were omitted from the fits). To fit this data, it was determined that 10 P-matrix parameters were needed to specify the unknown short range part of the interaction. One parameter was needed to specify the initial state absorption, one for the final state absorption, three to specify the $\overline{\Lambda}\Lambda \rightarrow \overline{\Lambda}\Lambda$ scattering, and five to specify the short-

range $\overline{p}p \rightarrow \overline{\Lambda}\Lambda$ couplings. The resulting fit to the data was good, with a reduced χ^2 of 1.15.

The dominant features of the Nijmegen model are evident upon examination of the cross sections in each partial-wave transition. The dominant tensor force results in a virtually zero contribution at all momenta from the singlet transitions, a large contribution from the ${}^3D_1 \rightarrow {}^3S_1$ transition with ${}^3F_2 \rightarrow {}^3P_2$ increasing with momentum, and important contributions from all of the triplet P waves as needed to reproduce the polarization data. The model is very sensitive to the inclusion of the K^* meson and not so to the scalar K_0^* and tensor K_2^*.

Determination of the ΛpK Coupling Constant

With a subset of the PS185 data used above, the Nijmegen coupled channels model was also used to extract the ΛpK coupling constant [56]. The same procedure and potentials as described above were used but with eight P-matrix parameters instead of 10. Then, instead of fixing the ΛpK coupling constant by SU(3) flavor symmetries, it was added as a ninth parameter. A tenth parameter had to be added to allow a scaling of the strength of the contribution from the K^*.

The fit of this model to the data, resulted in a value for the ΛpK coupling constant $f_{\Lambda pK}$ given by,

$$f^2_{\Lambda pK} = 0.071 \pm 0.007. \tag{3.9}$$

To check this result, the K mass was replaced with a parameter and allowed to vary in the fit. The resulting mass of 480 ± 60 MeV/c^2, in agreement with the experimental value, was interpreted by the authors as evidence for a one-kaon-exchange mechanism in the $\overline{p}p \rightarrow \overline{\Lambda}\Lambda$ process. Using the value determined for $f_{\Lambda pK}$ from the fit to the PS185 data to determine the $\alpha = F/(F+D)$ ratio and comparing with that found from weak semileptonic baryon decays, they reached the conclusion that a pseudovector coupling of the pseudoscalar mesons to baryons is favored over a pseudoscalar

coupling. Also, no evidence for violation of the SU(3)-determined relation,

$$f_{\Lambda NK} = -f_{NN\pi}(1 + 2\alpha)/\sqrt{3}, \tag{3.10}$$

was found in this analysis of the data.

3.4.4 The Washington-Colorado Quark-Based Model

The Washington-Colorado (WC) group has developed a model that, in strong contrast to the Nijmegen approach, focuses on the short-range physics by describing the strangeness production through the interactions of quarks and gluons [67].

In this model, a scalar "$^3P_0$" term, representing scalar multigluon exchange and/or the confining scalar force, and a vector "$^3S_1$" term, representing vector exchange of one or more gluons, are included. In a related work [66], the WC group has calculated the contribution of a pseudoscalar term and shown it to be negligible. The notation "$^3P_0$" and "$^3S_1$" refers to the strange quark production mechanism, not the partial waves of the composite baryons; thus the quotes are used. The operator for vector exchange is

$$I_v = g_v \sigma_3' \cdot \sigma_3 \tag{3.11}$$

and the operator for scalar exchange is

$$I_s = g_s \sigma_3' \cdot \left(\frac{\nabla_{3'} - \nabla_{6'}}{2m_s}\right) \sigma_3 \cdot \left(\frac{\nabla_3 - \nabla_6}{2m}\right), \tag{3.12}$$

with the 3 and the 6 referring to the annihilated quark and antiquark and the primed quantities referring to the final state quarks. For the strange quark mass, they used $m_s = 491$ MeV/c^2 and for the down and up quark masses, $m = 313$ MeV/c^2.

To calculate the observables resulting from this interaction model and to include initial- and final-state effects, a distorted-wave Born approximation was used. The matrix element for the reaction is

$$\mathcal{M}_{\overline{p}p \to \overline{\Lambda}\Lambda} = \langle X_{\overline{\Lambda}\Lambda} \phi(1'2'3') \phi(4'5'6') | (I_v + I_s) | \phi(123) \phi(456) X_{\overline{N}N} \rangle, \tag{3.13}$$

where $X_{\overline{\Lambda}\Lambda}$ and $X_{\overline{N}N}$ are the distorted waves of the final and initial states and ϕ is a gaussian wave function for the internal motion of the quarks:

$$\phi \sim \prod_{i=1}^{3} e^{-(\mathbf{r}_i - \mathbf{R}/2)^2/2b^2}. \tag{3.14}$$

The quantity $\mathbf{R}/2$ is the baryon c.m. coordinate, $\mathbf{r}_i$ is the coordinate of the ith quark, and b is the r.m.s. radius of the quark distribution. SU(3)-symmetric wave functions were used.

The distorted waves were determined from the initial- and final-state potentials using what has come to be fairly standard procedure. The initial-state potential

$$V_{\overline{N}N}(r) = U_{\overline{N}N}(r) + iW_{\overline{N}N}(r) \tag{3.15}$$

includes, in the real part $U_{\overline{N}N}$, central, tensor, spin-orbit, and spin-spin terms and, in the imaginary part $W_{\overline{N}N}$, a central potential to take care of annihilation. The long-range part of $U_{\overline{N}N}$ was determined by a G-parity transform of the Ueda one-boson exchange potential [82] and extrapolated from $r = 1$ fm to the origin with a Woods-Saxon form. The annihilation part of the initial-state potential, $W_{\overline{N}N}$, was also of Woods-Saxon form with parameters set by fits to $\overline{p}p$ data. None of these initial-state parameters were adjusted in the fits to the $\overline{p}p \to \overline{\Lambda}\Lambda$ data.

The final state potential used was of the same form (Eq. 3.15) as for the initial state. The long range part of $U_{\overline{\Lambda}\Lambda}$ was derived from the Nijmegen hyperon-nucleon potential [83] and smoothly extrapolated to the origin. The imaginary part $W_{\overline{\Lambda}\Lambda}$ was also of Woods-Saxon form. However, these potentials were only starting points and the parameters were varied for the fits to the $\overline{p}p \to \overline{\Lambda}\Lambda$ data.

This model was then applied to a global fit of the PS185 $\overline{p}p \to \overline{\Lambda}\Lambda$ data at eight antiproton momenta. This set consists of 356 data points including differential cross sections, polarizations, and spin-correlation coefficients. There were nine parameters varied in the fit: the strengths of the vector and scalar terms, g_V and g_S; the quark

wavefunction range parameter r_0 ($= 2b/\sqrt{3}$); and six parameters of the $\overline{\Lambda}\Lambda$ final-state potential. Three parameters in the real part of $V_{\overline{\Lambda}\Lambda}$ were varied: the strength of the central plus spin-spin term (V_c), the strength of the tensor term (V_T), and the strength of the spin-orbit term (V_{LS}). In the annihilation part of $V_{\overline{\Lambda}\Lambda}$, three parameters were varied: the strength, radius, and diffuseness ($W^0_{\overline{\Lambda}\Lambda}$, r_W, and a_W).

The resulting fit was of fairly good quality with a reduced χ^2 of 3.2. The resulting vector strength g_V converged to a value more than twice that of the scalar strength g_S. The diffuseness parameter a_W tended to zero and so was fixed at 0.01 while the values for $W^0_{\overline{\Lambda}\Lambda}$ and r_W converged to -1956 MeV and 0.66 fm. The result was a deep, sharp, final-state annihilation potential of about half a nucleon radius. The fits were not very sensitive to the V_c, V_T, and V_{LS} parameters having flat valleys in χ^2 space. Alternative fits with the vector and scalar terms alternately set to zero resulted in χ^2 values twice that of the best fit, showing that, in this model, both mechanisms are required for a good fit to the data.

3.4.5 More on Meson Exchange vs. Quark-Based Calculations

The Nijmegen meson-exchange model and the Washington-Colorado quark-based model detailed above provide insight into the two major approaches to describing the $\overline{p}p \rightarrow \overline{Y}Y$ process. It is interesting to note that, while focusing on different parts of the interaction distance scale, they both provide adequate descriptions to the PS185 $\overline{p}p \rightarrow \overline{\Lambda}\Lambda$ data. The Nijmegen model calculates the outer-region interaction with no parameterization while treating the inner region phenomenologically. The WC model takes the opposite approach, calculating the short-range interaction of quarks and, to a large degree, parameterizing the part where long-range meson exchange should be important. Are these two approaches equally valid?

In a recent effort, Eisenstein has examined [84] the resulting partial-wave amplitudes of the Nijmegen and WC models along with those resulting from the Tabakin, Eisenstein, and Lu, amplitude analysis that was explained in Section 3.4.1. The

most striking conclusion from this comparison is the difference in strengths of the off-diagonal ${}^3D_1 \rightarrow {}^3S_1$ and ${}^3F_2 \rightarrow {}^3P_2$ transitions between the two dynamical models. The Nijmegen model, because of the large tensor force due to the K and K^* exchanges, yields strong off-diagonal transitions. In the WC model, the quark-creation mechanism yields a very weak tensor force; the off-diagonal transitions are due predominantly to the tensor-force terms in the initial and final-state interactions. Even with these tensor force terms, the off-diagonal transitions are significantly smaller than in the Nijmegen model. The data are not able, however, to definitely separate these subtle effects and, therefore, select the better of the two approaches.

The idea of a measurement of the depolarization parameter D_{nn} has recently been proposed by Haidenbauer et al. [59,60]. They submit that this spin observable is more sensitive to spin-flip transitions that occur in the presence of a tensor force and is less affected by initial- and final-state effects. This measurement may have greater power to select between the quark-based and meson-exchange models. The proposed experiment would need a polarized target and is currently being investigated by the PS185 collaboration.

3.5 The $\bar{p}p \rightarrow \overline{\Sigma}^0\Lambda + c.c.$ Reaction and Theory

A thorough measurement of the $\bar{p}p \rightarrow \overline{\Sigma}^0\Lambda + c.c.$ reaction in the near threshold region should allow significant gains to be made in understanding the $\bar{p}p \rightarrow \overline{Y}Y$ process. The SU(3) flavor symmetries constrain, to some degree, how much the parameters of the above models can be adjusted to fit the data from the $\bar{p}p \rightarrow \overline{\Sigma}^0\Lambda + c.c.$ reaction along with that of $\bar{p}p \rightarrow \overline{\Lambda}\Lambda$. The Nijmegen model has all the machinery in place to address this new channel. Of course, there would have to be additional final-state interaction parameters added, but they should be limited in number. The same is true of the WC quark-based model. A replacement of a Σ^0 quark wave function for a Λ and an adjustment of the final-state interaction makes the model work for the

$\bar{p}p \rightarrow \overline{\Sigma}^0\Lambda + c.c.$ reaction.

What is expected to be seen in the $\bar{p}p \rightarrow \overline{\Sigma}^0\Lambda + c.c.$ data? From a meson-exchange perspective, the tensor force in this channel has quite a different character as compared to $\bar{p}p \rightarrow \overline{\Lambda}\Lambda$. The ΣpK coupling constant is reduced compared to the ΛpK coupling ($f_{\Lambda NK}/f_{\Sigma NK} \approx 3.4$ in the Nijmegen work [37,80]) and $f_{\Sigma NK^*}$ is of opposite sign and somewhat reduced as compared to $f_{\Lambda NK^*}$. Therefore, the K and K^* do not add to produce as strong a tensor force for $\bar{p}p \rightarrow \overline{\Sigma}^0\Lambda + c.c.$ as is seen in $\bar{p}p \rightarrow \overline{\Lambda}\Lambda$. This should be evident in the data as the reordering of the partial-wave amplitudes changes the character of the observables in the $\bar{p}p \rightarrow \overline{\Sigma}^0\Lambda + c.c.$ channel. Also, with a sufficiently complete data set for $\bar{p}p \rightarrow \overline{\Sigma}^0\Lambda + c.c.$, the ΣNK coupling constant could be extracted from the data as was done by the Nijmegen group for the ΛNK coupling [56].

From the quark perspective, the different quark wave function for the Σ^0 adds a new twist to the problem. In the Σ^0, the role of the s quark in the spin wave function is quite different. The singlet fraction for the $\bar{p}p \rightarrow \overline{\Sigma}^0\Lambda + c.c.$ reaction has been calculated to be $\frac{3}{7}$ using a vector [48] or scalar [62] $\bar{s}s$ creation mechanism. Unfortunately, since singlet to triplet transitions may occur also in the $\bar{p}p \rightarrow \overline{\Sigma}^0\Lambda + c.c.$ final state, the situation is somewhat clouded.

As might be imagined, since the $\bar{p}p \rightarrow \overline{\Sigma}^0\Lambda + c.c.$ final-state interaction is relatively unknown, predictions for the $\bar{p}p \rightarrow \overline{\Sigma}^0\Lambda + c.c.$ channel are somewhat scarce. However a recent calculation by Haidenbauer et al. [57,58] does address the $\bar{p}p \rightarrow \overline{\Sigma}^0\Lambda + c.c.$ data with their coupled-channels meson-exchange model. Prompted by the PS185 $\bar{p}p \rightarrow \overline{\Sigma}^0\Lambda + c.c.$ measurement at 1.695 GeV/c antiproton momentum, they have worked out the observables for this channel (with a calculation similar to that of the Nijmegen group). The results include, as for the $\bar{p}p \rightarrow \overline{\Lambda}\Lambda$ channel, sizeable P-wave production due to S-wave suppression. However, the division among P waves is somewhat different as compared to $\bar{p}p \rightarrow \overline{\Lambda}\Lambda$. The off diagonal $^3F_2 \rightarrow {}^3P_2$ transition is not as strong due to the reduced tensor force and the $^3P_1 \rightarrow {}^1P_1$ transition, not

forbidden for $\overline{p}p \rightarrow \overline{\Sigma}^0\Lambda + c.c.$, is appreciable. The contribution of the singlet states ($^1S_0$,$^1P_1$,$^1D_2$) are also considerably larger: the calculation at 1.695 GeV/c antiproton momentum gives a $\overline{p}p \rightarrow \overline{\Sigma}^0\Lambda + c.c.$ singlet fraction of approximately 0.2.

The PS185 $\overline{p}p \rightarrow \overline{\Sigma}^0\Lambda + c.c.$ data at 1.695 GeV/c along with the fits from Haidenbauer et al. are shown in Fig. 3.2. The model reproduces the data reasonably well, although the differential cross section data seem to be more strongly peaked than is reproduced by the fits. Unfortunately, the polarization data, due to the large errors, does little to constrain the model. Although a good start, it is evident that more $\overline{p}p \rightarrow \overline{\Sigma}^0\Lambda + c.c.$ data, with better precision is required.

More data on the $\overline{p}p \rightarrow \overline{\Sigma}^0\Lambda + c.c.$ reaction would help with the theoretical understanding of the $\overline{p}p \rightarrow \overline{Y}Y$ reaction dynamics. A high-precision measurement that includes spin observables at different momenta in the near-threshold region is clearly beckoned. Perhaps this new information could facilitate the construction of a model that includes both long-range meson exchange and short-range quark dynamics in a complete coupled-channels formalism with a minimum of phenomenology. This is possibly a goal only to be obtained in the far future as a complete understanding of the interactions of quarks and gluons is still beyond our grasp. But, this measurement of the $\overline{p}p \rightarrow \overline{\Sigma}^0\Lambda + c.c.$ reaction described in the following pages is a step in the proper direction.

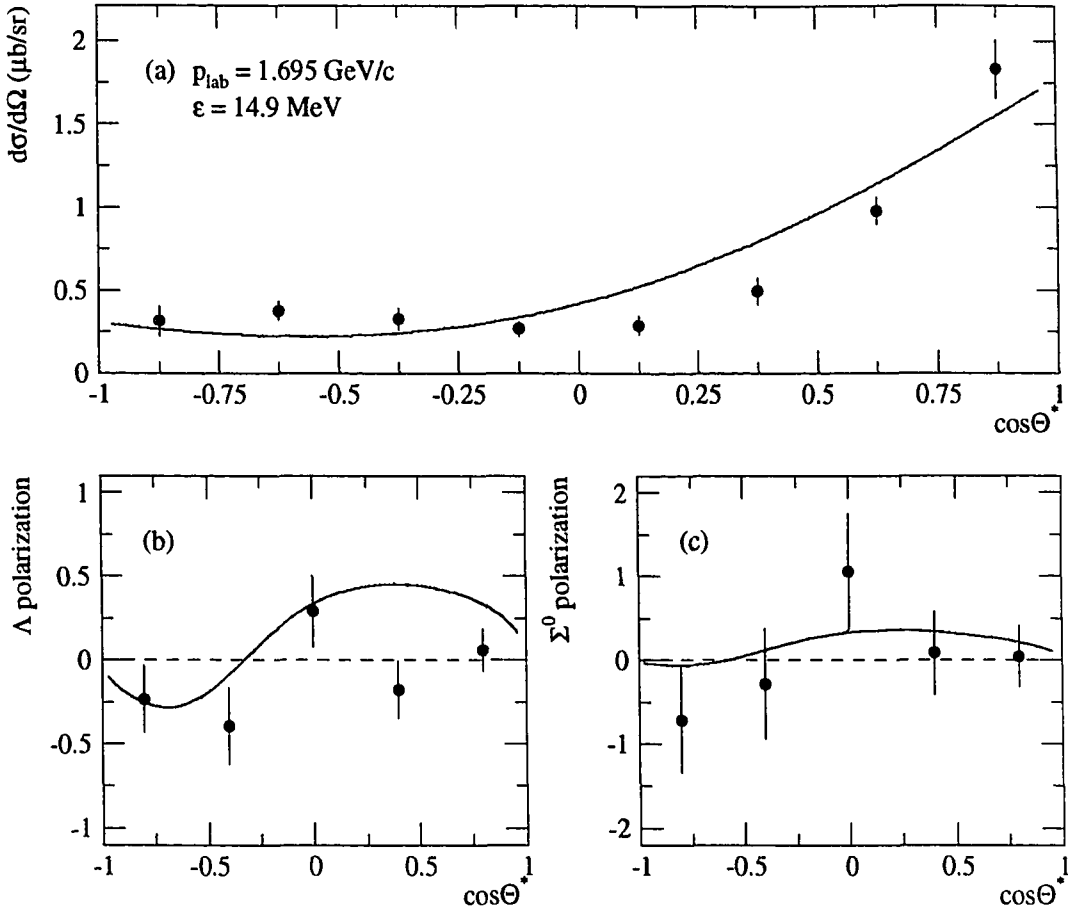

Figure 3.2: The PS185 $\bar{p}p \rightarrow \overline{\Sigma}^0\Lambda + c.c.$ data at 1.695 GeV/c with the fits by Haidenbauer et al. [58] to the (a) differential cross section, (b) Λ polarization, and (c) Σ^0 polarization.

Chapter 4

Experiment

To study the $\overline{Y}Y$ system, a source of illumination (the antiprotons) and a microscope (the detector) are needed. In this chapter, the LEAR antiproton source, the $\overline{p}p \rightarrow \overline{Y}Y$ reaction topology, and the PS185 detector are described. For both the antiproton source and the PS185 detector, specific details have changed from year to year as the accelerator has been upgraded and the detector improved. The situation described here is as it was for the data set studied in this work, taken with an extracted antiproton momentum of 1.729 GeV/c.

4.1 The Antiproton Source

The antiprotons used for the experiment PS185 are provided by the LEAR (Low Energy Antiproton Ring) facility at CERN. The antiprotons are produced by bombarding a metal target with a pulse of 26 GeV/c protons from the CERN proton synchrotron (PS). The antiprotons are collected and injected into the antiproton collector ring (AC) where they are stochastically cooled and moved into the antiproton accumulator storage ring (AA). In this manner, approximately 10^{10} antiprotons per hour are collected and up to approximately 10^{12} antiprotons are stored [85]. Upon request from the LEAR control, a "bunch" of approximately 10^{10} antiprotons from the AA is transferred to the PS, decelerated from 3.5 GeV/c to 0.609 GeV/c, and then transferred to LEAR [86]. The sections of the CERN accelerator complex relevant

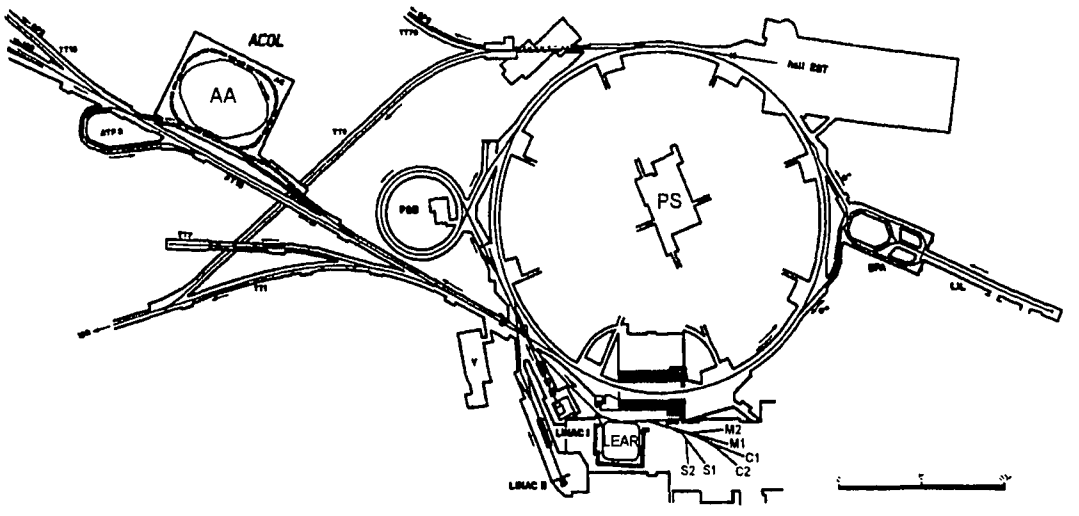

Figure 4.1: A diagram of a portion of the CERN accelerator complex showing the relative positions of LEAR, the antiproton accumulator (AA), and the proton synchrotron (PS) [87].

to the operation of LEAR are shown in Fig. 4.1.

After a bunch of antiprotons are loaded into LEAR, they are stochastically cooled for a few minutes before they are accelerated or decelerated to the desired momentum. The stochastic cooling reduces the phase space of the stored antiprotons which results in a beam of low divergence and small momentum width. The cooling is accomplished by sensing the velocity divergence of the beam with a "pickup" located on the ring and sending a compensating signal across the ring to a "kicker" located across the ring which adjusts the beam as it passes [86]. A diagram of LEAR with the layout of the stochastic cooling system is shown in Fig. 4.2.

After the antiprotons are cooled and accelerated or decelerated to the desired momentum, they can be used within the storage ring or extracted. For extraction, the longitudinal distribution is broadened and the outermost antiprotons are deflected out of the ring with electrostatic and magnetic septa [86]. The extracted beam is

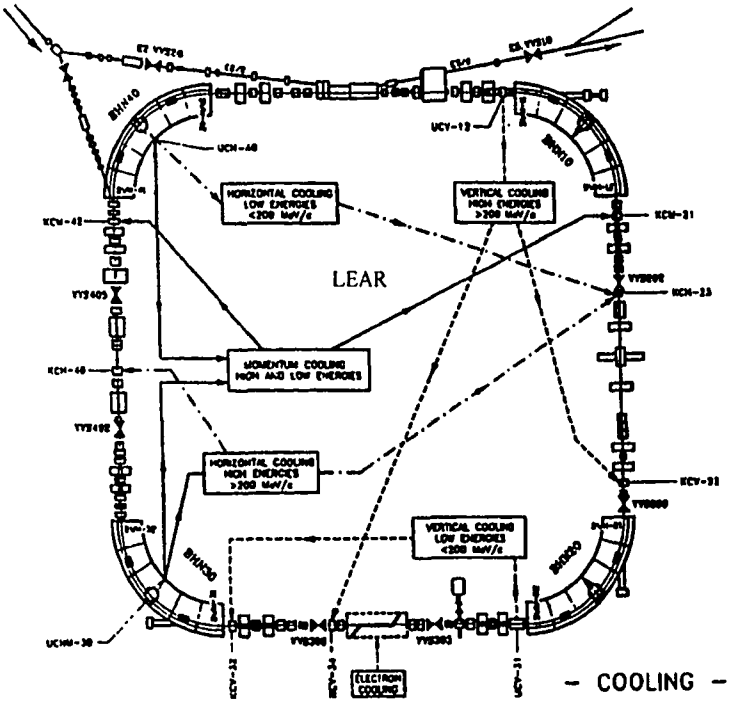

Figure 4.2: A diagram of LEAR with the layout of the stochastic cooling system. Antiprotons enter the ring along the line at the top left of the figure and are extracted to experiments along the line at the top right.

then delivered to any of several external beam lines. It is delivered continuously until the ring is emptied (a "spill") and then a new bunch of antiprotons is delivered from the AA and the cooling, acceleration, and extraction cycle is repeated.

The LEAR facility can provide extracted antiprotons with momentum ≈ 0.1 - 2.0 GeV/c at intensities up to $\approx 2 \times 10^6$ Hz with a duty factor of greater than 80%. The advantages of LEAR antiproton beam as compared to a non-cooled and non-stored beam are multifold. They include zero pion contamination, low momentum spread, reduced angular divergence, and small beam spot size.

hyperon	Λ	Σ^0
mass (GeV/c^2)	1.115684 ± 0.000006	1.19255 ± 0.00008
lifetime (s)	$2.632 \pm 0.020 \times 10^{-10}$	$7.4 \pm 0.7 \times 10^{-20}$
$c\tau$ (cm)	7.89	2.22×10^{-9}
main decay modes and	$\Lambda \rightarrow p\pi^-$ $(63.9 \pm 0.5\%)$	$\Sigma^0 \rightarrow \Lambda\gamma$ (100%)
branching fractions	$\Lambda \rightarrow n\pi^0$ $(35.8 \pm 0.5\%)$	

Table 4.1: Physical parameters of the Λ and Σ^0 hyperons [12].

The PS185 experiment is situated on the M1 extraction line (see Fig. 4.1) and is delivered antiprotons with momenta from the $\bar{p}p \rightarrow \overline{\Lambda}\Lambda$ threshold ($p_{\bar{p}} = 1.435$ GeV/c) to the maximum LEAR momentum at rates around 1×10^6 Hz. The beam is steered and focused onto the target with several magnets on the M1 extraction line using diagnostic information supplied by beam line chambers and the PS185 apparatus. For the data set described in this work, the extraction momentum was 1.729 ± 0.001 GeV/c and the average (beam-on) antiproton rate to the experiment was 5.9×10^5 Hz. A LEAR spill was delivered over the course of approximately 1 hour and the refilling to extraction time was about 10–15 minutes.

4.2 The Reaction Topology of $\bar{p}p \rightarrow \overline{Y}Y$

The topology of the $\bar{p}p \rightarrow \overline{Y}Y$ reactions dictate the design and operation of the PS185 detector. Therefore, an explanation of this topology is prerequisite to a description of the experimental apparatus. The factors that dictate the reaction topology are the hyperon decay modes and their lifetimes and the kinematics of the hyperon production and decay. These factors are explained in this section. The physical parameters of the Λ and Σ^0 hyperons relevant to this discussion are listed in Table 4.1.

The majority of the Λ ($\overline{\Lambda}$) hyperons of a $\bar{p}p \rightarrow \overline{\Lambda}\Lambda$ event decay through $\Lambda \rightarrow p\pi^-$ ($\overline{\Lambda} \rightarrow \bar{p}\pi^+$) with a branching fraction of 63.9%. With the exception of several rare

modes with branching fractions less than 0.2%, the remainder decay via $\Lambda \rightarrow n\pi^0$ ($\overline{\Lambda} \rightarrow \overline{n}\pi^0$). For precise Λ and $\overline{\Lambda}$ reconstruction, only the charged decay mode is considered. The total reaction chain detected is $\overline{p}p \rightarrow \overline{\Lambda}\Lambda \rightarrow \overline{p}\pi^+ p\pi^-$ with a double-decay branching fraction of 40.8%.

The Σ^0 hyperons in the $\overline{p}p \rightarrow \overline{\Sigma}^0\Lambda + c.c.$ channels decay through $\Sigma^0 \rightarrow \Lambda\gamma$ ($\overline{\Sigma}^0 \rightarrow \overline{\Lambda}\gamma$) with a branching fraction of 100%. All other decay modes are sufficiently rare to be considered negligible for this experiment[1]. The reaction chains for the $\overline{p}p \rightarrow \overline{\Sigma}^0\Lambda + c.c.$ channels are $\overline{p}p \rightarrow \overline{\Sigma}^0\Lambda \rightarrow \overline{p}\pi^+ p\pi^-\gamma$ and $\overline{p}p \rightarrow \overline{\Lambda}\Sigma^0 \rightarrow \overline{p}\pi^+ p\pi^-\gamma$, both identical to $\overline{p}p \rightarrow \overline{\Lambda}\Lambda$ except for the presence of the photon.

The neutral Λ has a relatively long lifetime and typically travels a few centimeters in the detector before decaying ($c\tau = 7.89$ cm). This, together with the detected two-charged-particle decay mode, is the characteristic signature of $\overline{p}p \rightarrow \overline{\Lambda}\Lambda$. The tracks of the charged particles in these events resemble two "V"'s displaced slightly from the target. This event pattern has acquired the familar name — "2-V event". The Σ^0 decays almost immediately after traveling a negligible distance in the detector ($c\tau = 2.22 \times 10^{-9}$ cm) and the mass of the Σ^0 is only about 6% larger than the Λ mass. The Σ^0-decay photon has energy 76.9 MeV in the Σ^0 rest frame. In the lab, at an antiproton momentum of 1.729 GeV/c, the Σ^0-decay photon has energy in the range 30-170 MeV. Therefore, the $\overline{p}p \rightarrow \overline{\Sigma}^0\Lambda + c.c.$ reactions have a charged-particle signature in the detector that is very similar to that of $\overline{p}p \rightarrow \overline{\Lambda}\Lambda$. The two reactions are distinguishable through the slightly different kinematics and the Σ^0-decay photon.

Because the Λ and Σ^0 masses are larger than the proton mass, the $\overline{p}p \rightarrow \overline{\Lambda}\Lambda$ and $\overline{p}p \rightarrow \overline{\Sigma}^0\Lambda + c.c.$ reactions are endothermic. That is, in the c.m. system, especially near threshold, the momenta of the final state hyperons are much smaller than the momenta of the initial state $\overline{p}$ and p. This has the result, after the boost to the lab frame, that the lab momentum vectors of the hyperons are constrained to a

[1]The decay mode $\Sigma^0 \rightarrow \Lambda\gamma\gamma$ has an experimental upper limit of 3% and $\Sigma^0 \rightarrow \Lambda e^+ e^-$ has a QED-calculated value of 5×10^{-3} [12].

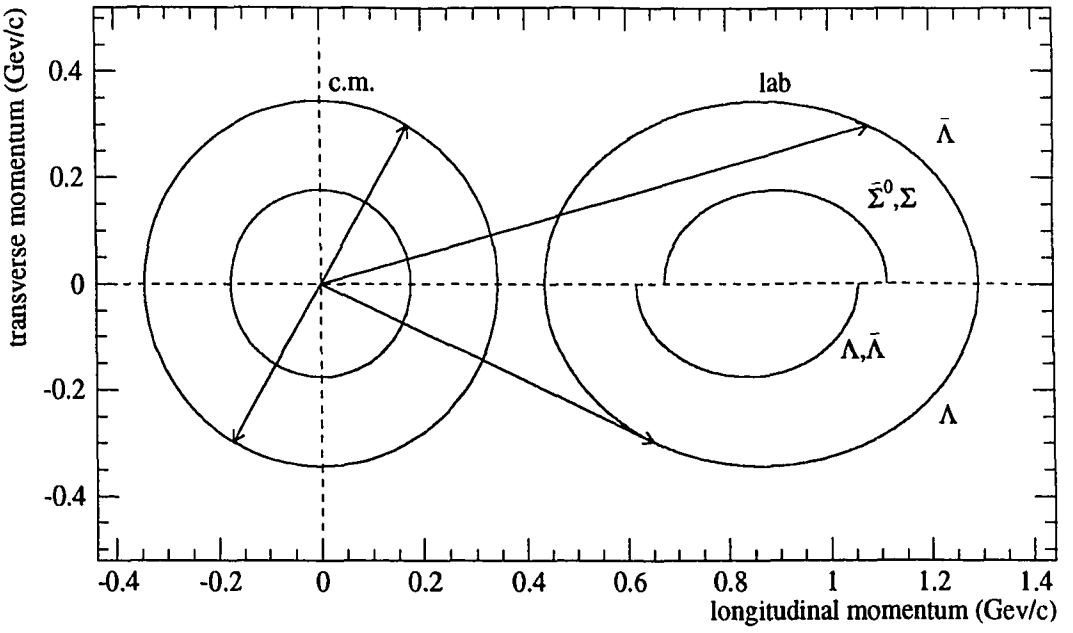

Figure 4.3: Kinematic ellipses for the $\overline{p}p \rightarrow \overline{\Lambda}\Lambda$ and $\overline{p}p \rightarrow \overline{\Sigma}^0\Lambda + c.c.$ reactions for an antiproton (lab) momentum of 1.729 GeV/c. The longitudinal and transverse momentum values of the final state hyperons are constrained to lie on the circles in the c.m. system and on the ellipses in the lab. The outer (inner) curves are for the $\overline{p}p \rightarrow \overline{\Lambda}\Lambda$ ($\overline{p}p \rightarrow \overline{\Sigma}^0\Lambda + c.c.$) reaction. The arrows illustrate a $\theta^* = 60°$, $\overline{p}p \rightarrow \overline{\Lambda}\Lambda$ event in both the c.m. and lab frames.

narrow forward cone around the beam direction. This is best illustrated with the use of kinematic ellipses illustrated in Fig. 4.3. It is evident from this figure that the transverse momentum is small compared to the effect of the boost in the $\overline{p}p \rightarrow \overline{\Lambda}\Lambda$ and $\overline{p}p \rightarrow \overline{\Sigma}^0\Lambda + c.c.$ reactions near threshold. For lower beam momenta, the ellipses become smaller and move slightly down in momentum. Exactly at threshold, they become points with zero transverse momentum.

The decay of the Σ^0 has a relatively small effect on the kinematics. The kinematic ellipse of the Σ^0-decay Λ, if plotted, is similar to that of the Σ^0 with the addition of an approximately 100 MeV/c "smearing" of the ellipse due to the momentum carried by the Σ^0-decay photon.

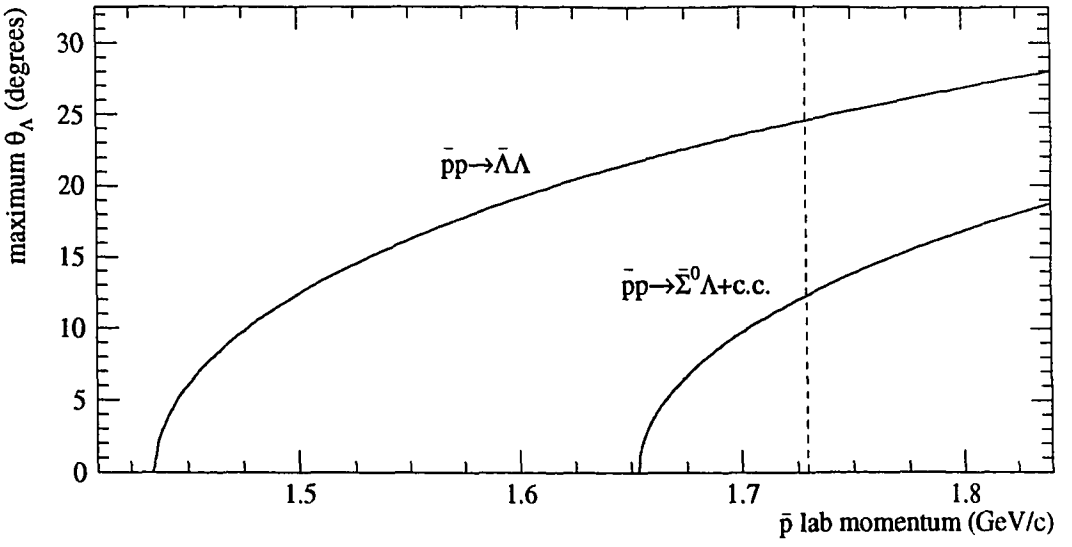

Figure 4.4: Maximum Λ angle as a function of antiproton lab momentum for the $\overline{p}p \to \overline{\Lambda}\Lambda$ and $\overline{p}p \to \overline{\Sigma}^0\Lambda + c.c.$ reactions. The dotted line indicates the momentum of this measurement, 1.729 GeV/c.

The maximum lab angle of the Λ and $\overline{\Lambda}$ with respect to the beam direction for the $\overline{p}p \to \overline{\Lambda}\Lambda$ as a function of antiproton momentum is shown in Fig. 4.4. The maximum Λ ($\overline{\Lambda}$) angle for the $\overline{p}p \to \overline{\Sigma}^0\Lambda$ ($\overline{p}p \to \overline{\Lambda}\Sigma^0$) reaction is shown on the same plot. The maximum Σ^0 angle is slightly smaller due to the larger mass of the Σ^0 hyperon. The maximum possible lab angle of the Σ^0-decay Λ is approximately equal to that of a directly-produced Λ due to the possibility of a transverse momentum "kick" from the Σ^0-decay photon.

The decay products of the Λ and $\overline{\Lambda}$ are also forward boosted. The maximum angle of the proton and pion with respect to the parent-Λ direction as a function of Λ lab momentum is plotted in Fig. 4.5. The momentum range plotted corresponds to the range of Λ momenta in the $\overline{p}p \to \overline{\Lambda}\Lambda$ reaction at 1.729 GeV/c as can be seen from Fig. 4.3. For all Λ momenta possible in the PS185 experiment, the decay protons are constrained to the forward hemisphere. At 1.729 GeV/c incident antiproton momentum, the maximum decay-proton angle is approximately 20°. These protons

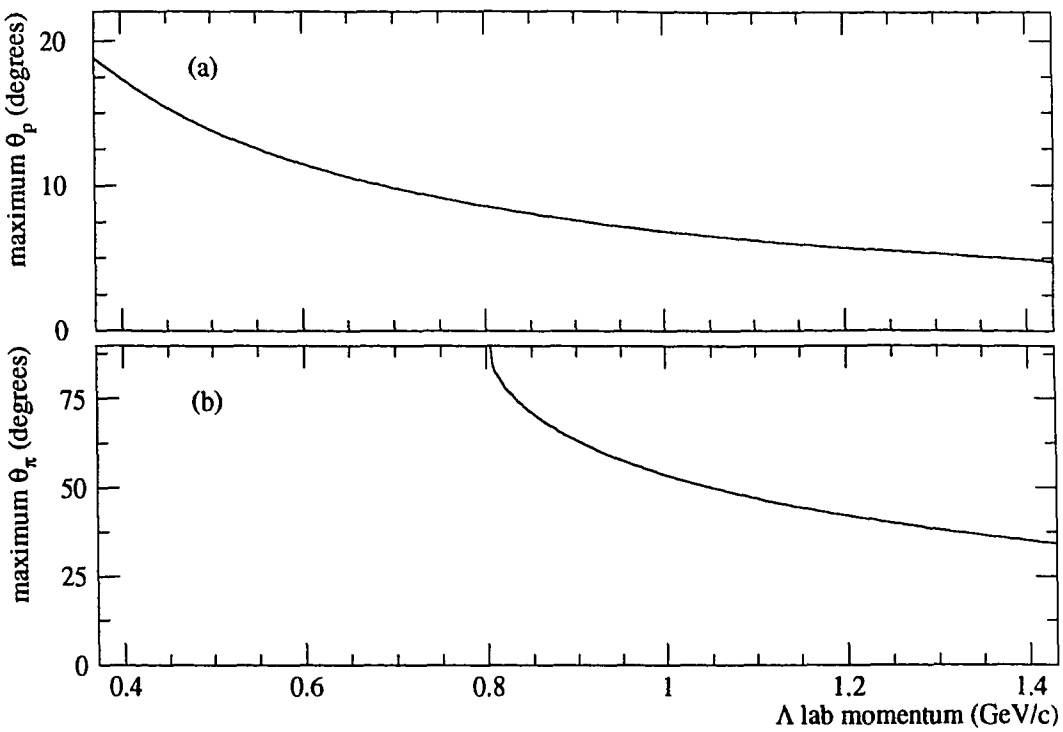

Figure 4.5: Maximum (a) p, $\overline{p}$ and (b) π^-, π^+ angles in the decays $\Lambda \rightarrow p\pi^-$ and $\overline{\Lambda} \rightarrow \overline{p}\pi^+$ with respect to the direction of the parent Λ,$\overline{\Lambda}$ as a function of parent lab momentum. Below 0.8 GeV/c, pions of all angles are possible.

are from the lowest momentum Λ's in the $\overline{p}p \rightarrow \overline{\Lambda}\Lambda$ reaction. However, the pions are constrained to the forward hemisphere only for Λ's with momenta greater than 0.8 GeV/c. For pions from lower momenta Λ's, all angles are possible. These decays have the additional feature that, for all Λ momenta possible in the PS185 experiment, for a specific decay, the proton decay angle is always smaller than that of the pion.

In summary, the $\overline{p}p \rightarrow \overline{\Lambda}\Lambda$ and $\overline{p}p \rightarrow \overline{\Sigma}^0\Lambda + c.c.$ reactions are detected through the decay chains: $\overline{p}p \rightarrow \overline{\Lambda}\Lambda \rightarrow \overline{p}\pi^+p\pi^-$, $\overline{p}p \rightarrow \overline{\Sigma}^0\Lambda \rightarrow \overline{p}\pi^+p\pi^-\gamma$, and $\overline{p}p \rightarrow \overline{\Lambda}\Sigma^0 \rightarrow \overline{p}\pi^+p\pi^-\gamma$. For all incident antiproton momenta in the PS185 range, the final-state Λ's have lab angles within a narrow forward cone. Due to the relatively long lifetime of the Λ, the Λ decay vertex is typically displaced a few centimeters from the production

point. The Λ-decay protons are also constrained to lie within a narrow forward cone in the lab.

4.3 The PS185 Apparatus

To successfully collect and reconstruct $\bar{p}p \rightarrow \overline{Y}Y$ events, the PS185 experimental apparatus must perform several important functions. These functions and the detector components that carry them out are listed below.

- The kinematics of the incident antiprotons and the interaction point must be precisely determined. This is necessary to sufficiently constrain the reaction kinematics. It is achieved through the use of the high-quality LEAR antiproton beam, a system of silicon microstrip detectors upstream of the target, and a small target system.

- A fast signal (the trigger) is needed in order to collect $\bar{p}p \rightarrow \overline{Y}Y$ events while rejecting the more ubiquitous elastic, $\bar{n}n$, and multipion events. This trigger is formed with the information from a scintillator array that surrounds the target and a downstream scintillator hodoscope.

- The Λ decay products must be accurately tracked in order to reconstruct the hyperon trajectories. Two tracking chambers, a multiwire proportional chamber (MWPC) and a drift chamber (DC), provide the charged particle coordinates that enable this tracking.

- The charge of the Λ decay products must also be measured so that the Λ and $\overline{\Lambda}$ may be distinguished. A tracking chamber (MACH) within a magnetic solenoid is implemented for this purpose.

- The $\bar{p}p \rightarrow \overline{\Sigma}^0\Lambda + c.c.$ reactions are better constrained if the Σ^0-decay photon is detected. A lead/scintillating-fiber calorimeter and system of veto scintillators

is installed and provides the information to be used when this constrain is necessary.

Because the $\overline{\Lambda}$ and Λ and the decay protons are limited to small production angles, good acceptance for the entire 4π of c.m. solid angle is obtained with a detector covering only the forward region of the lab solid angle. Also, the two-body nature of the reaction and the Λ decays allow the kinematics to be completely reconstructed by measuring track directions only — a momentum analyzing magnet is not needed. Because of these aspects of the reactions, the PS185 detector is fairly compact, simple, and economical. The PS185 apparatus is shown in Fig. 4.6 along with a Monte Carlo generated $\overline{p}p \rightarrow \overline{\Lambda}\Lambda$ event. The individual detectors are described in detail in the following sections.

Two right-handed orthogonal coordinate systems are used in the experiment and subsequent analysis. They are diagrammed in Fig. 4.7 along with a view of the MWPC. The xyz system is oriented with the z axis along the beam direction and the x and y axes are aligned with the orientation of the DC, hodoscope, and MACH. The origin is defined to be in the plane of the front foil of the MWPC. The uvz system is rotated 45° around the z axis with respect to the xyz system and is aligned with the orientation of the MWPC and the microstrip detectors. The different orientations are necessary to allow unambiguous 3-dimensional particle tracks to be formed from the coordinate information gathered by the detectors.

In the following descriptions, "upstream" is used to indicate the direction antiparallel ($-\hat{z}$) to that of the incident antiprotons and "downstream" is the direction parallel ($+\hat{z}$).

4.3.1 Microstrip Detectors

The silicon microstrip detectors are situated upstream of the target and are used to measure the direction of the incident antiproton beam. With these detectors, the

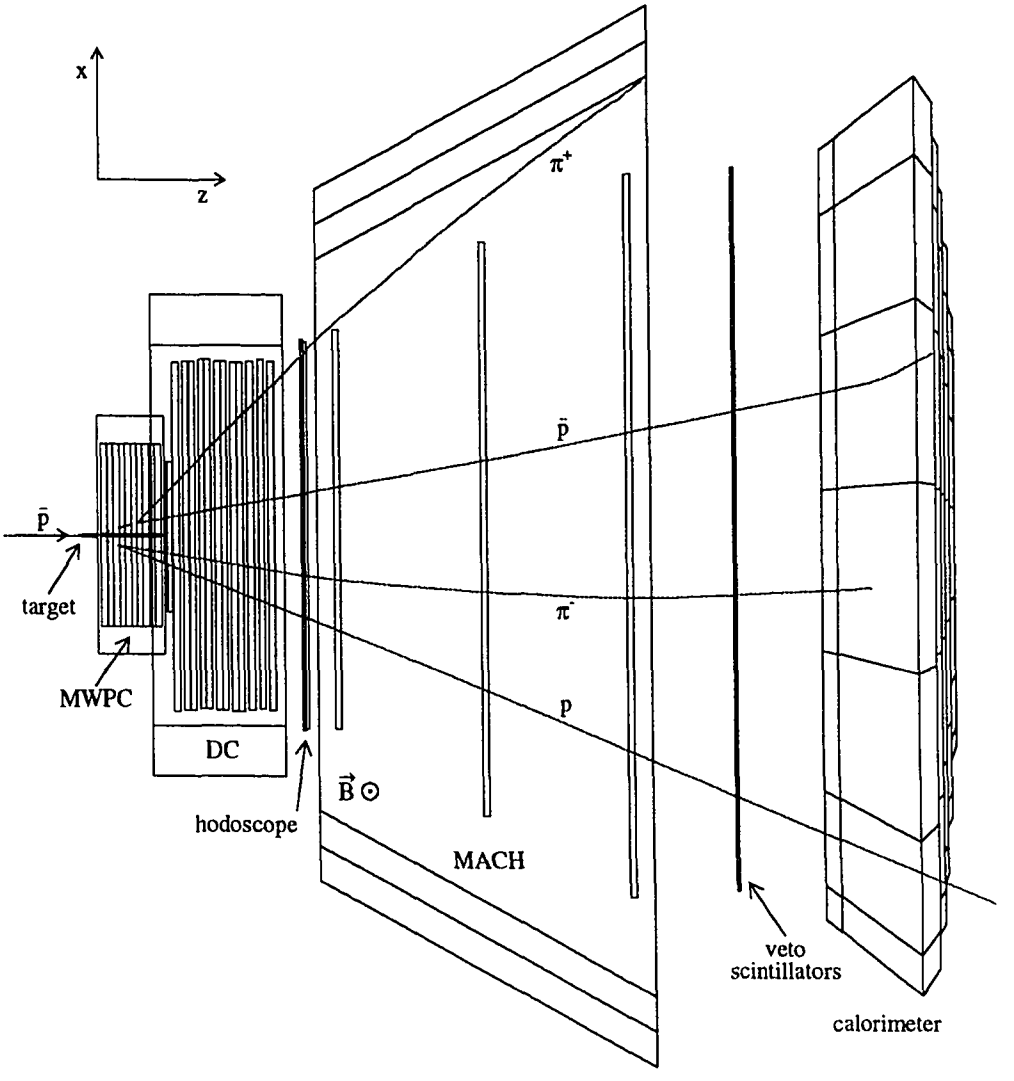

Figure 4.6: A schematic diagram of the PS185 experimental apparatus with a Monte Carlo $\overline{p}p \rightarrow \overline{\Lambda}\Lambda$ event generated with an antiproton momentum of 1.729 GeV/c.

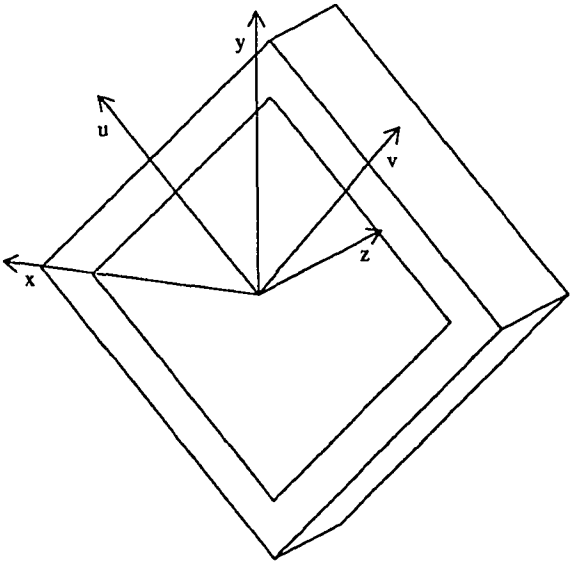

Figure 4.7: A diagram of the xyz and uvz coordinate systems superimposed on an isometric view of the MWPC.

beam direction and focus may be determined which helps with the beam steering process. This event-by-event measurement of the antiproton direction also helps to constrain the kinematics of the initial $\overline{p}p$ system. The charge liberated by the antiproton as it passes through the thin silicon detector is collected, amplified, and, recorded with an ADC [89]. Each plane is divided into thin strips of 100 or 200 μm width which allow the determination of the antiproton coordinate to an accuracy equal to approximately the strip width. For the 1.729 GeV/c data, there were four planes with parameters listed in Table 4.2.

4.3.2 Target System

The target system provides a source of protons and a portion of the information needed to form the event triggers (described in Sec. 4.4). It consists of four small cylinders of polyethylene (CH_2) and one of carbon (C) surrounded by a system of scintillators as shown in Fig. 4.8. The disk-shaped S1A, S1B, and S0 together function

plane #	orientation	thickness (μm)	# of strips	strip width (μm)	z position (cm)
1	v	500	16	200	-26.3
2	u	500	16	200	-25.9
3	v	300	20	100	-9.5
4	u	300	20	100	-9.1

Table 4.2: Parameters of each microstrip detector plane.

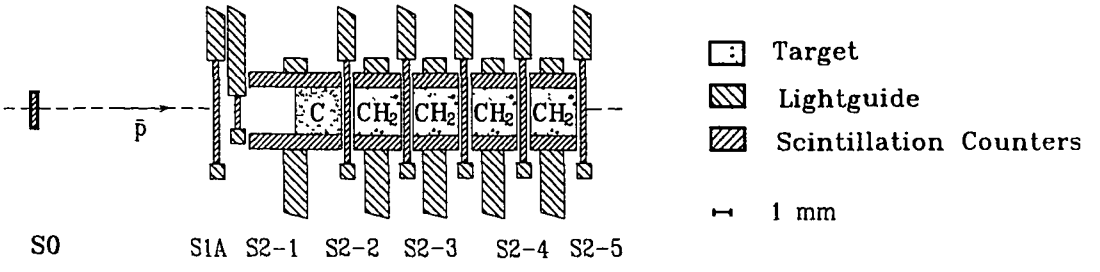

Figure 4.8: A cut view of the target system.

to determine the beam. In addition, the S0 scintillator provides the time reference signal ("t_0") for the entire experiment. The five disk-shaped S3 counters are used to measure the antiproton flux into each target cell and to provide a portion of the signals needed for the neutral trigger. The S2 scintillators are cylindrical barrels that surround each target cylinder and provide additional trigger signals. This entire system is centered on the nominal beam axis approximately 1.5 cm upstream of the MWPC ($z = -1.5$ cm). Each scintillator is connected to a phototube and the charge and time information of the phototube signal was recorded with an ADC and a TDC.

This small system of target cells surrounded by scintillators allows the cell of interaction to be determined. This gives the coordinate of hyperon production with accuracy equal to the size of the target cell (2.5 mm). Five separate cells are used in order to increase the probability of an interaction without increasing the error

target cell	1	2	3	4	5
$\overline{p}$ momentum (GeV/c)	1.72750	1.72661	1.72598	1.72530	1.72465
total c.m. energy (GeV)	2.33448	2.33417	2.33394	2.33370	2.33347

Table 4.3: Momentum and total c.m. energy for each target cell with an incident antiproton momentum of 1.729 GeV/c as calculated with a Monte Carlo simulation.

on the production point. A target cell of pure carbon is installed to monitor the background from $\overline{p}p \rightarrow \overline{Y}Y$ reactions occurring on carbon in the CH_2 cells. The five cells also allow measurement of the reactions at five different, closely grouped, momentum points due to the energy loss of the incident antiproton as it traverses each cell of the target. The momentum loss per cm of target material is 4.26 MeV/c cm for carbon and 2.07 MeV/c cm for CH_2, so the four CH_2 target cells correspond to four momentum bins of width $\approx$ 0.5 MeV/c spaced $\approx$ 0.5 MeV/c apart. The actual momentum loss is slightly larger due to the additional materials present. The most likely momentum loss of the incident antiproton from the exit of the beam vacuum line to the first target cell is $\approx$ 1.0 MeV/c due to material upstream of the target. The calculated central momentum and total c.m. energy values at the center of each cell are listed in Table 4.3. The CH_2 cells are separated by about 0.65 MeV/c momentum or 0.25 MeV total c.m. energy.

4.3.3 Multiwire Proportional Chamber

The multiwire proportional chamber (MWPC) measures the coordinates of the charged Λ-decay products so that the kinematics of the event may be reconstructed. It is constructed with ten planes of 160 wires (the anodes) of diameter 10 μm and length 20.3 cm on a spacing of 1.27 mm. The wire planes are spaced 1 cm apart and separated by a 10 μm thick aluminum foil (the cathode). Five planes are oriented to measure the u coordinate and five to measure v, although, for the collection of this data set, one u and one v plane were inoperable. The parameters of each plane are

plane #	coordinate measured	z position (cm)	active area (cm^2)
1	u	1.0	not functioning
2	v	2.0	not functioning
3	u	3.0	20.3×20.3
4	v	4.0	20.3×20.3
5	u	5.0	20.3×20.3
6	v	6.0	20.3×20.3
7	u	7.0	20.3×20.3
8	v	8.0	20.3×20.3
9	u	9.0	20.3×20.3
10	v	10.0	20.3×20.3

Table 4.4: Summary of parameters for each plane of the multiwire proportional chamber (MWPC).

summarized in Table 4.4. The volume of the MWPC is filled with a gas mixture consisting of 72% argon, 23.5% isobutane, 4% methylal, and 0.5% freon [27]. A 4.7 kV potential is maintained between the cathode and anode.

The ionization electrons created by a passing charged particle drift toward the anode wire and the positive ions drift toward the cathode. Close to the anode wire the electric field becomes very large. This results in an avalanche effect which creates more electron-ion pairs thereby amplifying the original signal [90] and the liberated charge creates a signal on the wires. This system yields the charged particle coordinates with accuracy on the order of the wire spacing. The wires within a 5 mm diameter circle centered on the nominal beam axis are electroplated to avoid amplification of the ionization charge due to the primary beam. The signal from each wire, if larger than a preset threshold, is read with the PCOS II system manufactured by LeCroy Research Systems. This system groups adjacent hits in each wire plane

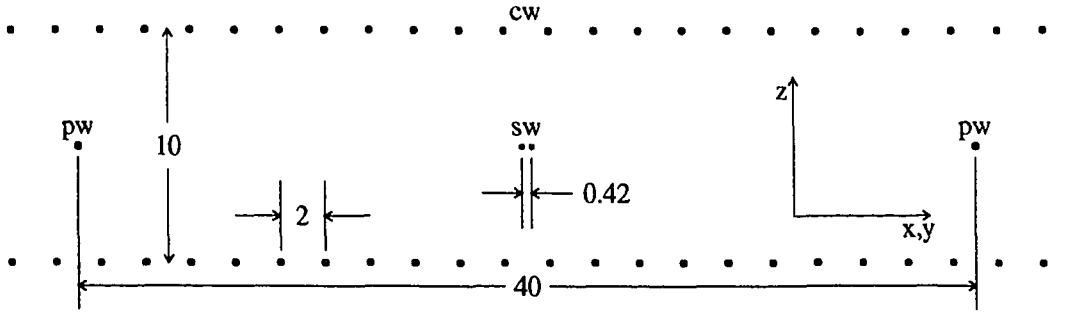

Figure 4.9: A diagram of the wire arrangement in a drift chamber cell showing the locations of the sense wires (SW), potential wires (PW), and cathode wires (CW). All dimensions are in mm. One DC cell spans the distance between adjacent potential wires (40 mm). The cathode and potential wires have radii of 40 μm and the sense wires have a radius 10 μm.

into clusters and stores and holds the central wire address and cluster size for later readout.

4.3.4 Drift Chamber

The drift chamber (DC) also measures the coordinates of the charged Λ-decay products to enable the kinematic reconstruction of the event. It consists of 13 planes of drift cells with a drift cell wire arrangement as diagrammed in Fig. 4.9 [91]. There are 14 such cells in each plane with the exception of plane 1 which consists of six cells. Seven of the planes were oriented so as to measure the x coordinate and six to measure y. The parameters of each plane are summarized in Table 4.5. The volume of the chamber is filled with a 67.6% argon, 30% isobutane, 2.4% methylal gas mixture [27]. The potential wires are were held at -3.3 kV while the sense (anode) wires are held at $+1.9$ kV. The potential values on the cathode wires are graded so that the electric field is constant for almost the entire width of the cell. A plot of the calculated equipotential lines in a drift cell is shown in Fig. 4.10 [92].

When a charged particle crosses the cell, the ionization electrons drift toward

plane #	coordinate measured	z position (cm)	active area (cm^2)
1	x	12.0	24.0×24.0
2	x	13.0	56.0×56.0
3	y	14.7	56.0×56.0
4	y	15.7	56.0×56.0
5	x	17.4	56.0×56.0
6	x	18.4	56.0×56.0
7	y	20.1	56.0×56.0
8	y	21.1	56.0×56.0
9	x	22.8	56.0×56.0
10	x	23.8	56.0×56.0
11	y	25.5	56.0×56.0
12	x	27.2	56.0×56.0
13	y	28.8	56.0×56.0

Table 4.5: Summary of detector parameters for each plane of the drift chamber (DC).

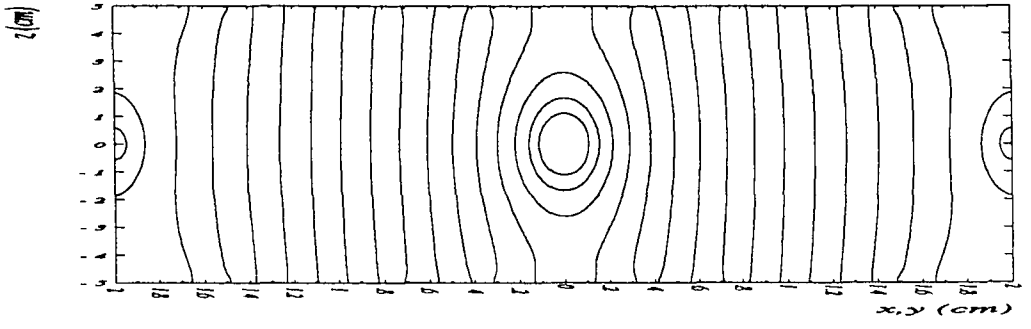

Figure 4.10: The calculated potential values in a drift cell. The orientation is the same as in Fig. 4.9. The contours are the equipotential lines with each corresponding to a potential change of 200 V.

the sense wires, are amplified, and create a signal on the wires as explained for the MWPC. However, unlike the MWPC, an additional piece of information is used to obtain a more accurate coordinate measurement. By measuring the drift time of the ionization charge, the drift distance and the coordinate of the particle track is determined. It is important that the electric field be constant so there is a linear relationship between drift time and drift distance. The accuracy of the DC is dictated by the statistics of ion production and the diffusion of the charge as it drifts. It is also a function of the angle of incidence of the particle track and the distance of the track from the sense wire. The error on the coordinate measurement ranges from ≈ 150 μm for tracks perpendicular to the DC plane to ≈ 1 mm for tracks incident at 60°. The time of arrival of each signal above a preset threshold is recorded with a multihit TDC [93]. The multihit TDC allows more than one hit per wire to be recorded for an event which is necessary due to the large width of the cell. The sense wires are arranged in pairs to eliminate, albeit with a loss of efficiency, the left-right ambiguity problem that accompanies single sense wire drift chambers [94]. The sense wire nearest the nominal beam center is electroplated for 1 cm along its length to avoid detecting the ionization charge of the primary beam.

4.3.5 Hodoscope

The scintillation hodoscope provides information on the charge multiplicity of the event for use in the neutral trigger (described in Sec. 4.4. It also provides rough coordinate information; however, this was not exploited in the final analysis of this dataset. The hodoscope consists of two planes, one oriented to measure the x coordinate and the other to measure y. Each plane contains 21 elements, the outer 20 are $0.4 \times 3.0 \times 61.0$ cm^3 scintillator slabs. The element in the center of each plane consists of two scintillator pieces, $0.4 \times 1.0 \times 30.0$ cm^3 and separated in the center by 1.0 cm to allow a hole for the primary beam. A phototube is attached to both ends of each of the 42 scintillator elements and the charge and time information from

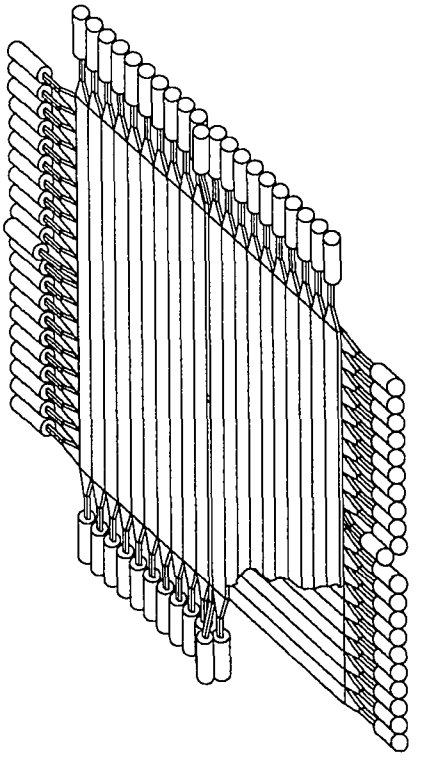

Figure 4.11: An isometric view of the hodoscope including the lightguides and phototubes. Part of the x plane is cut away to reveal the y plane behind.

plane #	coordinate measured	z position (cm)	active area (cm^2)
1	x	34.2	61.0×61.0
2	y	34.7	61.0×61.0

Table 4.6: Summary of parameters for each plane of the hodoscope.

the phototube is recorded using an ADC and a TDC. A diagram of the hodoscope is shown in Fig. 4.11 and a summary of the parameters of each plane is listed in Table 4.6.

plane #	coordinate measured	z position (cm)	active area (cm^2)
1	x	39.9	64.0×70.0
2	x	64.4	92.0×94.0
3	x	88.9	116.0×116.0

Table 4.7: Summary of parameters for each plane of the drift chamber in the magnetic solenoid (MACH).

4.3.6 Baryon Identification Detector

The baryon identification detector determines the charge of the Λ-decay products so that the Λ and $\overline{\Lambda}$ may be distinguished. It consists of a drift chamber (MACH) situated within a magnetic solenoid that maintains a 0.9 kG magnetic field along the $\hat{y}$ direction. Particles that pass through the solenoid are deflected in a direction normal to the magnetic field. The deflection is measured by tracking the particles with the MACH, which, together with the sign of the magnetic field, determines the particle charge. The solenoid consists of water-cooled aluminum coils wound inside an iron yoke. A current is maintained in the coils which establishes a fairly uniform field contained within the yoke. The coils are separated slightly around the midsection to allow the primary beam to pass unimpeded. A diagram of the solenoid is shown in Fig. 4.12. The MACH is of the same design as the DC described above, with three planes of 16, 23, and 29 drift chamber cells as diagrammed in Fig. 4.9. As in the DC, the central sense wire is electroplated near the beam center so as not to amplify the beam ionization. The time information of the signals above a threshold is recorded with a multihit TDC, also as in the DC. The parameters of each MACH plane are listed in Table 4.7.

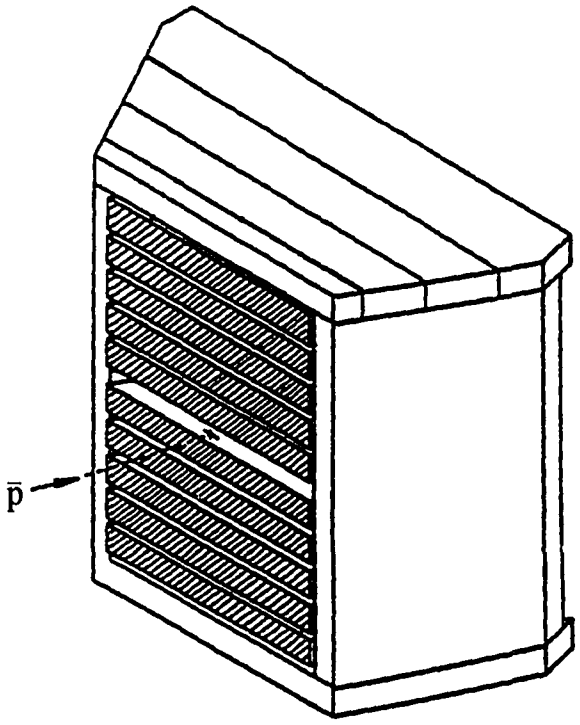

Figure 4.12: An isometric view of the magnetic solenoid.

4.3.7 Calorimeter and Veto Scintillators

A segmented calorimeter and system of veto scintillators were added to the PS185 apparatus in preparation for this run to enable the detection of Σ^0-decay photons from the $\overline{p}p \rightarrow \overline{\Sigma}^0\Lambda + c.c.$ reactions. The calorimeter consists of an array of 240 modules 20 cm long constructed of 1 mm-diameter scintillating plastic fibers embedded in a lead/antimony material [95]. The modules were machined into trapezoidal shapes so that they fit together closely forming several rings of modules. The fibers in each module point toward a region $\approx$ 60 cm downstream of the target. With this geometry, incident particles intersect the calorimeter at a slight angle that remains

fairly constant across the face of the calorimeter.

When a photon enters the calorimeter, an electromagnetic shower develops rapidly due to the density and high-Z of the lead. The charged particles of the shower create light in the scintillating fibers in proportion to the product of their number and track length which is proportional to the energy of the incident photon. The energy resolution for the device as employed in this experiment is given by $\sigma/E \approx 8\%/\sqrt{E}$ with E in GeV yielding $\sigma/E \approx 25\%$ for a 100 MeV photon. The position resolution, determined by the energy sharing of the shower between modules is approximately 0.5 cm [95]. A light guide is attached to the back of each module to channel the light from the fibers to a phototube. The phototube signals are recorded with an ADC. A drawing of the device is shown in Fig. 4.13.

The scintillator system consists of 48 pie-shaped scintillators arranged to match the ϕ divisions of the calorimeter to enable a veto on the calorimeter signals due to charged-particles. Each scintillator is attached to a phototube and each signal is recorded with an ADC. This calorimeter/scintillator system is a subset of the final device which was later used for the JETSET experiment at LEAR [96].

4.4 The Trigger, Scalers, and Data Acquisition

During the running of the experiment, the incident antiprotons strike the target at a rate of approximately 500 kHz. It is not possible (or desirable) to record the signal for every event. The function of the trigger is to provide a selection criterion to select the subset of events to record. The trigger is generated when the pattern of detector signals matches the desired pattern. The principal trigger of the PS185 experiment is the neutral trigger, which selects for $\overline{p}p \rightarrow \overline{Y}Y$ events. Several other triggers are used in addition to select events for diagnostic and calibration purposes.

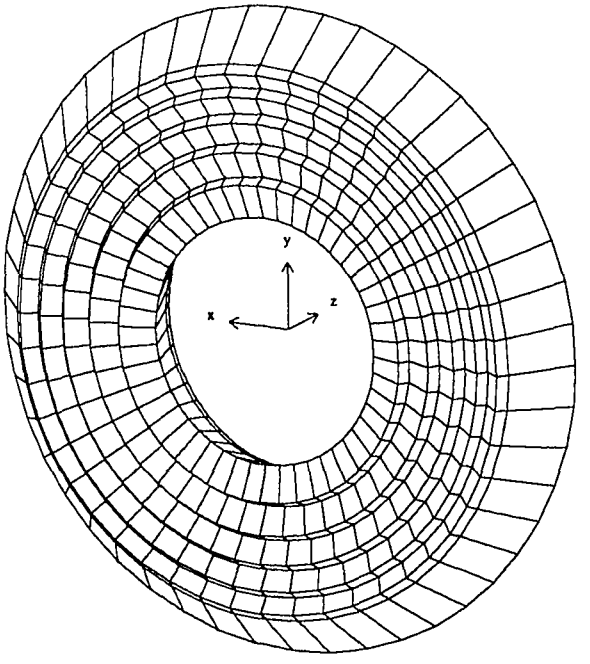

Figure 4.13: An isometric drawing of the lead/scintillating-fiber calorimeter as employed in the PS185 experiment. There are five rings of 48 individual modules. The light guides and phototubes are not shown.

4.4.1 The Neutral Trigger

The neutral trigger is designed to select, from the many possible, $\overline{p}p \rightarrow \overline{\Lambda}\Lambda$ and $\overline{p}p \rightarrow \overline{\Sigma}^0\Lambda + c.c.$ events. As seen by the detector, these events may be described as an antiproton into the target in coincidence with zero charged particles exiting and the detection of the charged Λ-decay products downstream. Thus, the event pattern desired is "charged→neutral→charged". The target scintillator information is used to form the "charged→neutral" portion and to determine in which target cell the interaction occurred. The scintillator hodoscope information is used to form the "→charged" portion.

For the target portion of the neutral trigger, the signal from each of the target

Neutral	S2 hit pattern					S3 hit pattern				
Cell #	1	2	3	4	5	1	2	3	4	5
1	−	0	0	0	0	−	0	0	0	0
2	−	−	0	0	0	+	−	0	0	0
3	−	−	−	0	0	0	+	−	0	0
4	−	−	−	−	0	0	0	+	−	0
5	−	−	−	−	−	0	0	0	+	−
+ = hit, − = not hit, 0 = not considered										

Table 4.8: Required hit pattern of each S2 and S3 target counters for the neutral target condition of the neutral trigger.

phototubes is passed to a discriminator which produces a logic signal if the analog signal is larger than a preset threshold level and the target component is considered to be "hit". These logic signals are routed to coincidence units where the neutral cell decision is made.

First it is required that the S0, S1A, and S1B are all hit. This is called the "pbar" requirement. Next, the selection for exclusively neutral production is made. This is accomplished by requiring a target scintillator pattern that is consistent with an antiproton entering one of the target cells with no charged particles exiting that cell. For a particular target cell pattern, the S3 immediately upstream is hit while the S3 immediately downstream and the surrounding S2 are not. These logical patterns for each target cell are listed in Table 4.8. If one of these patterns is satisfied and the pbar condition is fulfilled, the neutral target condition is satisfied and the target cell of the interaction (the "neutral cell") is assigned.

The "→charged" part of the neutral trigger is formed by requiring that the hodoscope have at least one hit element in the x plane and one hit element in the y plane. If both the hodoscope and neutral target conditions are fulfilled for an event, a neutral trigger is generated. The average rate of the neutral trigger during this

experimental run was 140 Hz.

4.4.2 Calibration and Diagnostic Triggers

For diagnostic and calibration purposes several other triggers are used, either in parallel with the neutral trigger or in separate runs, to accept events of other types. For calibration of the calorimeter and to observe other neutral reactions such as $\overline{p}p \rightarrow \overline{n}n$ and $\overline{p}p \rightarrow n(\pi^0)$, the "$\pi^0$" trigger is implemented. It is formed with the requirements that the neutral target condition is fulfilled and that no element of the hodoscope has a hit. This trigger was used for the 1.729 GeV/c data to accept events in parallel with the neutral trigger. The rate was lowered by prescaling one of the input signals to be approximately 4% that of the neutral trigger.

For diagnostic purposes, a minimum-bias, "beam" trigger is used. It consists of simply the pbar condition. The pbar signal was prescaled so that the beam trigger rate was approximately 2% that of the neutral trigger rate.

An "elastic" trigger is used to select $\overline{p}p \rightarrow \overline{p}p$ events for drift chamber calibration and general diagnostic purposes. It is formed with the pbar condition combined with the requirement that there is exactly one hit in each hodoscope plane. The near-beam region of the hodoscope is used as a veto in order to select only larger-angle elastic events. For this data set, this trigger was used alone in several runs per day to collect tapes of pure "elastic" events with which to calibrate and/or examine the tracking chambers.

4.4.3 Scalers

In addition to the charge and time information, it is also desirable to count the number of signals from the detectors. The discriminated signals from many of the detectors and logical combinations thereof are routed to scalers. The scalers count the number of signals independent of the event trigger. The information is for diagnostic purposes to obtain the correct normalization for the cross section calculations. The

Beam	S2 hit pattern					S3 hit pattern				
Cell #	1	2	3	4	5	1	2	3	4	5
1	−	0	0	0	0	0	0	0	0	0
2	−	−	0	0	0	+	0	0	0	0
3	−	−	−	0	0	+	+	0	0	0
4	−	−	−	−	0	+	+	+	0	0
5	−	−	−	−	−	+	+	+	+	0
+ = hit, − = not hit, 0 = not considered										

Table 4.9: Required hit pattern of each S2 and S3 target counters for each beam cell condition.

most important count is the number of antiprotons incident on each target cell. For this purpose, the output of the "beam cell" definitions shown in Table 4.9 are routed to scalers. These definitions are the same as the corresponding neutral cell definitions except that the downstream S3 veto requirement is removed. Using these scaler values to calculate the cross section for each target cell ensures that the flux of antiprotons on each target cell is correctly counted.

4.4.4 Data Acquisition

The data acquisition system for the PS185 experiment for the collection of the 1.729 GeV/c data consisted of CAMAC and FASTBUS systems, a MBD-11 special interface computer, and a MicroVAX II computer. The FASTBUS system contained the TDC's and ADC's for the microstrips, DC, MACH, calorimeter, and veto scintillators. The CAMAC system contained the ADC's and TDC's for the target and hodoscope, the PCOS II MWPC readout module, and the scalers. It also contained a dual-port memory module to gather the FASTBUS data [93]. The MicroVAX II, manufactured by Digital Equipment Corporation, was used to run diagnostic and experimental-control programs and to write the data to tape via two 6250 bpi 9-track tape drives.

The MBD-11 (Microprogrammed Branch Driver), manufactured by Bi Ra Systems Inc., was used to read out the data from the CAMAC system and to transfer it to the MicroVAX memory.

When an event trigger is generated and the MBD is not busy processing a previous event, a signal is generated that gates the ADC's, provides the time reference signal for the TDC's, instructs the MWPC readout system to latch and gather the wire information, and sets an interrupt for the MBD. At this prompt, the MBD reads the data held in the various modules and stores it in a data buffer in shared memory in the MicroVAX [97]. This process is repeated until the data buffer is filled. The MicroVAX writes this buffer to tape while the MBD resumes filling the next buffer. The values from the scaler modules are read every 5 seconds and the totals written to tape in a separate buffer once a minute.

While the data acquisition was running, the data stored in the shared memory buffer was simultaneously used by various running on the MicroVAX programs to create histograms, make event plots, calculate detector efficiencies, and other tasks to monitor that the detector was functioning properly.

The data set analyzed for this work at an antiproton extracted momentum of 1.729 GeV/c was collected over a 60 hour run period in November of 1989. In this time, 5.5 Gbytes of data from 1.1×10^7 neutral triggers were written to approximately 50 tapes.

Chapter 5

Data Analysis

After the beam is turned off and the detector information is recorded on tape, this data must be read and interpreted. Thus begins the process of analysis. The data must be transformed from the binary information stored on tape into the physics observables that provide insight into the $\overline{p}p \rightarrow \overline{Y}Y$ reaction. This procedure, from decoding the data to calculation of the cross sections, is described in this chapter. The description of the extraction of the spin observables, the hyperon polarizations and spin correlations, due to its complexity and length is given an entire chapter which immediately follows.

5.1 Overview

The experimental data written to tape contains more than $\overline{p}p \rightarrow \overline{\Lambda}\Lambda$ and $\overline{p}p \rightarrow \overline{\Sigma}^0\Lambda +$ c.c. events. No trigger is perfect and other event types often satisfy the PS185 neutral trigger and are written to tape along with the events of interest. The task of the data analysis is to reconstruct the events on tape and apply numerous cuts to eliminate the uninteresting events and gather the $\overline{p}p \rightarrow \overline{\Lambda}\Lambda$ and $\overline{p}p \rightarrow \overline{\Sigma}^0\Lambda + c.c.$ events. After the events are selected, the detector acceptance must be calculated to determine the number of events corrected for losses. Then, the integrated luminosity of the experiment must be calculated. With these ingredients, the total and differential cross sections may be extracted.

The term "hit" is often used in experimental nuclear and particle physics. In Chapter 4 it was used to specify a piece of information associated to a detector that consists of ADC, TDC, and/or wire number information. In this chapter it is used to mean a piece of information consisting of spatial coordinates, energy, and/or time information. Not all experimental hits are considered hits in the analysis. Selection criteria are applied to eliminate the experimental hits that are undesirable for some reason in the analysis procedure.

A detector coordinate system is needed to reconstruct the particle trajectories for each event. The two systems used in the analysis are the same as those used in the description on the experimental apparatus and are illustrated in Fig 4.7. Both are defined with origins coincident with the front foil of the multiwire proportional chamber. The uvz system which is rotated by 45° is used primarily to describe tracks in this chamber, which are eventually rotated into the xyz system. The hits and tracks are all described using these systems.

5.2 Target and Microstrip Analysis

The purpose of the target scintillator array is, in addition to providing the signals to form the neutral trigger, to determine in which cell the $\overline{p}p \rightarrow \overline{Y}Y$ interaction occurred which yields the interaction point to within the size of the target cell. The measurement of the interaction point allows a better determination of the final $\overline{\Lambda}\Lambda$ kinematics through a more precise knowledge of the production angles. The silicon microstrips provide the information to determine the direction of the incident antiproton which further constrains the and interaction point and yields a more precise measurement of the kinematics of the initial $\overline{p}p$ kinematics.

5.2.1 Target Analysis

As explained in Chapter 4, the target cell of the interaction for the neutral trigger is assigned by combining the logic signals of the target components as shown in Table 4.8. This "neutral cell" as assigned in the experiment is recorded on tape and is called the "hardware cell". In addition to this information, the ADC and TDC values of the target components are also recorded. This information was used in the analysis to double-check and to refine, if necessary, the neutral cell as assigned using the hardware pattern.

The distributions of ADC and TDC values for the S2-3 and S3-3 target counters from elastic trigger events are shown in Fig. 5.1. The S2-3 is the scintillator barrel surrounding and S3-3 is the scintillator disk immediately downstream from the third target cell (see Fig. 4.8). The distributions from the other S2 and S3 counters are similar. Elastic trigger events were used because the S2 and S3 target counters are not used in the elastic trigger and so the resulting distributions are only slightly biased by the trigger. The window for the ADC values was set to eliminate noise hits and the window for the TDC values was set to contain the true peak as shown in the figure. The windows for the other counters were set in an analogous fashion.

With the ADC and TDC hits defined to be within these windows, the neutral cell for each event was determined based on the hit pattern from the target counters. These possible hit patterns with the assigned neutral cell are listed in Table 5.1. Note that the these patterns are slightly more strict than those used to form the hardware cell. In these hit patterns, all of the S3 counters upstream from the target cell must have a hit to satisfy the neutral cell assignment. The neutral cell resulting from the hits formed from the TDC information is called the "TDC cell"and that from the ADC information, the "ADC cell".

The hardware, TDC, and ADC cells were compared and the ambiguities were resolved by setting the neutral cell according to the pattern where two of the three

Neutral	S2 hit pattern					S3 hit pattern				
Cell #	1	2	3	4	5	1	2	3	4	5
1	−	0	0	0	0	−	0	0	0	0
2	−	−	0	0	0	+	−	0	0	0
3	−	−	−	0	0	+	+	−	0	0
4	−	−	−	−	0	+	+	+	−	0
5	−	−	−	−	−	+	+	+	+	−
+ = hit, − = not hit, 0 = not considered										

Table 5.1: Required hit pattern of each S2 and S3 target counter for each neutral cell assignment.

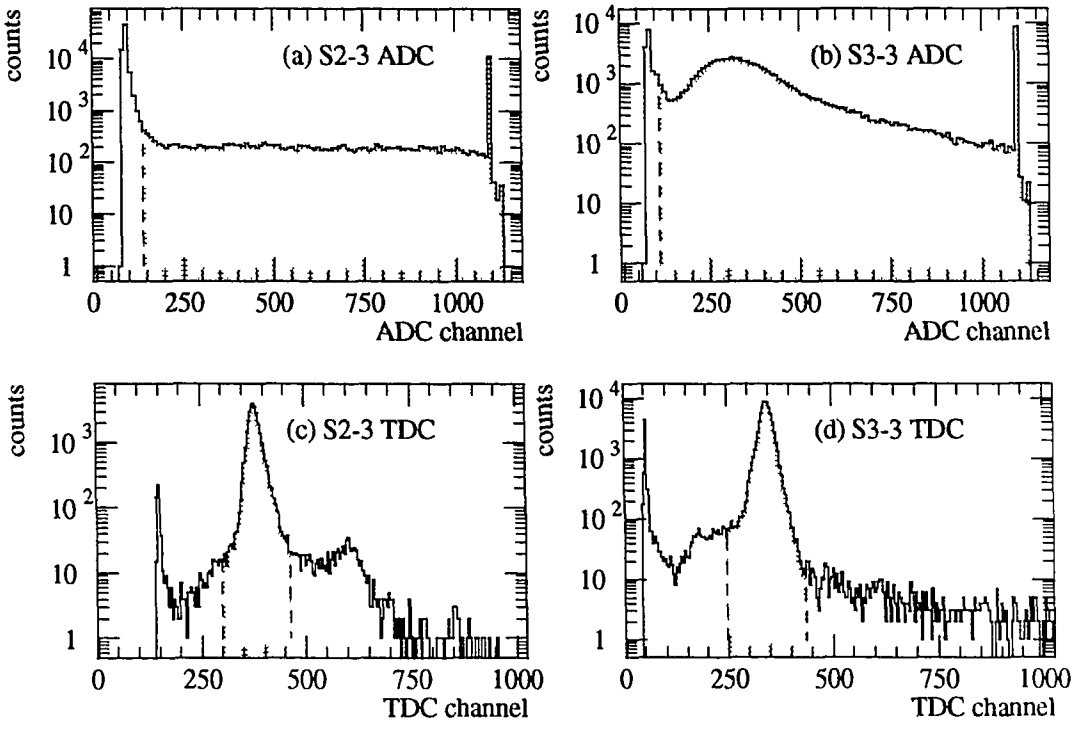

Figure 5.1: Distribution of the (a) S2-3 ADC, (b) S3-3 ADC, (c) S2-3 TDC, and (d) S3-3 TDC for elastic trigger events. The shaded area indicates the windows set for these counters. Note the logarithmic scale.

methods agreed. This was sufficient to set the neutral cell in all but 1–2% of the neutral trigger events. These events may be explained by the slight differences between thresholds and timing windows used in the experiment versus those set by the ADC and TDC windows used in the analysis. They may also be due to an "accidental" antiproton passing through the target closely in time as is fairly probable with the occasional 1–2 MHz beam rates that occurred during the running of the experiment. These events were rejected from the analysis and accounted for in the calculation of the cross section.

The neutral cell assignment sets the z position of the interaction to within the length of the target cell. The positions of the target cells are known through the detector survey. The z positions were more precisely determined from the density of reconstructed vertices in elastic trigger data in the target region. The x and y position of the interaction is also determined by the neutral cell assignment to within the dimensions of the target cell. But, it may be more precisely determined by using the antiproton track as reconstructed with the silicon microstrip detectors. This is described in the next section.

5.2.2 Microstrip Analysis

To determine the beam (antiproton) track for each event, the microstrip ADC values were used. If the ADC value of an individual microstrip channel was above a certain cut value then that strip was considered to be hit. The ADC distributions for a typical channel in each of the four microstrip planes and the positions of the ADC cut are shown in Fig. 5.2. This cut was set to be above the level of the noise.

The hits were grouped into clusters, where a cluster is defined as a group of contiguous hits in a plane. If there was exactly one cluster of hits in each microstrip plane for an event then the coordinates (in the u or v system) of each cluster are used to form the beam track for that event. The coordinates of each microstrip plane are known through the detector survey and were more precisely determined using a

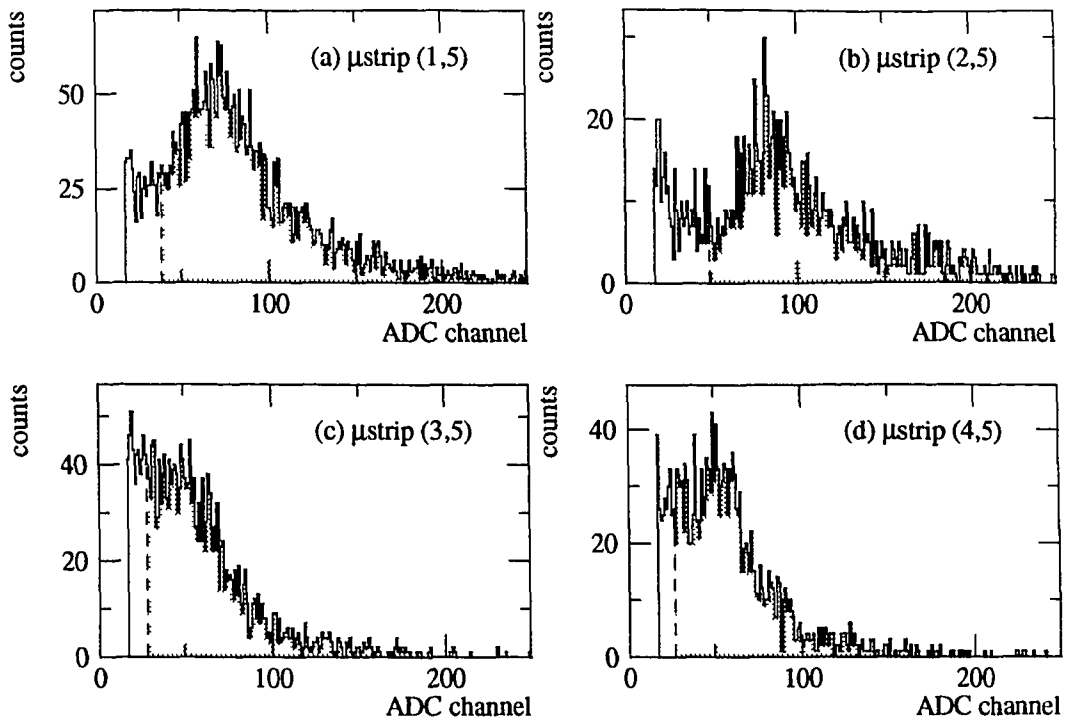

Figure 5.2: Microstrip ADC distributions from a typical channel in each of the four planes. The shaded area indicates the values passing the ADC cut.

calibration procedure that correlates the tracks from in the wire chambers with the hits in the microstrips. The errors on the coordinate measurement were set to be equal to the width of an individual strip in the plane (200 μm for planes 1 and 2 and 100 μm for planes 3 and 4). For ease of calculation and integration into the kinematic fit, the beam track was parameterized using x,y slopes and intercepts. The (4×4) error matrix for these parameters was calculated by propagating the coordinate errors to the slope and intercept values. The microstrip hit coordinates from a typical run are shown in Fig. 5.3 and the resulting beam x and y slopes are shown in Fig. 5.4.

For this data set, the cut on exactly one cluster per plane allowed a beam track measurement for only approximately 40% of the events. This relatively low number was due mainly to the low gain of the channels in microstrip plane 3 as can be seen

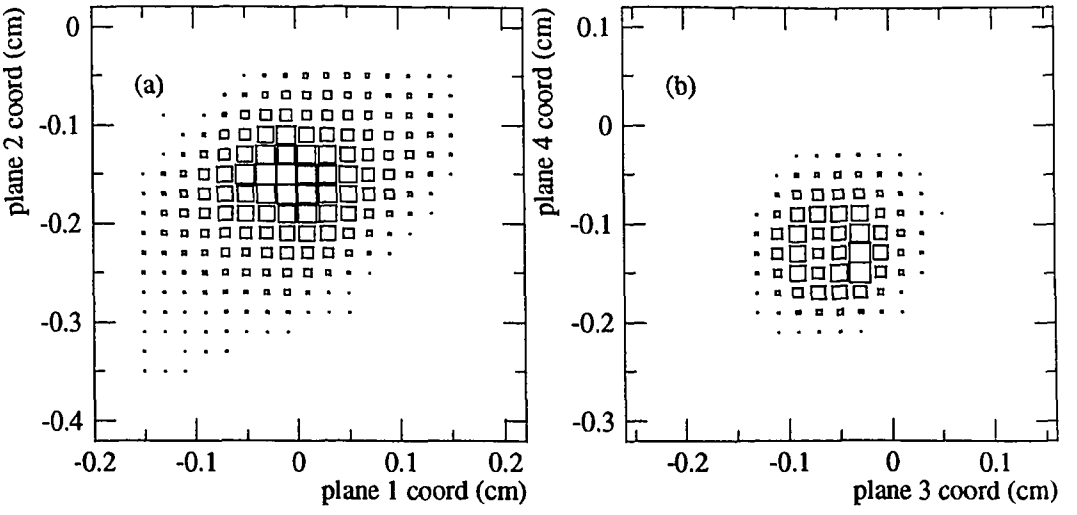

Figure 5.3: Microstrip coordinate distributions for a typical run shown as box plots for (a) plane 1 vs. plane 2 and (b) plane 3 vs. plane 4. The relative size of the box indicates the number of events in that channel. The width of each channel and the total active area is smaller for microstrip planes 3 and 4.

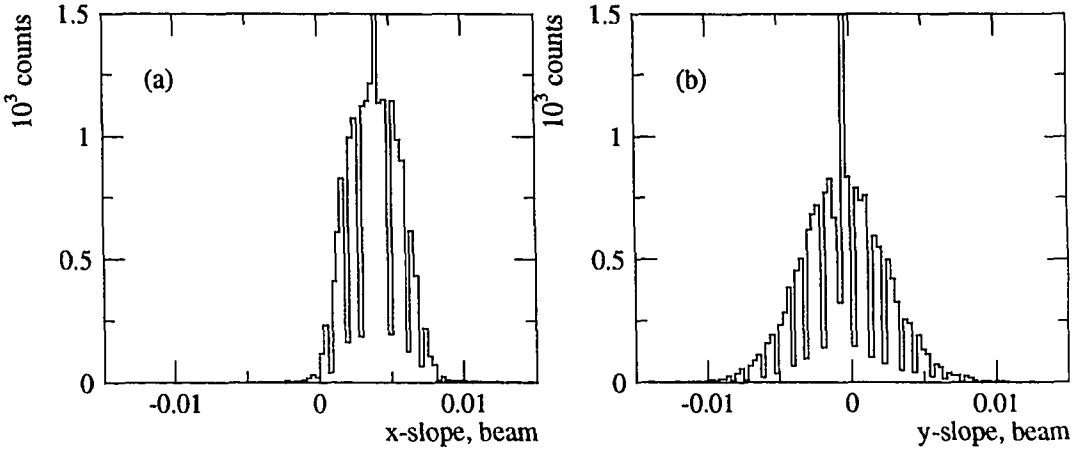

Figure 5.4: Microstrip beam vector measurements: (a) x slope and (b) y slope. The large number of counts in the center channel of each distribution is due to the events that did not allow a beam vector measurement and the average slope values were used.

in Fig 5.2. If a good beam track measurement was unavailable for an event, the average beam track and error matrix was used. Even with only the average beam track, there was a considerable improvement in constraining the kinematics of an event over a situation with no microstrips. The average beam track was monitored for the different runs of this data set and if the parameters changed, due to beam steering or focusing, a new set of beam track parameters was calculated and used for the average beam track for subsequent runs.

5.3 Hodoscope Analysis

The ADC and TDC values for the hodoscope were decoded and associated to a hodoscope element number. Only those elements with signals above a preset threshold were written to tape. If data for a hodoscope element were written to tape, this element was considered as hit in the analysis — no ADC or TDC cuts were applied. Each hit was assigned an xz or yz coordinate pair which is known for each hodoscope element through the detector survey and via a calibration procedure that correlates tracks from the wire chambers with the hodoscope hits.

In the final version of the analysis, the hodoscope was used only for a cut on number of elements hit per event. It was required that there were more than 2 and less than 20 hits in both the x and y planes of the hodoscope. It was determined that essentially all $\overline{p}p \rightarrow \overline{\Lambda}\Lambda$ and $\overline{p}p \rightarrow \overline{\Sigma}^0\Lambda + c.c.$ events that pass the cuts of the later stages of the analysis fulfill this requirement. Thus, this hodoscope cut could be applied which efficiently removes a large fraction of undesired events.

It is possible to use the hodoscope hits for additional particle-track coordinates to reduce ambiguous combinations or to use the ADC information to determine particle energy loss through the scintillator. But this was deemed not necessary for this analysis and is left for future work.

5.4 Calorimeter and Veto Scintillator Analysis

The information from the calorimeter and veto scintillators was used to find potential Σ^0-decay photon candidates in the data and to analyze a neutral reference reaction for the target normalization correction (see Sec. 5.13.3). Although, in the final analysis, it was determined that the Σ^0-decay photon information was of limited utility for this data set due to the low acceptance of the calorimeter. However, the procedures were developed and implemented and are described in this section.

The ADC and TDC information from the veto scintillators was decoded. For each scintillator, if the ADC value was above the level of the noise and the TDC value was within the true peak, a hit was formed. The ADC information from the calorimeter was decoded and a hit formed with the respective calorimeter module position and an energy value. The locations of the individual scintillator wedges and calorimeter modules are known through the detector survey and determined more precisely by correlating hits in the detectors with tracks from the chamber stack.

The calorimeter ADC-value to energy calibration was determined in the following way. As a first step, elastic trigger events were used and cuts applied to select events where a particle passes through the calorimeter without interacting. Events of this type create a calorimeter ADC distribution with a fairly sharp peak. The energy lost by a minimum ionizing particle in the scintillator of the calorimeter was calculated and a first approximation for the ADC to energy calibration constant for each calorimeter module was determined.

In the next step, elastic trigger events were used and cuts applied to obtain a sample of events that contained one or more π^0 mesons[1]. The π^0's decay into two photons which, for a fraction of the events, are detected in the calorimeter. With these events, the hits in the calorimeter were used to form clusters, where a cluster is

[1]Events taken with the elastic trigger contain a reasonable number of π^0's due to the presence of $\bar{p}p \rightarrow \pi^0 + X$ reactions that satisfy the trigger.

a group of neighboring calorimeter modules that contain some energy. The energies of the modules were summed to form the cluster energy and the energy-weighted average cluster position calculated. A cluster was considered a neutral cluster candidate if there were no hit scintillator wedges within an azimuthal angle of 7.5° of the cluster center. With the hypothesis that each cluster was due to a π^0-decay photon, the invariant mass of the possible photon pairs was formed.

The invariant mass of a photon pair is given by

$$M_{2\gamma} = \sqrt{2E_1E_2(1-\cos\theta)} \tag{5.1}$$

where E_1 and E_2 are the energies of two photons and θ is angle between the two photon lab momentum vectors. An invariant mass distribution was formed for each calorimeter module, with events added if the calorimeter module was a member of a cluster for that event. Using these distributions, the offset of the invariant mass peak from the π^0 mass was used to adjust the calibration constants. The new calibration constants were then used to form another set of distributions and the second iteration constants were extracted. This process was repeated until the peaks in the invariant mass distributions converged on the π^0 mass.

In practice, the number of events was not sufficient to adjust the constants for each individual module, so each calorimeter ring was adjusted together. The final two photon invariant mass distributions for all rings together and for each ring individually are shown in Fig 5.5. The invariant mass for a cluster pair was accepted if the energies of both clusters were greater than 0.3 GeV, the angle between them was greater than 25°, and the center of the either cluster was not within 5 cm of the inner or outer edge of the calorimeter. An invariant mass combination was used for the individual ring spectra if that ring contained 30% or more of the total energy of both clusters.

Candidate Σ^0-decay photons were selected in the neutral trigger sample by requiring a cluster to be a neutral candidate (as described above) and that the energy

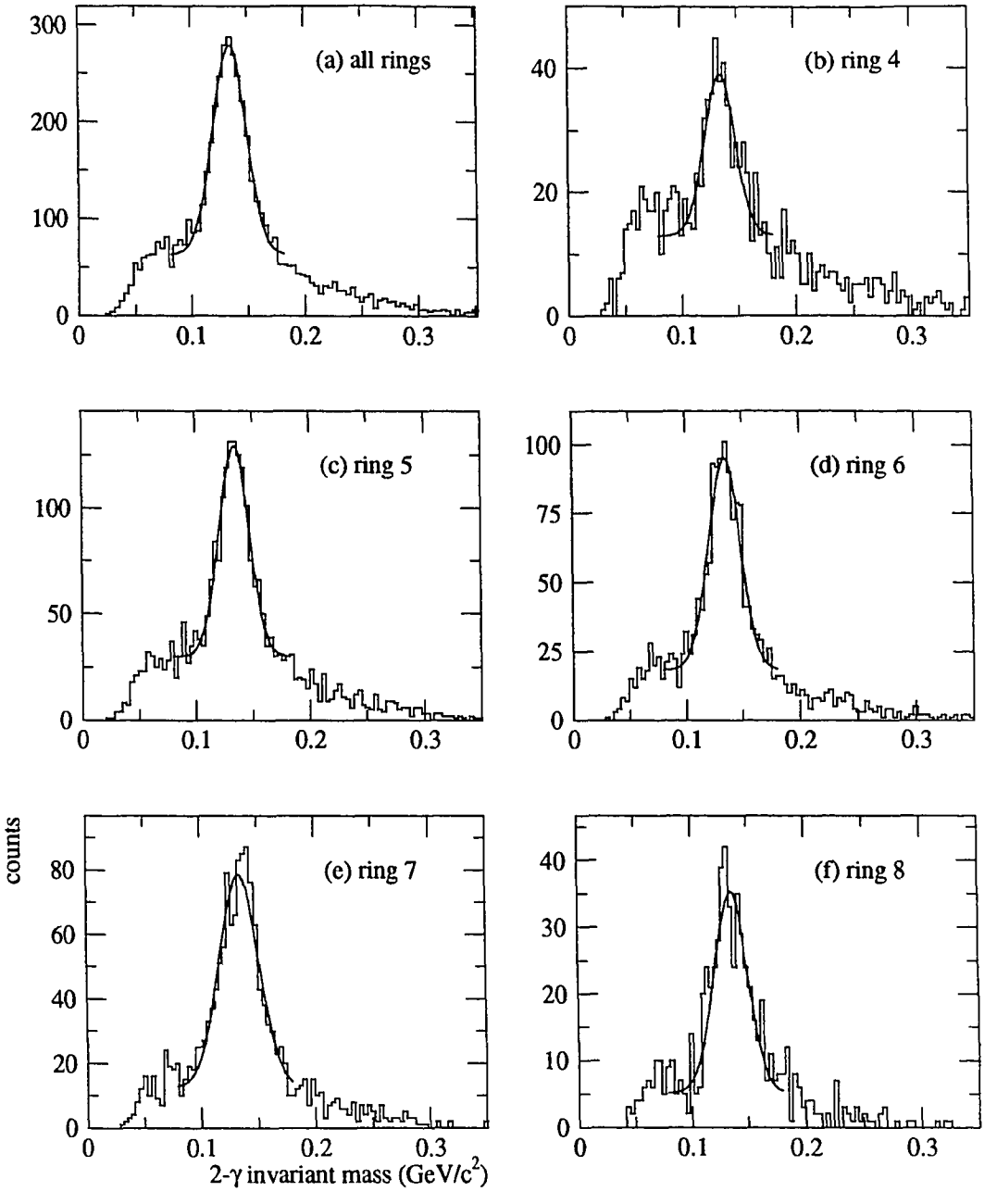

Figure 5.5: Calorimeter 2-γ invariant mass distributions from neutral cluster candidates for (a) all calorimeter rings and (b)-(f) rings 4-8. The curves are the result of fitting the distributions to a Gaussian plus a constant over the range 0.8-1.8 GeV/c^2. All fits resulted with the Gaussian mean within 1% of the π^0 mass.

of the cluster be within the range 0.08-0.2 GeV. The energy range of Σ^0-decay photons within the solid angle covered by the calorimeter is kinematically constrained to 0.12-0.17 GeV. If desired, the clusters passing these cuts with energy and position as determined by the calorimeter may be used in the kinematic fit along with the rest of the event information. The error on the x and y position of the cluster was estimated to be 0.5 cm and the error on the energy parameterized by $\sigma/E = 8\%\sqrt{E(GeV)}$. It was assumed that the x, y, and energy errors are independent.

5.5 Tracking Coordinates

Accurate tracking of the Λ-decay products is the paramount task in the analysis of the PS185 data. If it is not done correctly the reconstruction efficiency and precision suffers tremendously. To obtain accurate tracks, the coordinates of the charged particles as measured by the tracking chambers must be carefully and correctly determined.

5.5.1 Multiwire Proportional Chamber Coordinates

The information recorded from the multiwire proportional chamber (MWPC) consists of, for each cluster of wires in a plane, a data word containing a central wire address and cluster size. For each data word, the cental wire address is mapped to either a u or v coordinate (depending upon the plane). This coordinate, the z coordinate of the plane, and the cluster size are stored as a MWPC hit. If the cluster size is an odd number, the coordinate of the central wire is used; if it is even, the coordinate halfway between the two central wires is used. The situation for two typical tracks is illustrated in Fig. 5.6.

The MWPC is a digital detector; that is, if a wire is hit, the exact position of the particle track at the z of the wire plane is uncertain by an amount equal to the wire spacing. The error usually assigned for digital detectors is $\sigma = d/\sqrt{12}$ where d is the width of the detector elements, which is the square root of the variance of

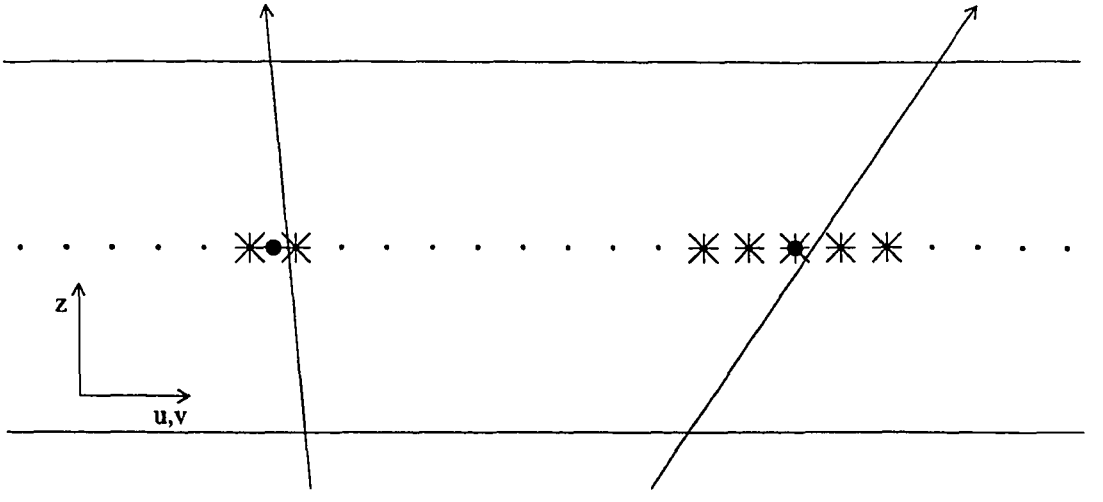

Figure 5.6: An illustration of MPWC wires hit and the coordinate assigned for two typical tracks. The crosses indicate the wires hit and the circles indicate the assigned coordinates.

a top-hat function [98]. With the exception of a slight complication, discussed in in Sec. 5.6.1, this error assignment was used for this analysis with d set to the MWPC wire spacing, 0.127 cm.

The experimental coordinate system is defined as fixed to the MWPC with each sense wire plane spaced exactly 1.0 cm apart and perpendicular to the z axis. The front mylar sheet of the MWPC contains the origin. These assumptions are reasonable considering the precision of the wire spacing of the MWPC. The positions of the other detectors and the beam direction are determined using this coordinate system.

5.5.2 Drift Chamber Coordinates

The information recorded from the drift chamber (DC) consists of a data word containing the wire address and a drift time for each wire signal detected. For each data word, the drift distance is calculated from the drift time using a time to distance

calibration function. A coordinate is calculated from this drift distance and the position of the wire and is stored, together with the z position of the plane, as a DC hit.

To achieve accurate coordinates, it is important that the position of each wire is precisely known. These positions are known to a few millimeters through the detector construction and survey. However, to reach the tracking precision of $\approx$ 100–200 μm that the DC is capable of, a calibration procedure is necessary. The time to distance calibration function must also be determined accurately. A simple function based on the geometry of the ionization drift paths may be used but this is not adequate for the desired precision. To accurately determine the time to distance function and the wire positions, a calibration procedure using particle tracks was used. This procedure is described, in detail, in Appendix A. The resulting time to distance function, DC positions, and resolution function, allow the DC coordinates with associated errors to be determined.

5.6 Tracking

The multiwire proportional chamber and drift chamber measure track coordinates in in two dimensions. The goal of tracking procedure is to form the particle direction vectors in three dimensions (3D) from the information provided by these detectors. The first step is to recognize and form potential tracks in each of the four two dimensional (2D) projections. Then, valid combinations of these 2D tracks are combined to form 3D tracks which give the particle direction vectors.

5.6.1 Two Dimensional Tracking

The tracking chambers provide uz,vz,xz, or yz coordinate pairs. The task of the 2D tracking is to recognize all plausible tracks that can be formed from the hits in each of these four orientations. Since the magnetic field in these detectors is negligible

and in the limit that the multiple scattering is small, the process reduces to finding and fitting hits that form straight lines. To find these lines, the "road-building" technique [99] is used.

The search for 2D tracks proceeds independently through each of the four chamber projections. The hits from each projection are first sorted according to the plane number or z and by measured coordinate (u, v, x or y). The road-building algorithm begins with choosing two points, the "pivot points", in the planes at opposite ends of the chamber in z, the "pivot planes". A "road" of a certain width is formed that connects the two pivot points. The planes between the pivot planes, the "support planes" are searched for hits that lie on the road. If a hit is found that lies on the road, it is added to the candidate track. After all support planes have been searched the candidate track is considered final if at least one hit on one support plane has been found (at least three hits are needed for a track) and the number of support planes without hits on the track is below a certain tolerance. The hits of the resulting final track are removed from the list of available hits and are fit to a straight line. The resulting track fit parameters (slope and intercept) are stored.

After all hits on the pivot planes are used as pivot points and the support planes are searched, the pivot planes are moved in and the previous support plane becomes a pivot plane and the road building algorithm is repeated. The pivot planes are systematically moved in (together in z) until all possible combinations of pivot planes are exhausted. In this way, all possible combinations of hits are checked as track candidates.

For this analysis, it was determined that the track road tolerance was best set to 4σ where σ is the error of the candidate hit on the support plane. That is, if the hit is within 4σ on either side of the center of the road, it is added to the candidate track. Thus, the road is of variable width, set by the error on the hit being checked. By scaling the 2D track tolerance to the error, the uncertainty of the hits is treated correctly. The factor of 4 is wide enough to account for the error on the line between

the pivot hits due to the error on the pivot hits, yet not too wide to allow many noise hits or to "steal" hits from other tracks. The maximum number of support planes with missing hits for a track was set to 2 planes for the DC and 1 plane for the MWPC. This was determined for the DC by considering the efficiency. If each plane is more than 90% efficient, there is a less than 0.1% chance of having a track with no hits in three planes between planes with hits. For the MWPC this value was, in practice, not important since there were only four functioning planes for each projection. This allowed for some degree of inefficiency in the tracking chambers yet did not allow many tracks due to noise hits.

Only tracks up to 60° were considered in the 2D track finding. From the work on the DC calibration (Appendix A), it was evident that the DC time to distance was adequate only for tracks below this angle. Also, the planar geometry of the chambers yields a low efficiency for tracks with angles larger than 60°. The efficiency is also hard to determine for large angle tracks. So, it was decided to put a firm cut at 60° where the efficiency is easily determined.

As is common with any implementation of tracking, there are several details of the algorithm that are specific to these particular detectors.

For DC tracks:

- Since the time to distance function depends on angle, the coordinate (x or y) and error must be calculated for each hit using the angle of the candidate track. This requires that the coordinates of the hit be calculated multiple times, once for each time the hit is considered for a candidate track and once again when (and if) the final track is fit to a line.

- Large angle tracks through a drift cell often cause multiple hits due to the large spread in the time of arrival of the charge at the sense wire. To account for this, as each candidate track is formed, clusters of hits that are likely due to a single track are put together as one hit and the coordinate calculated from

the hit with the earliest time. These hits that are clustered are then removed from the list of available hits. This eliminates the problem of the formation of multiple tracks from the clusters of hits that are due to one large-angle track.

For MWPC tracks:

- The MWPC provides hits in the form of wire clusters. Sometimes, due to inefficiencies of the chamber, one track may cause more than one cluster of hits in one plane of the MWPC. This becomes more likely with large-angle tracks due to the decrease in track path length in a single wire cell. This is corrected by looking for "broken" clusters in each plane as each candidate track is formed. If two clusters are found in one plane that are likely due to a single track, then the broken cluster is repaired and a new coordinate calculated. As in the DC, this serves to eliminate extra spurious large angle tracks.

These methods to eliminate extra hits and the feature of the algorithm that removes used hits from the available hit list may cause another problem. That is, assigning a hit to one track when it should belong to different track. This can happen when tracks overlap or, as is often the case with the Λ decay products, they originate from a point close to a tracking plane. To mitigate this problem, an additional feature was added to the track finding algorithm. After all possible 2D tracks were found, the hits that were assigned to a track were searched again to check the hypothesis that they may also belong on another track. If they are on another track, to within tolerances, they are added to this track and the track is refit. They are not removed from the original track; they are "shared" by the two tracks. It is the case that sharing hits does not eliminate the problem of tracks that are completely missed when hits are assigned to another track and made unavailable. But it has been determined that few tracks are missed due to this problem and it is outweighed by the gain in reducing the number of spurious tracks formed if all hits can be on multiple tracks.

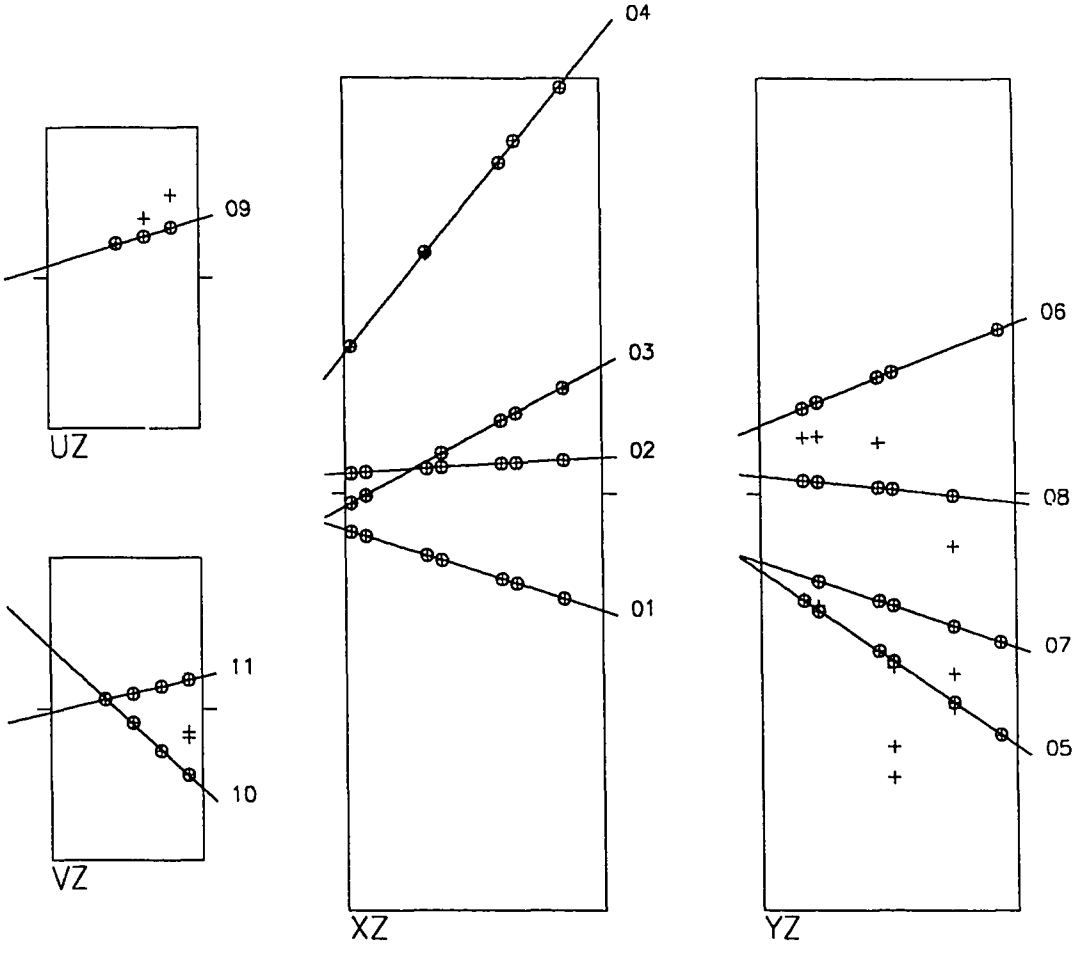

Figure 5.7: The results of the 2D tracking for a 2-V event. The crosses are the chamber hits; those encircled were determined to be on a track.

The tracking algorithm was thoroughly checked by examination of hundreds of event display pictures that show the hits and the tracks formed from these hits. An example is shown in Fig. 5.7. The least-squares sum and stretch function distributions for tracks were also checked thoroughly.

The least-squares sum (often called, imprecisely, the chi-square) is defined for

each track as [98]

$$X^2 = \sum_{i=1}^{n} \left(\frac{x_{i,\text{fit}} - x_{i,\text{meas}}}{\sigma_i} \right)^2, \tag{5.2}$$

where n is the number of hits on the track. Here, for the ith hit, $x_{i,\text{fit}}$ is the track-fit predicted coordinate, $x_{i,\text{meas}}$ is the measured coordinate, and σ_i is the error assigned to the hit. If the errors are assigned correctly and there are no extra hits due to noise or other tracks, this quantity should be distributed as the familiar chi-square distribution. This distribution has mean and variance equal to the number of degrees of freedom ν and a maximum at $\nu - 2$. For a 2D track fit to a straight line, ν is equal to $n - 2$.

The hit stretch function is defined for the i-th hit on a track as [98]

$$z_i = \frac{x_{i,\text{fit}} - x_{i,\text{meas}}}{\sqrt{\sigma_i^2 - \sigma_i'^2}}, \tag{5.3}$$

where σ_i' is the error on $x_{i,\text{fit}}$ and the other quantities are the same as for the least-squares sum. This quantity, again with correct errors and no noise hits, should be distributed as a Gaussian with zero mean and unit variance.

The least-squares sum and stretch function distributions were checked as a function of chamber plane, individual wire cells, track angle, number of hits on a track, tracks with and without hit clusters, and (for the DC) hit drift time. A subset of these distributions from neutral trigger events is shown in Fig. 5.8. As can be seen in this figure the least-squares sum and stretch functions follow the expected distributions well. There is a slight excess of large X^2 and z_i tracks which is due to some erroneous tracks or extra uncorrelated hits on good track. This is not unexpected with neutral triggers due to the large number of hits in a typical event. The MWPC distributions exhibit a jaggedness which is due the the digital nature of this detector.

The final values of the errors on hits from the DC and MWPC were adjusted by examining these distributions for different track angles. For the DC, the errors obtained from the DC calibration procedure and shown in Fig. A.5 were used as

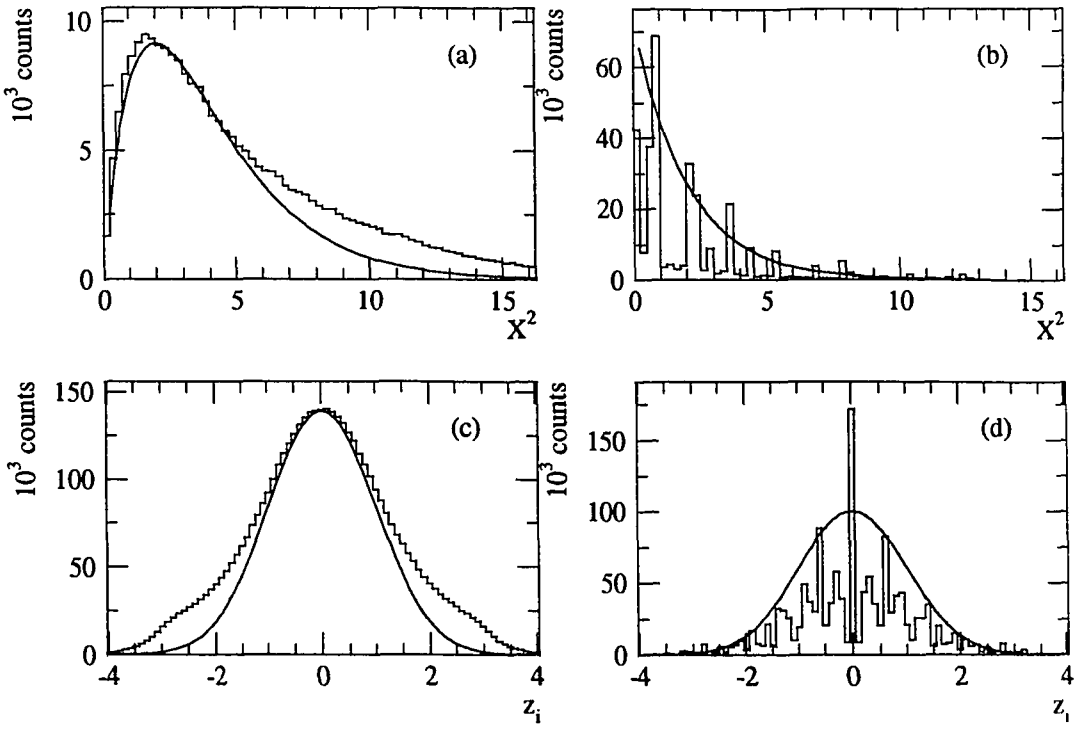

Figure 5.8: Least-squares sum distributions for (a) DC 6-hit tracks and (b) MWPC 4-hit tracks. Stretch function distributions for all (c) DC and (c) MWPC tracks. The curves in (a) and (b) are chi-square distributions with four and two degrees of freedom respectively. The curves in (c) and (d) are Gaussians of mean zero and unit variance. The curves are for comparison only; they are not fits to the data.

a starting point. These errors were then scaled for each angular range such that the stretch function distributions were of unit width. This required a scale factor somewhat less than one for the lower angular ranges. This is reasonable considering that the distributions fit to obtain these errors included the error on the fit track. By considering the stretch function distributions, this error on the track is properly taken into account. For the MWPC, as mentioned in Sec. 5.5.1 an error of $d/\sqrt{12}$ was used, where d is the width of a MWPC cell, along with an extra term. This additional term added a factor of $(n_{\text{expected}} - n_{\text{measured}})d/\sqrt{12}$ to the error if the measured hit cluster size n_{measured} was smaller than that expected n_{expected}. The

expected hit cluster size was calculated from the track angle and the geometry of the MWPC wire planes. This accounted for the extra uncertainty on a hit if it had missing wires in the cluster. This assignment resulted in reasonable least-squares sum and stretch function distributions. This choice of errors was used for the plots shown in Fig. 5.8.

5.6.2 Three Dimensional Tracking

The 3D tracking involves combining the 2D tracks to form 3D tracks. The relative 45° rotation between the xyz system of the DC and the uvz system of the MWPC allows this to be done more efficiently. If both detectors were oriented with the same system, xyz for example, all xz 2D tracks would have to be combined with all yz tracks to form the possible 3D tracks. The two tracking orientations reduces this number considerably.

For each combination of the uz and vz tracks, a 3D track is formed and rotated into the xyz system. This combination of 2D tracks projects into the xyz system as a 3D track described by

$$x = \frac{1}{\sqrt{2}}[(a_u - a_v)z + (b_u - b_v)] \tag{5.4}$$

$$y = \frac{1}{\sqrt{2}}[(a_u + a_v)z + (b_u + b_v)], \tag{5.5}$$

where a_u, a_v are the u, v slopes and a_u, a_v are the u, v intercepts describing the 2D tracks in the uz and vz orientations. This 3D track is then parameterized by the slopes and the coordinates of the line at a point midway between the MWPC and the DC (z = 11 cm). Each xz track and each yz track is then compared to this line and, if both the slope and coordinate of the track are equal to within tolerances, the xz and/or yz tracks are added to the 3D track and a 3D track is found. In a similar fashion, each combination of xz and yz tracks is rotated into the uvz system and the combinations are formed. This procedure forms "4-match" 3D tracks ($xyuv$

combinations) and "3-match" tracks (xyu, xyv, xuv and yuv combinations). All combinations of xy and uv tracks that are not matched after all are checked are used to form "2-match" tracks (xy and uv combinations).

The resulting combinations are then fit to a 3D line using the original coordinates and errors of the hits from each 2D track of the combination. The 3D line is parameterized with a 4-vector consisting of the x and y slopes and intercepts. The (4×4) covariance matrix of these parameters is also calculated using the errors assigned to the original hits.

The slope and coordinate difference distributions for neutral trigger events for the each xz and uz 2D track comparison are shown in Fig. 5.9. The yz and vz distributions are similar. These differences quantities are normalized with the calculated error and should be distributed as a Gaussian of unit width. As can be seen in the figure, they are well described by this form. All combinations are checked and contribute to these distributions so there is a flat background due to uncorrelated combinations. The tolerance to accept a 2D projection for the 3D track is set to 4σ for both the slope and coordinate normalized differences as shown in the figure.

Figure 5.10 shows the least-squares sum distribution for the the 3D tracks accepted with 20 hits. This distribution should be described as a chi-square distribution with the number of degrees of freedom $\nu = 20 - 4 = 16$ and is shown on the plot for comparison.

5.7 Vertex Recognition

After the 3D tracks are formed, the next task is to find the pairs of 3D tracks that come from the same point in space and are likely due to the decay of the Λ into a proton and a pion, that is, to find the Λ and $\overline{\Lambda}$ vertices.

This procedure begins with forming all possible combinations of two 3D tracks that have passed the previous cuts. For each combination, the distance of closest

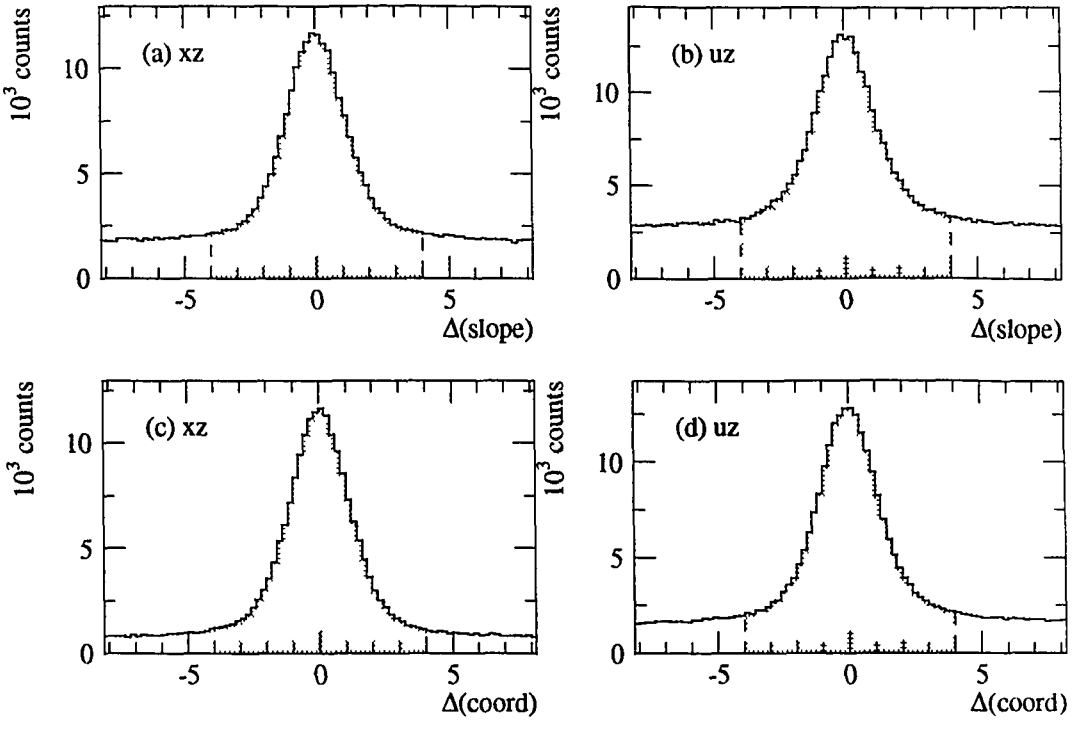

Figure 5.9: Normalized slope difference distributions for (a) the xz projection and (b) the uz projection and the normalized coordinate difference distributions for (c) the xz projection and (d) the uz projection. The shaded areas indicate the combinations accepted with the 4σ cut.

approach (DCA), the point of closest approach (PCA) of the two tracks, and the plane of the vertex are calculated. Using the vertex plane, the distance from this plane to the target point (VTD) is calculated. The target point is set to be in the center of the assigned neutral cell. These quantities are illustrated in Fig. 5.11. Two 3D tracks from the decay products of a Λ originate at a point and (in the absence of experimental errors) DCA is equal to zero. If the Λ is produced at the target point, momentum conservation for the decay implies that VTD is equal to zero.

If the DCA and VTD quantities satisfy these conditions within certain tolerance values, the combination of two 3D tracks is considered to be a vertex candidate and the parameters of the vertex plane are stored. A 3D track can belong to more

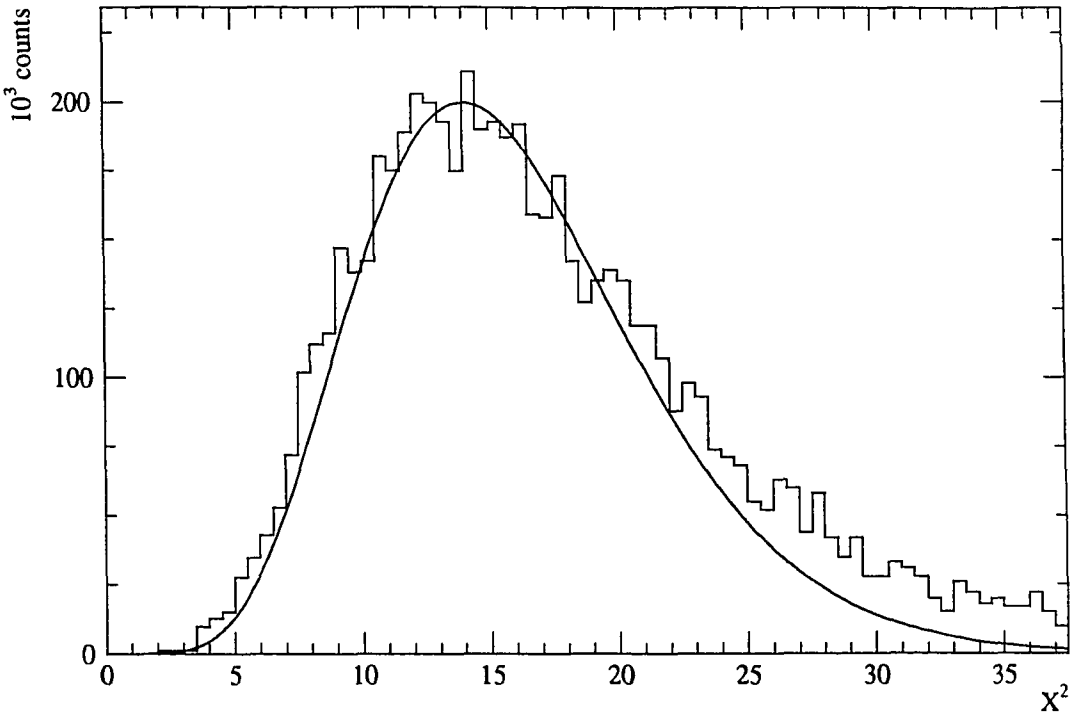

Figure 5.10: Least-squares sum distribution for fit 3D tracks with 20 hits. The curve is a chi-square distribution with 16 degrees of freedom, shown for comparison.

than one vertex combination and all combinations of 3D tracks are tested except the unphysical case where both 3D tracks consist of a common 2D track.

The distribution of DCA, normalized by the calculated error on this quantity, and the distribution of VTD for all 3D track combinations from neutral events are shown in Fig. 5.12. The quantity VTD is very non-linear in the 3D track parameters resulting in a difficult error calculation; therefore the unnormalized quantity was used. The cut on normalized DCA was set at ± 6.0 which corresponds to about 0.3 cm. The VTD cut was set at ± 1.5 cm. Both of these cuts are kept rather wide; at this stage only the obviously incorrect combinations were removed from the sample.

Figure 5.13 shows the distribution of points of closest approach of the candidate vertices in the neutral event sample. Note the large density of vertices found along

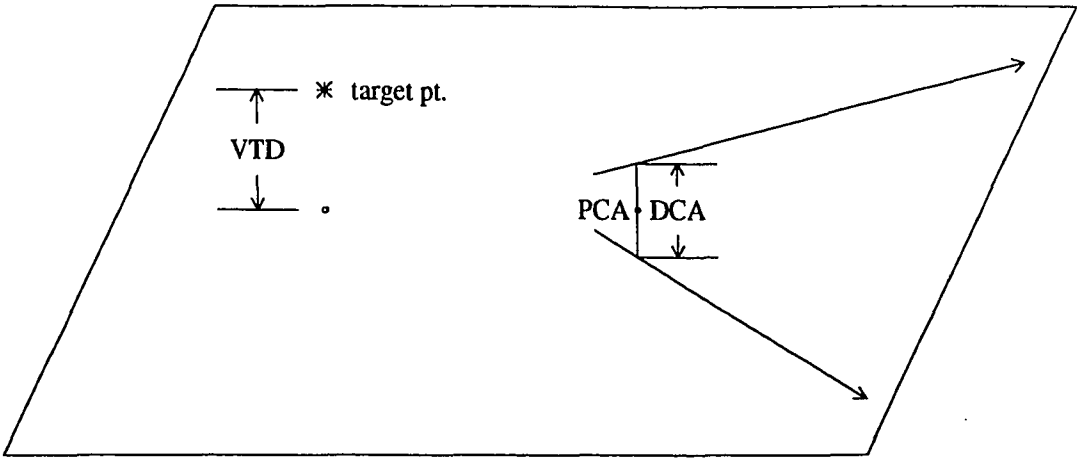

Figure 5.11: An illustration showing the vertex quality parameters, DCA and VTD. The plane illustrated is that of the vertex containing the point of closest approach, PCA, which is halfway along the shortest line connecting the two 3D tracks.

the beam (z) axis near the target location ($z \approx -1.5$ cm). To eliminate unsatisfactory candidate vertices, a cut was applied that kept those vertices with the vertex point (PCA) inside a "cone of acceptance", illustrated in Fig. 5.14. The minimum z of the cone was set to a value 1.0 cm downstream from the center of the assigned neutral target cell. This value was determined to be the minimum value possible to have a sufficient "lever-arm" with which to constrain the hyperon production angle. The value of the maximum z was not very critical to the analysis; it was set to the maximum value for which a vertex could be reconstructed in the chambers. The minimum radius of the cone was set to 0.5 cm and the cone half-angle, 25.4°, was determined by the maximum Λ lab angle at this momentum.

With the candidate vertices and the hypothesis that the decaying particle was a Λ, the momentum vectors of the Λ and the decay proton and pion may be calculated. The momenta of the Λ hyperons for the reactions studied here are such that the proton always has a smaller decay angle than that of the pion. This allows the

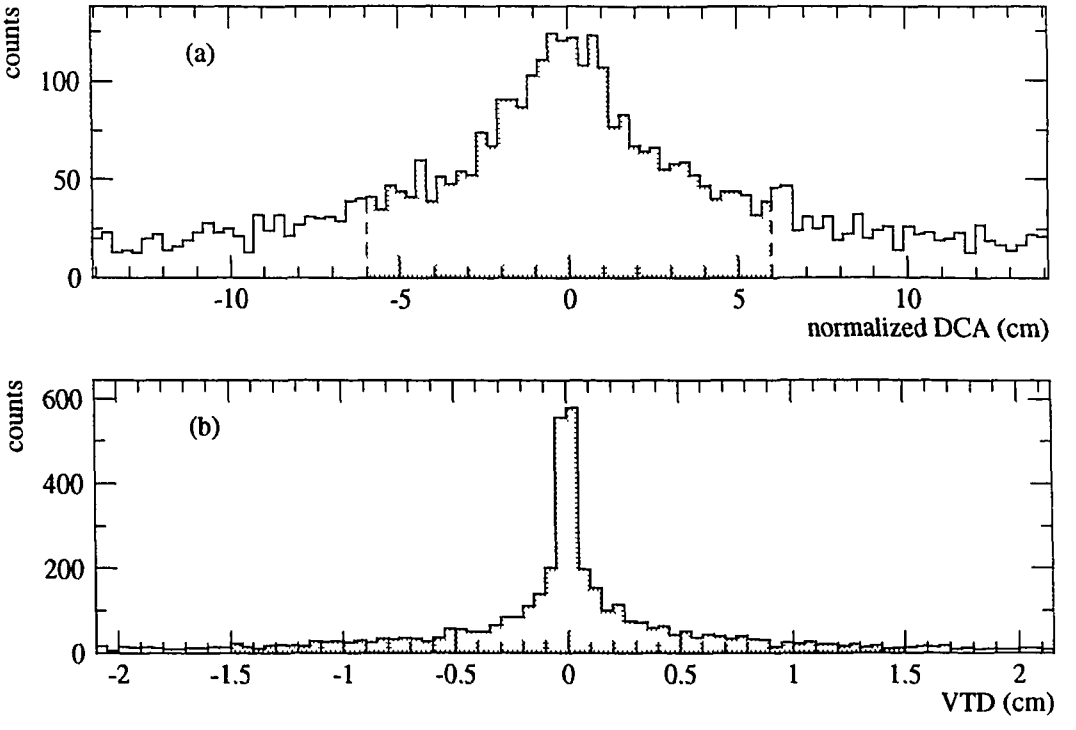

Figure 5.12: Vertex recognition distributions: (a) distance of closest approach (DCA) normalized by the calculated error and (b) vertex plane–target point distance (VTD). The shaded area indicates those combinations accepted by the vertex quality cuts.

unambiguous assignment of particle type to each leg of the vertex. Also, the kinematics of the Λ decay allow for a fairly precise determination of the Λ momentum from the decay angles of the daughter tracks.

The momentum of the Λ as calculated from the vertex parameters is shown in Fig. 5.15(a). The range of allowed Λ momenta in the $\overline{p}p \rightarrow \overline{\Lambda}\Lambda$ reaction is approximately 0.4 - 1.3 GeV/c (see Fig. 4.3). The peak at around 0.3 GeV/c is due largely to vertices formed from incorrect 3D track combinations. A fairly loose cut was implemented on candidate vertices with reconstructed Λ momenta outside of the range set 0.2–1.7 GeV/c, as indicated in Fig 5.15(a). The Λ momentum may be used to calculate the mass of the recoil particle with the hypothesis that the reaction was

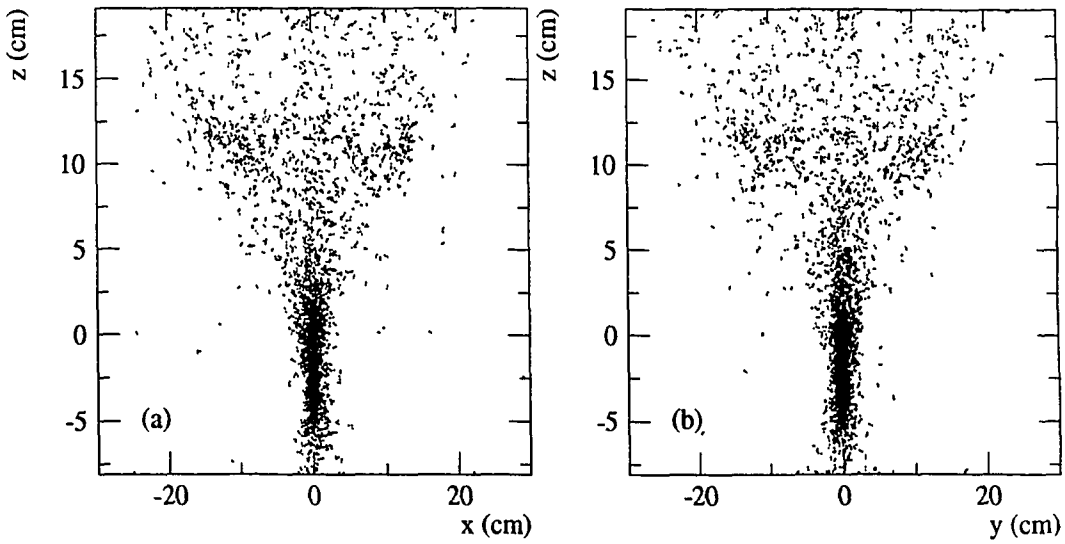

Figure 5.13: Postion of candidate vertices from neutral events in the (a) xz and (b) yz planes.

$\overline{p}p \rightarrow \Lambda X$. The distribution of the mass of X, the recoil mass, is shown if Fig. 5.15(b). No cuts were implemented on this quantity. Note the excess of events at the Λ mass (1.115 GeV/c^2), a clear signature for the $\overline{p}p \rightarrow \overline{\Lambda}\Lambda$ reaction even at this early stage of the analysis.

5.8 Vertex Pairing

After the vertex recognition phase of the analysis, the candidate vertices remaining in the sample are subjected to the vertex pairing procedure. All combinations of two candidate vertices, except for those that share a 3D track or use the same 2D tracks, are formed. Using the momentum vectors formed from these vertex pairs and the momentum vector of the beam, the momentum sums of the event along the three axes of the lab system are calculated. The distributions of these quantities are shown in Fig 5.16.

The excess of combinations that result in a z momentum sum less than zero is due

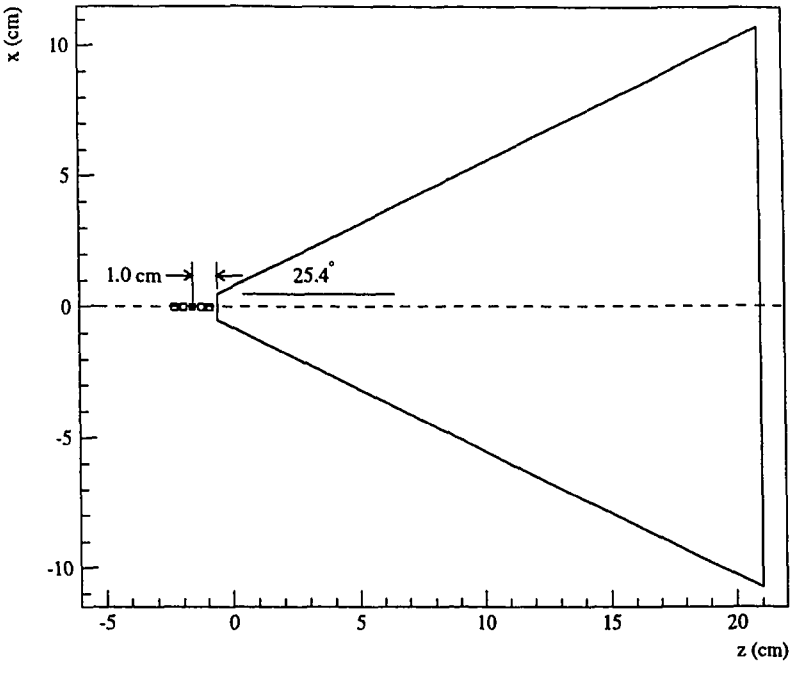

Figure 5.14: An illustration of the vertex "cone of acceptance projected onto the xz plane.

to the combinations of vertices with a momenta less than the lower limit dictated by the kinematics. The cuts on these sums were determined by examining these distributions for events that passed the kinematic fit cuts (described below) and for Monte Carlo events. For $\bar{p}p \rightarrow \overline{\Lambda}\Sigma^0 + c.c.$ events the momentum sums do not equal zero by the amount of momentum carried by the Σ^0-decay photon. But, since the photon is of relatively low energy (0.077 GeV in the c.m.), fairly strong cuts can still be made without a loss of good events. It was determined that the cuts should be placed at ± 0.15 GeV/c for the x and y momentum sums and at ± 0.35 GeV/c for the z momentum sum as shown in Fig 5.16. The vertex combinations that pass this cut are considered vertex pair candidates.

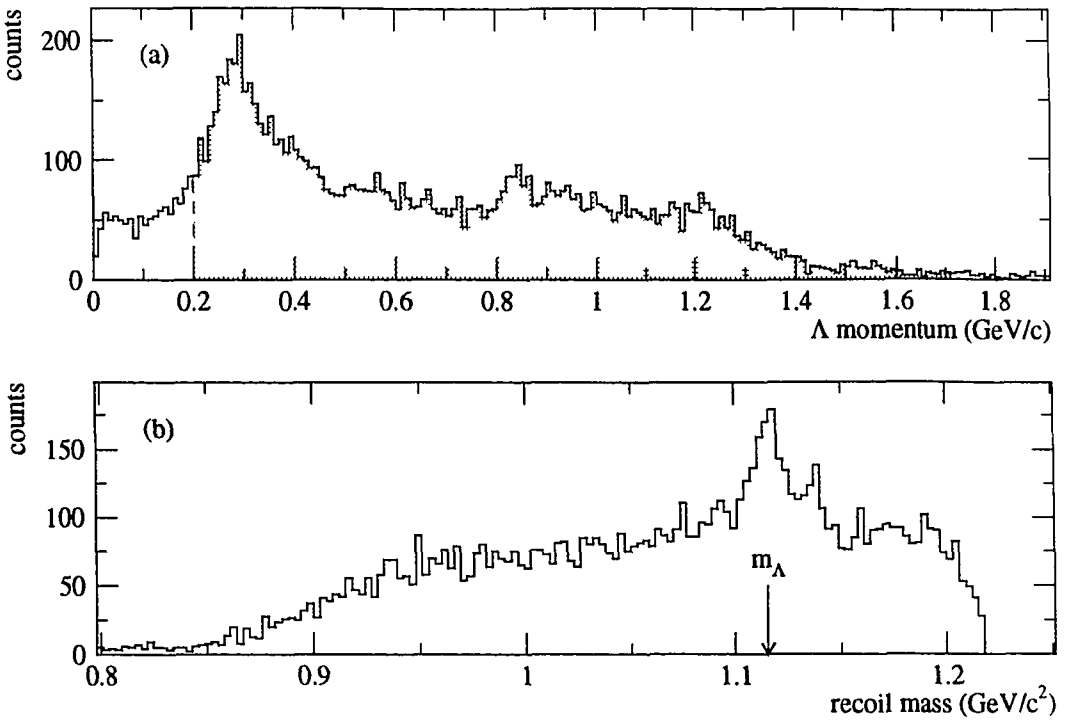

Figure 5.15: Vertex kinematic distributions: (a) Λ momentum and (b) mass of recoil particle for the $\bar{p}p \rightarrow \Lambda X$ hypothesis. The shaded area of (a) indicates the values accepted in the Λ momentum cut.

The recoil masses as calculated from the vertex pair candidates from a subset of the 1.729 GeV/c data are shown in Fig. 5.17. The $\bar{p}p \rightarrow \overline{\Lambda}\Lambda$ events are clearly seen in the scatter plot as an increased density of points where the recoil masses 1 and 2 are equal to the Λ mass (1.115 GeV/c^2). There is also an increased density where the recoil masses are both equal to Σ^0 mass (1.192 GeV/c^2), showing that there are $\bar{p}p \rightarrow \overline{\Lambda}\Sigma^0$ and $\bar{p}p \rightarrow \overline{\Sigma}^0\Lambda$ events in the sample as well.

5.9 Kinematic Fitting

The final task in the analysis chain to complete before the final $\bar{p}p \rightarrow \overline{\Lambda}\Lambda$, $\bar{p}p \rightarrow \overline{\Lambda}\Sigma^0$, and $\bar{p}p \rightarrow \overline{\Sigma}^0\Lambda$ event sample is selected is the kinematic fitting. This involves using

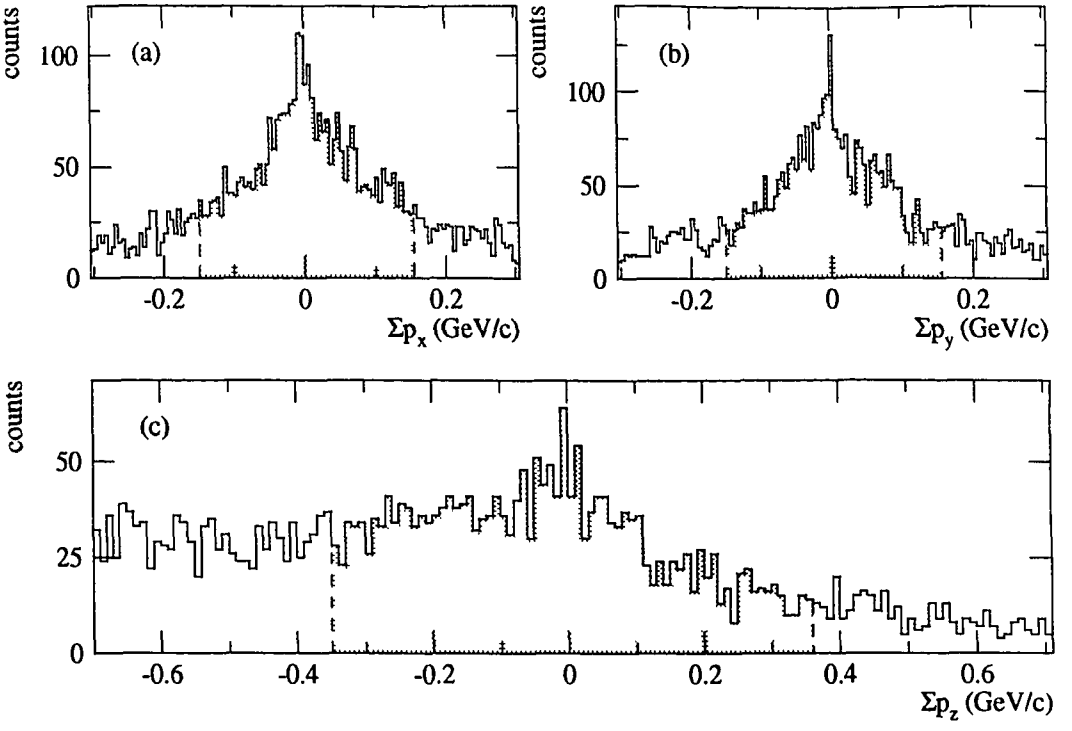

Figure 5.16: Vertex pair kinematic distributions: Sum of the (a) x, (b) y, and (c) z momentum components as calculated from the vertex pair. The shaded areas indicate the values accepted in the vertex pair cut.

the detector information needed to specify an event, parameterized in some way and with errors, and fitting these parameters to the hypothesis that the event was one of the type desired. The fitting procedure adjusts the parameters to satisfy the momentum, energy, and spatial constraints of the reaction hypothesis and finds the "best-fit" values for these parameters. If the event fits one of these hypotheses satisfactorily then it is considered to be a "good" event and a $\overline{p}p \rightarrow \overline{\Lambda}\Lambda$, $\overline{p}p \rightarrow \overline{\Lambda}\Sigma^0$, or $\overline{p}p \rightarrow \overline{\Sigma}^0\Lambda$ has been found. The best-fit parameters are then used to calculate the desired observables.

As is usually the choice of methods for problems of this type, a procedure is implemented that minimizes the least-squares sum for the event subject to the constraints

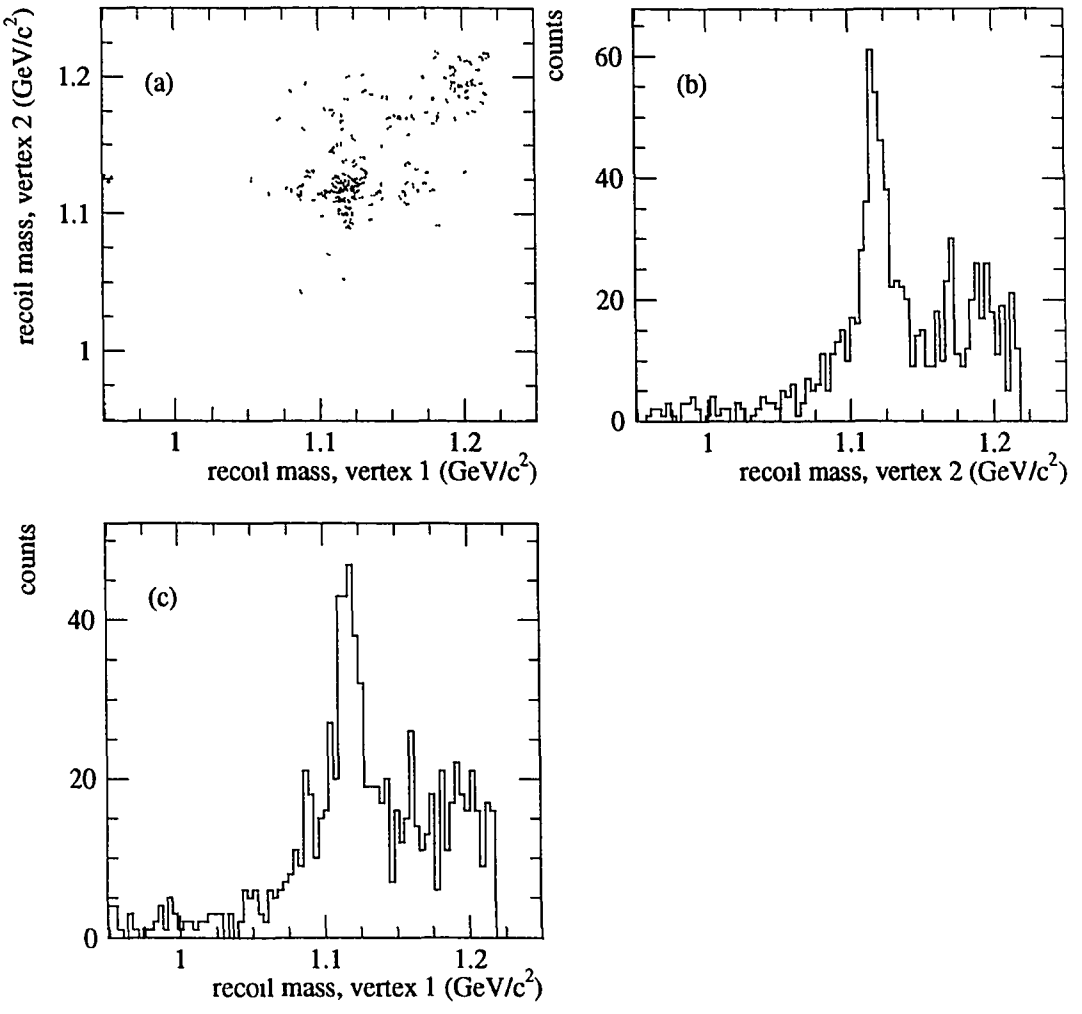

Figure 5.17: Recoil mass distributions for vertex pairs: (a) scatter plot of recoil mass for vertex 1 vs recoil mass for vertex 2, (b) recoil mass for vertex 2, and (c) recoil mass for vertex 1. One tape ($\approx 2\%$) of the total 1.729 GeV/c data set) of data was used to form these distributions.

imposed by the particular event hypothesis. The constraints are nonlinear in the parameters which prevents an analytical solution and the minimization procedure must progress iteratively. A computing problem of this type is extremely complex, to write the code from scratch would be a daunting task. Instead, the routine E04UCF from the NAG (Numerical Algorithms Group) Fortran Library [100] is used. This routine determines the values of parameters that minimize a function while satisfying the constraint equations. The user supplies the initial values for fit parameters and the corresponding error matrix. The user must also write the routines that calculate the function to be minimized, the values of the constraints, and the derivatives of the function and constraints with respect to the parameters.

The kinematic fit is performed for each candidate vertex pair for each event hypothesis. The kinematics of the $\overline{p}p \rightarrow \overline{\Lambda}\Lambda$ and $\overline{p}p \rightarrow \overline{\Lambda}\Sigma^0 + c.c.$ reactions are very similar; none of the cuts up to this stage of the analysis are sufficient to separate the reactions. So, each vertex pair is fit to the hypotheses that the event is a $\overline{p}p \rightarrow \Lambda\Lambda$ *and*, that it a $\overline{p}p \rightarrow \Lambda\Sigma$. These reactions are intentionally written without the correct particle-antiparticle differentiation because the decay-particle charge assignments have yet to be made. And, as far as the kinematic fit is concerned, the Λ decay is no different than a $\overline{\Lambda}$ decay because of the identical masses. The particle-antiparticle identification is done after the kinematic fit procedure.

Each $\overline{p}p \rightarrow \Lambda\Sigma$ hypothesis is fit twice, once with Λ_1 identified as the daughter of the Σ^0 and once with Λ_2 as the daughter of the Σ^0. Here Λ_1 and Λ_2 are the Λ's associated with vertex 1 and 2, respectively, of the candidate vertex pair. Also, each of these two $\overline{p}p \rightarrow \Lambda\Sigma$ fits can be performed with two different methods, one with the momentum components of the Σ^0-decay photon as free parameters and the other using the momentum components of the photon as measured by the calorimeter. That is, of course, if there is a candidate photon signal measured in the calorimeter for that event (see Sec. 5.4). The kinematic fit using the measured photon information is called a $\overline{p}p \rightarrow \Lambda\Sigma_\gamma$ fit. So, each candidate vertex pair is fit with three event

hypotheses and, if desired, with two more for each photon candidate measured in the calorimeter.

The core group of parameters describing the event information for the kinematic fit procedure is listed in Table 5.2. These 28 parameters are common to the fits with all three of the event hypotheses: $\overline{p}p \rightarrow \Lambda\Lambda$, $\overline{p}p \rightarrow \Lambda\Sigma$, and $\overline{p}p \rightarrow \Lambda\Sigma_\gamma$. The additional parameters required for the $\overline{p}p \rightarrow \Lambda\Sigma$ and $\overline{p}p \rightarrow \Lambda\Sigma_\gamma$ fits are listed in Table 5.3. A parameter is either "measured" or "unmeasured" [98]. The measured parameters are, as the name implies, those measured with the detector or otherwise, such as the slopes and intercepts of the final charged particles and the beam momentum. The "unmeasured" parameters are those not directly measured and are needed to solve the constraint equations, such as the momenta of the hyperons and their decay products. The parameters could be limited in the fitting procedure by assigning upper and lower bounds; however, for only the z coordinate of the interaction point z_t was this of importance. This parameter was limited by the edges of the target cell in which it was determined the reaction took place. The final value of z_t often ended up on the bounds, especially for the $\overline{p}p \rightarrow \Lambda\Sigma$ hypothesis, but it was determined that this does not effect the quality of the fit. The constraints imposed for the fit procedure are listed below.

- The two tracks from the Λ decays must intersect at a point in space. This yields two equations; one for each decay.
- The hyperon production must obey momentum and energy conservation. The yields four equations.
- Each Λ decay must obey momentum and energy conservation. This yields eight equations; four at each vertex.
- The Σ decay must obey momentum and energy conservation. For the $\overline{p}p \rightarrow \Lambda\Sigma$ and $\overline{p}p \rightarrow \Lambda\Sigma_\gamma$ fits, this yields four additional equations.

#	name		description	#	name		description
1	p_b		$\overline{p}$ momentum	15	a_2		p_2, x slope
2	z_t	†	interaction, z	16	b_2		p_2, x intercept
3	a_b		$\overline{p}$, x slope	17	c_2		p_2, y slope
4	b_b		$\overline{p}$, x intercept	18	d_2		p_2, y intercept
5	c_b		$\overline{p}$, y slope	19	e_2		π_2, x slope
6	d_b		$\overline{p}$, y intercept	20	f_2		π_2, x intercept
7	a_1		p_1, x slope	21	g_2		π_2, y slope
8	b_1		p_1, x intercept	22	h_2		π_2, y intercept
9	c_1		p_1, y slope	23	k_1	†	Λ_1, momentum
10	d_1		p_1, y intercept	24	k_2	†	Λ_2, momentum
11	e_1		π_1, x slope	25	k_3	†	p_1, momentum
12	f_1		π_1, x intercept	26	k_4	†	π_1, momentum
13	g_1		π_1, y slope	27	k_5	†	p_2, momentum
14	h_1		π_1, y intercept	28	k_6	†	π_2, momentum

Table 5.2: The core parameters for to the $\overline{p}p \rightarrow \Lambda\Lambda$, $\overline{p}p \rightarrow \Lambda\Sigma$, and $\overline{p}p \rightarrow \Lambda\Sigma_\gamma$ fits. The $\overline{p}$ is the beam particle; Λ_1, p_1, and π_1 are the particles associated with vertex 1; and Λ_2, p_2, and π_2 are the particles associated with vertex 2. A † after the parameter name indicates that that is an unmeasured parameter.

The number of parameters, constraints, and degrees of freedom (d.o.f.) of the kinematic fit are tabulated for each event hypothesis in Table 5.4. The number of d.o.f for each fit is simply the number of constraints imposed minus the number of unmeasured parameters that are introduced.

The function minimized for each fit, the least-squares sum, is calculated for each iteration of the fit using the matrix equation [98],

$$X^2(\boldsymbol{\eta}) = (\mathbf{y} - \boldsymbol{\eta})^T V^{-1} (\mathbf{y} - \boldsymbol{\eta}), \tag{5.6}$$

where $\mathbf{y}$ is the vector of the measured parameters, $\boldsymbol{\eta}$ is the vector of the estimated

$\overline{p}p \rightarrow \Lambda\Sigma$			$\overline{p}p \rightarrow \Lambda\Sigma_\gamma$		
#	name	description	#	name	description
29	$p_{x,\Sigma}$ †	Σ, x momentum	29	$p_{x,\Sigma}$ †	Σ, x momentum
30	$p_{x,\Sigma}$ †	Σ, y momentum	30	$p_{x,\Sigma}$ †	Σ, y momentum
31	$p_{x,\Sigma}$ †	Σ, z momentum	31	$p_{x,\Sigma}$ †	Σ, z momentum
32	$p_{x,\gamma}$ †	γ, x momentum	32	x_γ	γ, x position
33	$p_{x,\gamma}$ †	γ, y momentum	33	y_γ	γ, y position
34	$p_{x,\gamma}$ †	γ, z momentum	34	E_γ	γ, energy

Table 5.3: The additional parameters needed for the $\overline{p}p \rightarrow \Lambda\Sigma$ and $\overline{p}p \rightarrow \Lambda\Sigma_\gamma$ fits. A † after the parameter name indicates that that is an unmeasured parameter.

fit hypothesis	$\overline{p}p \rightarrow \Lambda\Lambda$	$\overline{p}p \rightarrow \Lambda\Sigma$	$\overline{p}p \rightarrow \Lambda\Sigma_\gamma$
total parameters	28	34	34
measured parameters	21	21	24
unmeasured parameters	7	13	10
number of constraints	14	18	18
number of degrees of freedom	7	5	8

Table 5.4: Summary of unknowns, constraints, and number of degrees of freedom for each fit hypothesis.

parameters for the current iteration, and V is the covariance (or error) matrix for the measured parameters. The covariance matrix V is set using the covariance matrices for each subgroup of the measured parameters. That is, there is one error parameter for the momentum of the beam, one 4×4 covariance matrix for the beam track, and one 4×4 covariance matrix for each of the four decay particle tracks. These 4×4 covariance matrices are calculated from the least-squares fit to the tracks with the information provided by the microstrips and tracking chambers.

Careful examination of the kinematic fit least-squares sum and stretch function

distributions for different types of events showed that the errors as described above were adequate with the exception of the lower-energy decay-pion and decay-proton tracks. For these tracks, multiple scattering in the detector is a non-negligible process and must be accounted for in the covariance matrices. To quantify this, the effects of matter are estimated to cause an angular deviation of the particle track that is Gaussian in shape and of width [12]

$$\theta_0 = \frac{13.6 \text{ MeV}}{\beta cp}\sqrt{x/X_0}, \tag{5.7}$$

where p and βc are the momentum and velocity of the particle and x/X_0 is the amount of material in radiation lengths traversed by the particle. This quantity is determined for each decay-particle track and the covariance matrix due to multiple scattering is calculated. It is then added to the covariance matrix as calculated from the track hits to form the final covariance matrix that is used in the kinematic fit.

In the final implementation of the analysis, each candidate vertex pair was fit to the $\overline{p}p \rightarrow \Lambda\Lambda$ and $\overline{p}p \rightarrow \Lambda\Sigma$ hypotheses and the vertex pair that yielded the lowest value of the kinematic fit X^2 was selected as the "best" fit pair.

If the best-fit X^2 was below a certain cut value and the best-fit hypothesis was $\overline{p}p \rightarrow \Lambda\Lambda$, the event was considered a candidate $\overline{p}p \rightarrow \Lambda\Lambda$ event. If the best-fit X^2 was below a different cut value and the fit hypothesis was $\overline{p}p \rightarrow \Lambda\Sigma$, the event was considered a candidate $\overline{p}p \rightarrow \Lambda\Sigma$ event. The X^2 cut values were set to correspond to a χ^2 probability of 99%, which is 18.5 for the 7 d.o.f. $\overline{p}p \rightarrow \Lambda\Lambda$ hypothesis and 15.1 for the 5 d.o.f $\overline{p}p \rightarrow \Lambda\Sigma$ hypothesis [98].

The values of the best-fit X^2 for each event are histogrammed in Fig. 5.18, separated into $\overline{p}p \rightarrow \Lambda\Lambda$ and $\overline{p}p \rightarrow \Lambda\Sigma$ candidate events. The curves superimposed on these histograms are the chi-square distributions with the number of degrees of freedom corresponding to that particular event hypothesis. The distributions are described by this form remarkably well. There is a slight excess of events with larger values of the best-fit X^2. These events include a particle scattered in the detector

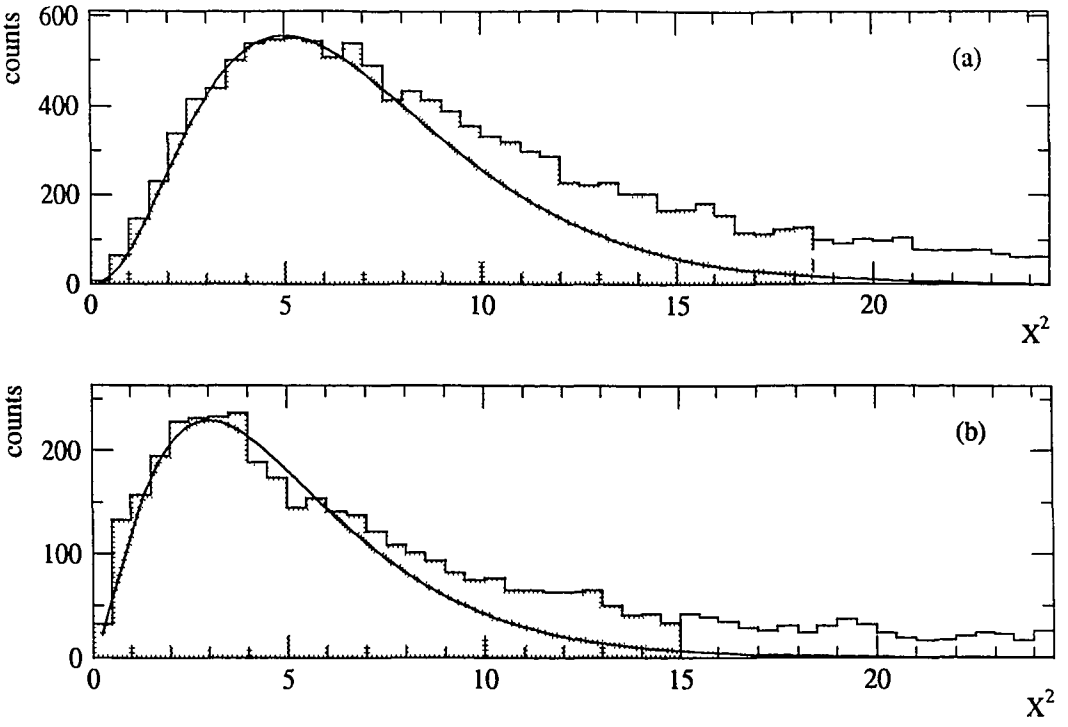

Figure 5.18: Best-fit X^2 distributions from the kinematic fit for (a) $\bar{p}p \rightarrow \Lambda\Lambda$ candidate events and (b) $\bar{p}p \rightarrow \Lambda\Sigma$ candidate events. The curves are the chi-square distribution for (a) 7 and (b) 5 degrees of freedom scaled for the data; they are not fits. The shaded area indicates events accepted by the kinematic fit X^2 cut.

by more than is accounted for with the multiple scattering error or a track that is erroneous for some other reason not accounted for with Gaussian errors. There is no evidence for background from events other than those considered here. This will be further supported by examination of the Monte Carlo data.

Events that were selected as $\bar{p}p \rightarrow \Lambda\Sigma$ candidates and included a candidate photon in the calorimeter were refit with the $\bar{p}p \rightarrow \Lambda\Sigma\gamma$ hypothesis. The results of these fits were less than satisfactory. The best-fit X^2 values for a subset of the $\bar{p}p \rightarrow \Lambda\Sigma$ candidate events are histogrammed in Fig. 5.19. More work is needed to verify that the kinematic fit with this hypothesis is working correctly and that the candidate photon used in the fit is a true photon. With these fits, only 6% of the

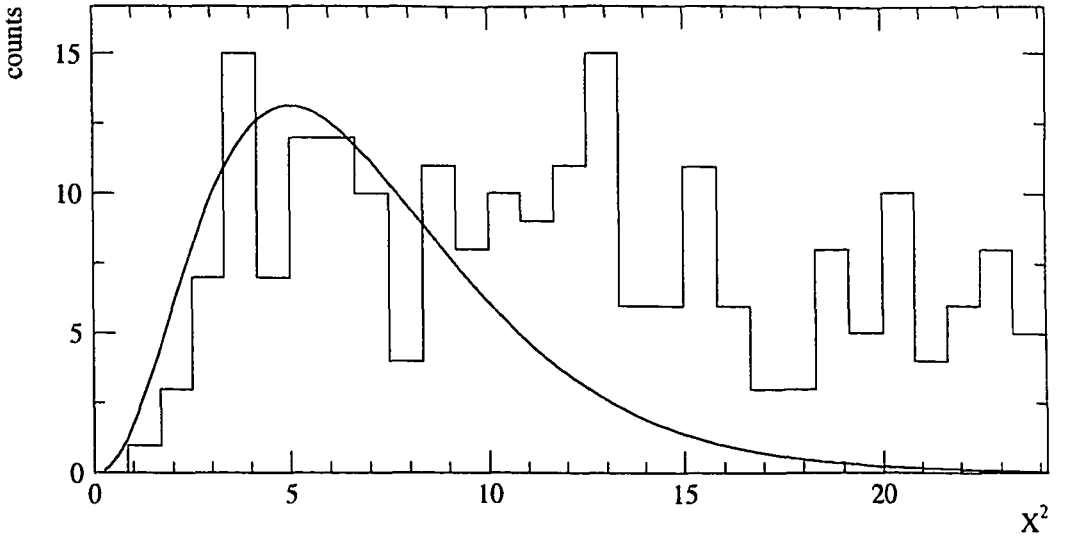

Figure 5.19: Best-fit X^2 distributions from the kinematic fit to a subset of the $\bar{p}p \rightarrow \Lambda\Sigma$ candidate events for the $\bar{p}p \rightarrow \Lambda\Sigma_\gamma$ hypothesis. The curve is the chi-square distribution for 8 degrees of freedom scaled to the data.

$\bar{p}p \rightarrow \Lambda\Sigma$ were successfully fit to the $\bar{p}p \rightarrow \Lambda\Sigma_\gamma$ hypothesis. This low acceptance is due, at least in part, to the low geometrical acceptance of the calorimeter for photons in the $\bar{p}p \rightarrow \overline{\Lambda}\Sigma^0 + c.c.$ events and the harsh cuts needed to obtain a unambiguous photon signal. This number was also verified with Monte Carlo events. Because of this low acceptance and the fact that $\bar{p}p \rightarrow \Lambda\Sigma$ candidate events are successfully fit and separated for $\bar{p}p \rightarrow \Lambda\Lambda$ *without* using the calorimeter information, it was decided to complete the analysis of the data without using the photon information provided by the calorimeter. It may turn out that the calorimeter is needed for the analysis of the data at other momenta, but that is a task for future work.

5.10 Baryon Identification

After candidate $\bar{p}p \rightarrow \overline{\Lambda}\Lambda$ and $\bar{p}p \rightarrow \overline{\Sigma^0}\Lambda + c.c.$ events are selected on the basis of the kinematic fit results, they are subjected to the baryon identification (BID) procedure.

This involves using the data provided by the three drift chamber planes that were situated in the magnetic solenoid (MACH). The hits in this chamber are formed as with the DC as explained in Sec. 5.5.2. The analysis of the hits allows (ideally) the particle charge to be assigned to each track of the candidate event as identified in the upstream tracking chambers. From these charge assignments, the baryon number of the hyperon associated with each vertex may be determined. If the more massive decay-particle from the vertex 1 has a positive charge, it was a proton and the vertex was caused by a Λ; if it has negative charge, it was an antiproton and the vertex was caused by a $\overline{\Lambda}$. Up to this stage of the analysis, there has been no distinction between an antihyperon and a hyperon vertex; the baryon identification allows this distinction to be made.

The predicted trajectory of each of the four tracks of the candidate event through the magnetic solenoid drift chamber (MACH) is calculated for the two different charge hypotheses. A portion of the pion trajectories do not intersect the MACH; these are excluded and the BID procedure uses the remaining tracks. This trajectory is predicted using the track direction and momentum as calculated in the kinematic fit. The most-likely momentum loss in the aluminum coil of the solenoid is subtracted from the fit momentum and the trajectory was calculated using the equation for the radius of a curvature of a unit charged particle in a magnetic field [99]:

$$R(\text{cm}) = 3356.41 \frac{P_{xz}(\text{GeV/c})}{B(\text{kG})}, \tag{5.8}$$

where R is the radius of curvature of the particle, P_{xz} is the momentum of the particle in the xz plane (normal to the magnetic field), an B is the value of the magnetic field. The magnetic field for this experiment was 0.9 kG which yields radii of curvature of a few hundred cm for pions to a few thousand cm for protons.

Each plane of the MACH is searched for hits that are within a certain tolerance of the hits predicted from the calculated trajectories. The tolerance value is set to be 2.5 times the total error calculated by adding, in quadrature, the error on the

measured hit together with the error on the predicted hit due to multiple scattering, momentum loss in the Al coil, and extrapolating the fit track. Any and all hits that are within the the tolerance value of the predicted hit are saved.

After all hits are checked, if there is at least one hit in each MACH plane consistent with one of the bending hypotheses for the track, a candidate MACH track has been found. If there is more than one hit per MACH plane or if a MACH track is found for both bending hypotheses for one extrapolated track, then the combination of hits that is most likely to have been created by a track of the predicted momentum is chosen as the candidate track. This choice is made by selecting the combination of three hits that minimizes the prediction difference R,

$$R \equiv x_{\text{hit}} - x_{\text{pred}}, \tag{5.9}$$

where x_{hit} is the coordinate of the measured hit in the center MACH plane and x_{pred} is the coordinate at this plane as predicted by the two hits in the outer planes and the momentum of the track. Note that this method of predicting the hit does not rely on the particle passing through the Al coil of the solenoid undeflected.

With the selected MACH tracks, each consisting of three hits, the deflection distance S is calculated for each, using the definition:

$$S \equiv x_{\text{str}} - x_{\text{hit}}, \tag{5.10}$$

where x_{str} is the x coordinate at the center MACH plane of a straight line connecting the two hits from the outer two MACH planes. The situation is illustrated in Fig. 5.20. The deflection distance for MACH tracks for candidate events as a function of momentum and separated into proton and pion tracks is shown in Fig. 5.21. Note the very clear separation of particles of different charges.

Using the deflection distance S_i for the ith candidate MACH track, the deflection distance sum is defined:

$$W \equiv \sum_i I_i w_i S_i, \tag{5.11}$$

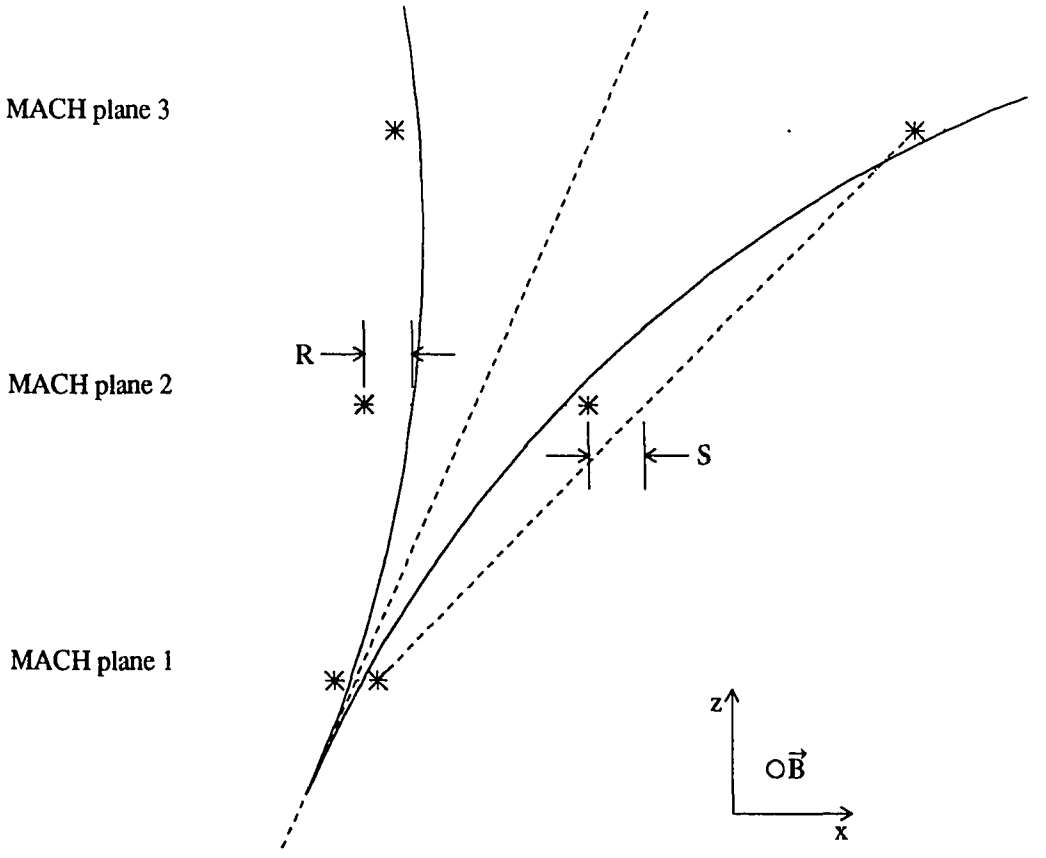

Figure 5.20: An illustration of the baryon number identification using the magnetic solenoid drift chamber (MACH). The measurement of the prediction difference R and the deflection difference S are shown. The deflections and hit offsets are greatly exaggerated for the figure.

where the sum runs over all candidate MACH tracks and I_i is $+1$ or -1, chosen such that tracks consistent with assignment of the Λ to vertex 1 would contribute a positive value to the sum. The quantity w_i is defined as,

$$w_i \equiv \min(\frac{\sigma(R_i)}{R_i}, 1.0), \tag{5.12}$$

where R_i is the prediction difference for the ith candidate track and $\sigma(R_i)$ is the calculated error on R_i. The addition of this term weights the sum inversely proportional to the prediction difference, thus giving less weight to the tracks that fit the

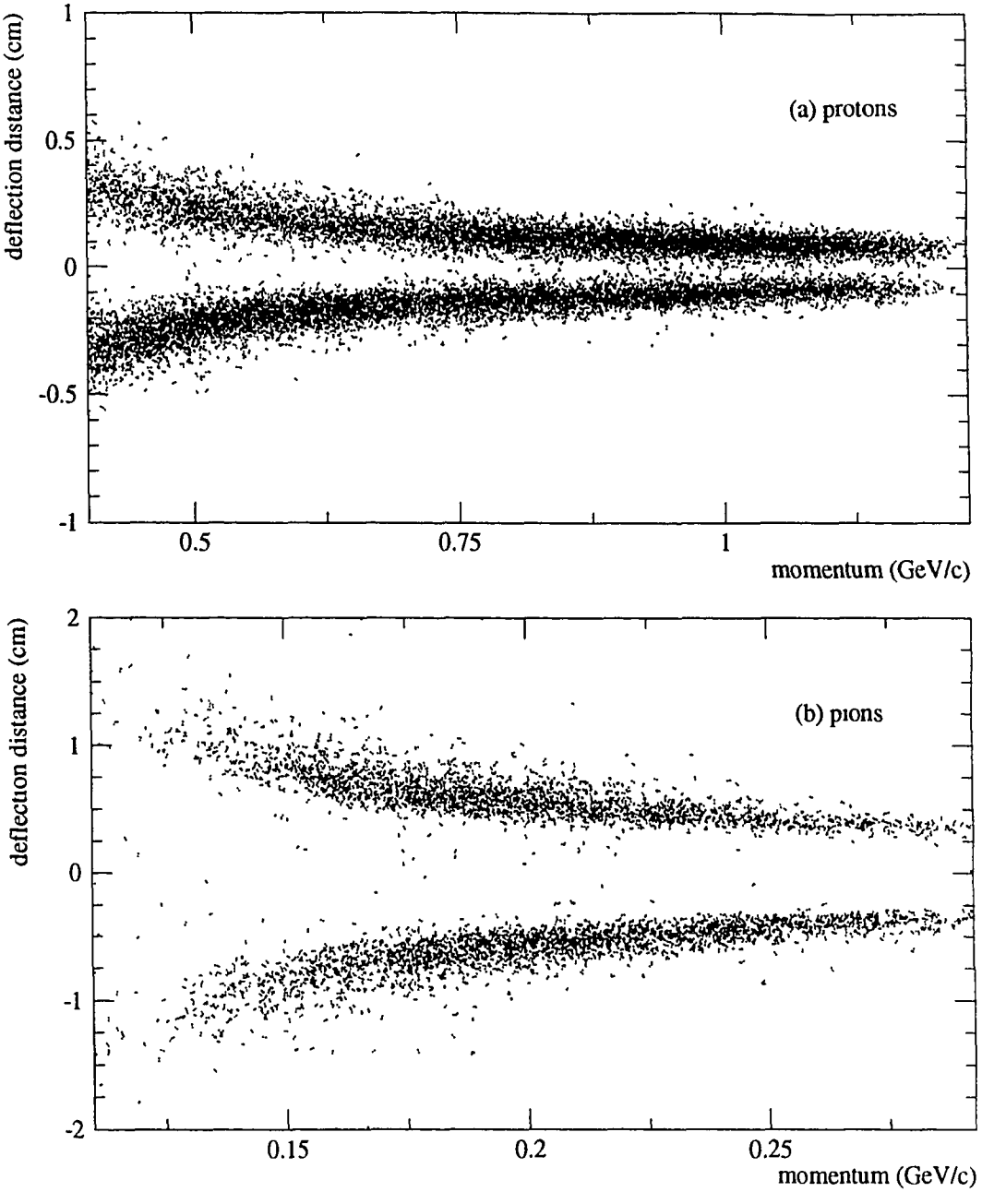

Figure 5.21: Scatter plot of MACH deflection distance S as a function of particle momentum for (a) proton and (b) pion tracks.

prediction poorly. For each event, each vertex is assigned a baryon number based on the value of W. If $W > 0$, the Λ is assigned to vertex 1 and the $\overline{\Lambda}$ to vertex 2. If $W < 0$, the opposite assignment is made.

The number of candidate MACH tracks found for $\bar{p}p \rightarrow \overline{\Lambda}\Lambda$ and $\bar{p}p \rightarrow \overline{\Lambda}\Sigma^0 +$ *c.c.* events is histogrammed in Fig. 5.22(a). The deflection distance sum W for these events and for events with different numbers of MACH tracks is shown in Fig. 5.22(b)–5.22(e). The requirement for an event to be considered successfully "baryon identified" is that the number of MACH tracks is at least one and that the absolute value of W be greater than 0.05 cm.

5.11 Data Reduction

The $\bar{p}p \rightarrow \overline{\Lambda}\Lambda$ and $\bar{p}p \rightarrow \overline{\Sigma}^0\Lambda + c.c.$ events are selected from the large amount of raw data by subjecting each event to each stage of the analysis and eliminating those that do not pass the cuts from further consideration. The events that remain at the end of the analysis chain are considered to be $\bar{p}p \rightarrow \overline{\Lambda}\Lambda$ and $\bar{p}p \rightarrow \overline{\Sigma}^0\Lambda + c.c.$ events and are used to extract the observables.

The final values for the cuts were checked and adjusted (especially the later-stage cuts) by analyzing a subset of raw events with all cuts relaxed. The distributions of the cut variables were then examined for events that were determined by the kinematic fit procedure to be $\bar{p}p \rightarrow \overline{\Lambda}\Lambda$ and $\bar{p}p \rightarrow \overline{\Sigma}^0\Lambda + c.c.$ events. These distributions allowed the determination of how the cuts should be set to efficiently remove unwanted events without eliminating too many of the events of interest.

A summary of the cuts applied at each stage of the analysis and described in previous sections is listed in Table 5.5. They are divided into quality cuts and number cuts. A quality cut requires each object formed (a track, a vertex, a vertex pair, etc.) to satisfy certain quality constraints; a number cut requires the number of these objects in each event to be within a certain range.

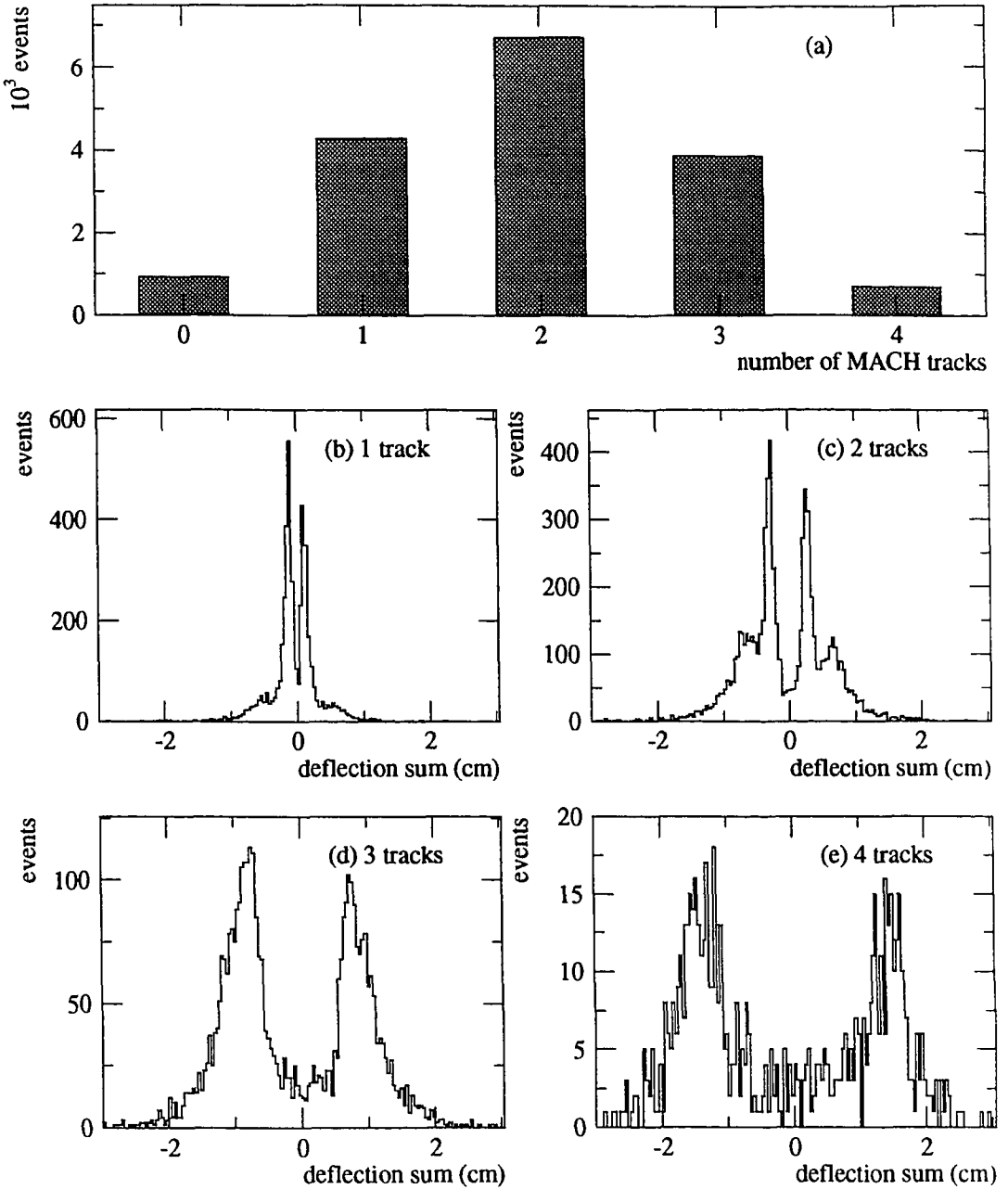

Figure 5.22: Final BID distributions of (a) number of candidate MACH tracks for $\overline{p}p \to \overline{\Lambda}\Lambda$ and $\overline{p}p \to \overline{\Lambda}\Sigma^0 + c.c.$ events and the MACH deflection sum W for events with (b) 1, (c) 2, (d) 3, and (e) 4 good MACH tracks.

analysis task	quality cut	number cut
Target Analysis	good target pattern	
Hodoscope Analysis		$2 \leq \#\ x$ hits≤ 20 and $2 \leq \#\ y$ hits≤ 20
DC coordinates		$3 \leq \#\ x$ hits ≤ 70 and $3 \leq \#\ y$ hits ≤ 70
2D Tracking	track road width $= 4\sigma$	$1 \leq \#\ x$ tracks ≤ 20 and $1 \leq \#\ y$ tracks ≤ 20
3D Tracking	track slope tolerance $= 3.5\sigma$ track coord tolerance $= 3.5\sigma$	$2 \leq \#$ 3D tracks ≤ 30
Vertex Recognition	$\|\text{DCA}\| \leq 5\sigma$ $\|\text{VTD}\| \leq 1.5$ cm PCA in cone of acceptance $0.2 \leq p_\Lambda \leq 1.7$ GeV/c	$2 \leq \#$ vertices ≤ 20
Vertex Pairing	$\|\sum p_x\| \leq 0.15$ GeV/c $\|\sum p_y\| \leq 0.15$ GeV/c $\|\sum p_z\| \leq 0.35$ GeV/c	$1 \leq \#$ vertex pairs ≤ 20
Kinematic Fit	best-fit $X^2 \leq 25$	
Baryon ID	$\|W\| \geq 0.05$ cm	

Table 5.5: Analysis cut summary.

After all analysis, the 1729 MeV/c data yielded 10451 $\bar{p}p \rightarrow \overline{\Lambda}\Lambda$, 1522 $\bar{p}p \rightarrow \overline{\Sigma^0}\Lambda$, and 1757 $\bar{p}p \rightarrow \overline{\Lambda}\Sigma^0$ events. A representative $\bar{p}p \rightarrow \overline{\Lambda}\Lambda$ event that passed all cuts is shown in Fig. 5.23 and an event that was determined to be a $\bar{p}p \rightarrow \overline{\Sigma^0}\Lambda$ is shown in Fig. 5.24.

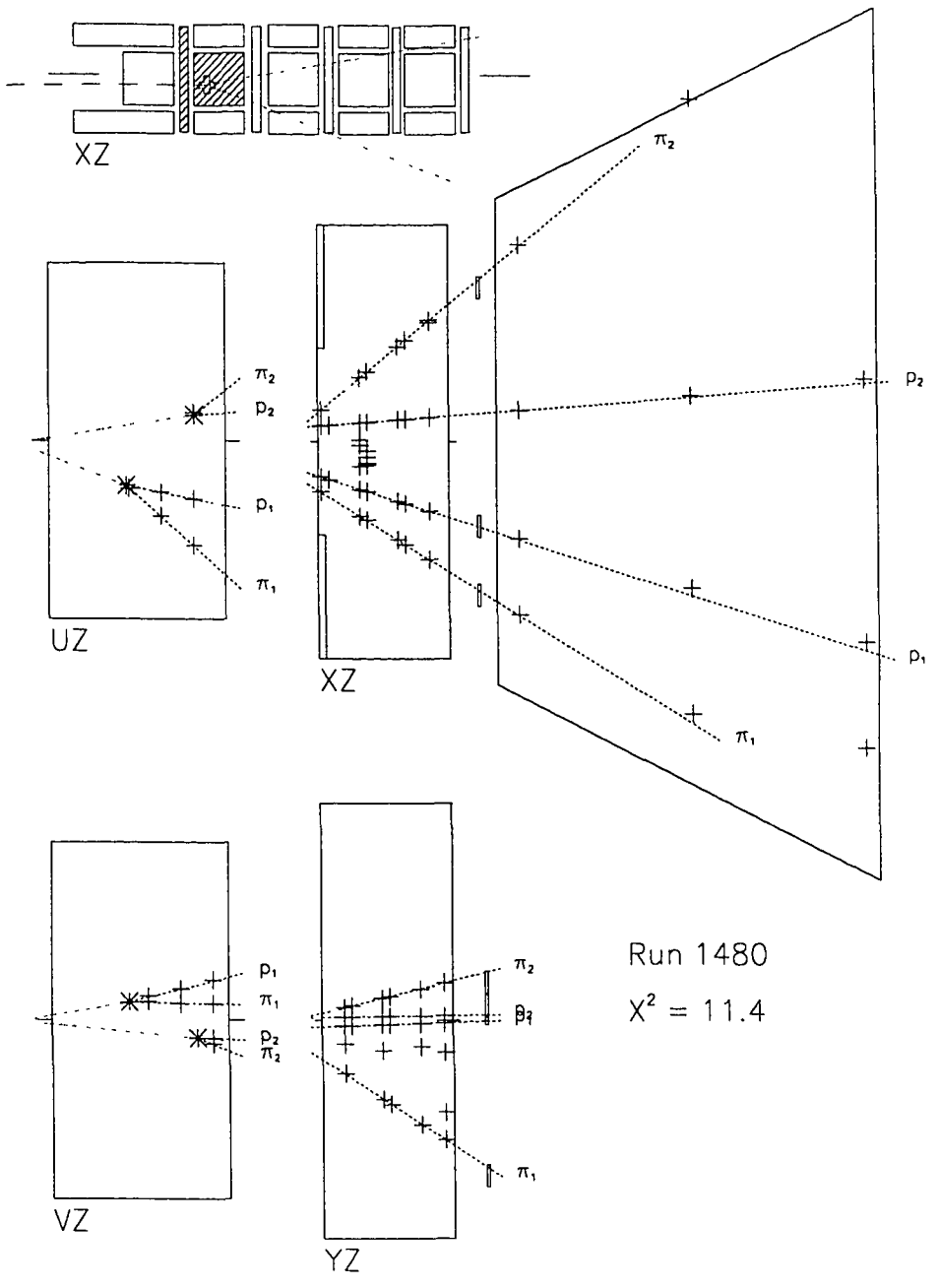

Figure 5.23: An event display plot of an event that was determined to be a $\overline{p}p \rightarrow \overline{\Lambda}\Lambda$. The tracks drawn are those resulting from the kinematic fit and do not indicate the deflection in the magnetic field.

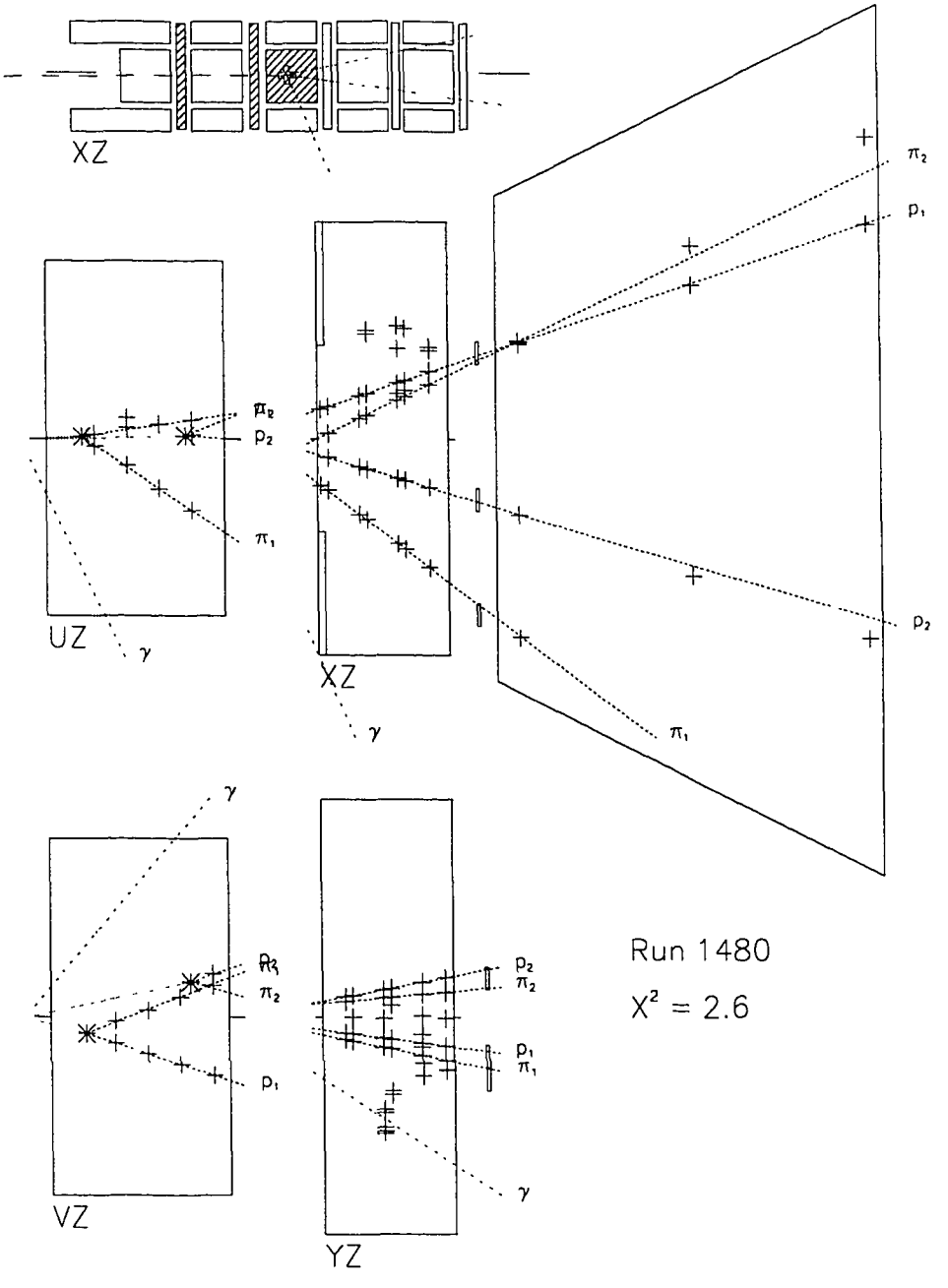

Figure 5.24: An event display plot of an event that was determined to be a $\overline{p}p \rightarrow \overline{\Sigma}^0\Lambda$. The tracks drawn are those resulting from the kinematic fit and do not indicate the deflection in the magnetic field.

5.12 Acceptance Calculation

After the $\bar{p}p \rightarrow \overline{\Lambda}\Lambda$ and $\bar{p}p \rightarrow \overline{\Sigma}^0\Lambda + c.c.$ events have been extracted from the data, the next task is to calculate the acceptance of the detector. The detector acceptance is the fraction of the total events that are successfully reconstructed in the detector. This fraction must be known as a function of several different kinematic variables to enable the calculation of the observables. In addition, the number of $\bar{p}p \rightarrow \overline{\Lambda}\Lambda$ events reconstructed as $\bar{p}p \rightarrow \overline{\Sigma}^0\Lambda + c.c.$ events and vice versa must be determined because this effects the detector acceptance as well. The GEANT Monte Carlo package [101] is a valuable tool to help with the acceptance calculation by providing an accurate simulation of the detector and the interactions of particles in it.

5.12.1 The GEANT Monte Carlo

A description of each subdetector of the PS185 experimental apparatus was entered into the simulation program [102] using the routines provided by the GEANT package [101]. This description includes the position in space, the shape, and the detector material. All parts of the detector, including supports and frames, that could conceivably be important through their effects on particle trajectories were entered. The picture shown in Chapter 4, Fig. 4.6, used to illustrate the detector, is actually the apparatus as described in the Monte Carlo program.

Each of the $\bar{p}p \rightarrow \overline{Y}Y$ reactions is simulated in full detail. The incident antiproton is generated 30 cm upstream of the target, just before the beam pipe beryllium exit window, with a direction vector chosen to yield the same distributions in the microstrip detectors as was measured in the experiment. This particle is then transported ("tracked") by the program downstream to the target until it reaches the point in one of the target cells where the reaction is to take place. This point is chosen by picking a z position randomly and uniformly within an interval given by the edges of the target array. The $\overline{\Lambda}\Lambda$, $\overline{\Sigma}^0\Lambda$, or $\overline{\Lambda}\Sigma^0$ reaction products are then generated

at this point with kinematics dictated by the momentum of the beam antiproton at the point it was stopped. During the tracking of the incident antiproton, energy loss and multiple scattering are considered. By generating the reactions in this way, a realistic simulation of the momentum and direction of the incident antiproton at the point of interaction is obtained.

The hyperons produced in the target are tracked by GEANT through the detector. The lifetimes are taken into account and the particle decays are simulated. Multiple scattering, energy loss, and interactions with the matter in the detector are also considered. Any secondary particles that would be produced in these decays or interactions are generated and tracked as well. Each particle is tracked until it decays, stops, or leaves the detector volume. As the particles are tracked through the active detectors, the details of the track are recorded so that a realistic approximation of the detector response may be generated. For efficient simulation, only the charged decay branch of the Λ and $\overline{\Lambda}$ was considered.

At the end of each event, when all particles, including the secondaries, have been tracked to completion, the recorded track information is used to produce the simulated detector response. The ADC values for the scintillator and silicon detectors are generated by multiplying the recorded energy loss in each detector by a conversion constant chosen such that the ADC distributions from the Monte Carlo approximate those from the experiment. The corresponding TDC values are generated by multiplying the Monte Carlo time of flight value by a conversion constant, also chosen so that the TDC distributions approximate those of the experiment. The intrinsic efficiency of these scintillator and silicon detectors needs no special treatment. It is accounted for in the accurate modeling of the energy loss. The geometric efficiency is correctly determined by positioning all detectors, including gaps and holes, as they were in the experiment. This scheme is adequate for the target, microstrip, hodoscope, and calorimeter detectors.

The process of converting the tracking chamber information to readout and mod-

eling the efficiency is somewhat more complicated. The physical processes involved with the drift of ionization charge from a charged particle passing through the proportional or drift chamber are not simulated in full. Instead, the behavior is parameterized and this parameterization is used to produce the hits from the track information. For the drift chamber, the time to distance function that was determined from the data is inverted and used to produce a drift time from the track coordinate. The measurement error of the chamber is simulated by adding a random offset to the data in accordance with the resolution function measured in the experiment. For the proportional chamber, the output addresses are calculated from the individual wires cells that were crossed by each track. The geometric efficiency for both of these tracking chambers is accounted for, as for the more simple detectors, through the accurate detector description and positioning. The intrinsic efficiency is simulated using a function that calculates the detection probability of the particle given the track parameters. The parameterization of these efficiency functions was determined from the experimental data and is described in Appendix B.

The data as generated with the Monte Carlo program is encoded exactly as the data from the experiment so that it can be read and analyzed with the data analysis program. A list of Monte Carlo words which consists the kinematic variables of the generated event, is added to the data so that the event as reconstructed by the analysis program can be compared with the event as generated.

The detector acceptance was determined by generating events with the Monte Carlo simulation and analyzing them with the analysis program using the same cuts that were used for the experimental data. Almost all of the different things that can cause the loss of an event are accounted at one time with the use of this accurate simulation program. Only a few additional corrections that are beyond the scope of the Monte Carlo will need to be added to calculate the cross sections.

The adequacy of the Monte Carlo program to simulate the experiment was checked by examining various quantities calculated with the analysis program using Monte

Carlo data and verifying they are distributed as with the experimental data. With two exceptions discussed in Sec. 5.12.3, the quantities examined passed this test. Three of these quantities, the best-fit least-squares sum from the kinematic fit for the three $\overline{p}p \rightarrow \overline{Y}Y$ channels, from both Monte Carlo and experimental data are shown in Fig. 5.25. These verify that the simulation is reproducing the experimental data accurately.

5.12.2 The Acceptance Matrix

The goal of the acceptance calculation is to obtain, for each $\overline{p}p \rightarrow \overline{Y}Y$ reaction channel, the detector acceptance as a function of $\cos\theta^*$, where θ^* is the c.m. scattering angle. A naive calculation would simply take the number of Monte Carlo events accepted from each reaction channel in each $\cos\theta^*$ bin and divide by the generated number of events from this reaction channel and $\cos\theta^*$ bin to obtain the acceptance. Unfortunately, this would not correctly account for the events that are reconstructed with an incorrect value of $\cos\theta^*$ or are improperly identified (e.g. $\overline{p}p \rightarrow \overline{\Lambda}\Lambda$ event identified as a $\overline{p}p \rightarrow \overline{\Lambda}\Sigma^0$ event). To account for these problems the *measured* angular distribution and cross section values must be considered. To do this, the acceptance matrix method [103] is used.

The acceptance matrix method allows the acceptance to be calculated while correcting for event type misidentification and incorrect reconstruction of $\cos\theta^*$. The acceptance matrix[2] C is defined,

$$C_{ijkl} \equiv \frac{\#\text{ reconstructed in bin } i, \text{channel } k;\ \text{generated in bin } j, \text{channel } l}{\text{total } \#\text{ generated in bin } j, \text{channel } l}, \quad (5.13)$$

where "bin" refers to a $\cos\theta^*$ bin and "channel" refers to one of the three $\overline{p}p \rightarrow \overline{Y}Y$ reaction channels. The analysis of Monte Carlo events was employed to calculate the elements of C.

[2]Actually, in this formulation, C is a tensor.

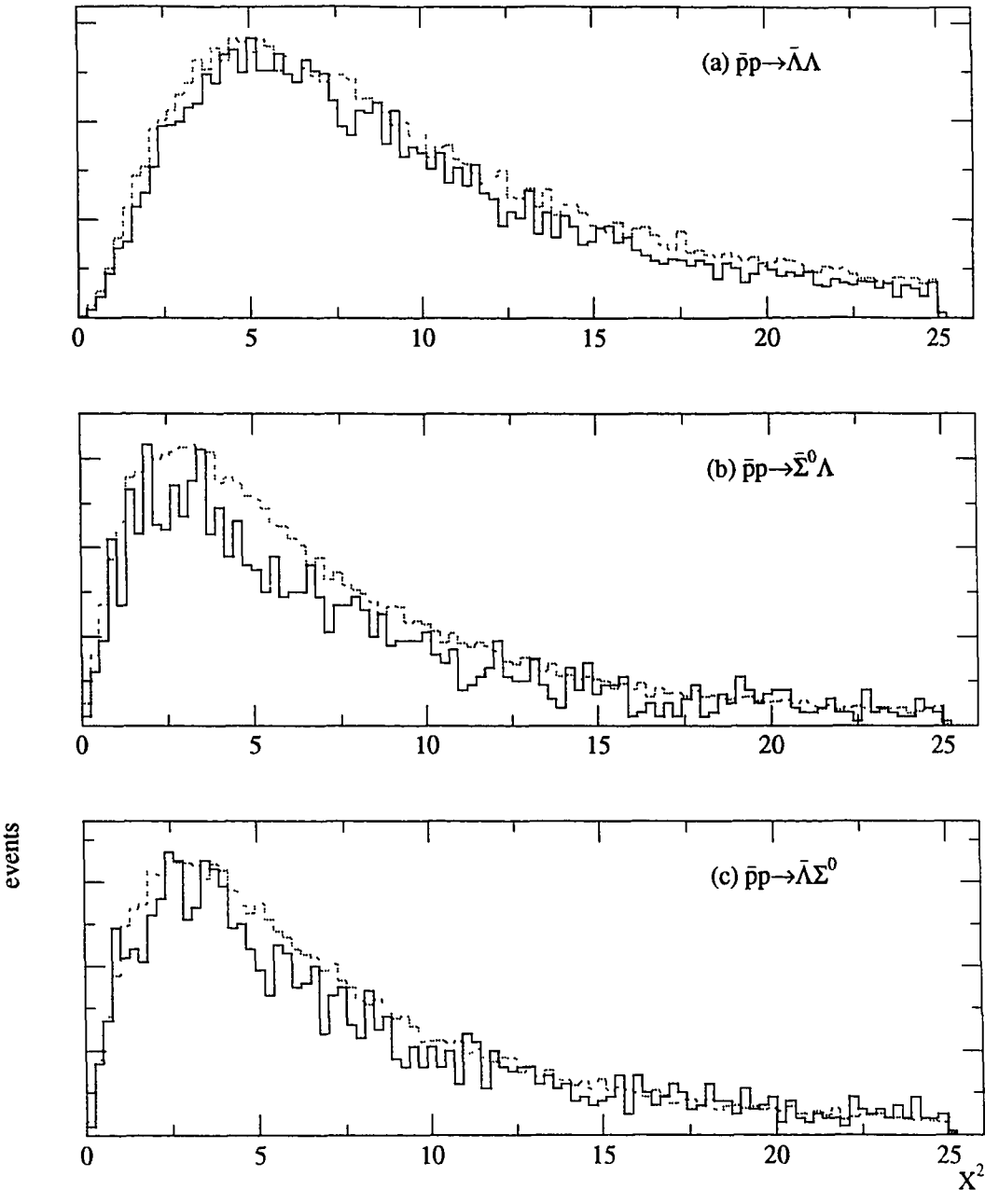

Figure 5.25: The best-fit least-squares sum distribution from the kinematic fit for the three $\overline{p}p \to \overline{Y}Y$ channels. The dotted line is that from Monte Carlo data, the solid is from the experimental data. The two distributions of each plot are normalized to the bin with the largest number of counts.

The number of experimental events reconstructed from the data in each $\cos\theta^*$ bin and reaction channel is given by

$$p_{ik} = \sum_{j,l} r_{jl} C_{ijkl}, \tag{5.14}$$

where p_{ik} is the number of events reconstructed in bin i, channel k and r_{jl} is the number of "true" events that where produced in bin j, channel l. The index j runs over the number of $\cos\theta^*$ bins and l runs over the number of reaction channels.

The obvious way to proceed would be to solve the system of equations implied by Eq. 5.14 for the true number of events, r_{jl}, using the Monte Carlo analysis to calculate the C_{ijkl}. Unfortunately this is an example of an "ill-posed problem" [104] and is not so easily done. The statistical errors present in the p_{ik} are strongly amplified in the inversion process, which results in solutions for the r_{jl} with unreasonably large errors. To circumvent this problem, a method of regularization [104] is used.

First, Eq. 5.14 is rewritten as

$$p_{ik} = r_{ik}\left(C_{iikk} + \sum_{j\neq i, l\neq k} \frac{r_{jl}}{r_{ik}} C_{ijkl}\right). \tag{5.15}$$

Then, the r_{ik} are solved for iteratively. For the nth iteration,

$$r_{ik}^{(n)} = \frac{p_{ik}}{A_{ik}^{(n)}}, \tag{5.16}$$

with

$$A_{ik}^{(n)} \equiv \left(C_{iikk} + \sum_{j\neq i, l\neq k} \frac{r_{jl}'^{(n-1)}}{r_{ik}'^{(n-1)}} C_{ijkl}\right). \tag{5.17}$$

The regularized solutions from the $(n-1)$th iteration, $r_{ik}'^{(n-1)}$, have been introduced to avoid the ill-posed problem. These regularized solutions are obtained by fitting the r_{ik} of the $(n-1)$th iteration to a Legendre polynomial over $\cos\theta^*$ and using the values of the fit, r'_{ik}, to obtain the values for the A_{ik} for the nth iteration. This, in effect, smooths the statistical fluctuations for the acceptance calculation. It should

be noted that the actual data is not smoothed, only the corrections. This process is repeated until the values for the A_{ik} have converged. The convergence criterion is

$$\sum_{i,k} \left(A_{ik}^{(n)} - A_{ik}^{(n-1)} \right) < 0.005, \tag{5.18}$$

and, for this data set, this criterion was satisfied after 8 iterations.

Each A_{ik}, from the final iteration, is the calculated acceptance for the ith $\cos\theta^*$ bin and kth reaction channel. If the acceptance matrix was diagonal (no misidentification of $\cos\theta^*$ or reaction channel), the acceptance would reduce to the naive formulation, $A_{ik} = C_{iikk}$. The actual calculated acceptance for bin i, channel k has an additional term due to events reconstructed in this bin and channel but generated in other bins and channels. This is the significance of the second term in Eq. 5.17. The final values of the A_{ik} may then be used, through Eq. 5.16 to calculate the number of events, corrected for detector acceptance.

For the acceptance calculations, 850k Monte Carlo events were generated for each $\overline{p}p \to \overline{Y}Y$ channel considered. They were generated with a forward-peaked $\cos\theta^*$ so that there were more Monte Carlo events and smaller statistical error in the $\cos\theta^*$ region where more experimental events were expected.

The fraction of Monte Carlo events accepted for each reaction channel, generated and reconstructed, is listed in Table 5.6. The fraction of accepted events that are reconstructed with the correct reaction channel is around 11.5% for all channels. There is a small fraction of $\overline{\Lambda}\Lambda$ events[3] that are reconstructed as $\overline{\Sigma}^0\Lambda$ or $\overline{\Lambda}\Sigma^0$ events and a negligible number of events generated as $\overline{\Sigma}^0\Lambda$ or $\overline{\Lambda}\Sigma^0$ and reconstructed as $\overline{\Lambda}\Lambda$. There is, however, an appreciable number of $\overline{\Sigma}^0\Lambda$ and $\overline{\Lambda}\Sigma^0$ events reconstructed as the charge conjugate event. Approximately 20% of the $\overline{\Sigma}^0\Lambda$ or $\overline{\Lambda}\Sigma^0$ events that are reconstructed are assigned to the charge conjugate channel.

The acceptance matrix as calculated with the Monte Carlo events that passed

[3]For the remainder of this section, the writing of the initial state is suppressed when indicating a $\overline{p}p \to \overline{Y}Y$ reaction channel.

Reconstructed reaction channel	Generated reaction channel		
	$\bar{p}p \to \overline{\Lambda}\Lambda$	$\bar{p}p \to \overline{\Sigma}^0\Lambda$	$\bar{p}p \to \overline{\Lambda}\Sigma^0$
$\bar{p}p \to \overline{\Lambda}\Lambda$	0.1168	$2. \times 10^{-5}$	$3. \times 10^{-5}$
$\bar{p}p \to \overline{\Sigma}^0\Lambda$	0.0006	0.1150	0.0316
$\bar{p}p \to \overline{\Lambda}\Sigma^0$	0.0012	0.0358	0.1174

Table 5.6: Fraction of Monte Carlo events passing the analysis cuts for each generated and reconstructed $\bar{p}p \to \overline{Y}Y$ reaction channel.

all cuts is illustrated in Fig. 5.26. The bands at $\cos\theta^*_{\rm rec} \approx \cos\theta^*_{\rm gen}$ in the plots on the diagonal (Figs. 5.26(a),5.26(e), and 5.26(i)) are due to those events that are reconstructed with the correct $\cos\theta^*$ and the correct reaction channel identification. The other structures in the plots indicate how $\cos\theta^*$ is incorrectly assigned if the event is reconstructed incorrectly. There are two possible independent errors that may contribute to reconstruct an event incorrectly.

1 The reconstructed kinematics are wrong. The kinematic fit forces the kinematics to obey one of the three event hypotheses; if the input measurements are somehow corrupted, it is possible that the event hypotheses that best fits the event is incorrect.

2 The baryon identification is wrong. If this occurs, the Λ vertex is assigned to the $\overline{\Lambda}$ and vice versa.

These two errors conspire to yield the incorrect reaction channel and/or $\cos\theta^*$ value for a fraction of the events. If an error of type 1 occurs a $\overline{\Lambda}\Lambda$ event may be reconstructed as a $\overline{\Sigma}^0\Lambda$ or $\overline{\Lambda}\Sigma^0$ and vice versa. This type of event is seen in Figs. 5.26(b), 5.26(c), 5.26(d), and 5.26(g). This error may also cause $\overline{\Sigma}^0\Lambda$ events to be reconstructed as $\overline{\Lambda}\Sigma^0$ and vice versa. This type of error occurs when the wrong vertex is assigned as the Σ-decay Λ. These events are seen as the wide bands along $\cos\theta^*_{\rm rec} = \cos\theta^*_{\rm gen}$ in Figs. 5.26(f) and 5.26(h). Error type 1 is most likely to occur

at $|\cos\theta^*| \approx 1$ where the kinematics of the Λ decay are less precisely determined by the lab angles of the decay products.

If an error of type 2 occurs in the $\overline{\Lambda}\Lambda$ channel, the event is reconstructed as a $\overline{\Lambda}\Lambda$ but with $\cos\theta^*_{\rm rec} \approx -\cos\theta^*_{\rm gen}$. This type of event causes the narrow band along $\cos\theta^*_{\rm rec} = -\cos\theta^*_{\rm gen}$ in Fig. 5.26(a). If this type of error occurs in the $\overline{\Sigma}^0\Lambda$ or $\overline{\Lambda}\Sigma^0$ channel, the event is incorrectly assigned to the charge conjugate channel *and* $\cos\theta^*_{\rm rec} \approx -\cos\theta^*_{\rm gen}$. This type of event may be seen in the narrow bands of Figs. 5.26(f) and 5.26(h) along $\cos\theta^*_{\rm rec} = -\cos\theta^*_{\rm gen}$. An error of type 2 may occur with approximately equal probability in $\cos\theta^*$.

If the errors of type 1 and 2 occur in the same event for the $\overline{\Sigma}^0\Lambda$ and $\overline{\Lambda}\Sigma^0$ channels, the reconstructed reaction channel is correct but $\cos\theta^*$ is reconstructed incorrectly. These type of events contribute to the additional events seen in Figs. 5.26(e) and 5.26(i) *not* along $\cos\theta^*_{\rm rec} = \cos\theta^*_{\rm gen}$.

The acceptance matrix is determined from the fraction of incorrectly reconstructed *Monte Carlo* events. To determine the fraction of incorrectly reconstructed *experimental* events and the experimental acceptance, the iterative procedure described above is employed. The calculated fraction of incorrectly identified events in the experimental data as a function of $\cos\theta^*$ for the $\overline{\Sigma}^0\Lambda$ and $\overline{\Lambda}\Sigma^0$ channels is shown in Fig. 5.27. The contribution of $\overline{\Lambda}\Lambda$ contamination in the $\overline{\Sigma}^0\Lambda$ and $\overline{\Lambda}\Sigma^0$ channels is sizeable because, even though the fraction of the $\overline{\Lambda}\Lambda$ events feeding through is small, the $\overline{\Lambda}\Lambda$ cross section is approximately 10 times larger than that of $\overline{\Sigma}^0\Lambda$ or $\overline{\Lambda}\Sigma^0$. The fraction of events feeding through from the $\overline{\Sigma}^0\Lambda$ and $\overline{\Lambda}\Sigma^0$ channels into the $\overline{\Lambda}\Lambda$ channel is negligible and not shown.

The calculated acceptance for each reaction channel, as defined in Eq. 5.17, as a function of $\cos\theta^*$, is shown in Fig. 5.28. The errors are statistical only. The falloff at $\cos\theta^* \approx \pm 1$ in the acceptance for $\overline{\Lambda}\Lambda$ is due to drift chamber inefficiency along the beam axis. It is not seen in the $\overline{\Sigma}^0\Lambda$ and $\overline{\Lambda}\Sigma^0$ channels because the lab polar angle distributions of protons from the Λ decays in these reactions are not so forward

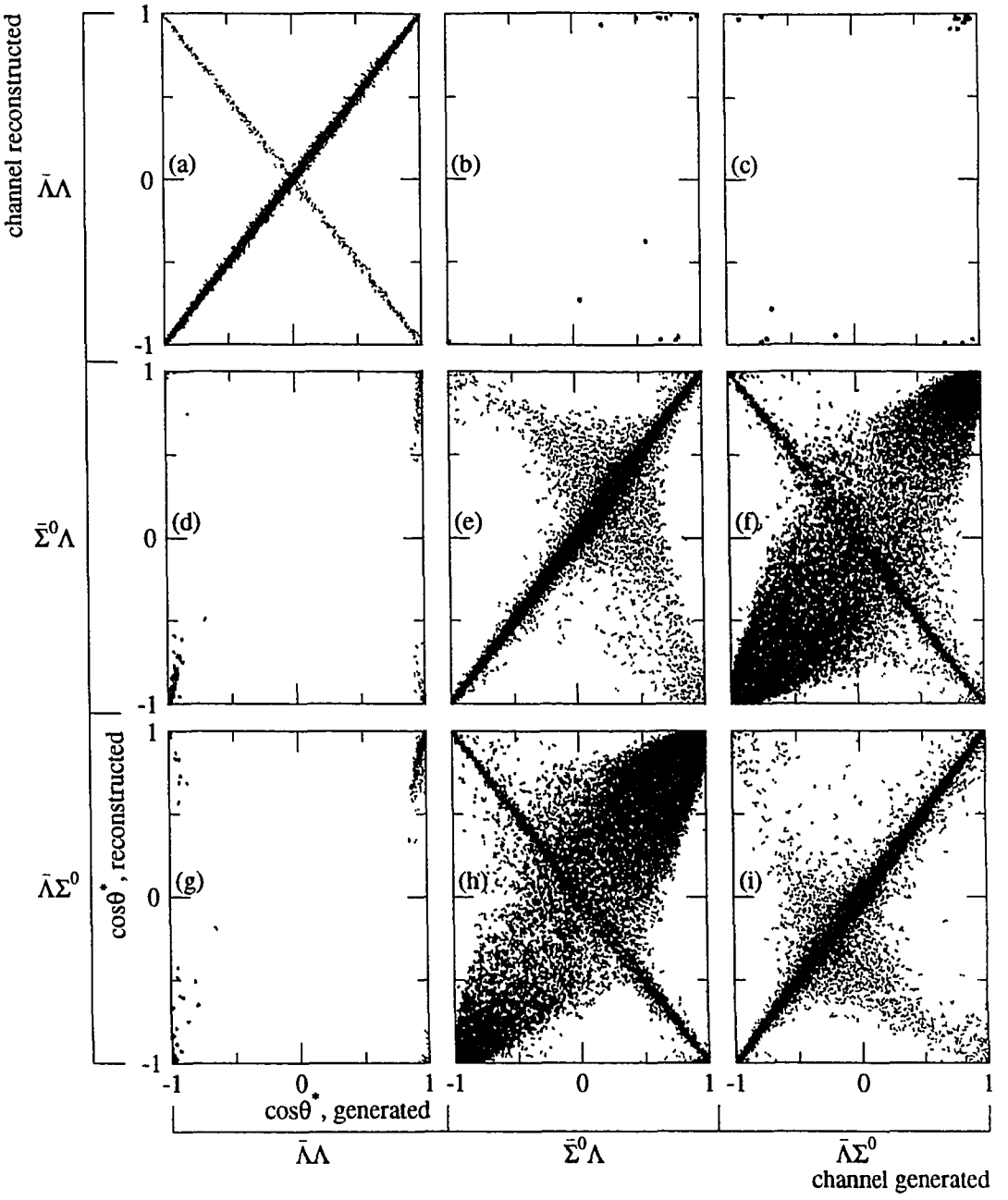

Figure 5.26: Scatter plots showing the acceptance matrix as calculated with Monte Carlo events. The density of the points is proportional to the size of the matrix element. Each row of plots corresponds to a $\overline{p}p \rightarrow \overline{Y}Y$ reaction channel generated, each column to a channel reconstructed. The individual plots show $\cos\theta^*$ generated vs $\cos\theta^*$ reconstructed.

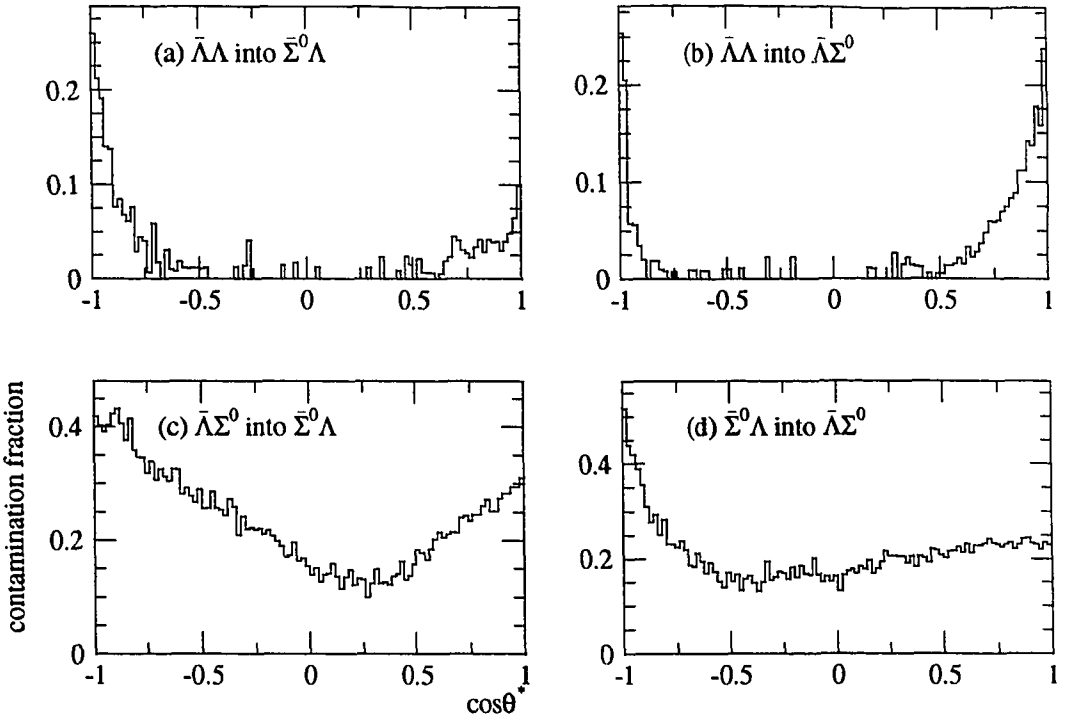

Figure 5.27: Estimated fraction of contamination in experimental data from other reaction channels in the measured $\overline{\Sigma}^0\Lambda$ and $\overline{\Lambda}\Sigma^0$ channels as a function of $\cos\theta^*$.

peaked. The peaking of the acceptance function of the $\overline{\Sigma}^0\Lambda$ and $\overline{\Lambda}\Sigma^0$ channels at $\cos\theta^* \approx -1$ is due to the large contamination from other events with $\cos\theta^* \approx +1$ that are reconstructed with $\cos\theta^* \approx -1$.

5.12.3 Additional Acceptance Function Corrections

The Monte Carlo simulation, detailed as it was, proved to be slightly inadequate to calculate the full acceptance function due to the inadequacy of the determination of drift chamber efficiency functions. Two additions were required to obtain the final acceptance.

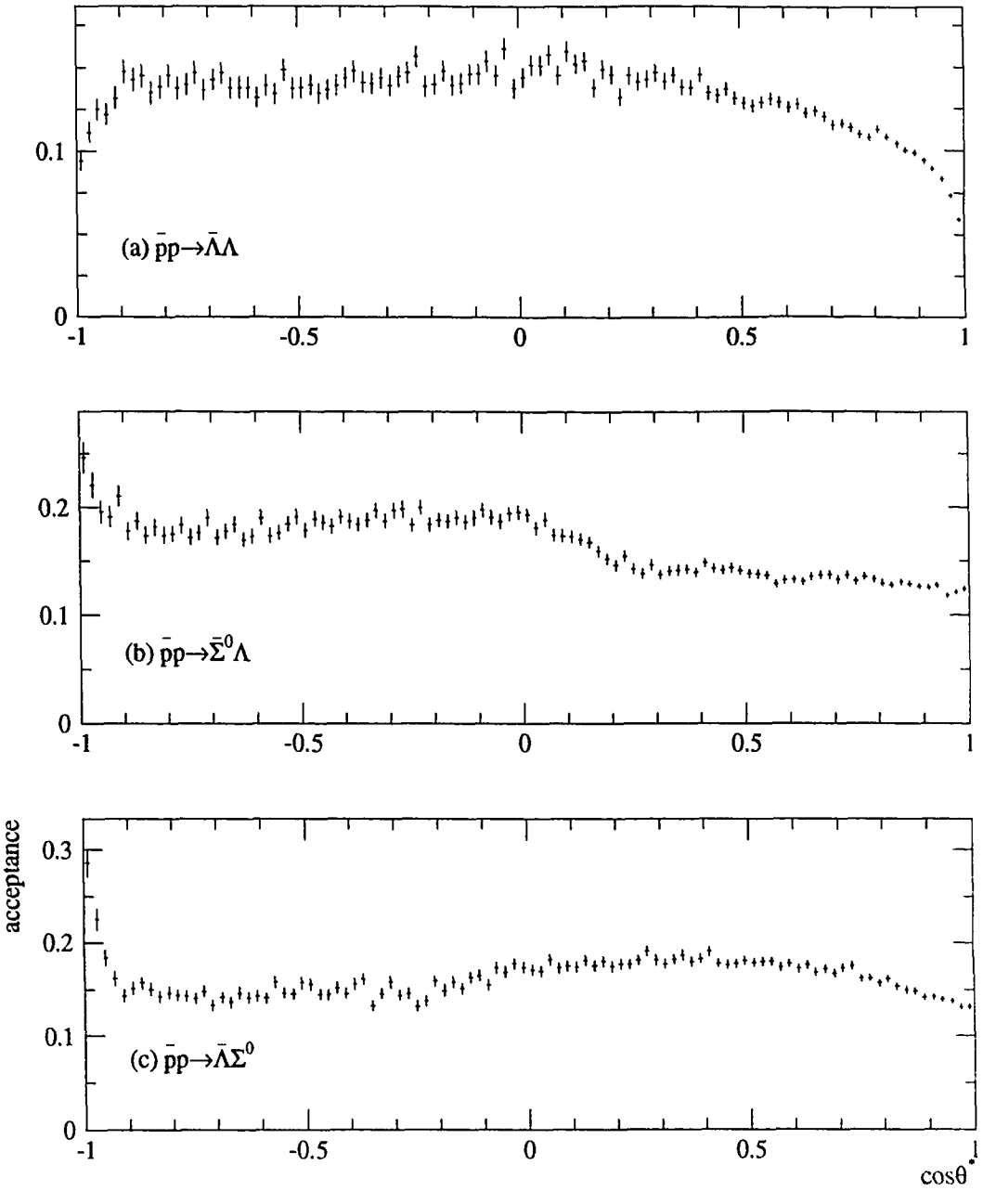

Figure 5.28: The acceptance as determined from the iterative procedure for each reaction channel as a function of $\cos\theta^*$. The errors are statistical only.

Additional Drift Chamber Dead Spot Correction

Due to inadequately known drift chamber efficiencies near the beam axis (the chamber desensitized region), the acceptance function required a modification for the $\overline{\Lambda}\Lambda$ channel. The kinematics of this reaction are such that, for events with $\cos\theta^* \approx \pm 1$, the Λ-decay protons are emitted quite frequently in a direction nearly coincident with the beam. Because of this the correct modeling of the desensitized region of the chamber is crucial to provide the correct acceptance. This problem was negligible for the $\overline{\Sigma}^0\Lambda, \overline{\Lambda}\Sigma^0$ channels because they involve lower momentum Λ's for which the decay proton angles are not so forward peaked.

The actual efficiency of the chambers near the beam axis is more complicated than described in the Monte Carlo. The additional correction needed to account for this for the $\overline{\Lambda}\Lambda$ reaction was estimated by examining the proton laboratory ϕ distributions for events with $|\cos\theta^*| \geq 0.9$. The difference in this distribution between experimental and Monte Carlo events allowed an estimate of the effect of the additional inefficiency on the acceptance. This resulted in an additional acceptance term, symmetric in $\cos\theta^*$, that smoothly varied from 1.0 at $|\cos\theta^*| = 0.9$ to 0.87 at $|\cos\theta^*| = 1.0$. The systematic error on this correction due to the uncertainty in the method was estimated to be 5% of the size of the correction.

Additional Baryon Identification Correction

The acceptance due to the baryon identification also required refinement from that calculated by the Monte Carlo. This was due to an incomplete knowledge of the efficiency of the drift chambers in the magnetic solenoid. The additional correction was obtained by examining the fraction of events as a function of $\cos\theta^*$ that included a successful baryon identification for Monte Carlo events and comparing with that fraction obtained from the experimental data. The difference between the two samples was used to calculate the additional correction needed to account for the

complete baryon identification acceptance. The correction resulted in an additional term, approximately constant with $\cos\theta^*$, that reduced the acceptance by $\approx 1\%$ for the $\overline{\Lambda}\Lambda$ channel and $\approx 2\%$ for the $\overline{\Sigma}^0\Lambda$ and $\overline{\Lambda}\Sigma^0$ channels.

Combining these two additions with the acceptance as calculated from the Monte Carlo yielded the final acceptance function used for the remainder of the analysis.

5.13 Calculation of the Cross Section

In order to calculate the total and differential cross sections, two numbers are needed: the number of events that occurred and the integrated luminosity. The first, the number of events that occurred, is determined from the number of reconstructed events and the acceptance for these events. The second, the integrated luminosity is determined from the count of antiprotons incident on target and the target proton density.

The acceptance function described in the previous section is only part of the acceptance needed to calculate the number of events that occurred. There are several other effects, not addressed by the Monte Carlo that need to included. However these additions do not effect the angular behavior of the acceptance; they are simply overall multiplicative factors. However, unlike the Monte Carlo acceptance, they do depend on the individual target cell of the interaction. For this reason they are calculated along with the integrated luminosity, which also varies among the target cells.

Because of the target cell dependence of these quantities, the cross section is calculated independently for each target cell. For this data set, at an antiproton momentum of 1.729 GeV/c which is relatively far from threshold, there is little interest in the behavior of the cross section across the small momentum steps of the target cells. So, after checking that the behavior with target cell is reasonable, the cross section values from each target cell are combined to form the results at the average momentum point.

5.13.1 Accepted and Corrected Event Distributions

The number of events from the experimental sample passing the analysis cuts for each $\overline{p}p \rightarrow \overline{Y}Y$ channel (the accepted event sample) and target cell are histogrammed in Fig. 5.29. The number of events passing all cuts is lower for the carbon cell (target cell 1) because events produced on carbon are less likely to satisfy the two body kinematics imposed by the kinematic fitter and vertex pair cuts. There is a larger fraction of $\overline{\Sigma}^0\Lambda$ and $\overline{\Lambda}\Sigma^0$ events accepted from the carbon cell because the kinematics are not so well constrained in these reactions compared to the $\overline{\Lambda}\Lambda$.

The $\cos\theta^*$ distributions for the accepted event sample are shown in Fig. 5.30. The $\overline{\Lambda}\Lambda$ sample reflects the strong falloff in detector efficiency at $|\cos\theta^*| \approx 1$ for this reaction channel. The corrected $\cos\theta^*$ distributions for each target cell and reaction channel were calculated with the raw distributions and the final acceptance function. These distributions are shown, summed over target cells, in Fig. 5.31.

5.13.2 Integrated Luminosity

The integrated luminosity is the product of the total number of antiprotons incident on target and the total proton density. This may be expressed,

$$\mathcal{L} = N_{\overline{p}} \sum_i \Gamma_i; \qquad \Gamma_i = N_A \frac{n_i t_i \rho_i}{A_i}, \tag{5.19}$$

where $N_{\overline{p}}$ is the number of incident antiproton and Γ_i is the proton density for the ith material. The sum runs over the contributing materials and includes the target cylinder and a contribution from the two S3 scintillators that are adjacent to the target cylinder. Monte Carlo studies have determined that events occurring in the edges of these scintillators can satisfy the neutral trigger and be reconstructed as accepted events. They contribute to the target an amount of material equivalent to the thickness of one of the scintillators. It is assumed that the quantities contributing to the proton density are the same for each CH_2 target cell. These quantities are defined and their values and errors are listed in Tab. 5.7.

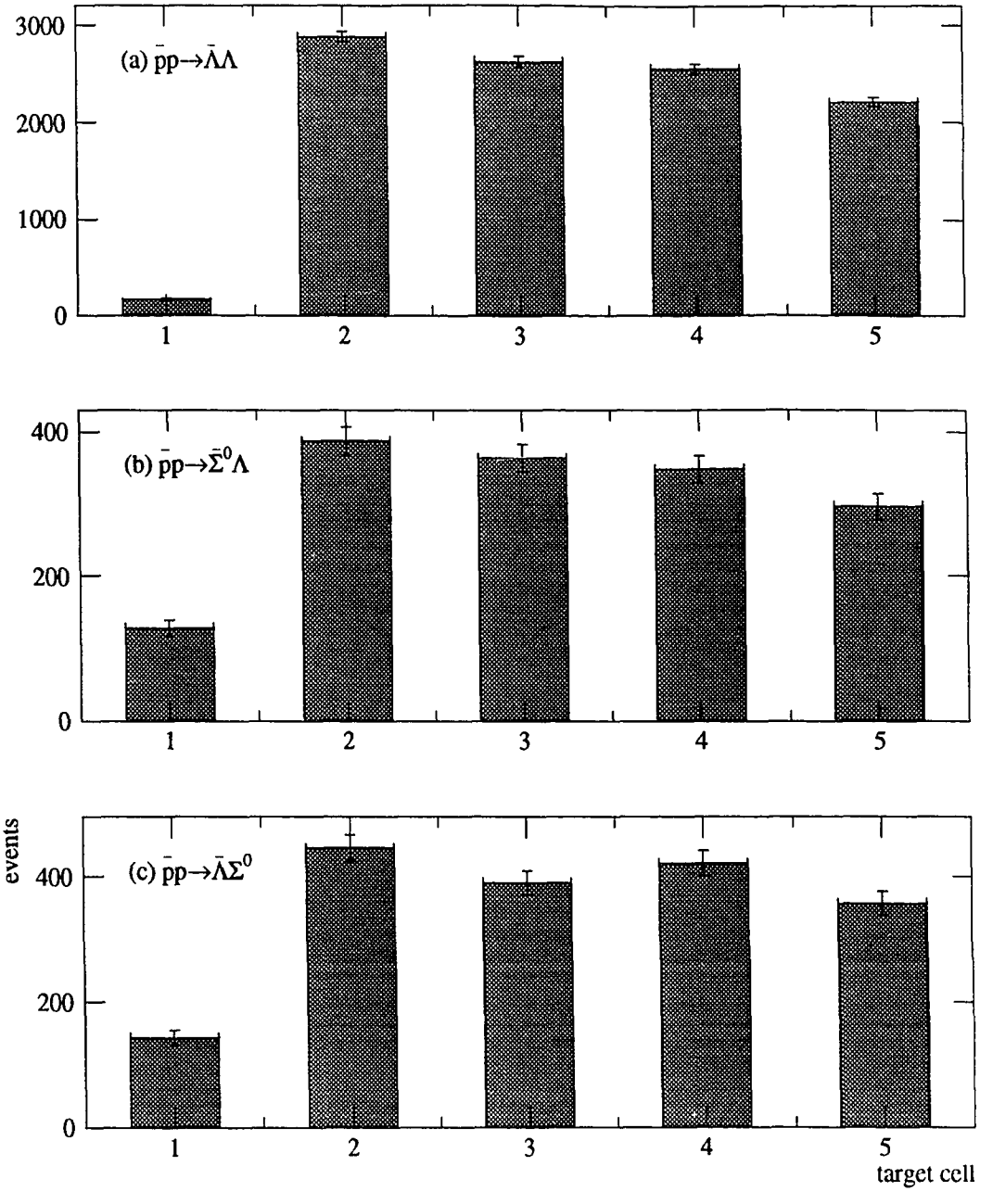

Figure 5.29: Number of accepted events as a function of target cell for each $\overline{p}p \to \overline{Y}Y$ reaction channel. The errors are statistical only.

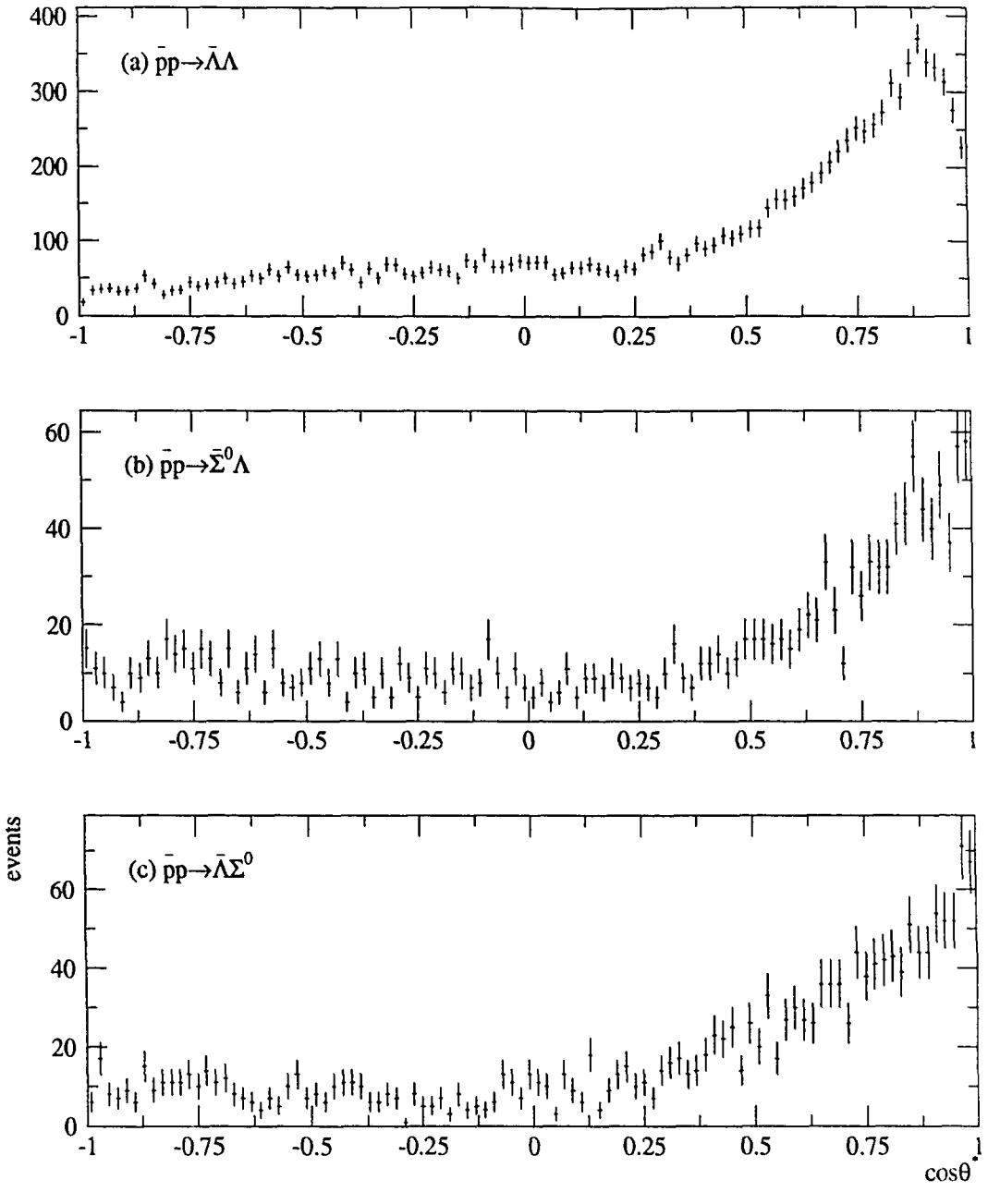

Figure 5.30: Distributions of $\cos\theta^*$ for accepted events for each reaction channel. The distributions contain events from all target cells. The errors are statistical only.

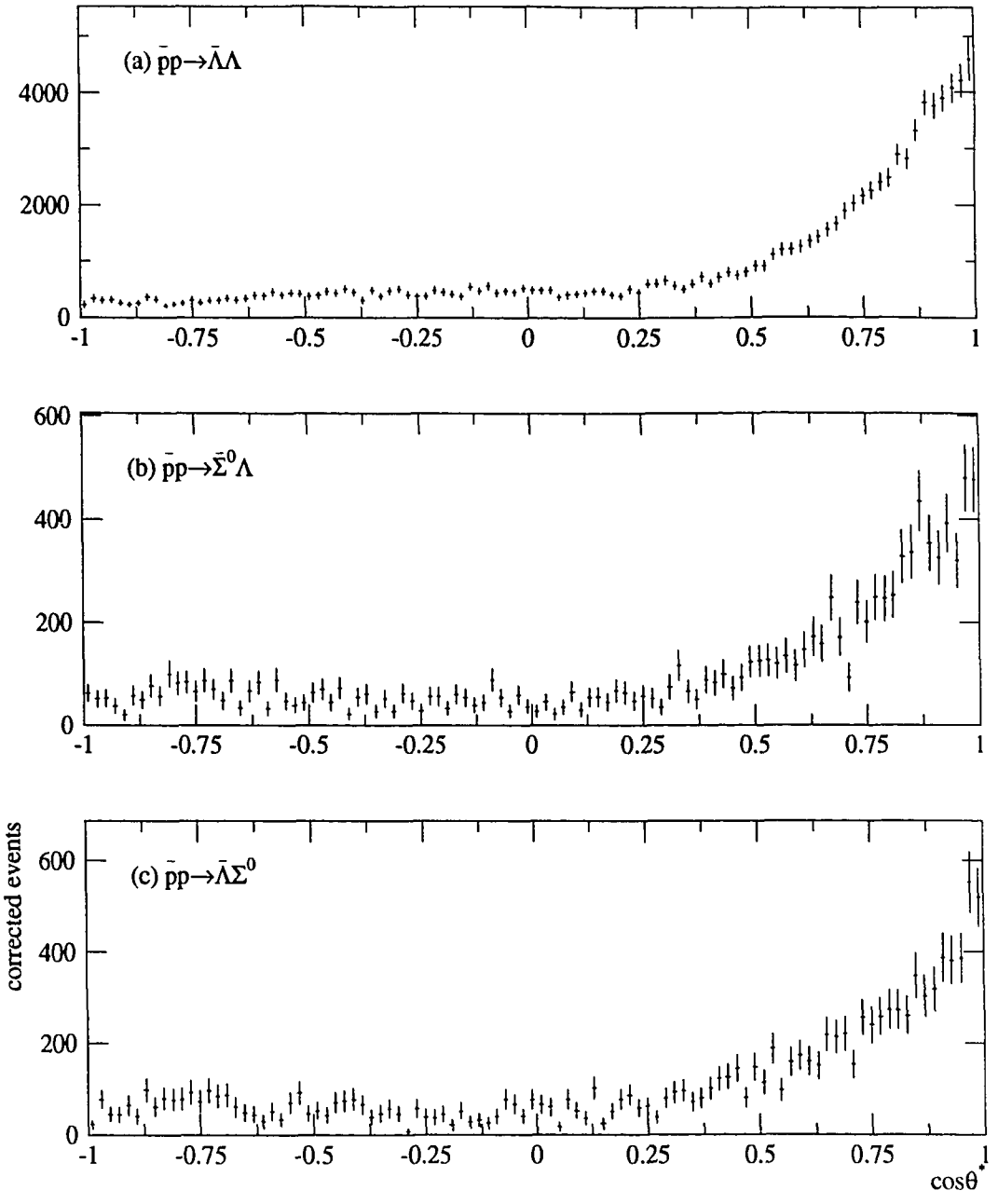

Figure 5.31: Distributions of $\cos\theta^*$ for corrected events for each reaction channel. The distributions contain events from all target cells. The errors are calculated from the statistics of accepted events and the contributions from the acceptance function.

quantity	target cylinder (CH_2)	scintillator ($CH_{1.1}$)
n_i - # of proton/molecule	2	1.1
t_i - thickness [cm]	0.2500 ± 0.0005	0.0200 ± 0.0002
ρ_i - density [g/cm^3]	0.916 ± 0.002	1.032 ± 0.002
A_i - molecular mass [g/mol]	14.016	13.11
N_A - Avogadro's number [1/mol]	6.022×10^{23}	
Γ_i - proton density [10^{-22}/cm^2]	1.9678 ± 0.0058	0.1043 ± 0.0011

Table 5.7: Values for the proton density calculation.

target cell	1	2	3	4	5
10^{10} antiprotons	6.2596	5.8909	5.6097	5.3402	5.0815
$\mathcal{L}$ [$10^3 \mu$barns^{-1}]	1.2971 $\pm$0.0037	1.2206 $\pm$0.035	1.1624 $\pm$0.0033	1.1065 $\pm$0.031	1.0529 $\pm$0.0030

Table 5.8: Number of antiprotons and resulting integrated luminosities for the 1.729 GeV/c data set.

The number of incident antiprotons was determined with the beam cell scalers (see Sec. 4.4.3). These scalers counted the number of antiprotons, incident on the target cell, that could result in a neutral event. The logic pattern of the target scintillators required to define a beam cell count for each target cell is listed in Table 4.9. By counting only those antiprotons that fulfilled these beam cell conditions, the flux losses in the target are correctly taken into account. These total number of antiprotons and the resulting integrated luminosities for each target cell are listed in Tab. 5.8. The error on the the integrated luminosity values is approximately 0.28% and is due to the uncertainty in target density and thickness.

5.13.3 Target Cell Acceptance Corrections

There are several angular-independent target cell-dependent acceptance corrections for the cross section calculation. These are gathered into a single factor for each target cell which may be expressed as

$$\mathcal{F}_i = \frac{F_{\mathrm{rate},i} F_{\mathrm{neut},i} F_{\mathrm{C},i}}{F_{\mathrm{BR}} F_{\delta\mathrm{ray},i}}. \tag{5.20}$$

The choice of whether to put these individual factors in the numerator or denominator is arbitrary and was made based on convenience. The calculation of each contribution is described in the following sections and listed in Table 5.9.

Charged Branching Ratio Fraction, F_{BR}

The Λ ($\overline{\Lambda}$) hyperons decay via $\Lambda \rightarrow p\pi^-$ ($\overline{\Lambda} \rightarrow \overline{p}\pi^+$) with a branching ration of $64.1 \pm 0.5\%$ [12]. The Monte Carlo simulation does not account for this as this branching ratio has been set to 100% for calculation efficiency. To take this into account, the cross section calculations must include a branching ratio correction, F_{BR}. This is set to 0.4109 ± 0.0064, the probability that both Λ's decayed via the charged branch.

Target δ ray Correction, $F_{\delta\mathrm{ray}}$

A neutral trigger event may be accompanied by a δ ray (a low energy electron) produced by the beam antiproton. If this δ ray causes the neutral trigger to be vetoed and does not veto the beam cell condition for that target cell, then the loss of this event should be corrected. This correction is not contained in the Monte Carlo acceptance because δ rays in the target were not simulated in the data to calculate acceptance. The δ ray correction was calculated for each target cell in a separate Monte Carlo study. This study showed that δ rays veto approximately 1% of the neutral triggers for all target cells.

Rate Dependent Correction, F_{rate}

The rate dependent correction consists of two separate corrections, the accidental S3 veto correction F_{S3} and the computer livetime correction F_{livetime}. Because these corrections are rate dependent, the product of the two must be integrated over the course of the run to obtain the total rate correction F_{rate}. This integral is approximated with a sum over the number of scaler reads, which were written to tape every minute.

The S3 veto correction is necessary because it is possible that an additional beam antiproton arrives at the target, fires the S3 counter within the time window allowed by the target electronics, and thereby vetoes a neutral trigger event. A rough calculation shows that the probability of this occurring is equal to the product of the time window of the S3 veto and the rate in the S3 counter. For this data set, the S3 veto time window was approximately 35 ns and the rate in the S3 counters was as high as 2 Mhz. With these numbers the probability to veto a neutral trigger with an accidental antiproton is 7%. To correct for this trigger inefficiency, the S3 veto correction is introduced. In practice, the details of the electronics and other effects makes the calculation of this correction somewhat more complicated. It was decided instead to measure the correction. The ratio of the neutral cell rate to beam cell rate scaled to yield one when extrapolated to zero rate is a measure on the fraction of accidentally vetoed neutral triggers. The reciprocal of this quantity integrated over the course of the run yields the S3 veto correction.

The computer livetime correction is needed because, for some fraction of the neutral triggers that occur, the computer is busy reading out a previous event. These lost triggers must be taken into account. It is calculated by integrating, over the course of the run, the ratio of neutral triggers generated to neutral triggers accepted.

Neutral Reference Reaction Correction, $F_{\rm neut}$

After the above corrections are calculated, a neutral reference reaction that is independent of target cell is examined and an additional correction is generated. This accounts for any complicated rate or acceptance effects in the target that are missed with the corrections above. To calculate this correction, the "π^0" trigger events were used (see Sec. 4.4.2). From this sample, events were selected that had zero hits in the tracking chambers, hodoscope, and calorimeter veto scintillators and one or more clusters in the calorimeter. The number of events selected for each target cell is histogrammed in Fig 5.32(a). These events were probably $\overline{p}p \rightarrow \overline{N}N$ or $\overline{p}p \rightarrow \pi^0\pi^0, \pi^0\pi^0\pi^0$ although, for this method, the reaction type is not important. It only has to be such that the reconstruction probability of the event is independent of target cell which is most certainly true since the calorimeter is ≈ 120 cm from the target. The number of events was then normalized for each target cell and a neutral reference reaction "cross section" calculated:

$$\sigma_{\rm neut,i} = \frac{1}{\mathcal{L}_{\rm i}} \frac{F_{\rm rate,i}}{F_{\delta \rm ray}} N_{\rm neut,i}, \tag{5.21}$$

where $N_{\rm neut,i}$ is the number of events passing the neutral reference reaction criteria. The neutral reference reaction cross section $\sigma_{\rm neut}$ is histogrammed for each target cell in Fig 5.32(b). The neutral reference reaction correction was calculated by the ratio of $\sigma_{\rm neut}$ for target cells 3-5 to that of target cell 2. Target cell 2 was used because it is the most upstream CH_2 cell with the simplest electronic logic for the beam cell and neutral cell definitions.

Carbon Background Subtraction Correction, $F_{\rm C}$

The target cells are constructed from polyethylene (CH_2), so for every two protons (hydrogen atoms) available for a reaction there is one carbon atom. To understand and quantify the background of events produced on carbon in the CH_2 target cells, a carbon (C) target cell is used (cell 1). The efficiency to trigger on and reconstruct

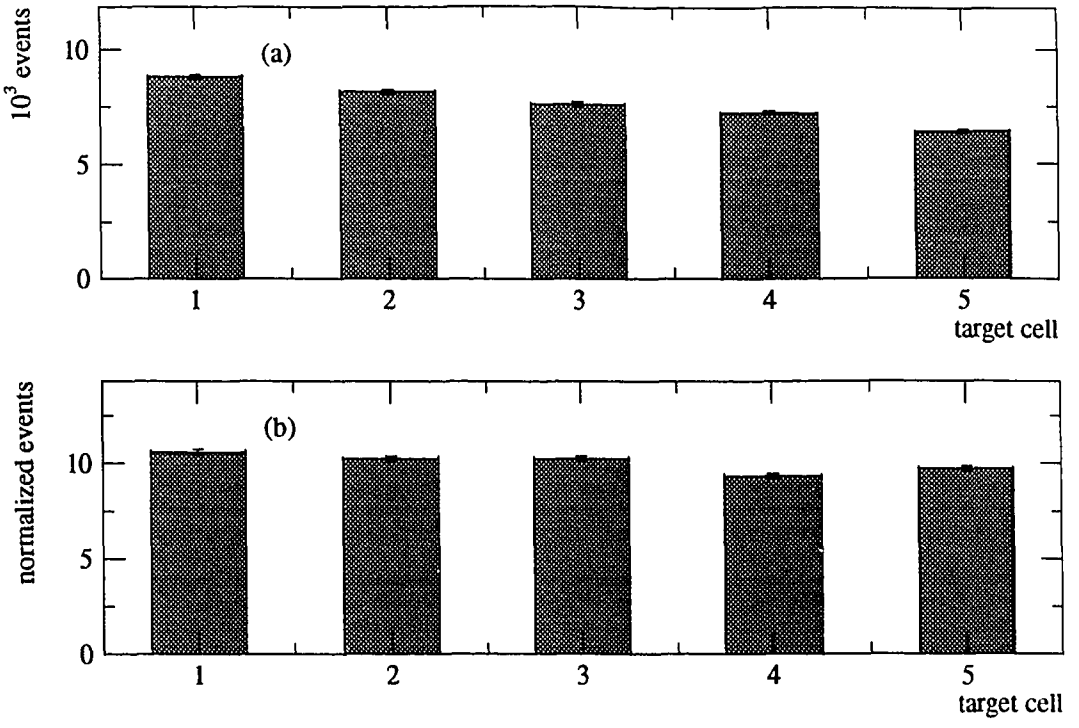

Figure 5.32: Neutral reference events for each target cell: (a) number of events with one or more calorimeter cluster and other detectors quiet and (b) these events normalized with the integrated luminosity and corrected for target inefficiencies.

a $\bar{p}p \rightarrow \overline{Y}Y$ event produced on C is fairly low as can be seen from the number of reconstructed events from target cell 1 (see Fig. 5.29), but the correction required is non-negligible. The carbon subtraction correction F_C for each reaction channel is calculated:

$$F_C = 1 - R_C \frac{\mathcal{L}_i E_i}{\mathcal{L}_1 E_1} \frac{N_1}{N_i}, \tag{5.22}$$

where $\mathcal{L}_i$ is the integrated luminosity in target cell i, E_i is the target cell efficiency ($E_i = \frac{F_{BR}}{F_{rate,i} F_{neut,i}}$) and N_i is the number of events reconstructed from cell i. The factor $R_C = 0.451 \pm 0.002$ is the ratio the density of C atoms in the CH_2 target cells to the density in the C target cell. So the carbon subtraction correction accounts for the number of events reconstructed on carbon in target cell i by scaling the number seen

in the C cell by the C density, target cell efficiency, and luminosity ratio. Since this is an angular independent correction, it is assumed that the angular distribution of the C events the same as that of proton events. This can be verified within the limited statistical accuracy by examining the distributions of $\cos\theta^*$ for events from the C cell in Fig. 5.33 and comparing to those from all cells in Fig. 5.31. Since the carbon correction is around 2.5% for $\overline{\Lambda}\Lambda$ and 15% for $\overline{\Sigma}^0\Lambda$ and $\overline{\Lambda}\Sigma^0$ events, the maximum systematic error introduced into the differential cross section with this assumption is negligible.

The target cell acceptance corrections described in the previous sections are listed in Table 5.9.

5.13.4 Cross Section Results

Using the quantities introduced in the previous sections the differential and total cross sections may be calculated. The differential cross section for target cell i and $\cos\theta^*$ bin j (assuming uniform width bins) is calculated,

$$\frac{d\sigma}{d\Omega}_{i,j} = \frac{1}{2\pi\Delta(\cos\theta^*)}\left(\frac{F_{\mathrm{rate},i}F_{\mathrm{neut},i}F_{\mathrm{C},i}}{F_{\mathrm{BR}}F_{\delta\mathrm{ray},i}}\right)\frac{N'_{i,j}}{\mathcal{L}_i} \tag{5.23}$$

where $\Delta(\cos\theta^*)$ is the $\cos\theta^*$ bin width, $\mathcal{L}_i$ is the integrated luminosity in target cell i, and $N'_{i,j}$ is the number of corrected events from target cell i, $\cos\theta^*$ bin j. The various F_i are the corrections described above.

The total cross section for each target cell is calculated by summing the differential cross section over $\cos\theta^*$ bins:

$$\sigma_i = 2\pi\Delta(\cos\theta^*)\sum_j \frac{d\sigma}{d\Omega}_{i,j} \tag{5.24}$$

$$= \frac{1}{F_{\mathrm{BR}}}\sum_j\left(\frac{F_{\mathrm{rate},i}F_{\mathrm{neut},i}F_{\mathrm{C},i}}{F_{\delta\mathrm{ray},i}}\right)\frac{N'_{i,j}}{\mathcal{L}_i}. \tag{5.25}$$

For the differential cross sections, it was decided to use 50 $\cos\theta^*$ bins for the $\overline{\Lambda}\Lambda$ data and 25 for $\overline{\Sigma}^0\Lambda$ and $\overline{\Lambda}\Sigma^0$. The differential cross sections as measured for each

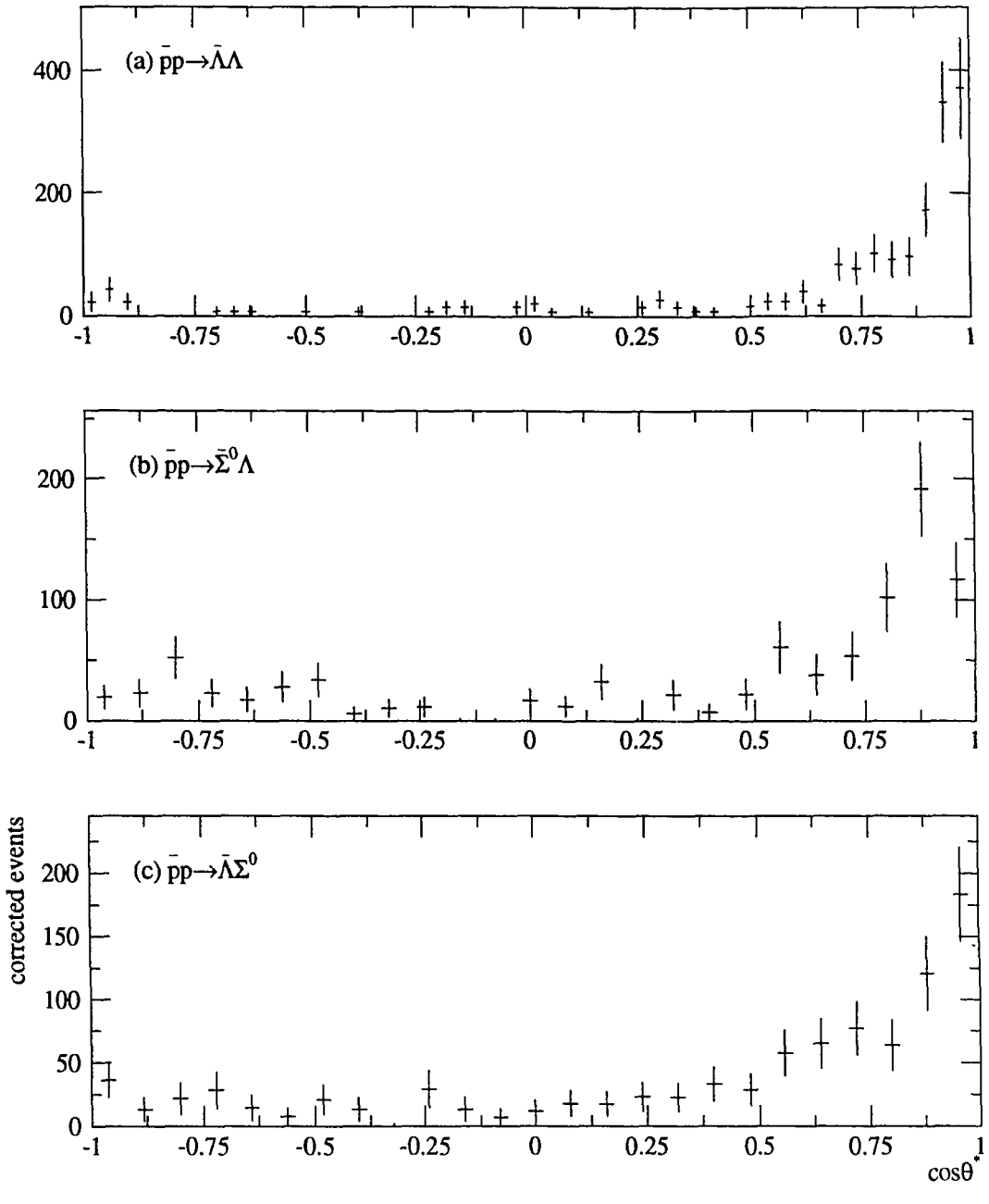

Figure 5.33: Distributions of $\cos\theta^*$ for corrected events from the carbon target cell for each reaction channel. The errors are calculated from the statistics of accepted events and the contributions from the acceptance function.

target cell	2	3	4	5
F_{br}	0.4109 ± 0.0064			
$F_{\delta\text{ray}}$	0.9908	0.9918	0.9909	0.9902
	± 0.0005	± 0.0004	± 0.0005	± 0.0005
F_{livetime}	1.3819	1.3811	1.3851	1.3803
F_{S3}	1.0966	1.1174	1.0240	1.1337
	± 0.0008	± 0.0008	± 0.0006	± 0.0007
F_{rate}	1.5202	1.5493	1.4194	1.5718
	± 0.0012	± 0.0012	± 0.0009	± 0.0011
F_{neut}	1.0000	0.9999	1.0978	1.0562
	± 0.0000	± 0.0192	± 0.0195	± 0.0199
$F_C(\overline{\Lambda}\Lambda)$	0.9750	0.9743	0.9751	0.9742
	± 0.0024	± 0.0025	± 0.0024	± 0.0025
$F_C(\overline{\Sigma}^0\Lambda)$	0.8569	0.8573	0.8593	0.8523
	± 0.0137	± 0.0140	± 0.0139	± 0.0150
$F_C(\overline{\Lambda}\Sigma^0)$	0.8613	0.8516	0.8700	0.8632
	± 0.0136	± 0.0150	± 0.0130	± 0.0140

Table 5.9: Target cell acceptance corrections. The carbon correction factor is tabulated for each reaction channel; the other factors are independent of reaction channel. The correction factors F_{livetime} and F_{S3} are contained within the total rate dependent correction F_{rate}.

CH_2 target cell are shown in Fig. 5.34. The total cross sections for each target cell and the average over target cells is shown in Fig. 5.35.

The differential cross sections for the $\overline{\Sigma}^0\Lambda$ and $\overline{\Lambda}\Sigma^0$ reactions summed over target cells are plotted together in Fig. 5.36. The total cross section for these reactions are plotted together in Fig. 5.35(b). Charge conjugation symmetry of the strong interaction implies that these differential and total cross section values should be

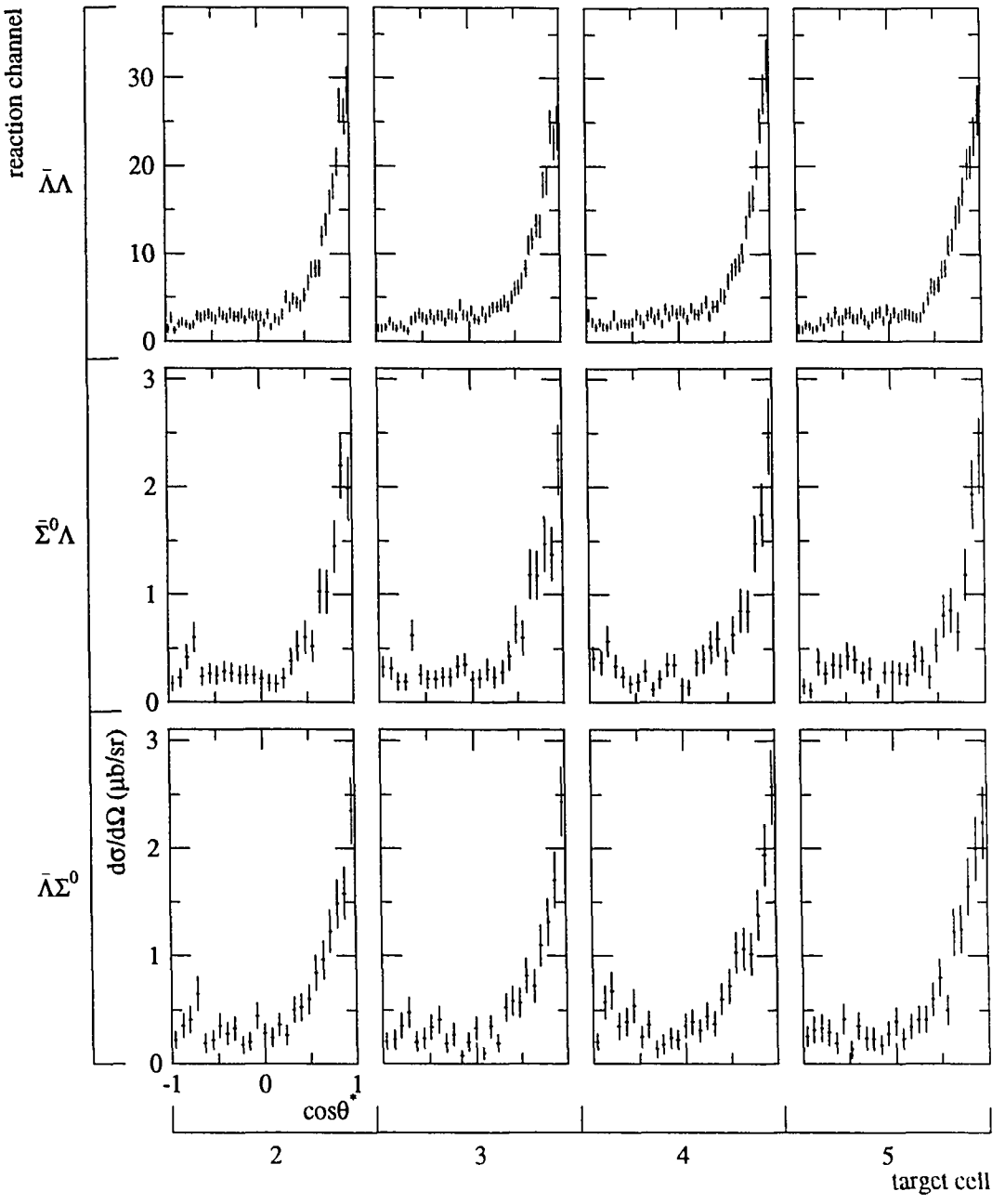

Figure 5.34: Differential cross section for each reaction channel and target cell. The errors on these plots include only the statistical contribution from the corrected number of events.

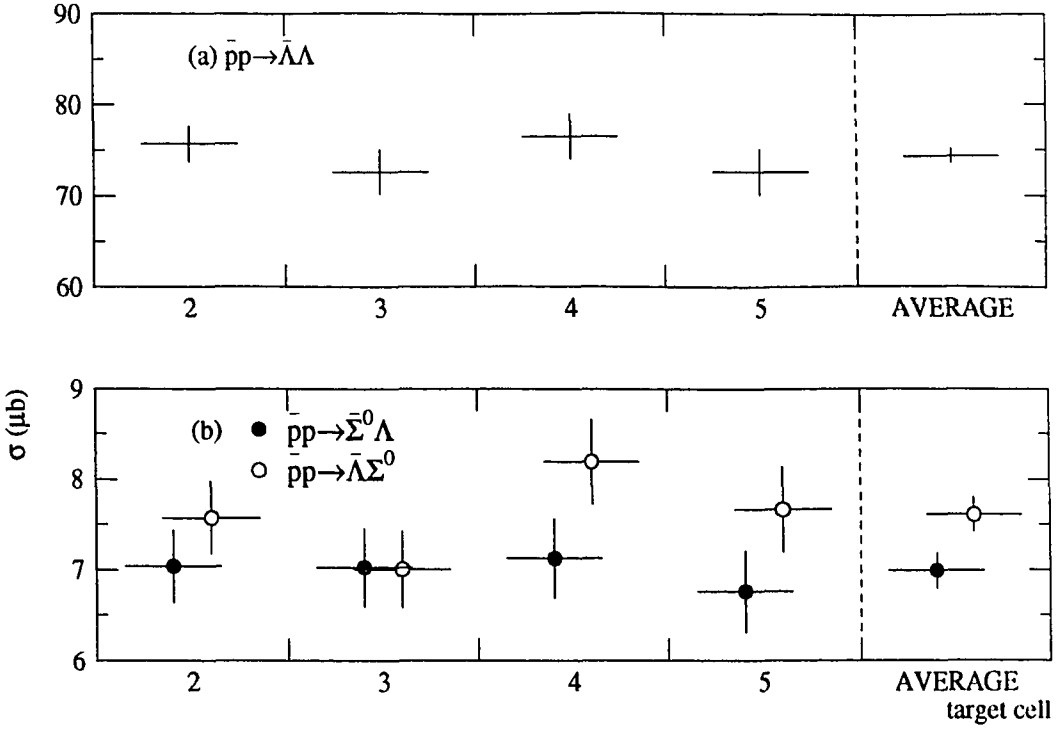

Figure 5.35: Total cross section for each reaction channel and target cell and the average over target cells. Note the suppressed zero of the scale.

equal (see Chapter 2).

Inspection of the figures does reveal agreement between the $\overline{\Sigma}^0\Lambda$ and $\overline{\Lambda}\Sigma^0$ reactions. The total cell averaged cross sections agree to within 8%. The fact that they agree within a few standard deviations when the acceptance for the two reactions, in some $\cos\theta^*$ regions, differs by 30% supports the conclusion that the Monte Carlo simulates the detector behavior rather well. The magnitude of the difference between the two reactions allows for an estimation of the systematic error on the Monte Carlo calculated acceptance.

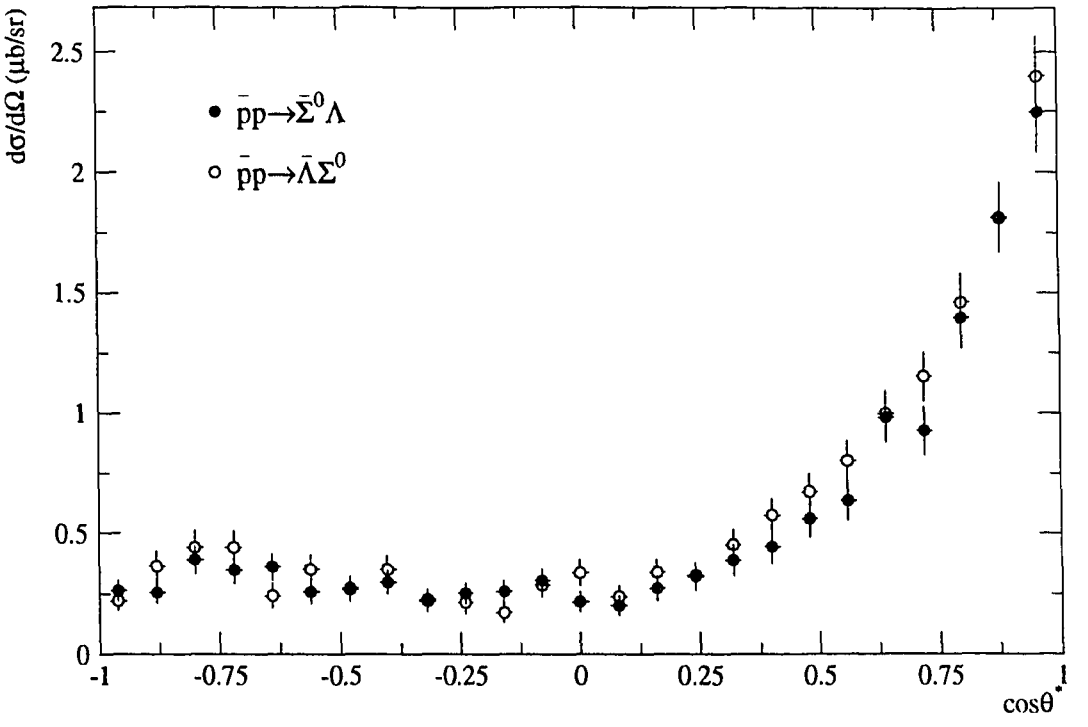

Figure 5.36: Differential cross sections as measured for the $\overline{p}p \to \overline{\Sigma}^0\Lambda$ and $\overline{p}p \to \overline{\Lambda}\Sigma^0$ channel separately.

5.13.5 Systematic Errors

The difference between the $\overline{\Sigma}^0\Lambda$ and $\overline{\Lambda}\Sigma^0$ differential cross sections, the difference in the baryon identification acceptance between the Monte Carlo and experimental data, and studies of the sensitivity of the acceptance as the detector parameters were varied, allowed for an estimate of the systematic error on the Monte Carlo calculated acceptance. This was estimated to be a constant term of 2% plus 5% times the event misidentification fraction (see Fig. 5.27). This results in an angular dependent and partially correlated systematic error. Unfortunately, there is no way to quantify the degree of correlation exactly. An estimate would be that the errors are strongly correlated between adjacent $\cos\theta^*$ bins and becoming less so as the $\cos\theta^*$ bin separation is increased. Also, there is likely to be some correlation between

widely separated $\cos\theta^*$ bins that are linked through the event misidentification. This average over $\cos\theta^*$ of this error is 2.3% for $\overline{\Lambda}\Lambda$ and 3.6% for $\overline{\Sigma}^0\Lambda$ and $\overline{\Lambda}\Sigma^0$.

It is estimated that the uncertainty in the integrated luminosity and target cell corrections, called the target cell error, contributes a 2% systematic error to the cross section independent of reaction type. The source of this error is the uncertainty in the rate dependent correction, the accuracy of the effective target thickness, and other unaccounted effects of target geometry and electronics subtleties. The error on the double charged branching fraction, since it is an overall multiplicative factor, contributes a 1.6% systematic error.

The target cell systematic error and the branching fraction error are added in quadrature to yield the total systematic of 2.6% on the differential cross section scale. The angular dependent systematic error is reported as a function along with the differential cross section and is not added explicitly into the differential cross section systematic error. For the systematic error on the total cross sections, the target cell error, the branching fraction error, and the average value of the angular dependent systematic error are added in quadrature. This results in an overall 3.4% systematic error on the total cross section for the $\overline{\Lambda}\Lambda$ channel and 4.4% for the $\overline{\Sigma}^0\Lambda$ and $\overline{\Lambda}\Sigma^0$ channels. These errors are listed in Table 5.10.

5.13.6 The Momentum Scale

The momentum of the antiproton beam in each target cell was determined by simulating the energy loss of the antiprotons, given an incident momentum of 1.729 GeV/c, as they passed through the target/scintillator array. (see Sec. 4.3.2). The momentum distribution of the antiprotons beam in each target cell, allowed the determination of the average momentum for each target cell. The average value of the momentum over the four target cells was used as the momentum for the reported cell-averaged differential and total cross sections. The error on this value is that due to the absolute uncertainty in the LEAR extraction momentum. The average

Systematic Errors		
	$\overline{\Lambda}\Lambda$	$\overline{\Sigma}^0\Lambda/\overline{\Lambda}\Sigma^0$
Differential Cross section		
target cell	2.0%	2.0%
branching fraction	1.6%	1.6%
total	2.6%	2.6%
Total Cross section		
target cell	2.0%	2.0%
branching fraction	1.6%	1.6%
average angular acceptance	2.3%	3.6%
total	3.4%	4.4%

Table 5.10: Summary of systematic errors.

momentum in the target, corresponding to the 1.729 GeV/c extraction momentum was 1.726 ± 0.001 GeV/c.

The final results for the total and differential cross sections for the $\overline{p}p \rightarrow \overline{\Lambda}\Lambda$ and $\overline{p}p \rightarrow \overline{\Sigma}^0\Lambda + c.c.$ reactions are presented along with discussion in Chapter 7.

Chapter 6

Spin Observable Analysis

The weak decays of the Λ hyperons in the $\overline{p}p \to \overline{\Lambda}\Lambda$ and $\overline{p}p \to \overline{\Sigma}^0\Lambda + c.c.$ reactions enable the spin observables of the reaction to be determined. Details of this are explained in Chapter 2. Using the $\overline{p}p \to \overline{\Lambda}\Lambda$ and $\overline{p}p \to \overline{\Sigma}^0\Lambda + c.c.$ sample that was selected from the data in the analysis described in the preceeding chapter, the detected proton and antiproton angular distributions are subjected to the spin observable analysis. This procedure determines the spin observables, the hyperon polarizations and spin correlation coefficients, and is described in this section.

6.1 Introduction

The expressions for the angular distributions of the detected antiprotons and protons in terms of the $\overline{Y}Y$ spin observables are derived in Chapter 2. With the proper normalization these expressions are equivalent to a probability density function (p.d.f.) for an event to occur with particle directions given by the $\hat{p}$. Here the $\hat{p}$ are the direction vectors of the Λ-decay proton and $\overline{\Lambda}$-decay antiproton in the parent particle rest frame. The components of $\hat{p} = (p_x, p_y, p_z)$ are commonly called the direction cosines.

As a first example consider the angular distribution of the detected antiproton and proton for the $\overline{p}p \to \overline{\Lambda}\Lambda$ reaction (Eq. 2.57). If this expression is normalized such that the integral over the entire solid angle of both antiproton and proton is equal

to 1, it becomes

$$I_{\overline{\Lambda}\Lambda}(\hat{p}_{\overline{p}}, \hat{p}_p) = \frac{1}{16\pi^2}\left[1 + \overline{\alpha}\mathbf{P}_{\overline{\Lambda}} \cdot \hat{p}_{\overline{p}} + \alpha\mathbf{P}_{\Lambda} \cdot \hat{p}_p + \overline{\alpha}\alpha \sum_{i,j} C_{ij} p_{\overline{p},i} p_{p,j}\right]. \tag{6.1}$$

Using this as a probability density function, the expectation values of the quantities $p_{i,\overline{p}}$, $p_{j,p}$, and $p_{i,\overline{p}}p_{j,p}$ may be calculated. These expectation values are

$$\langle p_{i,\overline{p}} \rangle = \iint p_{i,\overline{p}} I_{\overline{\Lambda}\Lambda}(\hat{p}_{\overline{p}}, \hat{p}_p) d\Omega_{\overline{p}} d\Omega_p, \tag{6.2}$$

$$\langle p_{j,p} \rangle = \iint p_{j,p} I_{\overline{\Lambda}\Lambda}(\hat{p}_{\overline{p}}, \hat{p}_p) d\Omega_{\overline{p}} d\Omega_p, \tag{6.3}$$

$$\langle p_{i,\overline{p}} p_{j,p} \rangle = \iint p_{i,\overline{p}} p_{j,p} I_{\overline{\Lambda}\Lambda}(\hat{p}_{\overline{p}}, \hat{p}_p) d\Omega_{\overline{p}} d\Omega_p. \tag{6.4}$$

These integrals are easily calculated yielding,

$$\langle p_{i,\overline{p}} \rangle = \frac{1}{3}\overline{\alpha} P_{i,\overline{\Lambda}}, \tag{6.5}$$

$$\langle p_{j,p} \rangle = \frac{1}{3}\alpha P_{j,\Lambda}, \tag{6.6}$$

$$\langle p_{i,\overline{p}} p_{j,p} \rangle = \frac{1}{9}\overline{\alpha}\alpha C_{ij}. \tag{6.7}$$

The experimental estimates for these expectation values are

$$\langle p_{i,\overline{p}} \rangle_{\text{exp.}} = \frac{1}{N}\sum_{k=1}^{N} p_{k,i,\overline{p}}, \tag{6.8}$$

$$\langle p_{j,p} \rangle_{\text{exp.}} = \frac{1}{N}\sum_{k=1}^{N} p_{k,j,p}, \tag{6.9}$$

$$\langle p_{i,\overline{p}} p_{j,p} \rangle_{\text{exp.}} = \frac{1}{N}\sum_{k=1}^{N} p_{k,i,\overline{p}} p_{k,j,p}, \tag{6.10}$$

where N is the number of events in the experimental sample. Equating the experimental estimates of the expectation values with those calculated from the probability density function $I_{\overline{\Lambda}\Lambda}(\hat{p}_{\overline{p}}, \hat{p}_p)$ and solving for the polarizations and spin correlation coefficients yields

$$P_{i,\overline{\Lambda}} = \frac{3}{\overline{\alpha}N}\sum_{k=1}^{N} p_{k,i,\overline{p}}, \tag{6.11}$$

$$P_{j,\Lambda} = \frac{3}{\alpha N}\sum_{k=1}^{N} p_{k,j,p}, \tag{6.12}$$

$$C_{i,j} = \frac{9}{\overline{\alpha}\alpha N}\sum_{k=1}^{N} p_{k,i,\overline{p}}p_{k,j,p}. \tag{6.13}$$

Thus, by measuring the directions of the final antiprotons and protons and averaging over the event sample, the spin observables of the reaction may be determined.

Unfortunately, with a finite efficiency detector the situation becomes more complicated. If the efficiencies for detecting antiprotons and protons in the detector are a function of the particle directions (which they most certainly are), acceptance functions must be introduced into $I_{\overline{Y}Y}(\hat{p}_{\overline{p}}, \hat{p}_p)$ and the integrals in the expectation value expressions (Eqs. 6.2–6.4) are not so easily calculated. The following sections describe the method of determining the spin observables including the effects of the finite acceptance of the detector.

6.2 Polarization Analysis with Detector Acceptance

First, consider the individual final-state particle acceptance functions A_i. These A_i represent the detection probability of a decay proton (or antiproton) and are functions of the decay particle direction $\hat{p}_i$. It is assumed in the following that the detection probability of the proton is independent of that of the antiproton so that the probability of reconstructing the event is a a simple product of the acceptance functions for each particle.

There is a potential complication for the $\overline{p}p \to \overline{\Sigma}^0\Lambda + c.c.$ reactions that merits an explanation. It is possible that the A_i for the decay proton from the Σ^0 branch also depends on the direction of the decay Λ since the lab angles of the final protons are a function of this Λ direction. If this were the case, the integrals over Λ directions that lead to the distribution functions for the $\overline{p}p \to \overline{\Sigma}^0\Lambda + c.c.$ reactions (Eqs. 2.60 and 2.61) would involve an additional function of the Λ direction and, therefore, not yield these simple expressions. Figure 6.1 shows the reconstruction efficiency separately

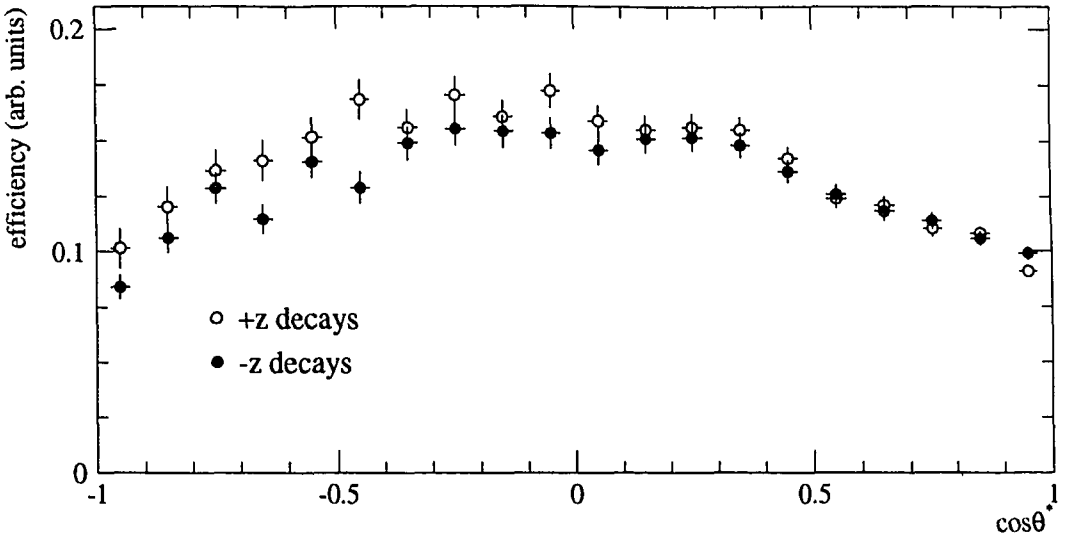

Figure 6.1: Efficiency for reconstructing $\overline{p}p \rightarrow \overline{\Sigma}^0\Lambda$ Monte Carlo events with the $\overline{\Sigma}^0$-decay $\overline{\Lambda}$ emitted in the $+z$ hemisphere and emitted in the $-z$ hemisphere in the $\overline{\Sigma}^0$ rest frame ($+z$ is along the direction of motion of the $\overline{\Sigma}^0$).

for Monte Carlo $\overline{p}p \rightarrow \overline{\Sigma}^0\Lambda$ events with forward $\overline{\Sigma}^0$-decay $\overline{\Lambda}$'s and for those with backward $\overline{\Sigma}^0$-decay $\overline{\Lambda}$'s. The figure shows approximately equal acceptances for the two event classes. There appears to be a slight systematic difference in the $\cos\theta^* \leq 0$ region, but this difference is small and, compared to the other error contributions, it is negligible. This allows the acceptance functions of the decay protons from the Σ^0 branch to be written as functions of the proton direction only.

Using these acceptance functions with the decay distribution functions derived in Chapter 2 (Eqs. 2.57, 2.60, and 2.61), the probability density functions for each reaction channel become

$$I_{\overline{\Lambda}\Lambda}(\hat{p}_{\overline{p}}, \hat{p}_p) = \frac{1}{16\pi^2}\left[1 + \overline{\alpha}\mathbf{P}_{\overline{\Lambda}} \cdot \hat{p}_{\overline{p}} + \alpha\mathbf{P}_\Lambda \cdot \hat{p}_p + \overline{\alpha}\alpha \sum_{i,j} C_{i,j} p_{\overline{p},i} p_{p,j}\right] A_{\overline{p}}(\hat{p}_{\overline{p}}) A_p(\hat{p}_p), \tag{6.14}$$

$$I_{\overline{\Sigma}^0\Lambda}(\hat{p}_{\overline{p}},\hat{p}_p) = \frac{1}{16\pi^2}\left[1-\frac{1}{3}\overline{\alpha}\mathbf{P}_{\overline{\Sigma}^0}\cdot\hat{p}_{\overline{p}}+\alpha\mathbf{P}_\Lambda\cdot\hat{p}_p - \frac{1}{3}\overline{\alpha}\alpha\sum_{i,j}C_{i,j}p_{\overline{p},i}p_{p,j}\right]A_{\overline{p}}(\hat{p}_{\overline{p}})A_p(\hat{p}_p), \tag{6.15}$$

$$I_{\overline{\Lambda}\Sigma^0}(\hat{p}_{\overline{p}},\hat{p}_p) = \frac{1}{16\pi^2}\left[1+\overline{\alpha}\mathbf{P}_{\overline{\Lambda}}\cdot\hat{p}_{\overline{p}}-\frac{1}{3}\alpha\mathbf{P}_{\Sigma^0}\cdot\hat{p}_p - \frac{1}{3}\overline{\alpha}\alpha\sum_{i,j}C_{i,j}p_{\overline{p},i}p_{p,j}\right]A_{\overline{p}}(\hat{p}_{\overline{p}})A_p(\hat{p}_p). \tag{6.16}$$

The normalization has been changed such that the probability of finding an event, integrated over the solid angle of the decay protons, with 100% acceptance, is unity.

Because of the large number of spin observables considered for each of the three reaction channels, it is convenient to express these p.d.f.'s in a more compact, matrix form:

$$I_{\overline{Y}Y}(\hat{p}_{\overline{p}},\hat{p}_p) = \frac{1}{16\pi^2}A_{\overline{p}}(\hat{p}_{\overline{p}})A_p(\hat{p}_p)p_{\overline{p}}D_{\overline{Y}Y}p_p^T, \tag{6.17}$$

where $\overline{Y}Y$ is used to indicate the $\overline{\Lambda}\Lambda$, $\overline{\Sigma}^0\Lambda$, or $\overline{\Lambda}\Sigma^0$ reaction. The (1×4) vectors $p_{\overline{p}}$ and p_p are the antiproton and proton direction vectors combined with the value 1:

$$p_{\overline{p}} = (1, p_{x,\overline{p}}, p_{y,\overline{p}}, p_{z,\overline{p}}), \tag{6.18}$$

$$p_p = (1, p_{x,p}, p_{y,p}, p_{z,p}). \tag{6.19}$$

The (4×4) matrix $D_{\overline{Y}Y}$ contains all of the spin observables and the various constants. It is handy to use because the factors of $-\frac{1}{3}$ that are present for the $\overline{p}p\to\overline{\Sigma}^0\Lambda+c.c.$ channels are buried inside which allows the derivation of the relevant equations for all $\overline{p}p\to\overline{Y}Y$ channels simultaneously. For each reaction channel, D is defined as,

$$D_{\overline{\Lambda}\Lambda}\equiv\begin{bmatrix} 1 & \alpha P_{x,\Lambda} & \alpha P_{y,\Lambda} & \alpha P_{z,\Lambda} \\ \overline{\alpha}P_{x,\overline{\Lambda}} & \alpha\overline{\alpha}C_{xx} & \alpha\overline{\alpha}C_{xy} & \alpha\overline{\alpha}C_{xz} \\ \overline{\alpha}P_{y,\overline{\Lambda}} & \alpha\overline{\alpha}C_{yx} & \alpha\overline{\alpha}C_{yy} & \alpha\overline{\alpha}C_{yz} \\ \overline{\alpha}P_{z,\overline{\Lambda}} & \alpha\overline{\alpha}C_{zx} & \alpha\overline{\alpha}C_{zy} & \alpha\overline{\alpha}C_{zz} \end{bmatrix}, \tag{6.20}$$

$$D_{\overline{\Sigma}^0\Lambda} \equiv \begin{bmatrix} 1 & \alpha P_{x,\Lambda} & \alpha P_{y,\Lambda} & \alpha P_{z,\Lambda} \\ -\frac{1}{3}\overline{\alpha}P_{x,\overline{\Sigma}^0} & -\frac{1}{3}\alpha\overline{\alpha}C_{xx} & -\frac{1}{3}\alpha\overline{\alpha}C_{xy} & -\frac{1}{3}\alpha\overline{\alpha}C_{xz} \\ -\frac{1}{3}\overline{\alpha}P_{y,\overline{\Sigma}^0} & -\frac{1}{3}\alpha\overline{\alpha}C_{yx} & -\frac{1}{3}\alpha\overline{\alpha}C_{yy} & -\frac{1}{3}\alpha\overline{\alpha}C_{yz} \\ -\frac{1}{3}\overline{\alpha}P_{z,\overline{\Sigma}^0} & -\frac{1}{3}\alpha\overline{\alpha}C_{zx} & -\frac{1}{3}\alpha\overline{\alpha}C_{zy} & -\frac{1}{3}\alpha\overline{\alpha}C_{zz} \end{bmatrix}, \tag{6.21}$$

$$D_{\overline{\Lambda}\Sigma^0} \equiv \begin{bmatrix} 1 & -\frac{1}{3}\alpha P_{x,\Sigma^0} & -\frac{1}{3}\alpha P_{y,\Sigma^0} & -\frac{1}{3}\alpha P_{z,\Sigma^0} \\ \overline{\alpha}P_{x,\overline{\Lambda}} & -\frac{1}{3}\alpha\overline{\alpha}C_{xx} & -\frac{1}{3}\alpha\overline{\alpha}C_{xy} & -\frac{1}{3}\alpha\overline{\alpha}C_{xz} \\ \overline{\alpha}P_{y,\overline{\Lambda}} & -\frac{1}{3}\alpha\overline{\alpha}C_{yx} & -\frac{1}{3}\alpha\overline{\alpha}C_{yy} & -\frac{1}{3}\alpha\overline{\alpha}C_{yz} \\ \overline{\alpha}P_{z,\overline{\Lambda}} & -\frac{1}{3}\alpha\overline{\alpha}C_{zx} & -\frac{1}{3}\alpha\overline{\alpha}C_{zy} & -\frac{1}{3}\alpha\overline{\alpha}C_{zz} \end{bmatrix}. \tag{6.22}$$

The next step of the calculation is to determine the elements of the D matrix (the spin observables) in terms of the expectation values which may be determined from the experimental data. Continuing with the matrix formulation, the expectation value matrix E is defined:

$$E \equiv \begin{bmatrix} \langle 1 \rangle & \langle p_{x,p} \rangle & \langle p_{y,p} \rangle & \langle p_{z,p} \rangle \\ \langle p_{x,\overline{p}} \rangle & \langle p_{x,\overline{p}} p_{x,p} \rangle & \langle p_{x,\overline{p}} p_{y,p} \rangle & \langle p_{x,\overline{p}} p_{z,p} \rangle \\ \langle p_{y,\overline{p}} \rangle & \langle p_{y,\overline{p}} p_{x,p} \rangle & \langle p_{y,\overline{p}} p_{y,p} \rangle & \langle p_{y,\overline{p}} p_{z,p} \rangle \\ \langle p_{z,\overline{p}} \rangle & \langle p_{z,\overline{p}} p_{x,p} \rangle & \langle p_{z,\overline{p}} p_{y,p} \rangle & \langle p_{z,\overline{p}} p_{z,p} \rangle \end{bmatrix}. \tag{6.23}$$

The reaction channel subscript has been dropped. There are three of these matrices, one for each$\overline{Y}Y$ reaction channel. The expectation values of the squares of the direction cosine values are also required. These are most handily introduced as the 4-vectors $\overline{F}$ and F:

$$\overline{F} \equiv (1, \langle p^2_{x,\overline{p}} \rangle, \langle p^2_{y,\overline{p}} \rangle, \langle p^2_{z,\overline{p}} \rangle) \tag{6.24}$$

$$F \equiv (1, \langle p^2_{x,p} \rangle, \langle p^2_{y,p} \rangle, \langle p^2_{z,p} \rangle) \tag{6.25}$$

The expectation value matrix may be evaluated in terms of the p.d.f. matrix as was done for the simple case in Eqs. 6.2–6.4. Preceding with this, the elements of the E matrices are,

$$E = \iint p_{\mu,\overline{p}} p_{\nu,p} I_{\overline{Y}Y}(\hat{p}_{\overline{p}}, \hat{p}_p) d\Omega_{\overline{p}} d\Omega_p, \tag{6.26}$$

$$= \iint \frac{1}{16\pi^2} p_{\mu,\overline{p}} p_{\nu,p} I_{\overline{Y}Y} A_{\overline{p}}(\hat{p}_{\overline{p}}) A_p(\hat{p}_p) p_{\overline{p}} D_{\overline{Y}Y} p_p^T d\Omega_{\overline{p}} d\Omega_p, \tag{6.27}$$

With the definition of the (4×4) matrices $\overline{\mathcal{A}}$ and $\mathcal{A}$,

$$\overline{\mathcal{A}}_{\mu,\nu} \equiv \int p_{\mu,\overline{p}} p_{\nu,\overline{p}} A_{\overline{p}} d\Omega_{\overline{p}}, \tag{6.28}$$

$$\mathcal{A}_{\mu,\nu} \equiv \int p_{\mu,p} p_{\nu,p} A_p d\Omega_p, \tag{6.29}$$

the expectation value matrix may be written in a convenient matrix form:

$$E = \frac{1}{16\pi^2} \overline{\mathcal{A}} D \mathcal{A}. \tag{6.30}$$

Using similar manipulations, the $\overline{F}$ and F 4-vectors become,

$$\overline{F} = \frac{1}{16\pi^2} \overline{\mathcal{B}} D \mathcal{C}, \tag{6.31}$$

$$F = \frac{1}{16\pi^2} \overline{\mathcal{C}} D \mathcal{B}, \tag{6.32}$$

with these additional definitions:

$$\overline{\mathcal{B}}_{\mu,\nu} \equiv \int p^2_{\mu,\overline{p}} p_{\nu,\overline{p}} A_{\overline{p}} d\Omega_{\overline{p}}, \tag{6.33}$$

$$\mathcal{B}_{\mu,\nu} \equiv \int p_{\mu,p} p^2_{\nu,p} A_p d\Omega_p, \tag{6.34}$$

$$\overline{\mathcal{C}}_{\mu} \equiv \int p_{\mu,\overline{p}} A_{\overline{p}} d\Omega_{\overline{p}} \; (= \overline{\mathcal{A}}_{\mu 0}), \tag{6.35}$$

$$\mathcal{C}_{\mu} \equiv \int p_{\mu,p} A_p d\Omega_p \; (= \mathcal{A}_{0\mu}). \tag{6.36}$$

By using the experimental estimates of the expectation values for E, F, and $\overline{F}$, determining the acceptance integrals $\overline{\mathcal{A}}$, $\mathcal{A}$, $\overline{\mathcal{B}}$, etc., and using Eqs. 6.30–6.32, the D matrices (and the spin observables) may be determined. Unfortunately, these acceptance integrals are not so easily determined. This is addressed in the next section.

6.2.1 Detector Acceptance

The Monte Carlo data allows the acceptance of the detector to be investigated in a form relevant to the polarization analysis and to estimate the acceptance integrals introduced above.

Figure 6.2 shows the distribution of the decay proton ϕ and p_z (measured in the parent rest frame) for successfully reconstructed $\overline{p}p \rightarrow \overline{\Lambda}\Lambda$ Monte Carlo events for four different $\cos\theta^*$ bins.[1] If the acceptance is constant for all decay-proton angles (in the Λ rest frame) then these plots would show a constant density of points for all ϕ and p_z. However there are "holes" (regions of low to near-zero acceptance) clearly visible. These are due to the small reconstruction efficiency for protons that are emitted nearly parallel to the direction of motion of the Λ. The efficiency is lower in these cases because the lab momentum vectors of the proton and pion are nearly parallel and the two tracks are more difficult to resolve.

When viewed in the Λ rest frame, these events can be separated into two types: those where the proton direction is (1) nearly parallel and (2) nearly antiparallel to the direction of the boost into the lab frame. Events of type (1) include a low (lab) momentum pion which undergoes more multiple scattering and energy loss than the pions in events of type (2). This results in an even smaller reconstruction efficiency for events of type (1). These two low efficiency regions can be seen as two holes in the plots of Fig. 6.2 at $\phi = 0$ and $\phi = \pm\pi$. The degree of the inefficiency and the position in p_z changes with $\cos\theta^*$ changes due to the details of the boost from the lab to the c.m. frame. Note also the approximate symmetry between $\overline{\Lambda}$'s at $\cos\theta^*$ and Λ's at $-\cos\theta^*$ ($\phi = 0$ in the $\overline{\Lambda}$ rest frame corresponds to $\phi = \pm\pi$ in the Λ frame due to the relative orientation of the two rest frames, see Fig. 2.1). This symmetry becomes exact in the limit where particles and antiparticles behave identically in the detector.

Figures 6.3 and 6.4 show these distributions projected onto the $p_x p_z$ and $p_y p_z$ planes. These plots are better for visualizing the result of the acceptance integrals of Eqs. 6.28 and 6.29. Note the asymmetry around $p_x = 0$ and $p_z = 0$ due to the effects described above. However, the acceptance seems to be symmetric around

[1] These plots and the conclusions drawn are essentially the same for the $\overline{p}p \rightarrow \overline{\Sigma}^0\Lambda$ and $\overline{p}p \rightarrow \overline{\Lambda}\Sigma^0$ channels.

$p_y = 0$. This is because, unlike for the $\hat{x}$ and $\hat{z}$ directions, there is no boost in the $\hat{y}$ direction ($\hat{y}$ is perpendicular to the production plane) so a proton with a $\hat{y}$ direction component p_y has the same lab momentum as a proton with a component $-p_y$. And, since the observables do not depend on the hyperon production c.m. angle ϕ which is the azimuthal angle of the production plane, there is an implicit average over this angle in all measured quantities. So, for this symmetry around $p_y = 0$ to hold, the only requirement is that the acceptance (at a given $\cos\theta^*$ value) for the $+p_y$ side of the production plane be the same as that for the $-p_y$ side, averaged over all c.m. ϕ. This is expressed as,

$$A_{\overline{p}}(p_x, p_y, p_z) = A_{\overline{p}}(p_x, -p_y, p_z), \tag{6.37}$$

$$A_p(p_x, p_y, p_z) = A_p(p_x, -p_y, p_z). \tag{6.38}$$

This symmetry may be violated slightly due to the finite decay lengths of the Λ hyperons but this is a small effect and negligible for this measurement.

The acceptance integral matrices $\overline{\mathcal{A}}$ and $\mathcal{A}$, calculated using $\overline{p}p \to \overline{\Lambda}\Lambda$ Monte Carlo events, as a function of $\cos\theta^*$ are shown in Fig. 6.5. The elements have been normalized such that $\overline{\mathcal{A}}_{00}$ and $\mathcal{A}_{00}$ are equal to unity for all $\cos\theta^*$. This, together with the fact that these matrices are symmetric, implies that they are completely specified by nine elements. The features of the acceptances that were discussed above can be seen in these acceptance integrals. The asymmetric acceptance in x and z results in relatively large values for the p_x, p_z elements of $\overline{\mathcal{A}}$ and $\mathcal{A}$ for some values of $\cos\theta^*$. The $p_x p_z$ elements are also non-negligible. In contrast, the elements involving odd powers of p_y are consistent with zero as would be expected from the arguments above.

Using the formalism developed in Sec. 6.2, one could proceed by using the experimental estimates to set the expectation value matrix E, using Monte Carlo data to set the matrices $\overline{\mathcal{A}}$ and $\mathcal{A}$, and then solving Eq. 6.30 to determine the matrix D. This would then yield the complete set of spin-observables. This method, however,

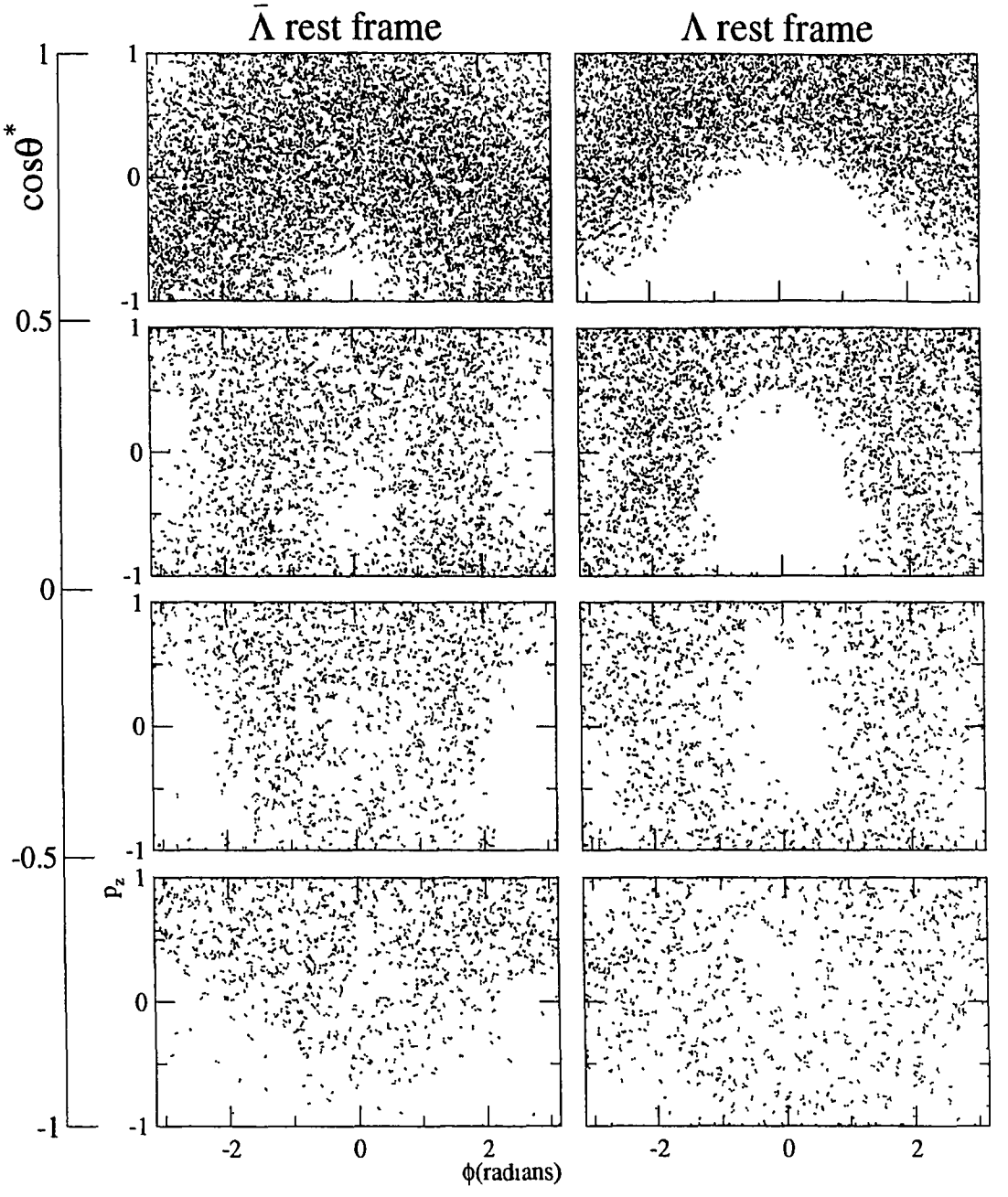

Figure 6.2: Distributions of ϕ and p_z in the $\overline{\Lambda}$ (left column) and Λ (right column) rest frames for successfully reconstructed $\overline{p}p \to \overline{\Lambda}\Lambda$ Monte Carlo events in the form of scatter plots. The four rows of plots correspond to four bins in $\cos\theta^*$. The scales are the same for all plots.

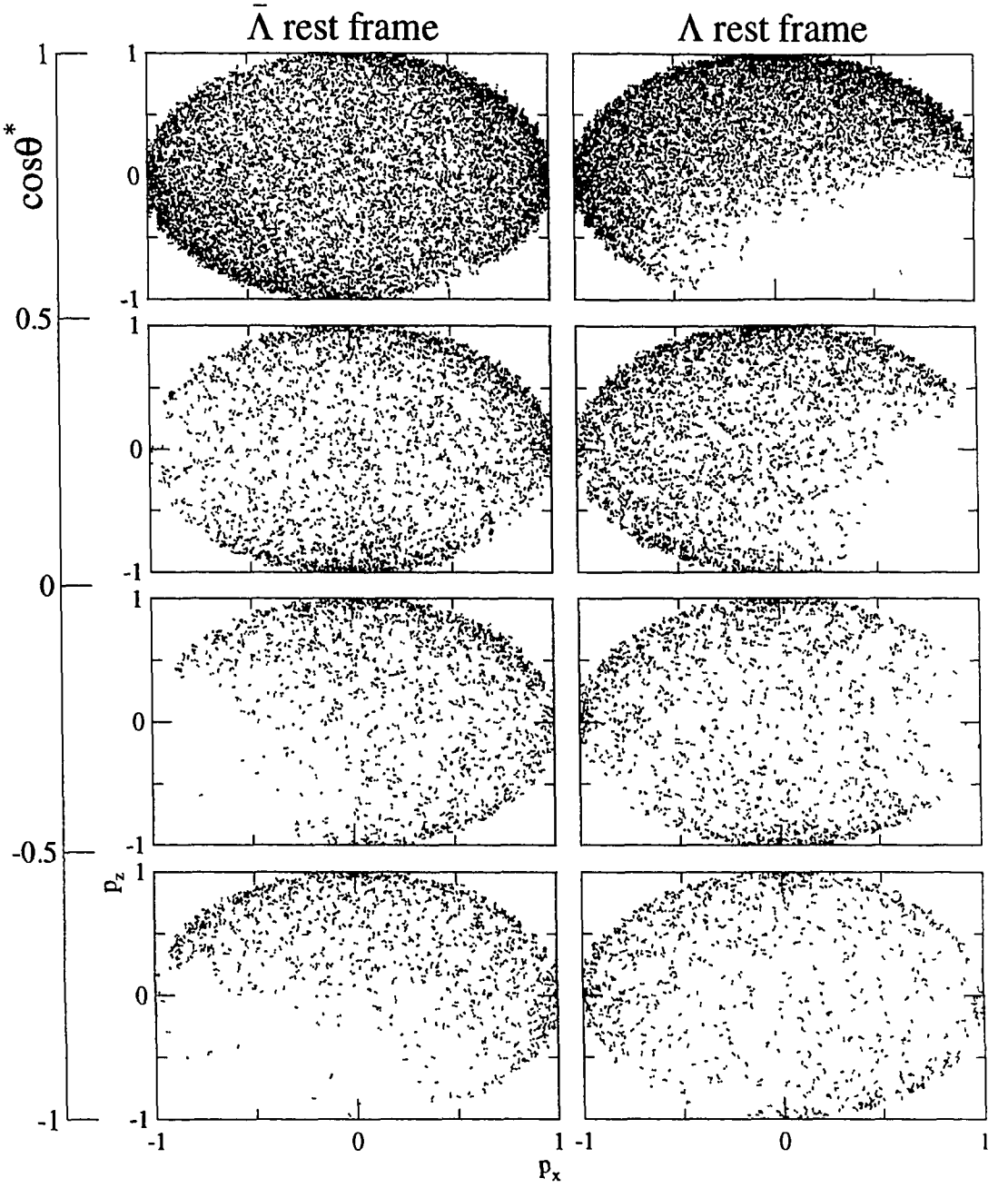

Figure 6.3: Distributions of p_x and p_z in the $\overline{\Lambda}$ (left column) and Λ (right column) rest frames for successfully reconstructed $\bar{p}p \rightarrow \overline{\Lambda}\Lambda$ Monte Carlo events in the form of scatter plots. The four rows of plots correspond to four bins in $\cos\theta^*$. The scales are the same for all plots.

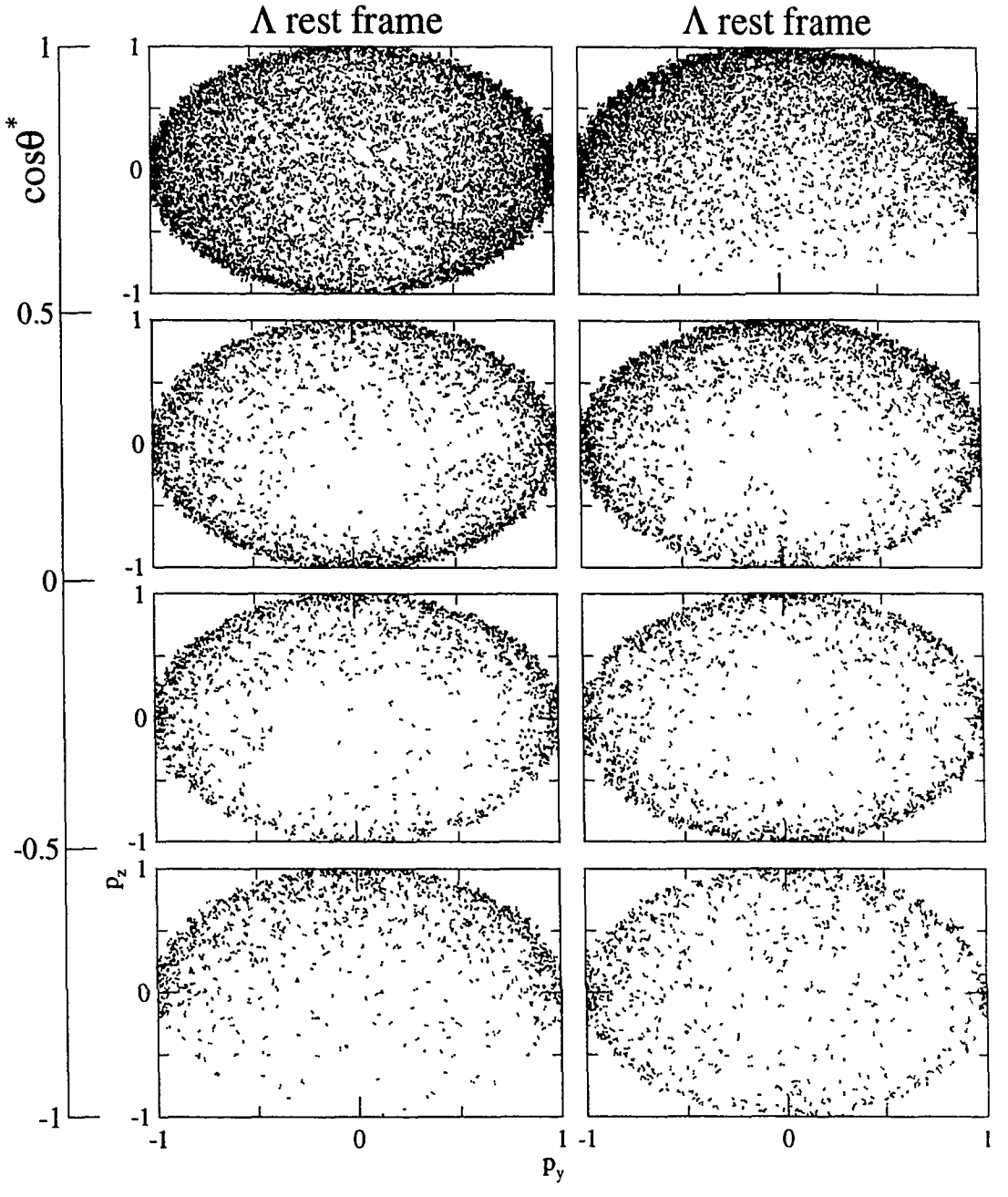

Figure 6.4: Distributions of p_y and p_z in the $\overline{\Lambda}$ (left column) and Λ (right column) rest frames for successfully reconstructed $\overline{p}p \rightarrow \overline{\Lambda}\Lambda$ Monte Carlo events in the form of scatter plots. The four rows of plots correspond to four bins in $\cos\theta^*$. The scales are the same for all plots.

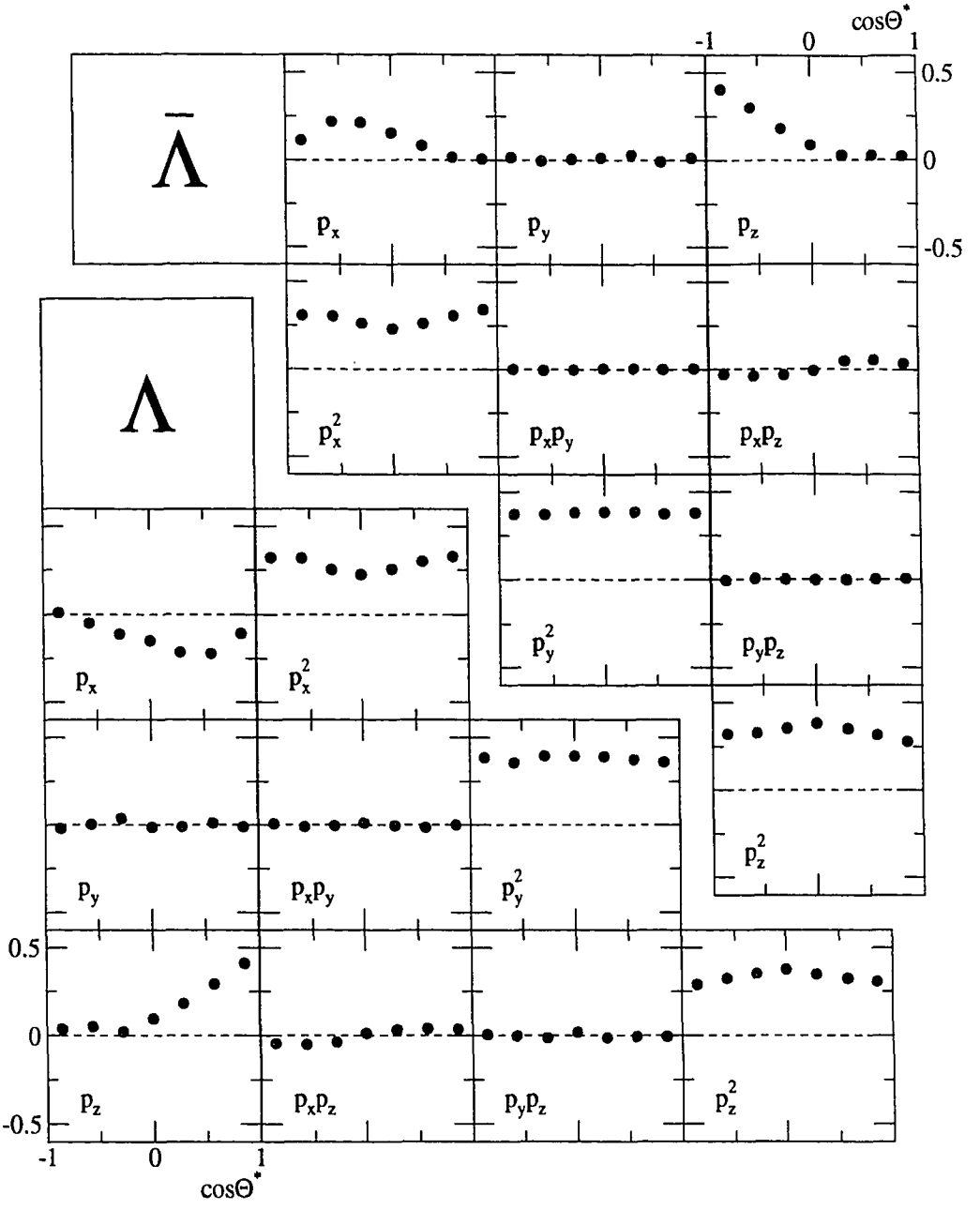

Figure 6.5: The upper right part of the $\overline{\mathcal{A}}$ matrix (labeled $\overline{\Lambda}$) and the lower left of the $\mathcal{A}$ matrix as a function of $\cos\theta^*$. These matrices are symmetric and the (0,0) element is normalized to unity so only these elements need to be shown. The labels on each plot indicate the term involved in the integration for that element. The scales are the same for all plots.

suffers from the disadvantage of relying on the Monte Carlo data to calculate the acceptance integrals of the $\overline{\mathcal{A}}$ and $\mathcal{A}$ matrices. A small error in the acceptance may be amplified in these integrals. For this reason, it is desirable to use a *Monte Carlo independent* method to determine $\overline{\mathcal{A}}$ and $\mathcal{A}$ and the spin observables.

6.2.2 Monte Carlo Independent Extraction of Spin Observables

For this method of polarization analysis, it is necessary to exploit the symmetries of the spin observables due to charge conjugation and parity symmetry of the strong interaction that were described in Chapter 2. Exploiting these symmetries allows 8 of the 16 elements of the D matrix to be set to zero. This eliminates many unknowns in the problem. The equality constraints between the spin observables imposed by these symmetries will not be exploited until after the solutions are determined in order to have a check on the method. In addition, the p_y symmetry of the detector that was explained above and observed in the Monte Carlo data is exploited. This allows the elements of the $\overline{\mathcal{A}}$ and $\mathcal{A}$ matrices that involve odd powers of p_y to be set to zero.

With these simplifications of the D, $\overline{\mathcal{A}}$, and $\mathcal{A}$ matrices the non-zero elements of D may be determined *without* the use of Monte Carlo data. There are few enough unknowns in the problem to determine, from the experimental data, the non-zero elements of $\overline{\mathcal{A}}$ and $\mathcal{A}$.

The form of the D matrix is now

$$D_{\overline{Y}Y} = \begin{bmatrix} 1 & 0 & D_{02} & 0 \\ 0 & D_{11} & 0 & D_{13} \\ D_{02} & 0 & D_{22} & 0 \\ 0 & D_{31} & 0 & D_{33} \end{bmatrix}. \tag{6.39}$$

And, the $\overline{\mathcal{A}}$ and $\mathcal{A}$ have the form,

$$\overline{\mathcal{A}} = \begin{bmatrix} \overline{\mathcal{A}}_{00} & \overline{\mathcal{A}}_{01} & 0 & \overline{\mathcal{A}}_{03} \\ \overline{\mathcal{A}}_{01} & \overline{\mathcal{A}}_{11} & 0 & \overline{\mathcal{A}}_{13} \\ 0 & 0 & \overline{\mathcal{A}}_{22} & 0 \\ \overline{\mathcal{A}}_{03} & \overline{\mathcal{A}}_{13} & 0 & \overline{\mathcal{A}}_{33} \end{bmatrix} \tag{6.40}$$

and

$$\mathcal{A} = \begin{bmatrix} \mathcal{A}_{00} & \mathcal{A}_{01} & 0 & \mathcal{A}_{03} \\ \mathcal{A}_{01} & \mathcal{A}_{11} & 0 & \mathcal{A}_{13} \\ 0 & 0 & \mathcal{A}_{22} & 0 \\ \mathcal{A}_{03} & \mathcal{A}_{13} & 0 & \mathcal{A}_{33} \end{bmatrix}. \tag{6.41}$$

Using these forms for D, $\overline{\mathcal{A}}$, and $\mathcal{A}$ and along with Eq. 6.30 yields an equation for each element of E. These are

$$E = \begin{bmatrix} \overline{\mathcal{A}}_{00}\mathcal{A}_{00} + \cdots & \overline{\mathcal{A}}_{00}\mathcal{A}_{01} + \cdots & \overline{\mathcal{A}}_{00}D_{02}\mathcal{A}_{22} & \overline{\mathcal{A}}_{00}\mathcal{A}_{03} + \cdots \\ \overline{\mathcal{A}}_{01}\mathcal{A}_{00} + \cdots & \overline{\mathcal{A}}_{01}\mathcal{A}_{01} + & \overline{\mathcal{A}}_{01}D_{02}\mathcal{A}_{22} & \overline{\mathcal{A}}_{01}\mathcal{A}_{03} + \\ & \overline{\mathcal{A}}_{11}D_{22}\mathcal{A}_{11} + \cdots & & \overline{\mathcal{A}}_{11}D_{13}\mathcal{A}_{33} + \cdots \\ \overline{\mathcal{A}}_{22}D_{20}\mathcal{A}_{00} & \overline{\mathcal{A}}_{22}D_{20}\mathcal{A}_{01} & \overline{\mathcal{A}}_{22}D_{22}\mathcal{A}_{22} & \overline{\mathcal{A}}_{22}D_{20}\mathcal{A}_{03} \\ \overline{\mathcal{A}}_{03}\mathcal{A}_{00} + \cdots & \overline{\mathcal{A}}_{03}\mathcal{A}_{01} + & \overline{\mathcal{A}}_{03}D_{02}\mathcal{A}_{22} & \overline{\mathcal{A}}_{03}\mathcal{A}_{03} + \\ & \overline{\mathcal{A}}_{33}D_{31}\mathcal{A}_{11} + \cdots & & \overline{\mathcal{A}}_{33}D_{33}\mathcal{A}_{33} + \cdots \end{bmatrix}. \tag{6.42}$$

Using the same form for D and similar simplifications for the $\overline{\mathcal{B}}$, $\mathcal{B}$, $\overline{\mathcal{C}}$, and $\mathcal{C}$ matrices, $\overline{F}$ and F become

$$\overline{F} = (\overline{\mathcal{A}}_{00}\mathcal{A}_{00} + \cdots, \overline{\mathcal{A}}_{11}\mathcal{A}_{00} + \cdots, \overline{\mathcal{A}}_{22}\mathcal{A}_{00} + \cdots, \overline{\mathcal{A}}_{33}\mathcal{A}_{00} + \cdots) \tag{6.43}$$

$$F = (\overline{\mathcal{A}}_{00}\mathcal{A}_{00} + \cdots, \overline{\mathcal{A}}_{00}\mathcal{A}_{11} + \cdots, \overline{\mathcal{A}}_{00}\mathcal{A}_{22} + \cdots, \overline{\mathcal{A}}_{00}\mathcal{A}_{33} + \cdots). \tag{6.44}$$

The $+\cdots$ in the equations above indicate additional terms that are smaller in magnitude than the leading terms and depend on non-zero elements of the D matrix. To

better understand these smaller terms, consider the expression for E_{00} with all terms included:

$$E_{00} = \overline{\mathcal{A}}_{00}\mathcal{A}_{00} + \overline{\mathcal{A}}_{01}D_{11}\mathcal{A}_{01} + \overline{\mathcal{A}}_{01}D_{13}\mathcal{A}_{03} + \overline{\mathcal{A}}_{03}D_{31}\mathcal{A}_{01} + \overline{\mathcal{A}}_{03}D_{33}\mathcal{A}_{03}. \qquad (6.45)$$

This expression shows that E_{00}, which is the acceptance of the detector integrated over the entire solid angle of both decay protons, has terms that depend on the correlations of the $\overline{\Lambda}$ and Λ spins. The other terms that are not written explicitly in Eq. 6.42 have similar forms. These terms and the magnitudes are examined as each $D_{\mu\nu}$ is determined.

The elements of D that contain the hyperon polarizations $P_{\overline{Y}}$ and P_Y are easily determined:

$$D_{20} = \frac{E_{20}}{\overline{F}_2} \qquad D_{02} = \frac{E_{02}}{F_2}. \qquad (6.46)$$

And the element that contains the spin correlation coefficient C_{yy} is

$$D_{22} = \frac{E_{22}}{\overline{F}_2 F_2}. \qquad (6.47)$$

The terms neglected in solving for these elements have been determined to introduce an error no larger than 1%. This is small compared to the statistical errors on these quantities and will not be considered. The D_{20} and D_{02} elements are also present in other elements of E. These could be solved to yield an additional two equations for each of these, but the errors are such that they would yield essentially no new information.

The elements of D that contain the spin correlation coefficients C_{xx}, C_{zz}, C_{xz}, and C_{zx} have a slightly different form. They are

$$D_{11} = \frac{E_{11} - E_{10}E_{01}}{\overline{F}_1 F_1}, \qquad D_{13} = \frac{E_{13} - E_{10}E_{03}}{\overline{F}_1 F_3},$$
$$D_{31} = \frac{E_{31} - E_{30}E_{01}}{\overline{F}_3 F_1}, \qquad D_{33} = \frac{E_{33} - E_{30}E_{03}}{\overline{F}_3 F_3}. \qquad (6.48)$$

The terms neglected to yield these solutions are not so easily dismissed. They may be as large as $10-20\%$, depending on the true values of the $D_{\mu\nu}$. This is a correction that is close to negligible given the size of the statistical errors. However, it has been decided to use the formulas above for a first iteration, use the measured values for the $D_{\mu\nu}$ to determine a correction, and use the correction to obtain a second and final iteration value for D_{11}, D_{13}, D_{31}, and D_{33}.

In summary, the expressions used to determine the entire D matrix are,

$$D = \begin{bmatrix} 1 & 0 & \frac{E_{02}}{F_2} & 0 \\ 0 & \frac{E_{11}-E_{10}E_{01}}{F_1F_1} + \Delta D_{11} & 0 & \frac{E_{13}-E_{10}E_{03}}{F_1F_3} + \Delta D_{13} \\ \frac{E_{20}}{F_2} & 0 & \frac{E_{22}}{F_2F_2} & 0 \\ 0 & \frac{E_{31}-E_{30}E_{01}}{F_3F_1} + \Delta D_{31} & 0 & \frac{E_{33}-E_{30}E_{03}}{F_3F_3} + \Delta D_{33} \end{bmatrix}, \tag{6.19}$$

where the ΔD are the second iteration corrections explained above. The polarizations and spin correlation coefficients may be extracted from the measured D matrix for each reaction channel by using the appropriate formulas relating the D matrix to the spin observables (Eqs. 6.20-6.22).

6.2.3 Statistical Errors

The statistical errors on the spin observables are determined by propagating the errors on the expectation values (the elements of the matrix E and the vectors $\overline{F}$ and F) through the expressions relating them to the spin observables. The statistical errors on the expectation values and their correlations are obtained from the elements of the covariance matrix for these quantities. The covariance matrix for functions f_i is estimated [98]:

$$\begin{aligned} V_{ij} &\simeq \frac{1}{N(N-1)} \sum_{k=1}^{N} \left(f_i - \overline{f_i}\right)\left(f_j - \overline{f_j}\right) \\ &= \frac{1}{N(N-1)} \left[\sum_{k=1}^{N} f_i f_j - \frac{1}{N}\left(\sum_{k=1}^{N} f_i\right)\left(\sum_{k=1}^{N} f_j\right)\right], \end{aligned} \tag{6.20}$$

where N is the number of events in the sample. In this analysis, the f_i are the various functions that appear in the expectation values: $p_{i,\bar{p}}$, $p_{i,p}$, and combinations of these.

As an example, the error estimate for E_{02}, which is the error of the expectation value $\langle p_{y,p} \rangle$, is expressed,

$$\begin{aligned} V(E_{02}) = \sigma^2(E_{02}) &= \frac{1}{N(N-1)} \left\{ \sum_{k=1}^{N} p_{y,p}^2 - \frac{1}{N} \left(\sum_{k=1}^{N} p_{y,p} \right)^2 \right\}, \\ &= \frac{1}{N-1} \left(\langle p_{y,p}^2 \rangle - \langle p_{y,p} \rangle^2 \right). \end{aligned} \tag{6.51}$$

The errors and covariances of the other expectation values are determined in this manner and are propagated through the formulae to yield the statistical errors on the spin observables.

6.2.4 The Measured Expectation Values

The expectation value matrix E for the $\bar{p}p \to \overline{\Lambda}\Lambda$ event sample using seven $\cos\theta^*$ bins is shown in Fig. 6.6. Upon examination of this figure and referring to Eq. 6.42, the structure of the y components of polarization and the C_{yy} spin correlation coefficient are evident in the $E_{\mu 0}$ column and the $E_{0\nu}$ row. In the other elements however, the dominant terms are due to the shape of the acceptance functions which must first be subtracted to obtain the C_{xx}, C_{zz}, C_{xz}, and C_{zx} spin correlation coefficients. This will be reflected in the final data as larger errors on these spin observables.

The expectation value vectors $\overline{F}$ and F, also extracted from the $\bar{p}p \to \overline{\Lambda}\Lambda$ data, are shown in fig. 6.7. These values serve as the normalization terms in the solutions for the elements of the D matrices. In the limit that the acceptances are constant for any decay proton direction, these elements would be equal to $\frac{1}{3}$ as seen in the equations derived at the beginning of this chapter with naive assumptions about the acceptances. The values measured for $\overline{F}$ and F are of this magnitude but differ somewhat depending upon the acceptances.

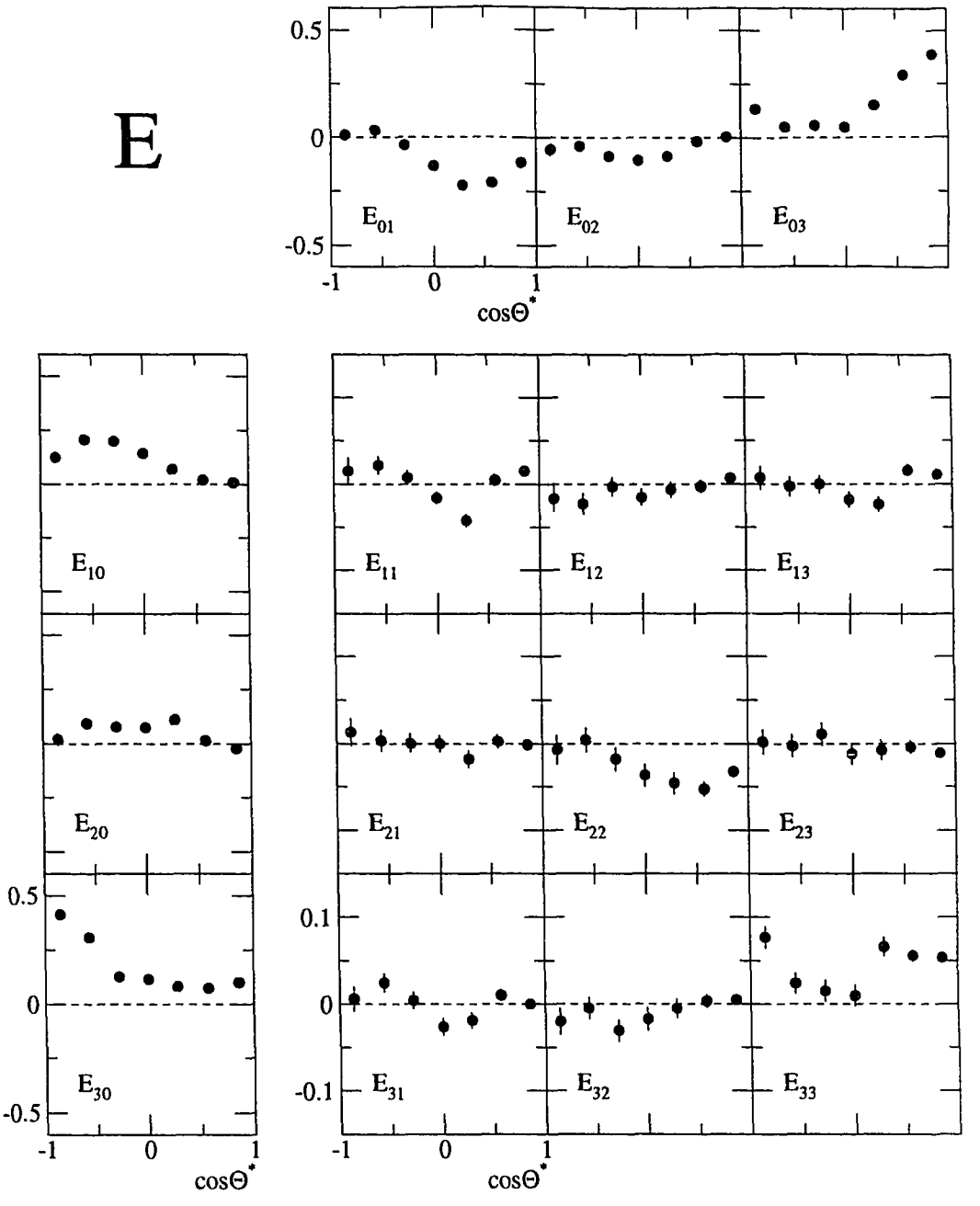

Figure 6.6: The values of the expectation value matrix E as determined from the $\overline{p}p \to \overline{\Lambda}\Lambda$ data for seven $\cos\theta^*$ bins. The E_{00} element is normalized to one and is not shown. The scales are the same for each group of plots. Only statistical errors are shown and, for the first row and column, are smaller than the markers and cannot be seen.

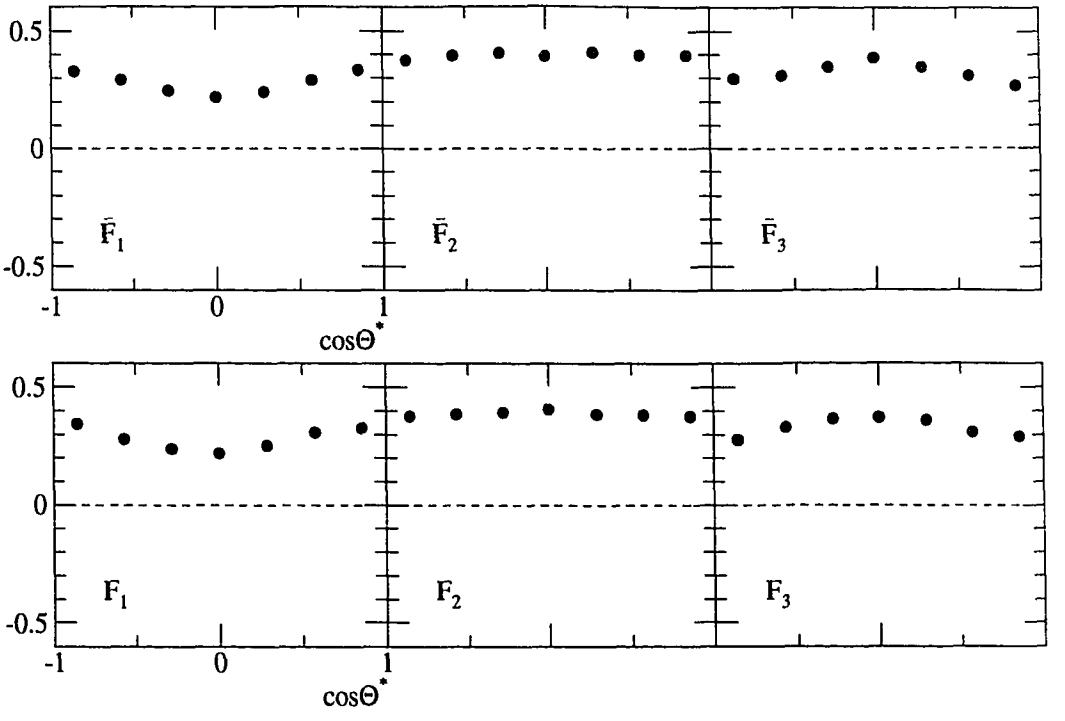

Figure 6.7: Values of the vectors $\overline{F}$ and F as determined from the $\overline{p}p \rightarrow \overline{\Lambda}\Lambda$ data for seven $\cos\theta^*$ bins. The $\overline{F}_0$ and F_0 elements are normalized to one and are not shown. The scales are the same for all plots. Errors are statistical only and are much smaller than the markers, so they cannot be seen.

6.3 Spin Observable Results

Using the method developed above, the spin observables for each reaction channel may be determined. From the data, the expectation values that comprise the E matrix and the $\overline{F}$ and F vectors are calculated and these values are used to determine the D matrix through Eq. 6.49. The complete set of seven spin observables for each channel are then calculated using Eqs. 6.20-6.22. The results of this process are shown in Figs. 6.8-6.10. The subscript y on the polarization values has been dropped since the x and z components have been set to zero. The errors shown in these plots are statistical only. The number of $\cos\theta^*$ bins has been chosen to be small enough

so that the number of events in each bin is sufficient for relatively small statistical errors yet large enough to show the structure of each observable as a function of $\cos\theta^*$. Unfortunately, the number of events in the $\overline{p}p \to \overline{\Sigma}^0\Lambda$ and $\overline{p}p \to \overline{\Lambda}\Sigma^0$ samples was not adequate to realize this exactly. This small number of events causes larger errors on the spin observables for these channels. In addition, the factor of $-\frac{1}{3}$ in the expressions for the D matrices further increases the errors on $P_{\overline{\Sigma}^0}$, P_{Σ^0}, and the C_{ij} for the $\overline{p}p \to \overline{\Sigma}^0\Lambda$ and $\overline{p}p \to \overline{\Lambda}\Sigma^0$ channels.

6.3.1 Physical Constraints

Each of the spin observables is limited, by definition, to be within the range -1 to $+1$. Some of the experimentally measured values, especially for the $\overline{p}p \to \overline{\Sigma}^0\Lambda$ and $\overline{p}p \to \overline{\Lambda}\Sigma^0$ channels, are outside of this range. However, this is not surprising considering the limited number of events. The expectation values used to calculate the spin observables are estimates of the true value and the accuracy is limited by the number of events in the sample. A statistically correct analysis shows that the measured spin observables are consistent with the physical limits and there are no values that are outside of these limits by more that 2σ.

As explained in Chapter 2, the symmetries of the strong interaction sets constraints among the spin observables. The constraints that require a subset of the spin observables to be equal to zero have been exploited in the method developed above to determine the remaining spin observables. Other constraints require, at $\cos\theta^* = 0, \pi$, that the polarizations and the C_{xz}, C_{zx} spin correlations are zero and that $C_{xx} = -C_{yy}$. The data are consistent with these constraints although the errors, especially for $\overline{p}p \to \overline{\Sigma}^0\Lambda + c.c.$, do not allow a stringent test.

The remaining spin observable constraints yield two constraint equations for the seven spin observables of $\overline{p}p \to \overline{\Lambda}\Lambda$ channel and seven constraints for the 14 spin observables of the combined $\overline{p}p \to \overline{\Sigma}^0\Lambda + c.c.$ reaction channel. Table 6.1 lists these constraints for both reaction channels. Figures 6.11 and 6.12 illustrate how well

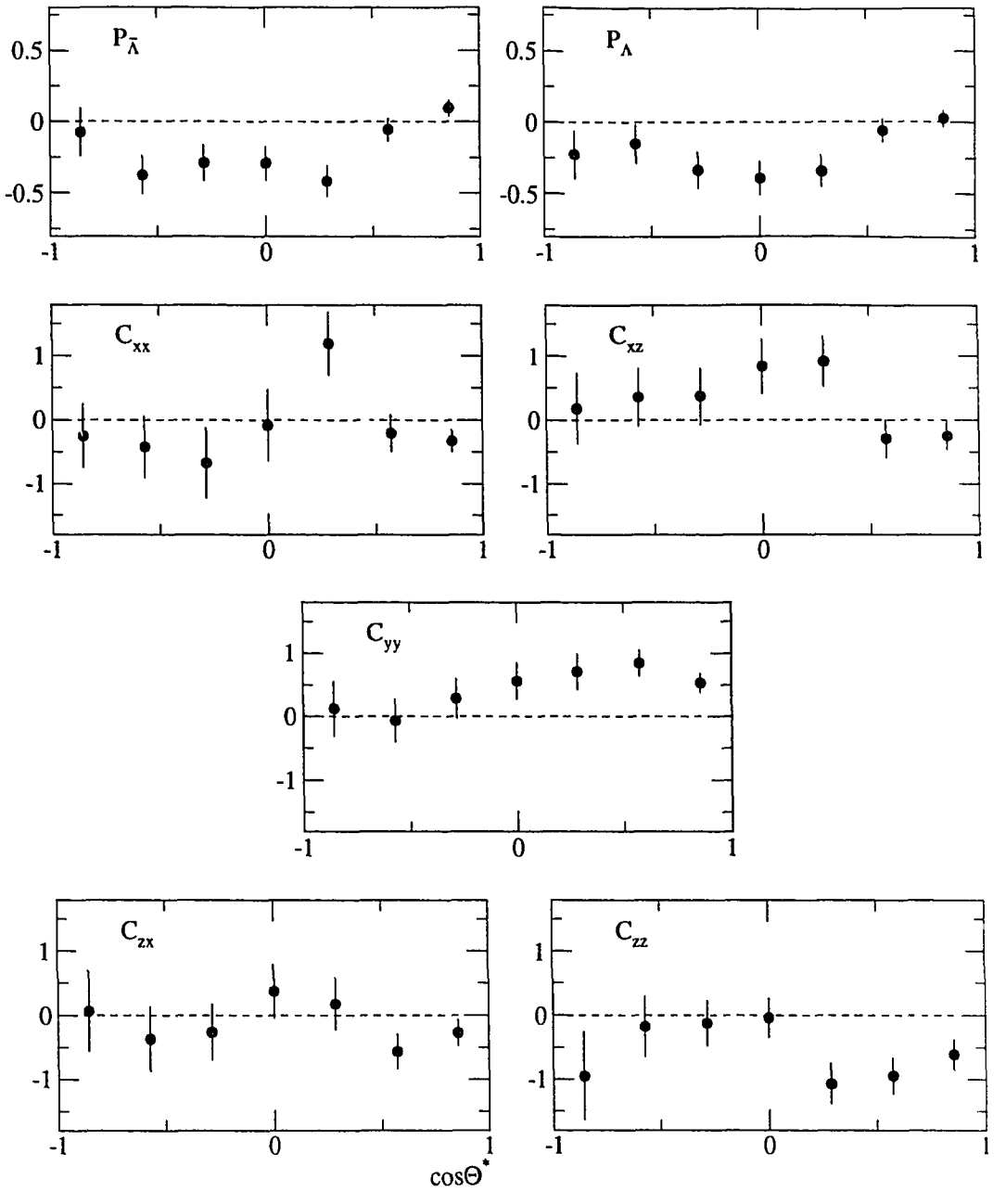

Figure 6.8: The non-zero polarizations and spin correlation coefficients for the $\bar{p}p \to \bar{\Lambda}\Lambda$ reaction for seven $\cos\theta^*$ bins. The errors are statistical only.

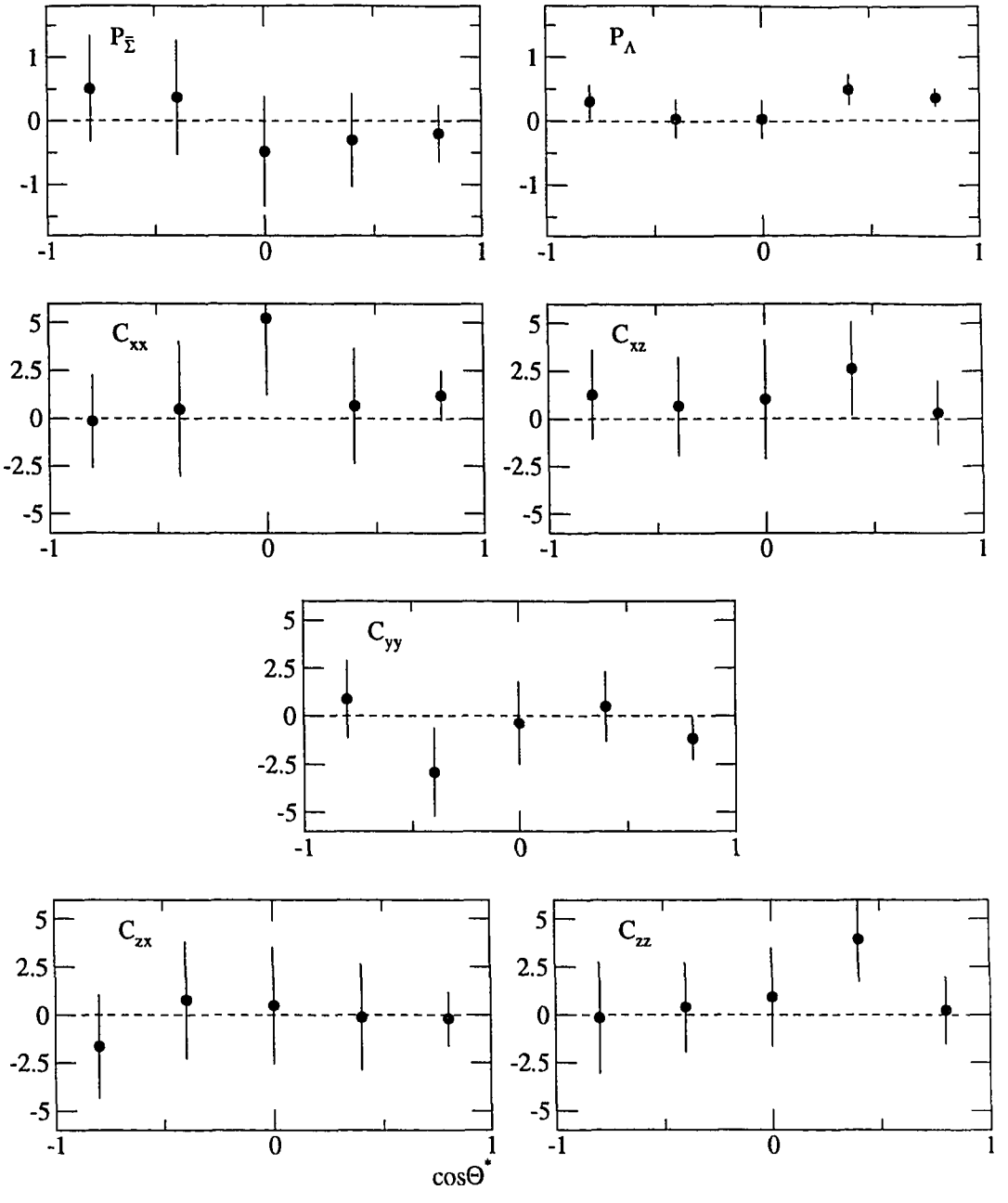

Figure 6.9: The non-zero polarizations and spin correlation coefficients for the $\bar{p}p \to \overline{\Sigma}^0\Lambda$ reaction for five $\cos\theta^*$ bins. The errors are statistical only.

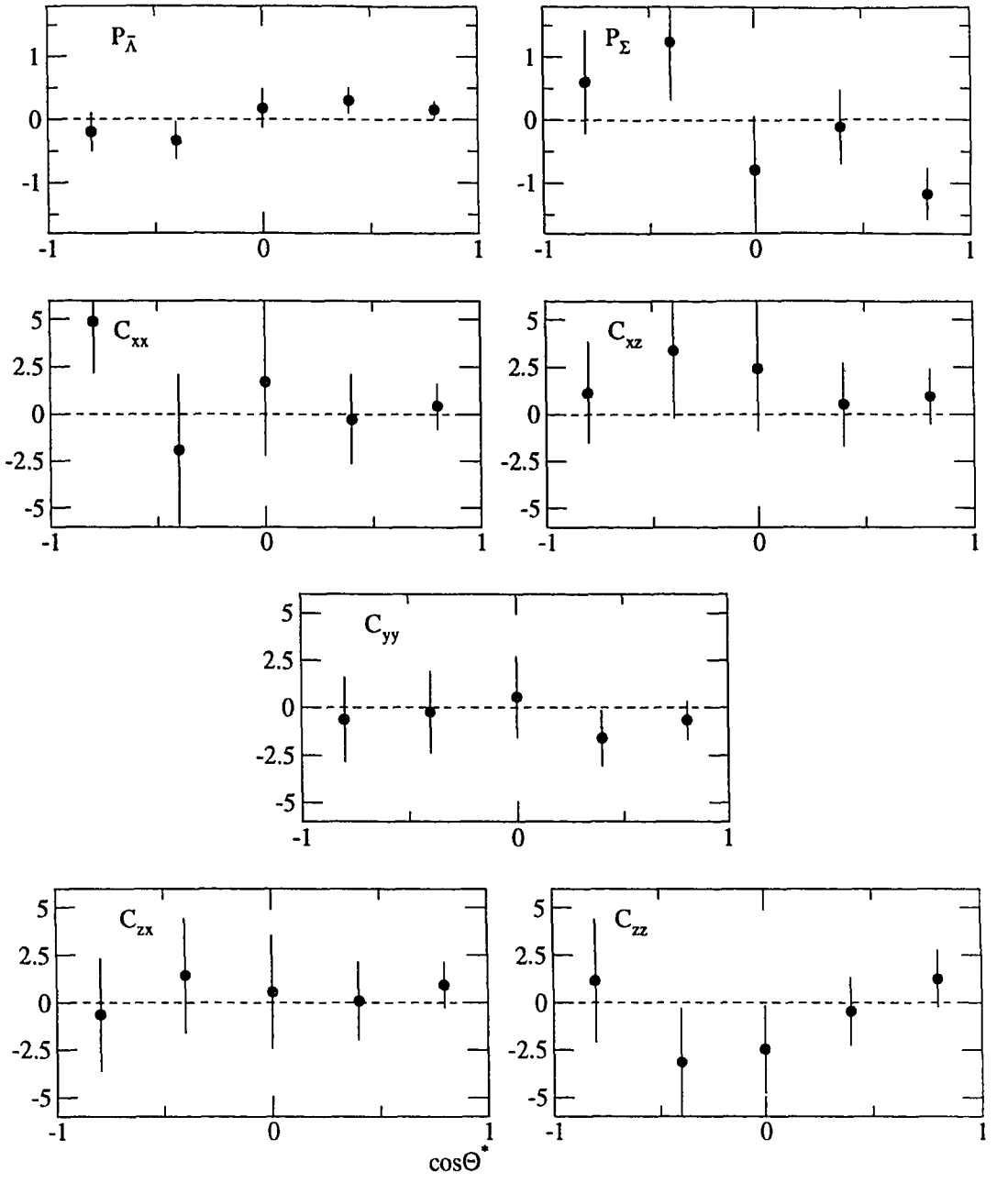

Figure 6.10: The non-zero polarizations and spin correlation coefficients for the $\overline{p}p \to \overline{\Lambda}\Sigma^0$ reaction for five $\cos\theta^*$ bins. The errors are statistical only.

$\overline{p}p \to \overline{\Lambda}\Lambda$	
observables/ constraints	averaged observable
$P_{\overline{\Lambda}} = P_{\Lambda}$	P_{Λ}
$C_{xz} = C_{zx}$	C_{xz}
C_{xx}	C_{xx}
C_{yy}	C_{yy}
C_{zz}	C_{zz}

$\overline{p}p \to \overline{\Lambda}\Sigma^0 + c.c.$	
observables/ constraints	averaged observable
$P_{\overline{\Sigma}^0}(\overline{\Sigma}^0\Lambda) = P_{\Sigma^0}(\overline{\Lambda}\Sigma^0)$	P_{Σ^0}
$P_{\Lambda}(\overline{\Sigma}^0\Lambda) = P_{\overline{\Lambda}}(\overline{\Lambda}\Sigma^0)$	P_{Λ}
$C_{xz}(\overline{\Sigma}^0\Lambda) = C_{zx}(\overline{\Lambda}\Sigma^0)$	C_{xz}
$C_{zx}(\overline{\Sigma}^0\Lambda) = C_{xz}(\overline{\Lambda}\Sigma^0)$	C_{zx}
$C_{xx}(\overline{\Sigma}^0\Lambda) = C_{xx}(\overline{\Lambda}\Sigma^0)$	C_{xx}
$C_{yy}(\overline{\Sigma}^0\Lambda) = C_{yy}(\overline{\Lambda}\Sigma^0)$	C_{yy}
$C_{zz}(\overline{\Sigma}^0\Lambda) = C_{zz}(\overline{\Lambda}\Sigma^0)$	C_{zz}

Table 6.1: Spin observable constraints and the spin observable resulting from the use of the constraint.

the data obey these constraints. The observables appear to be consistent with the constraint with the exception of a few possible systematic differences in some of the C_{ij} for the $\overline{p}p \to \overline{\Sigma}^0\Lambda + c.c.$ channels. These differences are most likely due to the errors introduced by misidentified events as discussed in Sec. 5.12.2. Several methods to correct for these misidentification errors, similar to those employed to correct the differential cross sections, were investigated, yet all failed for complicated, mostly pragmatic reasons. Also, any gains made by the correction schemes would be limited by the unavoidable, relatively large statistical errors. It was decided to use no correction scheme and simply estimate the systematic errors that misidentifications introduce.

6.3.2 Systematic Errors

The systematic errors were estimated to be proportional to the fraction of misidentified events that are present in the data sample as was done for the angular dependent systematic error on the differential cross section, explained in Sec. 5.13.5. A misiden-

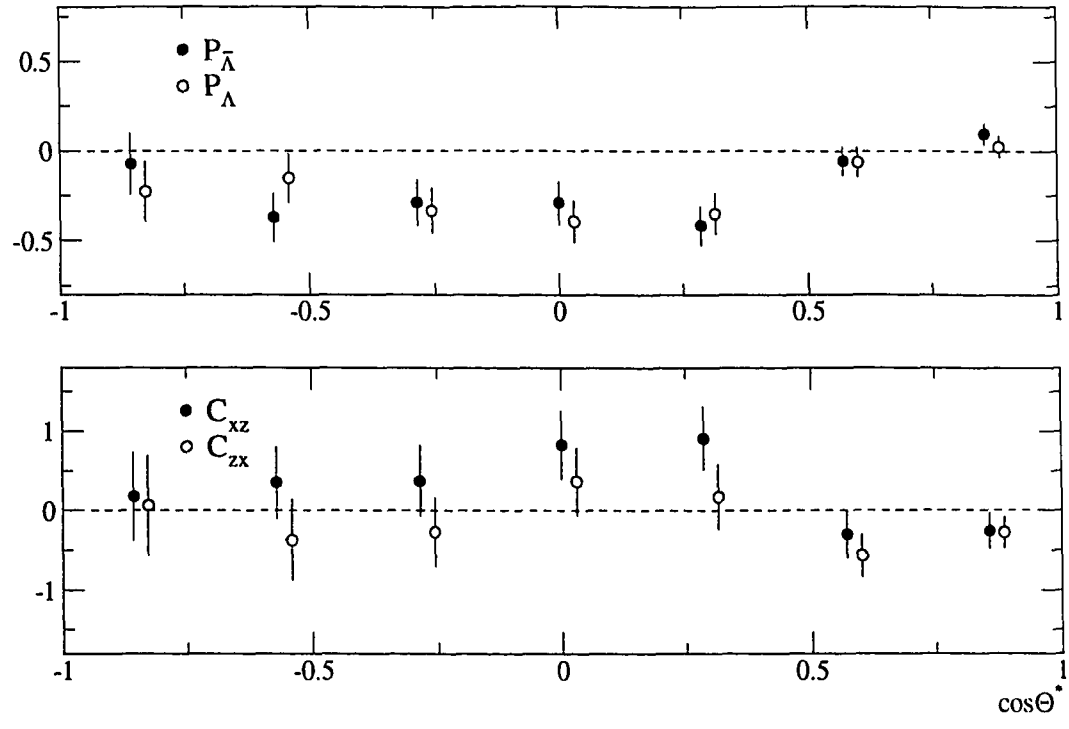

Figure 6.11: The spin observables for the $\bar{p}p \rightarrow \overline{\Lambda}\Lambda$ channel that are required to be equal by C invariance. The open points are offset slightly to the left to facilitate comparison. The errors are statistical only.

tified event is one that is assigned incorrectly to a reaction channel or is assigned the wrong value of $\cos\theta^*$. This misidentification fraction is a function of $\cos\theta^*$ and is discussed in Sec. 5.12.2. The constant of proportionality was chosen such that the χ^2, formed from the differences in the equality-constrained spin, has the correct distribution using the estimated systematic error. This systematic error is then added in quadrature with the statistical error to form the total error on each spin observable.

6.3.3 Final Reduced Spin Observables

Since C invariance is believed to be a good symmetry of the strong interaction, the equality constraints listed in Table 6.1 allow many of the spin observables to be com-

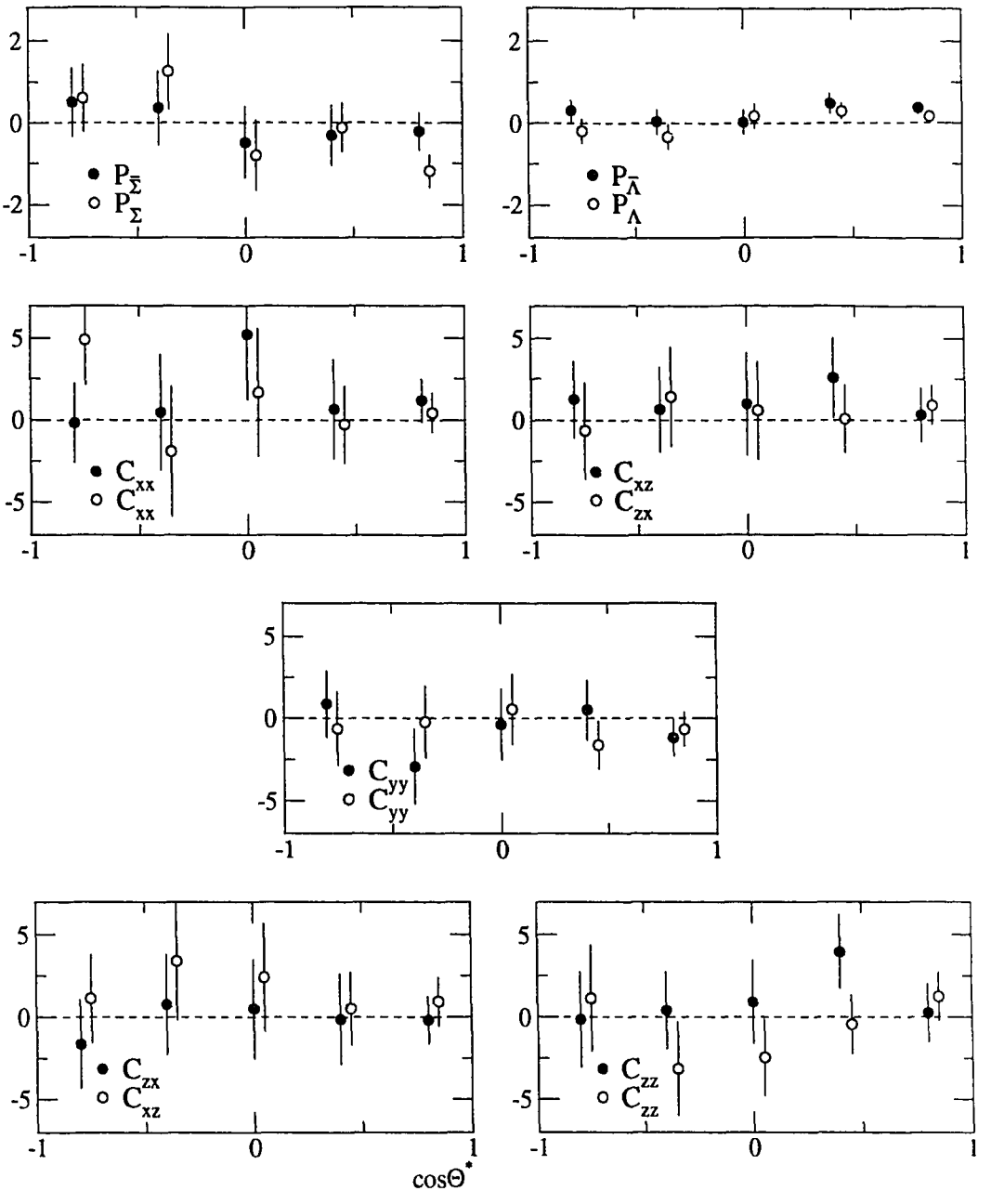

Figure 6.12: The spin observables for the $\overline{p}p \rightarrow \overline{\Sigma}^0\Lambda + c.c.$ channels that are required to be equal by C invariance. The closed points are the observables for $\overline{p}p \rightarrow \overline{\Sigma}^0\Lambda$. The open points are the observables for $\overline{p}p \rightarrow \overline{\Lambda}\Sigma^0$ and are offset to the left slightly to facilitate comparison. The errors are statistical only.

bined into a single averaged quantity. These quantities are combined using a weighted averaging procedure which considers the total errors. The naming conventions for the resulting averaged spin observables are also given in Table 6.1. This averaging procedure reduces the number of spin observables for the $\overline{p}p \rightarrow \overline{\Lambda}\Lambda$ channel from seven to five. And, the 14 total for the $\overline{p}p \rightarrow \overline{\Sigma}^0\Lambda$ and $\overline{p}p \rightarrow \overline{\Lambda}\Sigma^0$ channels is reduced to seven for the combined $\overline{p}p \rightarrow \overline{\Lambda}\Sigma^0 + c.c.$ channel.

These averaged spin observables for the $\overline{p}p \rightarrow \overline{\Lambda}\Lambda$ and $\overline{p}p \rightarrow \overline{\Sigma}^0\Lambda + c.c.$ channels will be shown together with the cross sections and a discussion of the results in Chapter 7.

Chapter 7

Results and Discussion

In this chapter, the final results of the $\bar{p}p \to \overline{\Lambda}\Lambda$ and $\bar{p}p \to \overline{\Sigma}^0\Lambda + c.c.$ measurement for the data set labeled with the extracted antiproton momentum of 1.729 GeV/c are reported. The observables include total and differential cross sections, hyperon polarizations, and spin correlation coefficients. In addition to these results, discussion and interpretations are offered.

7.1 Cross Sections

The average momentum at the center of the target was determined to be 1.726 ± 0.001 GeV/c (see Sec. 5.13.6). This corresponds to an excess energy value $\varepsilon = \sqrt{s} - m_{\overline{Y}} - m_Y$, the kinetic energy available to the final state hyperons, of 102.6 MeV for the $\bar{p}p \to \overline{\Lambda}\Lambda$ reaction and 25.7 MeV for $\bar{p}p \to \overline{\Sigma}^0\Lambda + c.c.$.

7.1.1 Results

The total cross sections measured for the $\bar{p}p \to \overline{\Lambda}\Lambda$, $\bar{p}p \to \overline{\Sigma}^0\Lambda$, $\bar{p}p \to \overline{\Lambda}\Sigma^0$ and $\bar{p}p \to \overline{\Sigma}^0\Lambda + c.c.$ combined reaction channels at an average antiproton momentum of 1.726 ± 0.001 GeV/c are listed in Table 7.1. The total cross sections for the $\bar{p}p \to \overline{\Lambda}\Lambda$ and $\bar{p}p \to \overline{\Sigma}^0\Lambda + c.c.$ reactions are shown together with previous PS185 results for these channels in Fig. 7.1.

The differential cross sections for $\bar{p}p \to \overline{\Lambda}\Lambda$ and $\bar{p}p \to \overline{\Sigma}^0\Lambda + c.c.$ are displayed

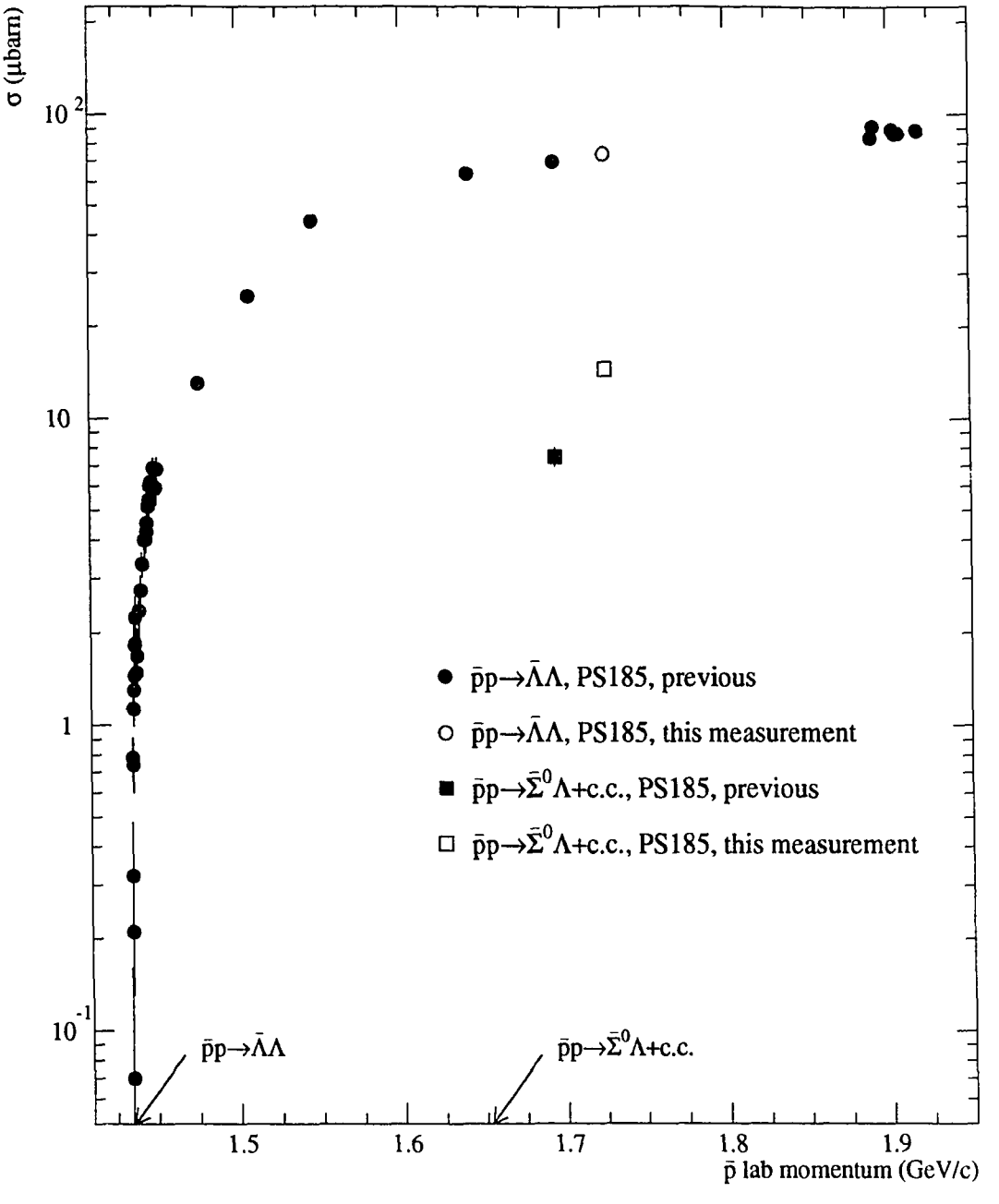

Figure 7.1: Total cross sections for the $\overline{p}p \to \overline{\Lambda}\Lambda$ and $\overline{p}p \to \overline{\Sigma}^0\Lambda + c.c.$ reactions from this measurement along with those reported previously by the PS185 collaboration. The arrows indicate the reaction thresholds.

$\bar{p}p \to \overline{Y}Y$ channel	cross section (μbarn)	statistical error (μbarn)	systematic error (μbarn)	total error (μbarn)
$\bar{p}p \to \overline{\Lambda}\Lambda$	74.36	0.80 (1.1%)	2.55 (3.4%)	2.67 (3.6%)
$\bar{p}p \to \overline{\Sigma}^0\Lambda$	6.99	0.19 (2.7%)	0.31 (4.4%)	0.36 (5.1%)
$\bar{p}p \to \overline{\Lambda}\Sigma^0$	7.61	0.19 (2.5%)	0.33 (4.4%)	0.38 (5.0%)
$\bar{p}p \to \overline{\Sigma}^0\Lambda + c.c.$	14.60	0.27 (1.8%)	0.64 (4.4%)	0.70 (4.8%)

Table 7.1: Total cross sections and errors, separated into statistical and systematic components for the $\bar{p}p \to \overline{Y}Y$ reactions of this study at an average antiproton lab momentum of 1.726 ± 0.001 GeV/c.

along with the angular dependent systematic error in Fig. 7.2. The other contributions to the systematic error result in a 2.6% uncertainty on the differential cross section scale (see Sec. 5.13.5).

7.1.2 Discussion

The most convenient way to examine these total cross section results is with the cross section ratio of the $\bar{p}p \to \overline{\Sigma}^0\Lambda + c.c.$ and $\bar{p}p \to \overline{\Lambda}\Lambda$ reactions. To eliminate, at least partially, the phase space differences between the two reactions, the ratio is best calculated at the same reaction excess energy values. The PS185 collaboration has measured the $\bar{p}p \to \overline{\Lambda}\Lambda$ reaction at approximately the same excess energy value as that for this measurement of $\bar{p}p \to \overline{\Sigma}^0\Lambda + c.c.$. In fact, this was the basis of the momentum choice for this measurement.

At 1.5076 GeV/c ($\varepsilon(\overline{\Lambda}\Lambda) = 25.4$ MeV), the $\bar{p}p \to \overline{\Lambda}\Lambda$ cross section was measured to be 25.1 ± 0.7 μbarn [24]. Using the results for the $\bar{p}p \to \overline{\Sigma}^0\Lambda + c.c.$ cross section at 1.726 GeV/c ($\varepsilon(\overline{\Sigma}^0\Lambda) = 25.7$ MeV) from this measurement to form the cross section ratio

$$\frac{\sigma(\Sigma^0\Lambda)}{\sigma(\overline{\Lambda}\Lambda)} = \frac{\sigma(\overline{\Lambda}\Sigma^0 + c.c.)/2}{\sigma(\overline{\Lambda}\Lambda)} \tag{7.1}$$

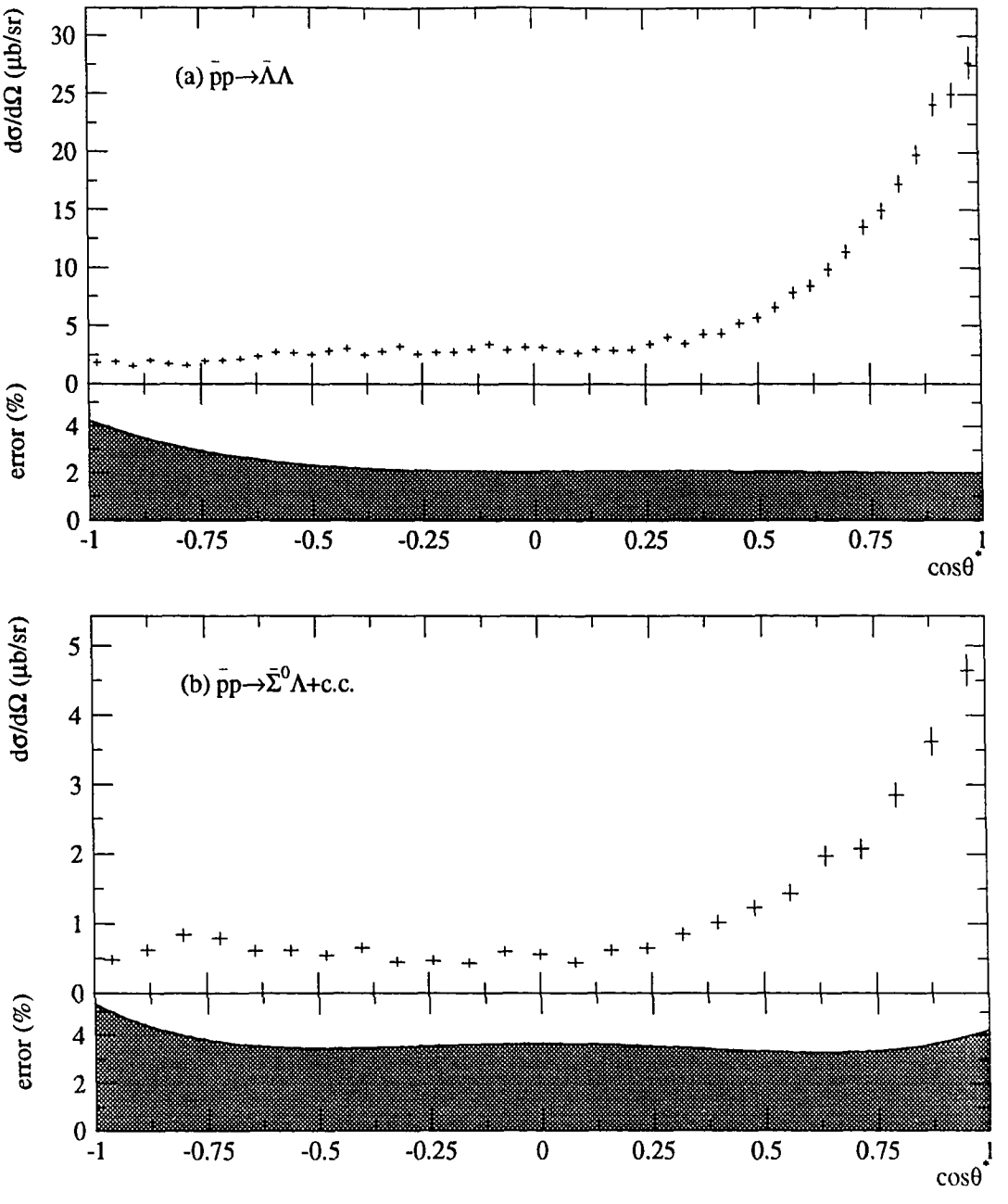

Figure 7.2: Differential cross sections for the (a) $\bar{p}p \to \bar{\Lambda}\Lambda$ reaction and (b) the $\bar{p}p \to \bar{\Sigma}^0\Lambda + c.c.$ combined reaction at an average antiproton momentum of 1.726 GeV/c. The angular dependent systematic error is plotted beneath each plot. The systematic error due of the target cell corrections combined with the uncertainty in the charged branching ratio of the Λ results in a error on the scale of 2.6% for both plots.

yields $\frac{\sigma(\Sigma^0\Lambda)}{\sigma(\overline{\Lambda}\Lambda)} = 0.29 \pm 0.02$. A naive calculation of this cross section ratio using the SU(3)-based ratio of the ΣpK to ΛpK coupling constants utilized by the Nijmegen group in their meson exchange calculation [37,80] yields

$$\frac{\sigma(\Sigma^0\Lambda)}{\sigma(\overline{\Lambda}\Lambda)} = \frac{f^2_{\Sigma NK}}{f^2_{\Lambda NK}} = 0.09. \tag{7.2}$$

Of course, this value is only a reference point since this simple calculation completely ignores the contribution from the K^*, interference effects between the K and K^*, and the initial and final state interactions, complications that are surely present in these reactions.

The PS185 collaboration has reported a total cross section for the $\overline{p}p \rightarrow \overline{\Sigma}^0\Lambda + c.c.$ reaction at another momentum point. At 1.695 GeV/c ($\varepsilon(\overline{\Sigma}^0\Lambda) = 14.8$ MeV) the $\overline{p}p \rightarrow \overline{\Sigma}^0\Lambda + c.c.$ cross section was measured to be 7.53 ± 0.53 μbarn [31]. This measurement was also done at an excess energy approximately equal to that from a previously measured $\overline{p}p \rightarrow \overline{\Lambda}\Lambda$ measurement. At 1.4765 GeV/c ($\varepsilon(\overline{\Lambda}\Lambda) = 14.4$ MeV) the $\overline{p}p \rightarrow \overline{\Lambda}\Lambda$ cross section was measured to be 13.0 ± 0.5 μbarn [24]. The cross section ratio resulting from these two measurements is also 0.29 ± 0.02.

Using a coupled channels meson exchange model, the group of Haidenbauer et al. has fit the $\overline{p}p \rightarrow \overline{\Sigma}^0\Lambda + c.c.$ data at 1.695 GeV/c and offered a prediction for the total cross section for $\overline{p}p \rightarrow \overline{\Sigma}^0\Lambda + c.c.$ at an excess energy value close to that of this measurement [59]. The cross section ratios at approximate excess energy values of 15 and 25 MeV resulting from this model are listed in Table 7.2 along with the measured values. The agreement of the data with the model prediction is fair. Haidenbauer et al. note that if the initial and final state interactions are neglected, the cross section ratios drop from these values to 0.08 at both excess energies. This points out the importance of considering the initial and final state effects carefully.

The differential cross sections for $\overline{p}p \rightarrow \overline{\Lambda}\Lambda$ and $\overline{p}p \rightarrow \overline{\Sigma}^0\Lambda + c.c.$ show the forward peaking that has come to be expected for these reactions. To quantify this, the

ε (MeV)	$\sigma(\overline{\Lambda}\Lambda)$ (μbarn)	$\sigma(\overline{\Lambda}\Sigma^0 + c.c.)$ (μbarn)	$\sigma(\Sigma^0\Lambda)/\sigma(\overline{\Lambda}\Lambda)$	comment
14.4	13.0 ± 0.5			experiment, [24]
14.8		7.53 ± 0.5		experiment, [31]
14.6			0.29 ± 0.02	experiment
14.8	15.06	7.84	0.26	model, [59]
25.4	25.1 ± 0.7			experiment, [24]
25.7		14.60 ± 0.70		experiment, this work
25.6			0.29 ± 0.02	experiment
24.0	25.08	11.38	0.23	model, [59]

Table 7.2: Total cross sections ratios from experiment and the model of Haidenbauer et al. [59] at $\varepsilon \approx 15$ and 25 MeV.

differential cross section data were fit with a function of the form

$$\frac{d\sigma}{d\Omega}(\theta^*) = \sum_{k=0}^{k_{\max}} a_k P_k(\cos\theta^*), \tag{7.3}$$

where the P_k are Legendre polynomials. The data were fit to this form using increasing values of $k_{\max}$ until the addition of more terms failed to improve the quality of the fit considerably. Both the $\bar{p}p \to \overline{\Lambda}\Lambda$ and $\bar{p}p \to \overline{\Sigma}^0\Lambda + c.c.$ data were well fit with these forms with $k_{\max} = 5$. The data with the fits are shown in Fig. 7.3. The parameters of these fits are listed in Table 7.3. It is interesting that the fits to the $\bar{p}p \to \overline{\Sigma}^0\Lambda + c.c.$ data with $\varepsilon(\overline{\Sigma}^0\Lambda) = 25.7$ MeV required as many terms as the $\bar{p}p \to \overline{\Lambda}\Lambda$ data with $\varepsilon(\overline{\Lambda}\Lambda) = 102.6$ MeV. However, interpretations should be made with caution since the statistical errors on this data are such that the uncertainty on the terms of the Legendre fit are rather large.

It is instructive to compare the differential cross section data at similar values of excess energy, as was done with the total cross sections, and to examine them in the context of the black disk model of scattering [32, 33]. Figure 7.4 shows this

channel	$\overline{p}p \to \overline{\Lambda}\Lambda$	$\overline{p}p \to \overline{\Sigma}^0\Lambda + c.c.$
$k_{\max}$	5	5
$X^2_{\rm red}$	0.74	0.94
$\sigma = 4\pi a_0$	74.324 ± 0.787	14.532 ± 0.272
a_0	5.915 ± 0.063	1.156 ± 0.022
a_1/a_0	1.421 ± 0.017	1.170 ± 0.033
a_2/a_0	1.340 ± 0.025	1.256 ± 0.044
a_3/a_0	1.009 ± 0.032	0.736 ± 0.056
a_4/a_0	0.426 ± 0.034	0.153 ± 0.061
a_5/a_0	0.018 ± 0.031	0.184 ± 0.060

Table 7.3: The parameters of the Legendre fits to the $\overline{p}p \to \overline{\Lambda}\Lambda$ and $\overline{p}p \to \overline{\Sigma}^0\Lambda + c.c.$ data.

differential cross section data in the form of $\frac{d\sigma}{dt'}$ for the $\overline{p}p \to \overline{\Lambda}\Lambda$ and $\overline{p}p \to \overline{\Sigma}^0\Lambda + c.c.$ reactions at excess energy values of approximately 15 and 25 MeV. Here t' is the reduced four momentum transfer. This quantity is defined,

$$t' \equiv t - t_{\rm min} = 2pq(\cos\theta^* - 1), \tag{7.4}$$

where t is the four momentum transfer (squared) and p and q are the incoming and outgoing c.m. momenta respectively. In the black disk model, $\frac{d\sigma}{dt'}$ should have the form $e^{-bt'}$. The fits of this form to the forward data for the four data sets are shown in Fig. 7.4. The radius of the black disk is given by $R = 2\hbar c\sqrt{b}$. The parameters and resulting black disk radii for each of the fits are listed in Table 7.4.

The data are well fit by this form in the forward $\cos\theta^*$ region as can be seen from examination of Fig. 7.4. The strong forward peaking noticed in the $\overline{p}p \to \overline{\Sigma}^0\Lambda + c.c.$ channel shows itself in these plots as a fairly steep slope of the fit to the data of this channel. The resulting black disk radii are 1.1–1.2 fm for $\overline{p}p \to \overline{\Lambda}\Lambda$ while the $\overline{p}p \to \overline{\Sigma}^0\Lambda + c.c.$ data yield a radii of 1.3–1.5 fm. This result of the consistently larger

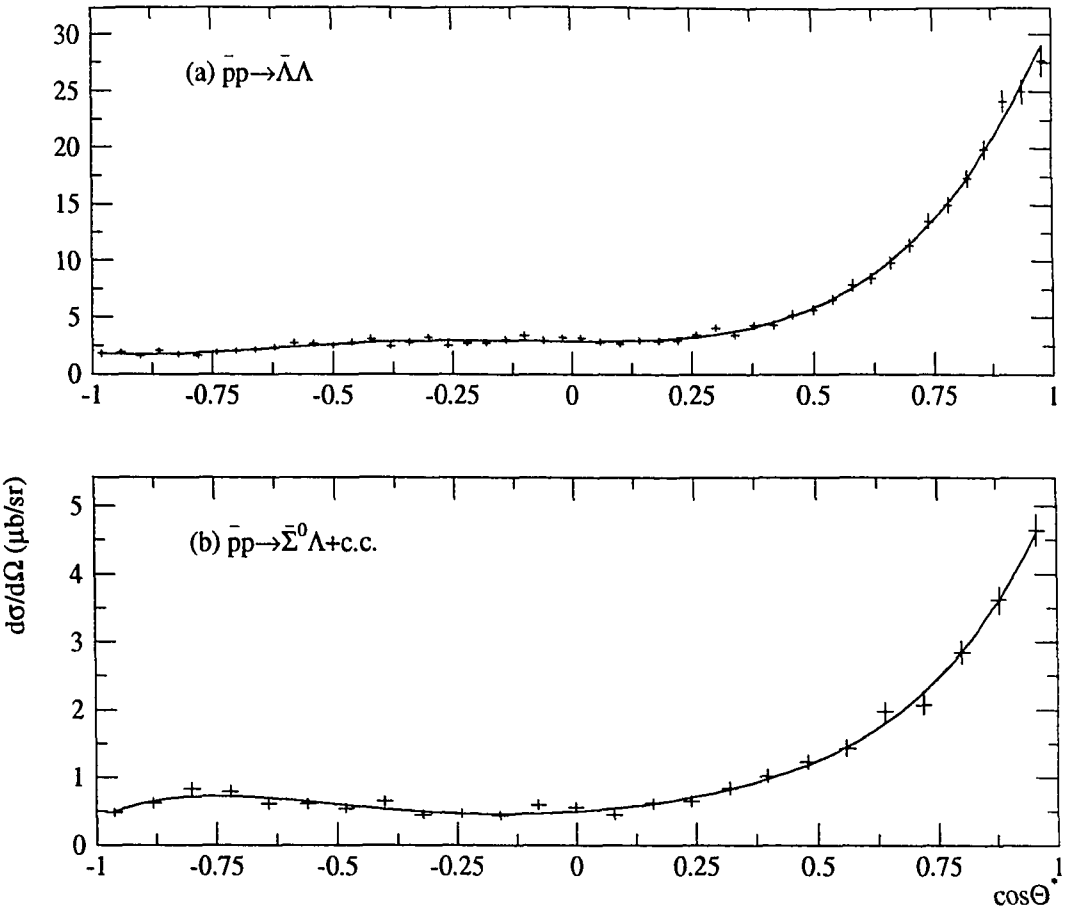

Figure 7.3: Differential cross sections for the (a) $\overline{p}p \to \overline{\Lambda}\Lambda$ reaction and (b) the $\overline{p}p \to \overline{\Sigma}^0\Lambda + c.c.$ combined reaction at an average antiproton momentum of 1.726 GeV/c. The curves are from a Legendre polynomial fit including terms up to order five.

values in the $\overline{p}p \to \overline{\Sigma}^0\Lambda + c.c.$ channels is interesting. It perhaps implies an even stronger absorption of the lower partial waves in this new channel.

7.2 Spin Observables

The averaged spin observables for the $\overline{p}p \to \overline{\Lambda}\Lambda$ and $\overline{p}p \to \overline{\Sigma}^0\Lambda + c.c.$ reactions at an average antiproton momentum of 1.726 ± 0.001 GeV/c are shown in Figs. 7.5 and

	$\overline{p}p \to \overline{\Lambda}\Lambda$		$\overline{p}p \to \overline{\Sigma}^0\Lambda + c.c.$		
ε (MeV)	b (GeV^{-2})	R (fm)	b (GeV^{-2})	R (fm)	reference
14.4	9.7 ± 0.9	1.2			[24]
14.8			14.1 ± 1.5	1.5	[31]
25.4	8.1 ± 0.6	1.1			[24]
25.7			11.0 ± 0.4	1.3	this work

Table 7.4: Results of the fits to the $\overline{p}p \to \overline{\Lambda}\Lambda$ and $\overline{p}p \to \overline{\Sigma}^0\Lambda + c.c.$ using the black disk form.

7.6. The quantities averaged to obtain these results and the naming conventions are listed in Table 6.1.

The $\overline{p}p \to \overline{\Lambda}\Lambda$ and $\overline{p}p \to \overline{\Lambda}\Sigma^0 + c.c.$ singlet fractions are shown in Fig 7.7. They are calculated using the averaged C_{ii} in the singlet fraction definition:

$$S = \frac{1}{4}(1 + C_{xx} - C_{yy} + C_{zz}). \tag{7.5}$$

The total errors on the C_{ii} are propagated through this equation to yield the errors on the singlet fraction.

7.2.1 Discussion

The spin observable data from the $\overline{p}p \to \overline{\Lambda}\Lambda$ reaction at 1.726 GeV/c is consistent with what has been observed in previous measurements. In particular, the oscillatory behavior of the polarization data has been consistently observed throughout the entire PS185 momentum range. It is interesting to compare the shape of the polarization data to that of the differential cross section. The $\overline{p}p \to \overline{\Lambda}\Lambda$ differential cross section and Λ polarization are shown together on the same plot as a function of t' in Fig. 7.8. The break in the $e^{-bt'}$ behavior of the differential cross section occurs in the same region of t' as the indicated zero crossing of the polarization. This same behavior occurs in all of the PS185 data and at approximately the same value of t'.

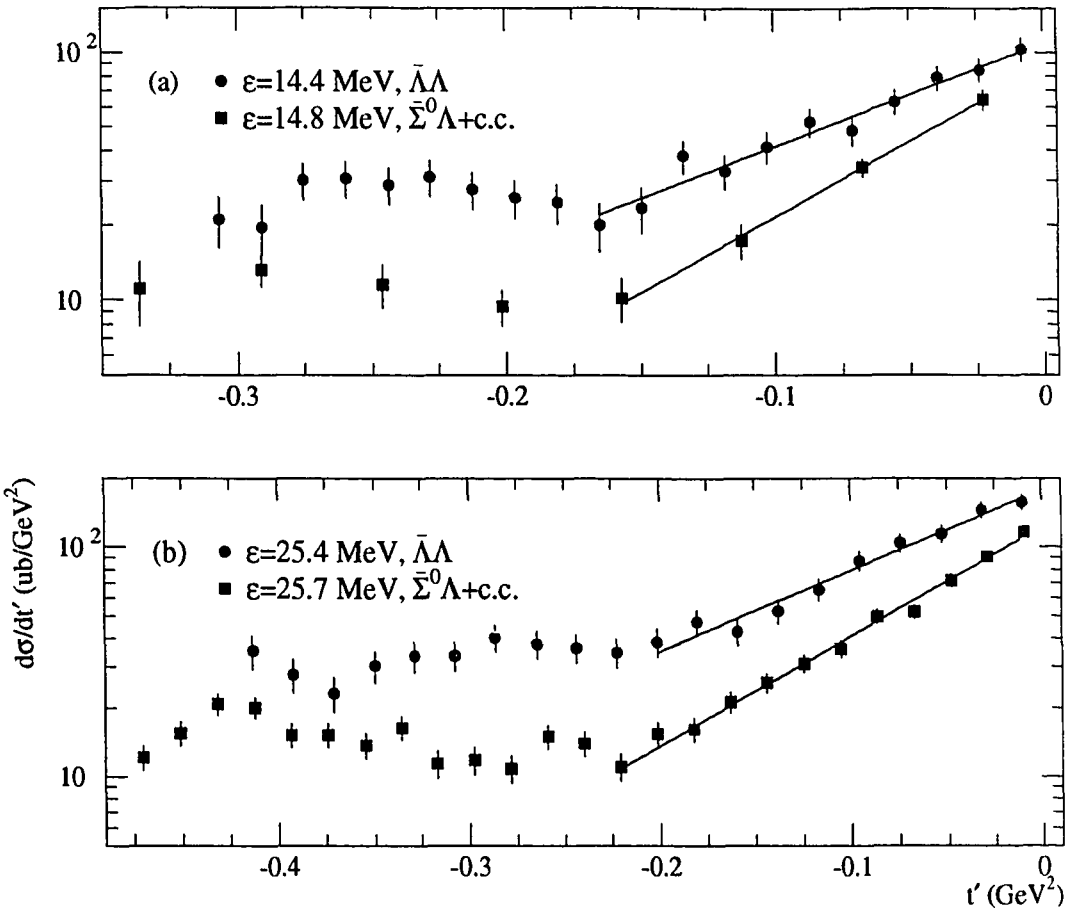

Figure 7.4: Differential cross sections $\frac{d\sigma}{dt'}$ for the $\overline{p}p \rightarrow \overline{\Lambda}\Lambda$ and $\overline{p}p \rightarrow \overline{\Sigma}^0\Lambda + c.c.$ reactions at approximate excess energy values of (a) 15 and (b) 25 MeV. Note the logarithmic scale.

As mentioned in Chapter 1, this correlation is observed in other hadron scattering processes and may be related to the distance scale of the interaction [34,35].

The spin correlation coefficients of $\overline{p}p \rightarrow \overline{\Lambda}\Lambda$ at 1.726 GeV/c indicate a behavior similar to that seen in the other PS185 $\overline{p}p \rightarrow \overline{\Lambda}\Lambda$ measurements. The singlet fraction shows little deviation from zero as has consistently been seen. The weighted average of the singlet fraction over the entire $\cos\theta^*$ range yields a value of -0.08 ± 0.05.

The spin observables from the $\overline{p}p \rightarrow \overline{\Sigma}^0\Lambda + c.c.$ reaction, with the exception

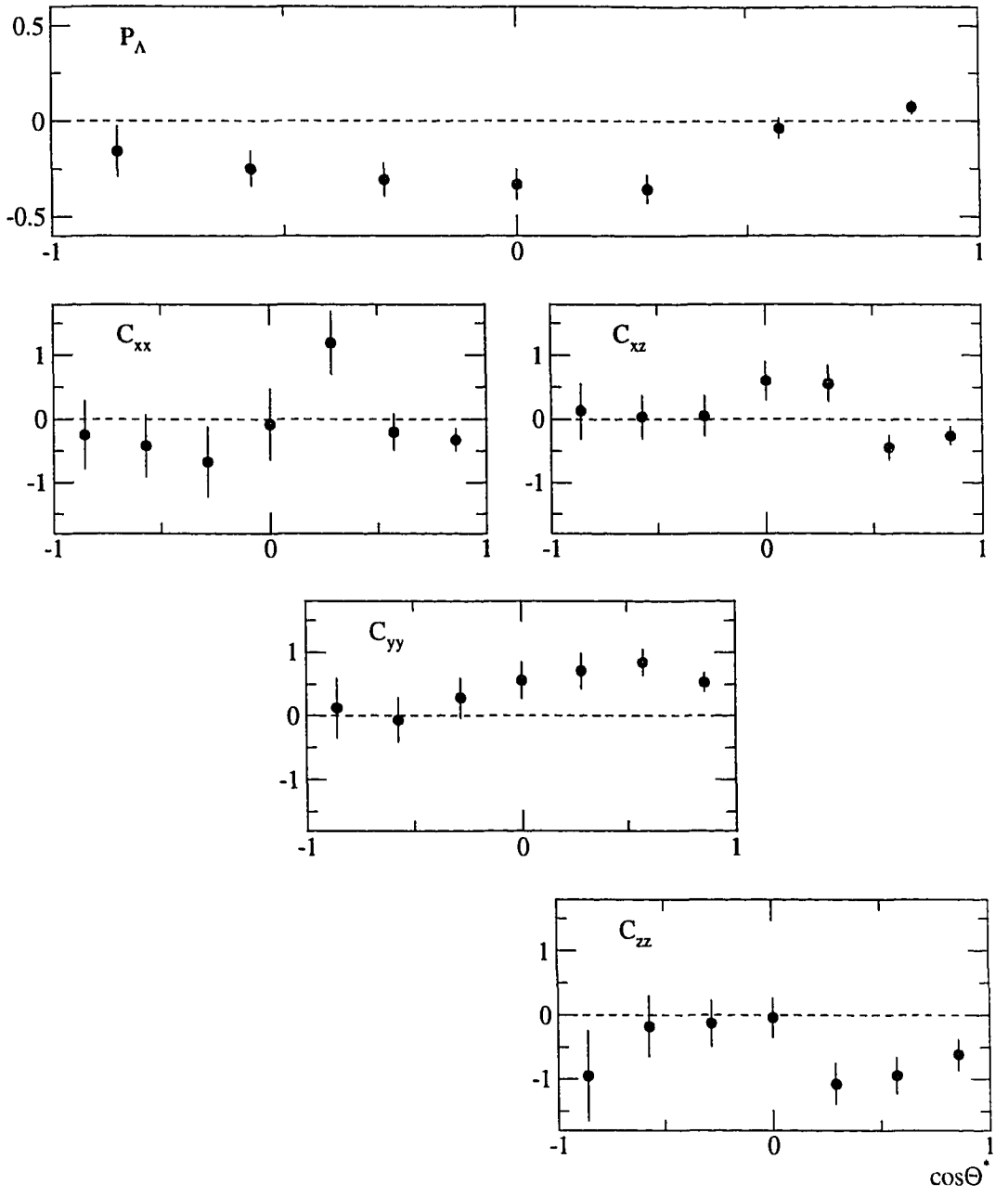

Figure 7.5: The average polarizations and spin correlation coefficients for the $\overline{p}p \rightarrow \overline{\Lambda}\Lambda$ reaction. Systematic errors are included.

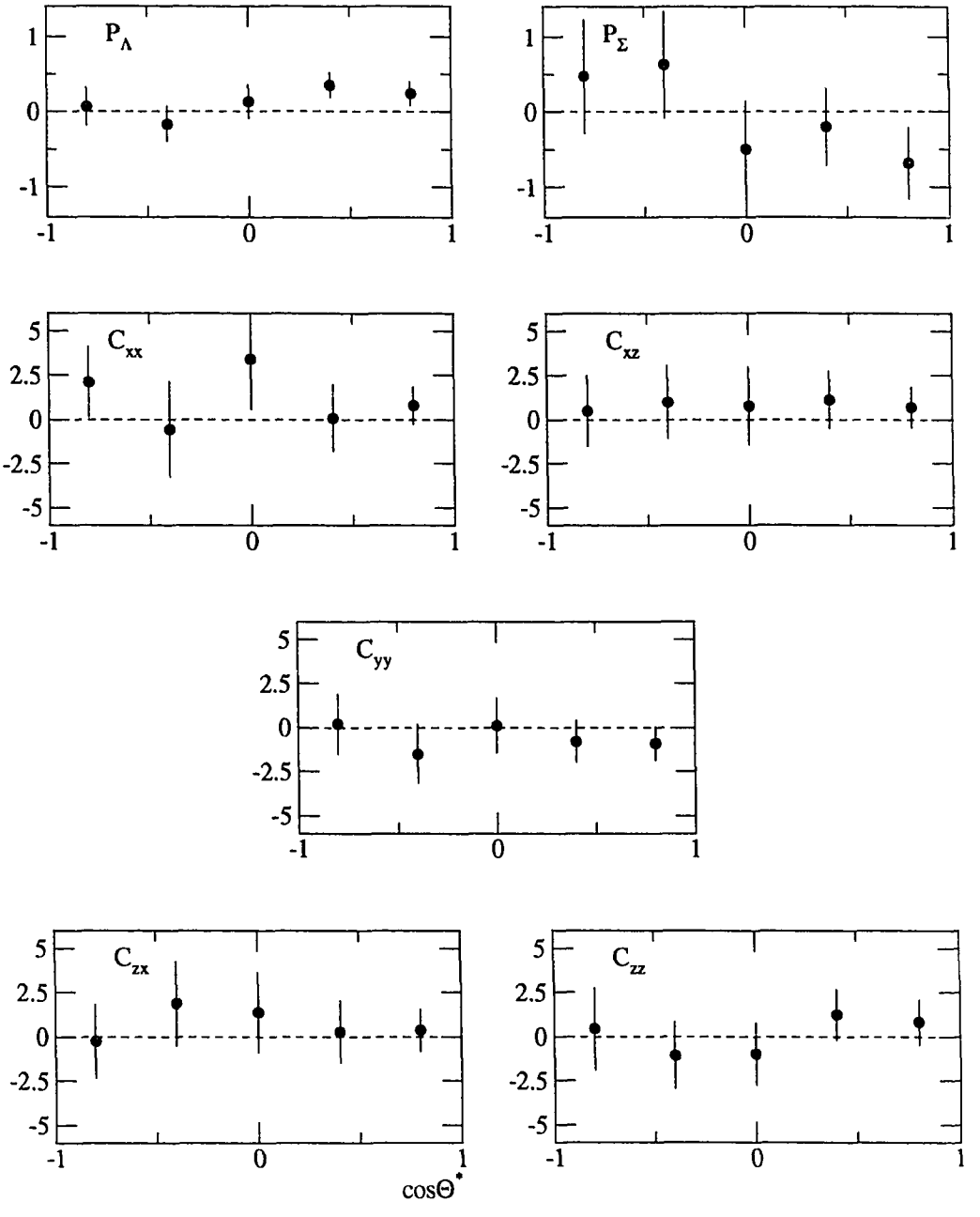

Figure 7.6: The average polarizations and spin correlation coefficients for the $\bar{p}p \to \bar{\Sigma}^0\Lambda + c.c.$ reaction. Systematic errors are included.

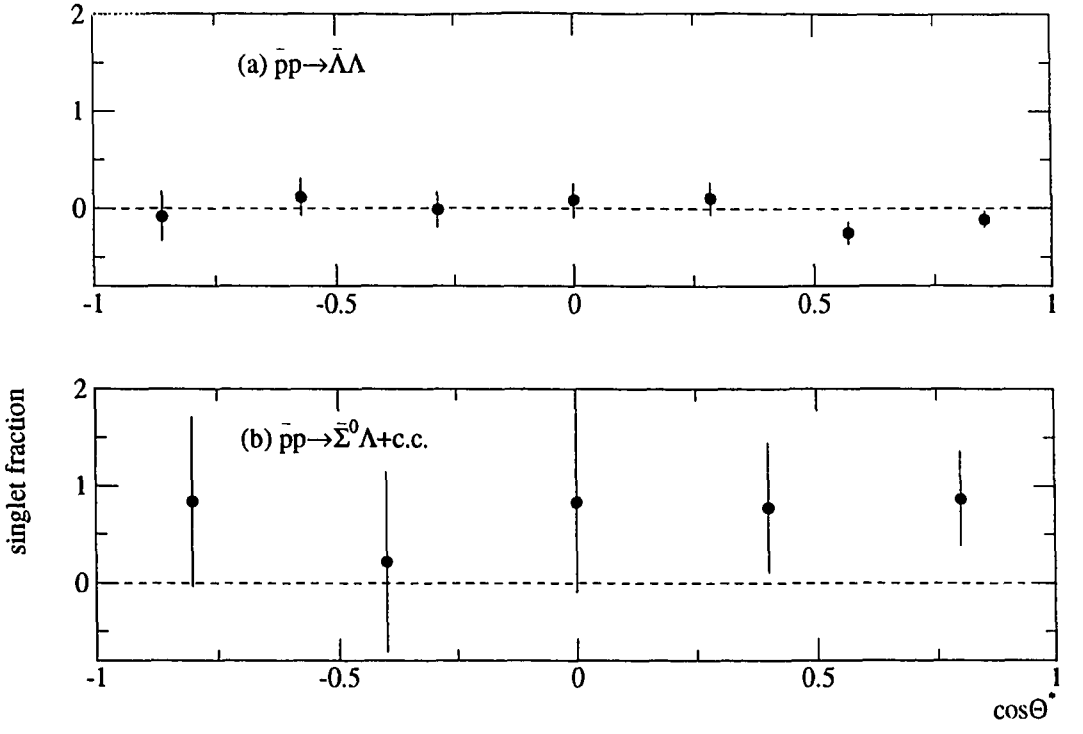

Figure 7.7: Singlet fraction for the (a) $\overline{p}p \to \overline{\Lambda}\Lambda$ and (b) $\overline{p}p \to \overline{\Lambda}\Sigma^0 + c.c.$ reactions. Systematic errors are included. The dashed line indicates zero and is not a fit.

of the data from 1.695 GeV/c [31] which included only statistically poor hyperon polarization results, provides the first look at this aspect of the reaction. The Λ polarization seems to indicate an oscillatory structure not entirely unlike that seen for the $\overline{p}p \to \overline{\Lambda}\Lambda$ channel. The differential cross section data and Λ polarization from $\overline{p}p \to \overline{\Sigma^0}\Lambda + c.c.$ are plotted together as a function of t' in Fig. 7.9. There is perhaps an indication of a zero crossing in the polarization at the same t' as the break in the $e^{-bt'}$ behavior of the differential cross section.

The Σ polarization data suffers from large statistical errors. They are larger than for the Λ polarization for this reaction because of the factor of $-\frac{1}{3}$ that arises due to the dilution of the polarization in the Σ^0 decay. In addition, if, as predicted by a non-relativistic quark model, the Σ^0 polarization is $\frac{1}{3}$ that of the Λ, there is little

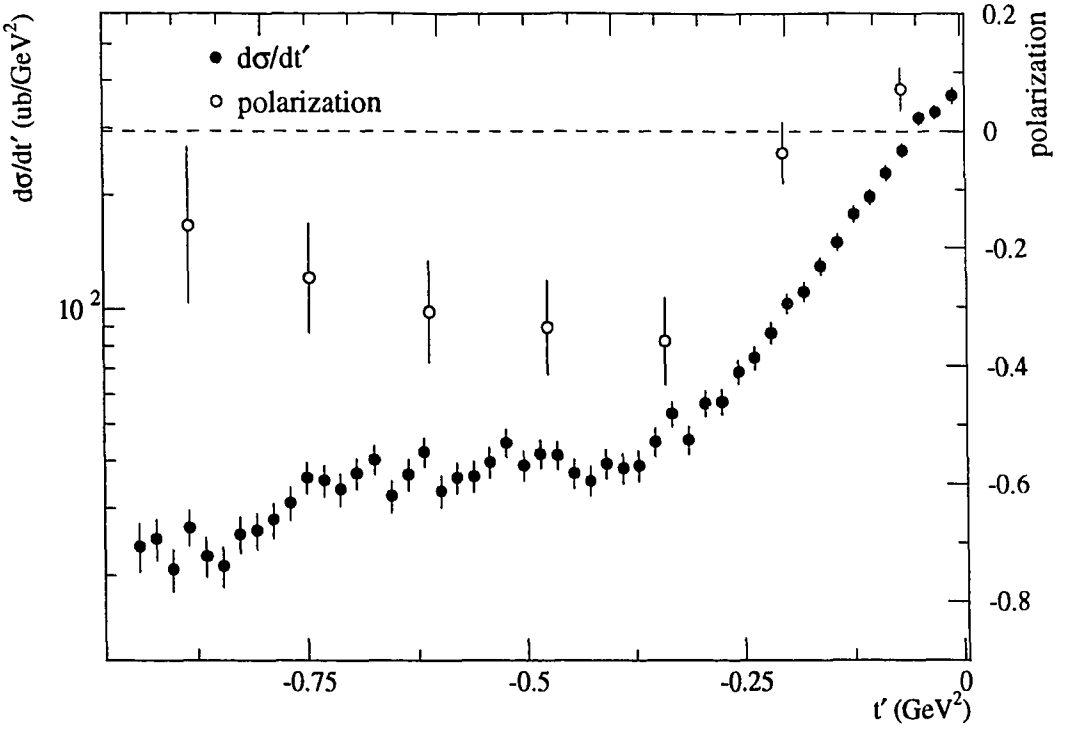

Figure 7.8: Differential cross section and Λ polarization for the $\bar{p}p \rightarrow \overline{\Lambda}\Lambda$ reaction at 1.729 GeV/c as a function of t'.

possibility of ever having the sensitivity to measure a value this small with these methods.

Little can be concluded from the $\bar{p}p \rightarrow \overline{\Sigma}^0\Lambda + c.c.$ spin correlation coefficients due to the large errors. Any predicted behavior of these observables that lies within the physical limits would be consistent with the data. The singlet fraction, since it is derived from the C_{ii}, has fairly large errors as well. However, the weighted average over the entire $\cos\theta^*$ range yields 0.76 ± 0.31. This is an indication that the well-established spin-triplet dominance of the $\bar{p}p \rightarrow \overline{\Lambda}\Lambda$ reaction does not carry over into the $\bar{p}p \rightarrow \overline{\Sigma}^0\Lambda + c.c.$ channel. This value is consistent with the quark model prediction of $\frac{3}{7}$ that results from a vector [48] or scalar [62] $\bar{s}s$ quark pair production mechanism. The group of Haidenbauer et al. have calculated a singlet fraction value

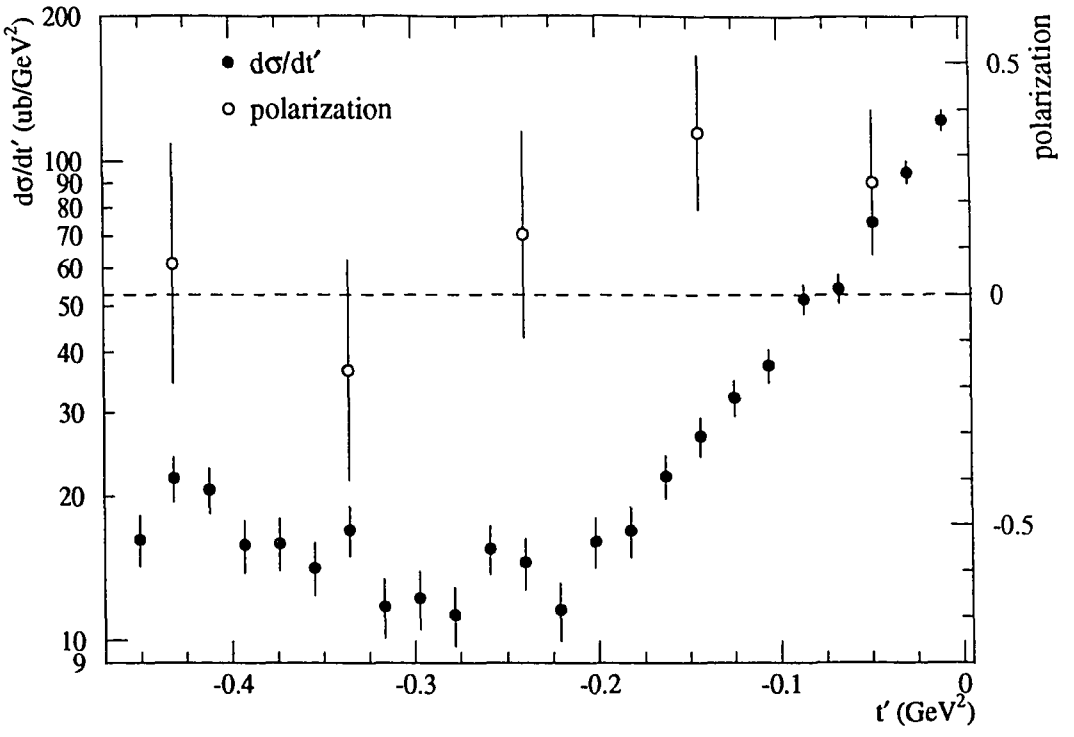

Figure 7.9: Differential cross section and Λ polarization for the $\bar{p}p \rightarrow \overline{\Sigma}^0\Lambda$ reaction at 1.729 GeV/c as a function of t'.

of 0.2 at 1.695 GeV/c. It is not evident how the the singlet fraction changes with momentum in the meson exchange calculation.

7.3 Summary

The results for the $\bar{p}p \rightarrow \overline{\Lambda}\Lambda$ reaction at 1.726 GeV/c average antiproton momentum show a behavior similar to that of the data collected by the PS185 experiment. This behavior includes a forward peaked differential cross section, an oscillatory structure of the Λ polarization with a zero crossing at a t' value approximately equal to the beginning of the sharp rise in the differential cross section, and a singlet fraction consistent with zero throughout the entire $\cos\theta^*$ range.

The new results for the $\bar{p}p \rightarrow \overline{\Sigma}^0\Lambda + c.c.$ reaction at this momentum share some

of the features of the $\bar{p}p \rightarrow \overline{\Lambda}\Lambda$ data. These include a forward peaked differential cross section and an indication of a similar oscillatory behavior of the Λ polarization. However, in the $\bar{p}p \rightarrow \overline{\Sigma}^0\Lambda + c.c.$ channel, the forward peaking of the differential cross section appears to be even stronger than that of $\bar{p}p \rightarrow \overline{\Lambda}\Lambda$ at the same excess energy value, perhaps indicating more absorption in the lower partial waves. The singlet fraction data indicates a non zero value, in contrast to the $\bar{p}p \rightarrow \overline{\Lambda}\Lambda$ data and as predicted by several models. This result is perhaps the best example of the different dynamics of the $\bar{p}p \rightarrow \overline{\Sigma}^0\Lambda + c.c.$ reaction. Hopefully, this measurement will spur on further theoretical work on this channel to directly address these results.

Chapter 8

Conclusions

We have reported in this thesis the motivation, explanation, execution, and results of a measurement of the $\overline{p}p \rightarrow \overline{\Lambda}\Lambda$ and $\overline{p}p \rightarrow \overline{\Sigma}^0\Lambda + c.c.$ reactions at an average antiproton momentum of 1.726 GeV/c. The results show, for the $\overline{p}p \rightarrow \overline{\Lambda}\Lambda$ reaction, a strongly peaked differential cross section, substantial polarization, and a zero singlet fraction. These are all consistent with what has come to be considered characteristic of this reaction in this low energy region.

The results for the $\overline{p}p \rightarrow \overline{\Sigma}^0\Lambda + c.c.$ reaction show several features that are similar to $\overline{p}p \rightarrow \overline{\Lambda}\Lambda$ and several that different. The forward peaking is present although it seems to be even stronger than $\overline{p}p \rightarrow \overline{\Lambda}\Lambda$. The Λ polarization in the $\overline{p}p \rightarrow \overline{\Sigma}^0\Lambda + c.c.$ reactions indicates an oscillatory structure similar to that of $\overline{p}p \rightarrow \overline{\Lambda}\Lambda$; however, the errors on this data prevent any definitive conclusions. The singlet fraction, in strong contrast to $\overline{p}p \rightarrow \overline{\Lambda}\Lambda$, shows a non-zero value in the $\overline{p}p \rightarrow \overline{\Sigma}^0\Lambda + c.c.$ channel. The spin-triplet dominance of the $\overline{p}p \rightarrow \overline{\Lambda}\Lambda$ channel appears to not carry over into $\overline{p}p \rightarrow \overline{\Sigma}^0\Lambda + c.c.$.

All of these speculations about the implications of the new results from the $\overline{p}p \rightarrow \overline{\Sigma}^0\Lambda + c.c.$ need to be substantiated by careful theoretical work. The strong interaction is a complicated process; there are many factors to consider and a seemingly valid argument may be invalidated due to the neglect of something important. It is our hope that this data provides the experimental constraints for this theoretical work.

The PS185 collaboration has collected data at other momenta that were not analyzed and presented here. There exists data at 1.767 GeV/c, a point higher than that of this measurement, and at four momenta closer to threshold. The techniques and computer code used for this measurement are directly applicable to analyze this additional data and extract the observables for the $\overline{p}p \rightarrow \overline{\Sigma}^0\Lambda + c.c.$ reaction. This will be initiated in the near future.

The data of this measurement and those to be analyzed will provide a very complete set for the $\overline{p}p \rightarrow \overline{\Sigma}^0\Lambda + c.c.$ reaction as has been collected by PS185 for $\overline{p}p \rightarrow \overline{\Lambda}\Lambda$. It is hoped that this will enable further advances in understanding the dynamics of strange hyperon production and the strong interaction.

Appendix A

Drift Chamber Calibration

The purpose of the drift chamber calibration procedure is to determine the drift chamber time to distance function and to determine the position of the drift chamber wire planes. Both of these are needed to obtain optimum tracking accuracy.

A.1 Event Selection and Procedure

For the DC calibration procedure, neutral trigger events are used. It has been determined that this trigger type is preferable to the other event trigger types (such as elastic) because of the larger number of tracks with angles greater than 30°. Large-angle tracks are necessary because the time to distance function has a fairly complicated angular behavior and it is important to examine this behavior with a wide range of track angles. Also, as is described below, the large-angle tracks enable a better determination of the chamber positions.

From the neutral trigger data, events are selected that contain one or more three dimensional (3D) tracks. For a 3D track to be considered, it must be formed from all four possible two dimensional (2D) projections (xz, yz, uz, and vz) . These are called "4-match" tracks. By working with 4-match tracks exclusively, the sample is likely to contain fewer spurious tracks even with the tracking tolerances set to large values. These large values are necessary when using the rough first guesses for the calibration parameters and chamber positions.

With each of the 4-match tracks, the two 2D projections formed with the DC (xz and yz) are removed. The remaining two 2D projections (uz and vz) from the MWPC are then used to form a new 3D track. This track is projected into the drift chamber and the intersection point with each DC plane ($x_{\rm fit}$) is compared to the measured coordinate from the removed 2D track at that plane ($x_{\rm meas}$). This is quantified for each drift cell by defining the residual:

$$\delta \equiv \kappa(x_{\rm meas} - x_{\rm fit}), \tag{A.1}$$

where κ is ± 1 depending on the direction of the drift in that drift cell.

Another quantity examined is the "modified residual" δ', which is given by the same formula but with a slightly different definition for $x_{\rm fit}$. Instead of using the 3D track from the MWPC projections, $x_{\rm fit}$ is defined by the 2D track of the xz or yz DC projection alone, with the measured hit removed.

The quantity δ is used to make sure that the DC calibration and position is consistent with the MWPC. But, the extrapolation of the track from the MWPC into the DC adds error to the distributions and it is not possible to check precisely the calibration with this quantity alone. The quantity δ', since it involves interpolations or small extrapolations of tracks, better allows the details of the DC behavior to be seen. However, this quantity cannot be used alone because it is possible that the calibration converges with values that make the δ' distributions look correct, but with the resulting DC coordinates systematically offset from those of the MWPC. Both δ and δ' are used in the calibration and positioning procedures.

A.2 First Iteration

A simple geometrical approximation [90] for the time to distance function is used for the first iteration of the calibration. It is based on the assumption that the ionization electrons that reach the sense wire first (and therefore determine the drift time) drift toward the sense wire on a line that is perpendicular to the particle track. For tracks

that cross the drift cell at an angle, it is possible that this line intersects the track outside of the drift cell. In this case it is assumed that the electrons drift along the edge of the cell until they reach the track perpendicular and then they drift radially toward the sense wire. These two situations are diagrammed in Fig. A.1. With this simple scenario, the time to distance function is

$$\begin{aligned} s &= \frac{w(t-t_0)}{\cos\theta} && \text{for} \quad (t-t_0) \leq \frac{d}{w\sin\theta} \\ s &= w(t-t_0) + \frac{d}{\sin\theta}\left(\frac{1}{\cos\theta} - 1\right) && \text{for} \quad (t-t_0) \geq \frac{d}{w\sin\theta}. \end{aligned} \tag{A.2}$$

Here t is the time of the hit, t_0 is the time offset for a particular drift cell, w is the drift speed, θ is the track angle of incidence with the center line of the chamber, and d is the half-width of the drift cell. The subtraction of t_0 is necessary due to the fact that there is an offset in the drift chamber TDC values. The actual drift time is $t - t_0$ and t_0 is the time corresponding to zero drift distance. The quantity s is the distance from the sense wire to the point where the track intersects the center line of the chamber (see Fig A.1). This choice of parameterization allows a hit to be specified by a coordinate along the chamber plane with an error and the z of that plane, assumed to have no error. All coordinates from a given plane have the same value for z.

In terms of the quantities introduced above, the drift chamber calibration procedure must determine:

- the time offsets t_0 for each DC drift cell;
- the drift speed w, assumed to be the same for all cells;
- the correct time to distance function, the same for all cells; and
- the x/y and z positions of each plane of the DC.

For the first iteration of the calibration, the t_0 values were determined by examining the time distributions of each drift cell. These distributions exhibit a rough

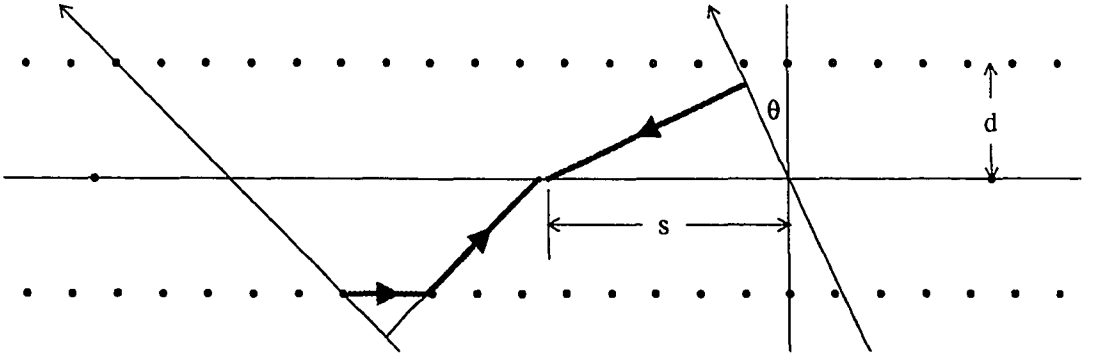

Figure A.1: Diagram illustrating the simple geometric approximation for the drift chamber time to distance calibration.

"top-hat" shape and indicate the active time-width of the cell. The first guess t_0 was set to the midpoint of the low-time edge of the top-hat, for each drift chamber cell. Figure A.2 shows the distributions from two typical drift cells and the position of the first-iteration t_0 set for these cells. The first-iteration drift speed was set to the value expected for the drift chamber gas mixture, $w = 50$ μm/ns $= 100$ μm/channel [90]. The time to distance function of Eq. A.2 was used with the parameters mentioned above for the first iteration and the wire plane positions were set to the nominal values as surveyed.

A.3 Subsequent Iterations

For each iteration of the calibration procedure, the selected tracks in the calibration sample were used to calculate the δ and δ' values. These values were stored for each time channel of each drift cell. After each run through the sample, the stored values were used to obtain a δ averaged over tracks for each time channel and drift cell. The averaged δ values for the same drift cells used in Fig. A.2 are shown in Fig. A.3 for the first and final iterations. For the two inner cells of each DC plane (closest to the beam), this data was fit to a straight line. The value of the fitted line at the

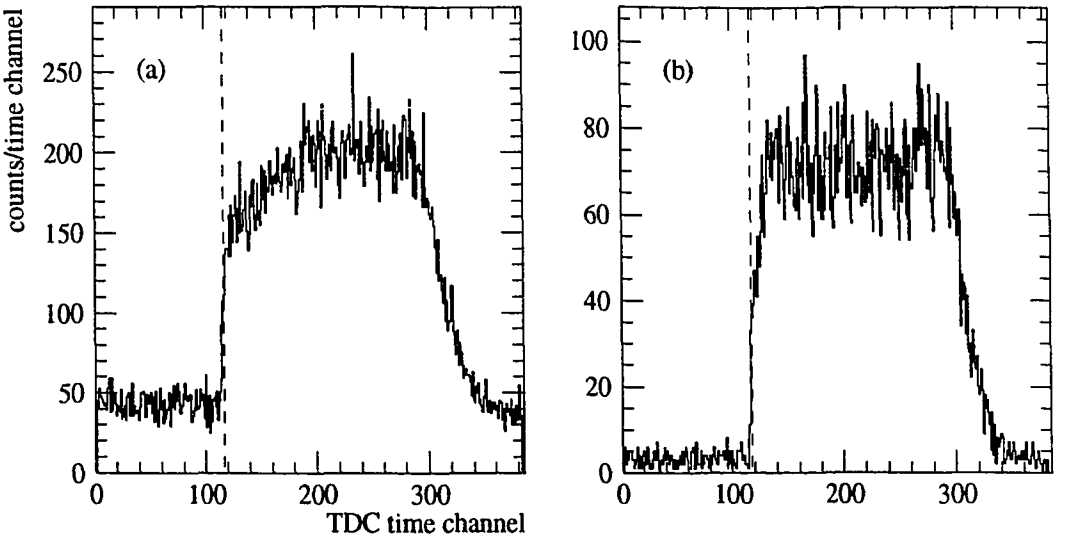

Figure A.2: Drift time distribution for two drift chamber cells. They are from (a) DC plane 5, cell 14, near the center of the chamber, and (b) DC plane 9, cell 4, near the edge . The dashed lines indicate the first-iteration t_0 values.

center of the cell determined the correction to the t_0 values for these inner cells. The slope of the line, averaged over all the inner cells, determined the correction to the drift speed. Only the inner cells were used to determine the drift speed because the majority of tracks through these cells are incident at $\theta = 0\,\mathrm{deg}$, where the time to distance function is most sensitive to this quantity. The remaining cells were fit to a line with zero slope (a weighted average) and the intercept determined the correction to t_0 for these cells. The dashed lines of Fig. A.3 indicate the results of these fits.

The δ' values as calculated from the event sample were stored as a function of time channel and track angle θ. The distributions were then examined to investigate the accuracy of time to distance function. By examining δ' as a function of θ, the quality of the time to distance function for a range of track angles could be evaluated.

The corrections to the positions of the chamber wire planes were determined for each iteration by examining the behavior of the corrected t_0 values for each pair of sense wires as a function of the position in the plane. Effectively all of the tracks

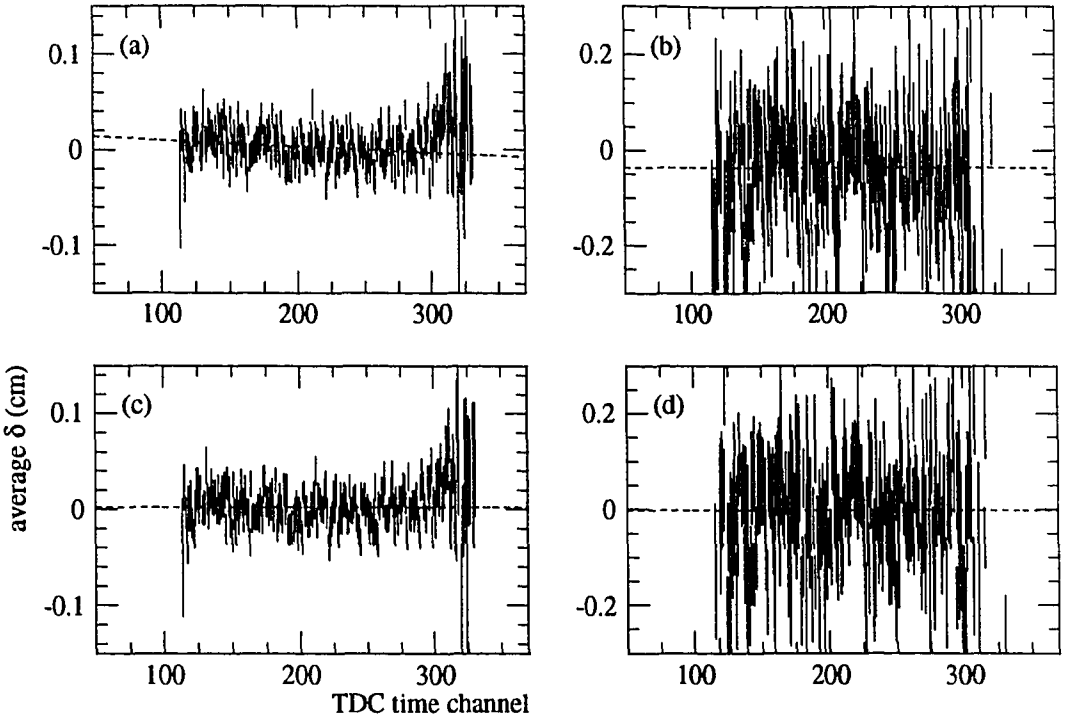

Figure A.3: Average δ as a function of time channel for (a) plane 5, cell 14 and (b) plane 9, cell 4 for the first iteration on the calibration procedure, and (c),(d) the same cells after the final iteration. The error bars indicate the statistical error on each point. The dashed lines show the fit to the distribution.

in the event sample originate near the target, so a given position along the chamber plane can be mapped to a track angle. The difference between the t_0 values of each sense wire pair should be normally distributed around a mean value and not correlated with the angle of tracks through the drift cell. If this correlation is seen, it must be due to the an incorrect position of the wire chamber plane, in x,y or z or both. The correlations were examined, parameterized with coordinate offsets, and the corrections generated.

After each run through the calibration event sample, the corrections were calculated and then implemented for the next iteration. This process was repeated until the procedures yielded negligible corrections. Many iterations were needed to deter-

mine the correct time to distance function because it is a multi-parameter function and it was determined principally by trial and error. If the correct function is known beforehand, the time offsets, drift speed, and chamber positions may be determined in two or three iterations.

A.4 Results

The time to distance function that was determined to be satisfactory is of the same form but somewhat more complicated than that given in Eq. A.2:

$$
\begin{aligned}
s &= \frac{w_0(t-t_0)}{\cos 0.9\theta} && \text{for } (t-t_0) \le \frac{d_{\text{eff}}}{w_0 \sin\theta} \\
s &= w(t-t_0) + \frac{d_{\text{eff}}}{\sin\theta}\left(\frac{1}{\cos 0.9\theta} - \frac{w}{w_0}\right) && \text{for } (t-t_0) \ge \frac{d_{\text{eff}}}{w_0 \sin\theta} \qquad \text{(A.3)} \\
w &= w_0 + 0.001 \sin^3 1.4\theta,
\end{aligned}
$$

with $w_0 = 50.7\ \mu$m/ns $= 101.4\ \mu$m/channel and $d_{\text{eff}} = 0.2$ cm. The t, t_0 and θ are time of the hit, the time offset for the drift cell, and the track angle respectively. The half-width of the cell d has been replaced by an effective distance d_{eff} and an angular-dependent drift speed w has been added. This fairly complicated function is the result of the calibration procedure modifying the simple time to distance function of Eq. A.2 is such a way as to more accurately model the drift path of the ionization charge. The final time offsets and chamber positions were determined and tabulated; all values were reasonable. The position corrections of the chambers eliminated the sense-wire-pair correlations that were discussed above and resulted with changes in the wire plane positions of up to 1 mm.

The δ distributions for two of the cells for the final iteration are shown in Figs. A.3(c) and A.3(d). The final iteration distributions of the quantity δ', summed over all drift cells, for 10 angular bins are shown in Fig. A.4 . As is verified with these plots, the final calibration works extremely well for track angles up to $\approx 45°$.

However, for larger track angles, it is difficult to determine the exact form of the time to distance function. It is possible that the form of Eq. A.3 is not adequate to handle the large angle behavior of tracks. However, it has been determined that, with the use of proper errors, this calibration function may be safely used for tracks with angles up to 60°.

The δ' distributions of Fig. A.4 allow the drift chamber resolutions to be determined as a function of the track angle and time channel. These distributions were divided into ten time channel bins and angular bins and fit with a Gaussian. The σ of the Gaussian may be equated with the drift chamber resolution. These σ values as a function of time channel for nine angular bins are shown in Fig. A.5. Only nine angular bins are shown due to the insufficient number of tracks with angles above 45°. For each angular bin, the resolution was parameterized with the form

$$\sigma(t) = C_1 e^{-C_2(t-t_0)} + C_3\sqrt{t-t_0}, \tag{A.4}$$

where the C_i are the parameters varied in the fits. This functional form is due to the contributions to the resolution from primary ion statistics (first term) which dominates at low times and the diffusion of the drift electrons (second term) which becomes dominant a higher times [90]. To estimate the resolution for the larger track angles, the behavior as a function of track angle was parameterized. It was determined that the resolution can be described (eliminating the time channel dependance) as

$$\sigma = 0.055 \tan^2\theta \text{ cm}. \tag{A.5}$$

Using this equation and the shape of the resolution function from the 40–45° angular bin, the drift chamber resolution was extrapolated to angles up to 60°.

The drift calibration procedure described in this appendix yielded the time to distance function with the associated parameters and the chamber plane positions. These were used in the analysis of the 1.729 GeV/c data.

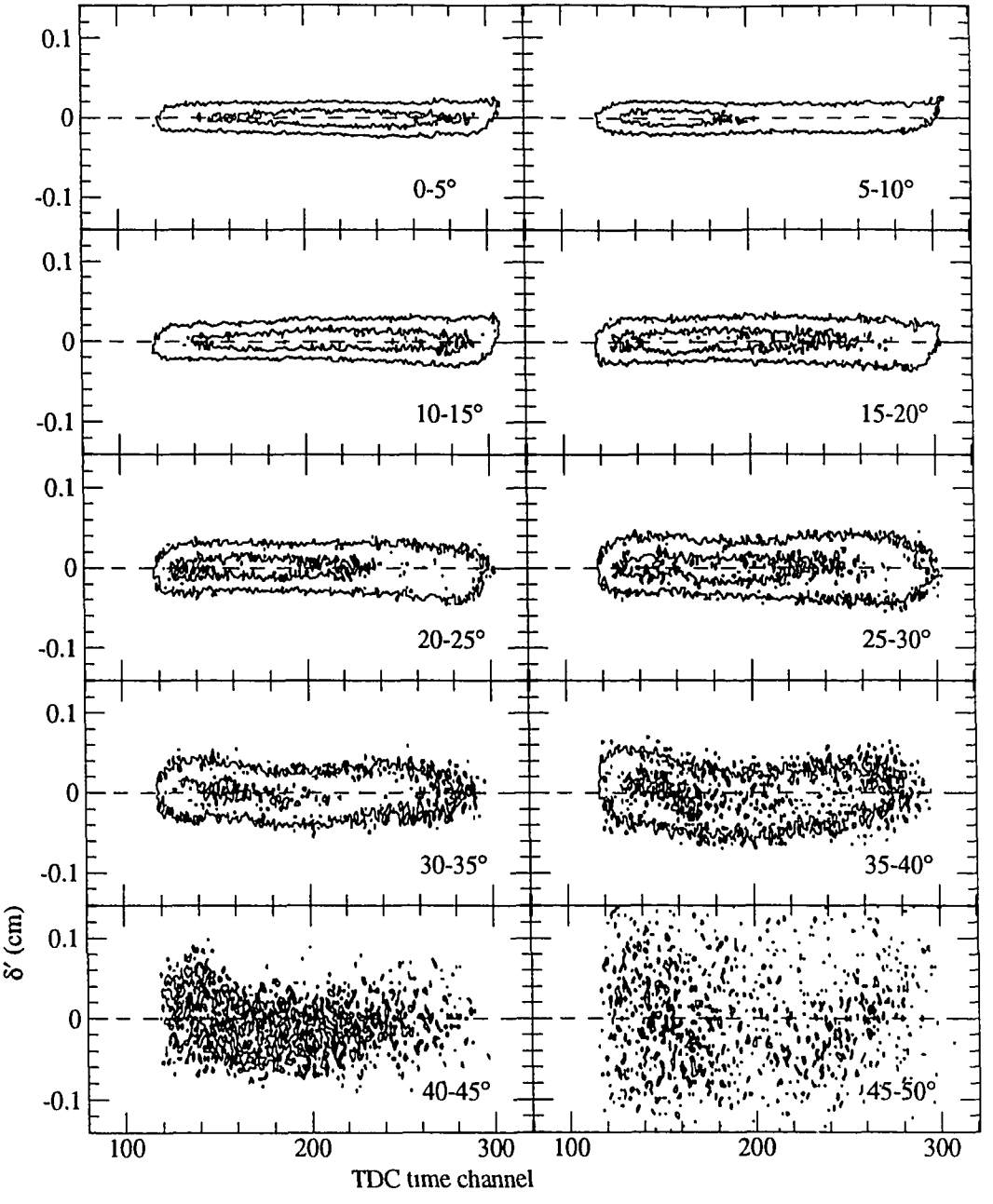

Figure A.4: Contour plots for the residual δ' as a function of time channel for 10 different track angular ranges from the final iteration of the DC calibration.

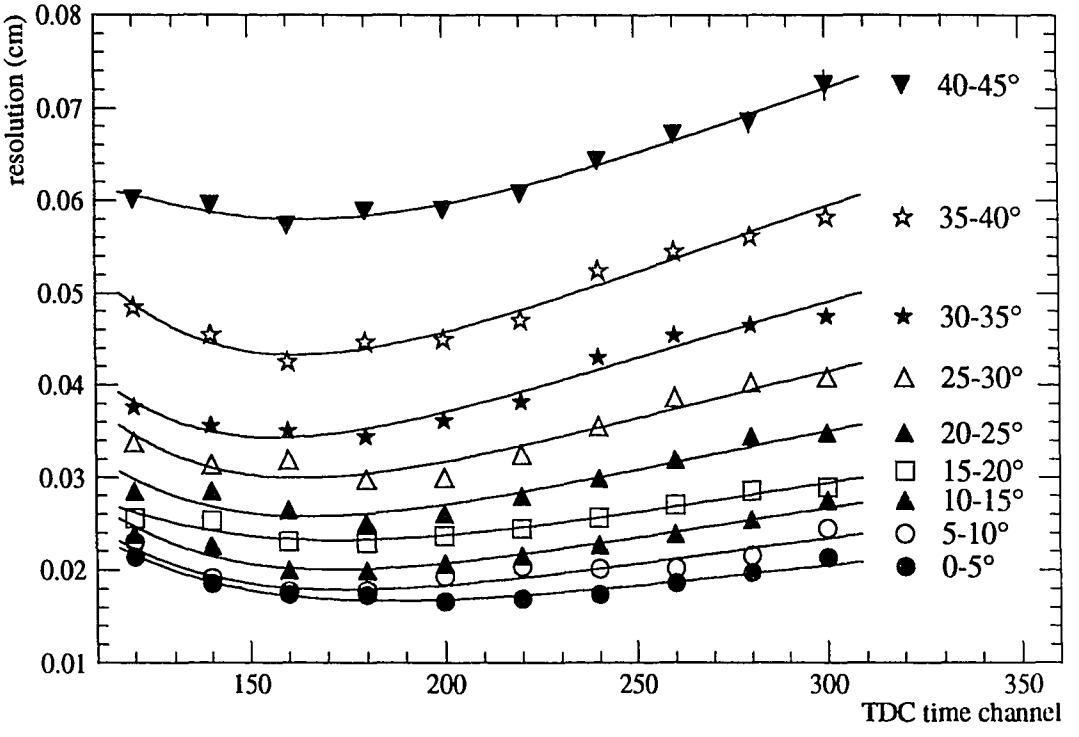

Figure A.5: The DC resolutions as calculated from the δ' distributions as a function of time channel for nine track angular bins. The curves are the results of fits to the form of Eq. A.4.

Appendix B

Tracking Chamber Efficiencies

The efficiency of the tracking chambers is determined by studying the properties of tracks and hits in the experimental data. These efficiencies, suitably parameterized, are used, in conjunction with the detector simulation program, to determine the tracking and reconstruction efficiency of the PS185 detector for $\bar{p}p \rightarrow \overline{\Lambda}\Lambda$ and $\bar{p}p \rightarrow \overline{\Sigma}^0\Lambda + c.c.$ events.

B.1 Multiwire Proportional Chamber Efficiency

The efficiency function of the multiwire proportional chamber (MWPC) was determined by studying the wire cluster size distributions in neutral event data as a function of track angle. If the efficiency of the MWPC was 100% the number of hits in a cluster would be described by

$$N(\text{hits/cluster}) = \frac{t \tan\theta}{w}, \tag{B.1}$$

where θ is the track angle and t and w are the wire cell thickness and width respectively. The cluster size distribution and this simple function is shown in Fig B.1. As can be seen in this figure the distributions from actual events show a behavior somewhat different than would be predicted if the chamber was 100% efficient. By studying these cluster-size distributions from Monte Carlo data with different efficiency models, an efficiency function that reproduces the data was determined.

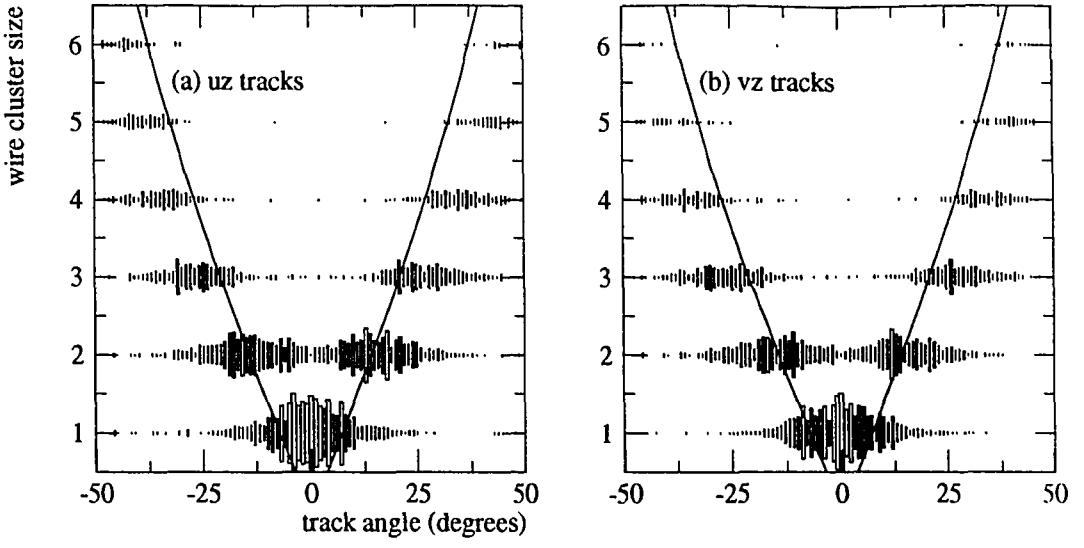

Figure B.1: A box plot of wire cluster size vs. track angle in the MWPC for (a) uz and (b) vz projection tracks. The curves illustrate the behavior expected for 100% efficiency.

The efficiency function includes an overall constant term, a term to model the dependence on track-sense wire distance, and a term to model the dependence on track length in the MWPC wire cell. The efficiency of a given MWPC wire to have a hit is well described by the function,

$$\epsilon_{\mathrm{MWPC}} = \alpha \left(1 - e^{-r/\rho}\right) \left(1 - e^{-\delta/d}\right), \tag{B.2}$$

where r is the length of the particle track through the cell and d is the distance of closest approach of the track to the sense wire. The efficiency parameters that best reproduce the cluster size distributions seen in the data are

$$\alpha = 0.98,\ \rho = 0.1 \text{ cm, and } \delta = 0.15 \text{ cm}. \tag{B.3}$$

B.2 Drift Chamber Efficiency

The efficiency of the drift chambers was studied by using 3D tracks that consist of all four 2D projections (xz, yz, uz, and vz) from neutral event data. This ensures that the tracks are due to particles and not spurious tracks formed from erroneous hits. For each track, each plane of the drift chamber is checked to see if it provides a hit on this track; if not, a "missing hit" is counted for this plane. By counting the number of missing hits and normalizing by the number of tracks, the efficiency of the drift chambers may be determined [105]. Scatter plots illustrating the missing hits for four of the drift chamber planes are shown in Fig. B.2.

There are several features of note illustrated with these plots.

- The "dead-spot" in the middle of the chamber. This is due to the desensitized region of the central sense wire.
- The extra lower efficiency bands in all planes. These are most probably due to "dirty" spots on the wires caused by aging. They are less prevalent in the more downstream planes (7 and 8).
- The multiple "stripes" running vertically in the two x planes (1 and 2) and horizontally in the two y planes (7 and 8). These are the inefficient regions around the sense wire pairs. This is a side effect of chambers utilizing closely spaced pairs of sense wires [94].
- The homogenous background inefficiency. This component of the inefficiency gets smaller for the downstream planes.

The dead spot for all drift chamber planes may be described by a completely inefficient region on the beam side of the desensitized pair for 0.85 cm along the wire and a 10% efficient region on the other side of the pair for 0.6 cm along the wire. The efficiency for the rest of the plain is described by a constant component with a

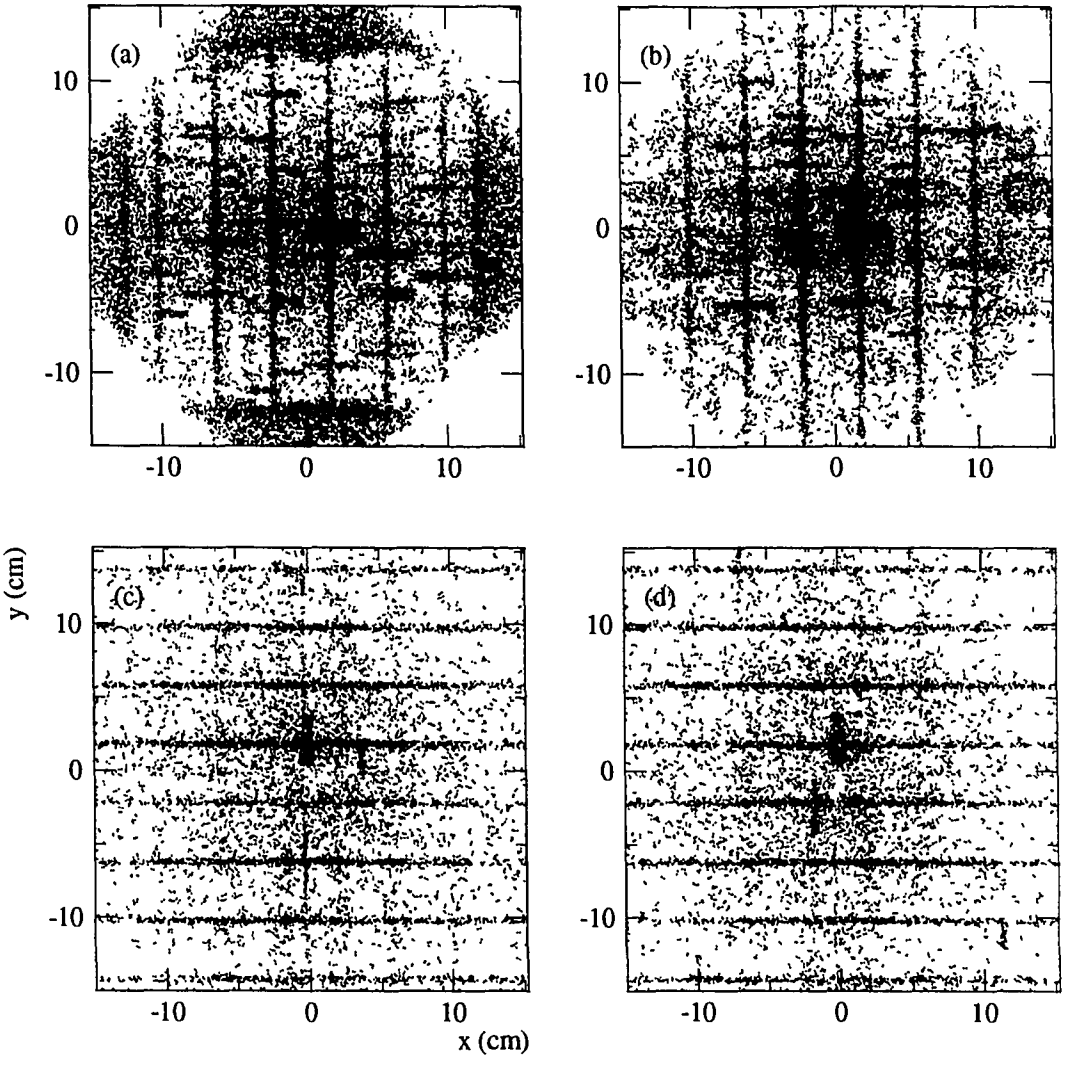

Figure B.2: Scatter plots showing the locations of missing hits in DC planes (a) 1, (b) 2, (c) 7, and (d) 8. In planes 1 and 2, the wires are strung vertically; in planes 7 and 8, they are strung horizontally. The shadowing from the MWPC can be seen in (a) and (b) and the edges of the active area of the smaller plane 1 is visible in (a)

DC plane #	β_1	β_2	DC plane #	β_1	β_2
1	0.909	0.712	8	0.943	0.642
2	0.915	0.761	9	0.950	0.674
3	0.938	0.692	10	0.946	0.691
4	0.943	0.689	11	0.949	0.556
5	0.937	0.709	12	0.968	0.641
6	0.942	0.710	13	0.970	0.563
7	0.942	0.629	$s_0 = 0.090$ cm for all planes		

Table B.1: Drift chamber efficiency constants.

gaussian shaped "hole" near the sense wire:

$$\epsilon_{DC} = \beta_1 - \beta_2 e^{-\frac{1}{2}\frac{s^2}{s_0^2}}, \tag{B.4}$$

where s is the track to sense wire distance. The constants β_1, β_2, and s_0, were determined by fitting the measured efficiency, for each plane and with the dead spot region excluded, to a function of this form. The values resulting for the constants for each plane of the drift chamber are listed in Table B.1.

There is a steady increase in efficiency with plane number. It is assumed that this is due to the increased effects of aging on those chambers closer to the target. The fit value of s_0 was effectively the same for all planes. For the magnet chamber (MACH) drift planes, the low track density did not allow for an efficiency determination so the function that described DC plane 13 was used for all three MACH planes. These efficiency functions were implemented into the Monte Carlo code. The efficiency analysis was tested with Monte Carlo data and the results agreed with those from the experimental data.

Appendix C

Tabulated Results

In this chapter the results with errors are given in tabulated numerical form for the $\overline{p}p \rightarrow \overline{\Lambda}\Lambda$ and $\overline{p}p \rightarrow \overline{\Sigma}^0\Lambda + c.c.$ reactions at an average antiproton momentum of 1.726 ± 0.001 GeV/c.

$\overline{p}p \rightarrow \overline{Y}Y$ channel	cross section (μbarn)	statistical error (μbarn)	systematic error (μbarn)	total error (μbarn)
$\overline{p}p \rightarrow \overline{\Lambda}\Lambda$	74.36	0.80 (1.1%)	2.55 (3.4%)	2.67 (3.6%)
$\overline{p}p \rightarrow \overline{\Sigma}^0\Lambda + c.c.$	14.60	0.27 (1.8%)	0.64 (4.4%)	0.70 (4.8%)

Table C.1: Total cross sections and errors, separated into statistical and systematic components for the $\overline{p}p \rightarrow \overline{\Lambda}\Lambda$ and $\overline{p}p \rightarrow \overline{\Sigma}^0\Lambda + c.c.$ reactions at an average antiproton lab momentum of 1.726 ± 0.001 GeV/c.

bin	$\cos\theta^*$	$\frac{d\sigma}{d\Omega}\left(\frac{\mu b}{sr}\right)$	error $\left(\frac{\mu b}{sr}\right)$	bin	$\cos\theta^*$	$\frac{d\sigma}{d\Omega}\left(\frac{\mu b}{sr}\right)$	error $\left(\frac{\mu b}{sr}\right)$
1	-0.98	1.81	0.26	26	0.02	3.14	0.27
2	-0.94	1.89	0.23	27	0.06	2.81	0.26
3	-0.90	1.57	0.20	28	0.10	2.69	0.25
4	-0.86	2.02	0.22	29	0.14	2.99	0.26
5	-0.82	1.70	0.21	30	0.18	2.90	0.27
6	-0.78	1.60	0.20	31	0.22	2.95	0.27
7	-0.74	1.94	0.21	32	0.26	3.41	0.29
8	-0.70	1.99	0.22	33	0.30	4.04	0.31
9	-0.66	2.12	0.23	34	0.34	3.44	0.29
10	-0.62	2.35	0.24	35	0.38	4.30	0.33
11	-0.58	2.74	0.27	36	0.42	4.34	0.33
12	-0.54	2.69	0.25	37	0.46	5.19	0.37
13	-0.50	2.55	0.25	38	0.50	5.64	0.39
14	-0.46	2.81	0.27	39	0.54	6.55	0.42
15	-0.42	3.06	0.28	40	0.58	7.83	0.46
16	-0.38	2.45	0.24	41	0.62	8.41	0.48
17	-0.34	2.79	0.27	42	0.66	9.81	0.53
18	-0.30	3.19	0.28	43	0.70	11.34	0.58
19	-0.26	2.52	0.25	44	0.74	13.46	0.64
20	-0.22	2.74	0.26	45	0.78	14.93	0.70
21	-0.18	2.76	0.26	46	0.82	17.26	0.75
22	-0.14	3.01	0.28	47	0.86	19.80	0.83
23	-0.10	3.38	0.29	48	0.90	24.12	0.97
24	-0.06	2.95	0.26	49	0.94	24.99	1.06
25	-0.02	3.17	0.27	50	0.98	27.69	1.38

Table C.2: Differential cross section values in 50 $\cos\theta^*$ bins for the $\overline{p}p \rightarrow \overline{\Lambda}\Lambda$ reaction at an average antiproton 1.726 ± 0.001 GeV/c. The angular-independent systematic errors result in a 2.6% error on the scale. The estimated angular-dependent systematic errors are shown in Fig. 7.2.

bin	$\cos\theta^*$	$\frac{d\sigma}{d\Omega}\left(\frac{\mu b}{sr}\right)$	error $\left(\frac{\mu b}{sr}\right)$
1	-0.96	0.48	0.06
2	-0.88	0.62	0.08
3	-0.80	0.83	0.09
4	-0.72	0.79	0.09
5	-0.64	0.60	0.08
6	-0.56	0.61	0.08
7	-0.48	0.54	0.07
8	-0.40	0.65	0.08
9	-0.32	0.45	0.06
10	-0.24	0.47	0.07
11	-0.16	0.43	0.06
12	-0.08	0.59	0.07
13	0.00	0.56	0.07
14	0.08	0.44	0.06
15	0.16	0.61	0.07
16	0.24	0.65	0.08
17	0.32	0.84	0.09
18	0.40	1.02	0.10
19	0.48	1.23	0.11
20	0.56	1.44	0.12
21	0.64	1.98	0.14
22	0.72	2.07	0.14
23	0.80	2.85	0.17
24	0.88	3.62	0.20
25	0.96	4.65	0.24

Table C.3: Differential cross section values in 25 $\cos\theta^*$ bins for the $\overline{p}p \rightarrow \overline{\Sigma}^0\Lambda + c.c.$ reaction at an average antiproton 1.726 ± 0.001 GeV/c. The angular-independent systematic errors result in a 2.6% error on the scale. The estimated angular-dependent systematic errors are shown in Fig. 7.2.

bin	$\cos\theta^*$	P_Λ	C_{xx}	C_{yy}
1	-0.8571	-0.16±0.14	-0.25±0.55	0.12±0.49
2	-0.5714	-0.25±0.09	-0.43±0.49	-0.07±0.35
3	-0.2857	-0.31±0.09	-0.68±0.56	0.28±0.31
4	0.0000	-0.33±0.08	-0.09±0.57	0.56±0.29
5	0.2857	-0.36±0.07	1.19±0.50	0.71±0.28
6	0.5714	-0.04±0.05	-0.21±0.29	0.84±0.20
7	0.8571	0.07±0.04	-0.33±0.18	0.53±0.15

bin	$\cos\theta^*$	C_{zz}	C_{xz}	F_s
1	-0.8571	-0.95±0.72	0.14±0.45	-0.08±0.26
2	-0.5714	-0.18±.48	0.03±0.34	0.11±0.19
3	-0.2857	-0.13±.36	0.05±0.31	-0.02±0.18
4	0.0000	-0.04±.31	0.60±0.30	0.08±0.18
5	0.2857	-1.07±.33	0.56±0.28	0.10±0.16
6	0.5714	-0.95±.29	-0.45±0.20	-0.25±0.11
7	0.8571	-0.62±.25	-0.27±0.15	-0.12±0.09

Table C.4: Spin observables in 7 $\cos\theta^*$ bins for the $\overline{p}p \to \overline{\Lambda}\Lambda$ reaction at an average antiproton momentum of 1.726 ± 0.001 GeV/c. F_s is the singlet fraction. Statistical and systematic errors are included.

bin	$\cos\theta^*$	P_Λ	P_{Σ^0}	C_{xx}	C_{yy}
1	-0.80	0.47±0.75	0.07±0.25	2.08±1.99	0.20±1.70
2	-0.40	0.62±0.70	-0.16±0.24	-0.57±2.70	-1.52±1.66
3	0.00	-0.50±0.65	0.13±0.22	3.41±2.84	0.11±1.58
4	0.40	-0.20±0.51	0.35±0.17	0.06±1.90	-0.79±1.20
5	0.80	-0.66±0.46	0.25±0.15	0.78±1.06	-0.90±0.94

bin	$\cos\theta^*$	C_{zz}	C_{xz}	C_{zx}	F_s
1	-0.80	0.41±2.31	0.50±2.01	-0.28±2.07	0.82±0.87
2	-0.40	-1.07±1.88	0.97±2.04	1.86±2.38	0.22±0.92
3	0.00	-0.97±1.76	0.76±2.20	1.37±2.27	0.83±0.92
4	0.40	1.24±1.45	1.11±1.63	0.25±1.77	0.77±0.67
5	0.80	0.80±1.29	0.69±1.16	0.34±1.18	0.87±0.48

Table C.5: Spin observables in 5 $\cos\theta^*$ bins for the $\overline{p}p \to \overline{\Sigma}^0\Lambda + c.c.$ reaction at an average antiproton momentum of 1.726 ± 0.001 GeV/c. F_s is the singlet fraction. Statistical and systematic errors are included.

References

[1] R.N. Cahn and G. Goldhaber, *The Experimental Foundations of Particle Physics*, (Cambridge University Press, Cambridge, 1989).

[2] J. Button et al., Phys. Rev. **121**, 1788 (1961).

[3] O. Chamberlain et al., Phys. Rev. **100**, 947 (1955).

[4] O. Chamberlain et al., Phys. Rev. **101**, 909 (1956).

[5] B. Cork et al., Phys. Rev. **104**, 1193 (1957).

[6] D.J. Prowse and M. Baldo-Ceolin, Phys. Rev. Lett. **1**, 179 (1958).

[7] H. Yukawa, Proc. Phys. Math. Soc. Japan, **17**, 48 (1935).

[8] C.D. Anderson, Phys. Rev., **43**, 491 (1933).

[9] M. Gell-Mann and Y. Ne'eman, *The Eightfold Way*, (Benjamin, New York. 1964).

[10] M. Gell-Mann, Phys. Lett. **8**, 214 (1964).

[11] F. Halzen and A.D. Martin, *Quarks and Leptons: An Introductory Course in Modern Particle Physics*, (Wiley, New York, 1984).

[12] Particle Data Group, Phys. Rev. D **50**, 1173 (1994).

[13] H.W. Atherton et al., Phys. Lett. B **30**, 494 (1969).

[14] H.W. Atherton et al., Nucl. Phys. B **69**, 1 (1974).

[15] J. Badier et al., Phys. Lett. B **25**, 152 (1967).

[16] C. Baltay et al., Phys. Rev. **140**, B1027 (1965).

[17] G.P. Fisher et al., Phys. Rev. **161**, 1335 (1967).

[18] N. Kwak et al., Phys. Rev. **186**, 1392 (1969).

[19] N. Kwak et al., Nuovo Cimento A **23**, 610 (1974).

[20] B. Jayet et al., Nuovo Cimento A **45**, 371 (1978).

[21] B.Y. Oh et al., Nucl. Phys B **51**, 57 (1973).

[22] H. Becker et al., Nucl. Phys. B **141**, 48 (1978).

[23] S.M. Jacobs et al., Phys. Rev. D **17**, 1187 (1978).

[24] P.D. Barnes et al., Phys. Lett. B **189**, 249 (1987).

[25] P.D. Barnes et al., Phys. Lett. B **229**, 432 (1989).

[26] P.D. Barnes et al., Nucl. Phys. A **526**, 575 (1991).

[27] H. Fischer, Ph. D. thesis, University of Freiburg, 1992.

[28] T. Sefzick, Ph. D. thesis, KFA Jülich, 1992.

[29] M. Ziolkowski, Ph. D. thesis, KFA Jülich, 1992.

[30] P.D. Barnes et al., Phys. Lett. B **331**, 203 (1994).

[31] P.D. Barnes et al., Phys. Lett. B **246**, 273 (1990).

[32] M.L. Perl, *High Energy Hadron Physics*, (Wiley, New York, 1974).

[33] D.H. Perkins, *Introduction to High Energy Physics*, 3rd ed. (Addison-Wesley, Menlo Park, California, 1987).

[34] J. Hüfner and A. de Shalit, Phys. Lett. **15**, 52 (1965).

[35] I.A. Gubkin, Nucl. Phys. A **111**, 605 (1968).

[36] F. Tabakin, R.A. Eisenstein and Y. Lu, Phys. Rev. C **44**, 1749 (1991) .

[37] R. Timmermans, T. Rijken, and J. de Swart, Phys. Rev. D **45**, 2288 (1992).

[38] M. Jacob and G.C. Wick, Ann. Phys. (N.Y.) **7**, 404 (1958).

[39] L. Durand and J. Sandweiss, Phys. Rev. **135**, B540 (1964).

[40] J.J. Sakurai, *Modern Quantum Mechanics*, (Benjamin/Cummings, Menlo Park, California, 1985).

[41] F. Tabakin and R.A. Eisenstein, Phys. Rev. C **31**, 1857 (1985).

[42] R. Timmermans, Ph. D. thesis, University of Nijmegen, 1991.

[43] P.D. Barnes et al., Phys. Lett. B **199**, 147 (1987).

[44] J.F. Donoghue, X.-G. He, and S. Pakvasa, Phys. Rev. D **34**, 833 (1986).

[45] J.F. Donoghue, B.R. Holstein, and G. Valencia, Phys. Lett. B **178**, 319 (1986).

[46] D.P. Roy, Phys. Rev. **146**, 1218 (1966).

[47] G. Plaut, Nucl. Phys. B **35**, 221 (1971).

[48] H. Genz and S. Tatur, Phys. Rev. D **30**, 63 (1984).

[49] J. Niskanen, Helsinki Preprint HU-TFT-85-28 (1985).

[50] M. Kohno and W. Weise, Phys. Lett. B **179**, 15 (1986).

[51] M. Kohno and W. Weise, Phys. Lett. B **206**, 584 (1988).

[52] M. Kohno and W. Weise, Nucl. Phys. A **479**, 433c (1988).

[53] P. LaFrance, B. Loiseau and R. Vinh Mau, Phys. Lett. B **214**, 317 (1988).

[54] P. LaFrance and B. Loiseau, Nucl. Phys. A **528**, 557 (1991).

[55] R. Timmermans, T. Rijken, and J. de Swart, Nucl. Phys. A **479**, 383c (1988).

[56] R. Timmermans, T. Rijken, and J. de Swart, Phys. Lett. B **257**, 227 (1991).

[57] J. Haidenbauer et al., Phys. Rev. C **45**, 931 (1992).

[58] J. Haidenbauer et al., Phys. Rev. C **46**, 2158 (1992).

[59] J. Haidenbauer, K. Holinde, and J. Speth, Phys. Rev. C **46**, 2516 (1992).

[60] J. Haidenbauer et al., Phys. Lett. B **291**, 223 (1992).

[61] H. Rubinstein and H. Snellman, Phys. Lett. B **165**, 187 (1985).

[62] S. Furui and A. Faessler, Nucl. Phys. A **468**, 669 (1987).

[63] M. Alberg, E. Henley, and L. Wilets, Z. Phys. A **331**, 207 (1988).

[64] M. Alberg, E. Henley, and L. Wilets, Phys. Rev. C **38**, 1506 (1988).

[65] M. Alberg, et al., Nucl. Phys. A **508**, 323c (1990).

[66] M. Alberg, E. Henley, and W. Weise, Phys. Lett. B **255**, 498 (1991).

[67] M. Alberg, et al., Nucl. Phys. A **560**, 365 (1993).

[68] M. Burkhardt and M. Dillig, Phys. Rev. C **37**, 1362 (1988).

[69] G. Brix, H. Genz, and S Tatur, Phys. Rev. D **39**, 2054 (1989).

[70] I. Shapiro, Nucl. Phys. A **478**, 665c (1988).

[71] O. Dalkarov, K. Protasov, and I. Shapiro, Int. J. Mod. Phys, A **5**, 2155 (1990).

[72] J. Carbonell, K. Protasov, and O. Dalkarov, Nucl. Phys. A **558**, 353c (1993).

[73] P. Kroll and W. Schweiger, Nucl. Phys. A **474**, 608 (1987).

[74] P. Kroll, B. Quadder, and W. Schweiger, Nucl. Phys. B **316**, 373 (1989).

[75] A. Kudriyavtsev and V. Samoilov, Mod. Phys. Lett. A **4**, 721 (1989).

[76] A. Schneider-Neureither et al., Z. Phys. A **344**, 317 (1993).

[77] Y. Lu and M.P. Locher, Z. Phys. A **346**, 143 (1993).

[78] J.M. Blatt and V.F. Weisskopf, *Theoretical Nuclear Physics*, (Wiley, New York, 1952).

[79] M. Nagels, T. Rijken, and J. de Swart, Phys. Rev. D **17**, 768 (1978).

[80] P. Maessen, T. Rijken, and J. de Swart, Phys. Rev. C **40**, 2226 (1989).

[81] R. Jaffe and F. Low, Phys. Rev. D **19**, 2105 (1979).

[82] T. Ueda, Prog. Theor. Phys **62**, 1670 (1979).

[83] M. Nagels, T. Rijken, and J. de Swart, Phys. Rev. D **20**, 1633 (1979).

[84] R.A. Eisenstein, in *1994 Proceedings of the Second Biennial Workshop on Nucleon-Antinucleon Physics, Moscow, Russia*, edited by Yu. Kalashnikova et al. (Sov. J. Nucl. Phys. **57**, 1751, 1994).

[85] E. Jones, in *Physics with Antiprotons at LEAR in the ACOL Era*, Proceedings of the Third LEAR Workshop, Tignes, Savoie, France, edited by U. Gastaldi et al. (Editions Frontières, Gif sur Yvette, France, 1985).

[86] P. Lefèvre, in *Physics at LEAR with Low Energy Antiprotons*, Proceedings of the Fourth LEAR Workshop, Villars-sur-Ollon, Switzerland, edited by C. Amsler et al. (Harwood, Chur, Switzerland, 1988).

[87] R. Billinge, in *Physics with Antiprotons at LEAR in the ACOL Era*, Proceedings of the Third LEAR Workshop, Tignes, Savoie, France, edited by U. Gastaldi et al. (Editions Frontières, Gif sur Yvette, France, 1985).

[88] J. Bosser, in *First Biennial Conference on Low Energy Antiproton Physics, Stockholm, Sweden*, edited by P. Carlson, A. Kerek, and S. Szilagyi (World Scientific, Singapore, 1991).

[89] R. Geyer, Ph. D. thesis, University of Erlangen-Nürnberg, 1993.

[90] F. Sauli, CERN Report 77-09 (1977).

[91] W. Dutty, Ph. D. thesis, University of Freiburg, 1988.

[92] M. Ruh, Diploma thesis, University of Freiburg, 1994.

[93] N. Hamann et al., Nucl. Instrum. Methods **A281**, 379 (1989).

[94] A. Breskin et al., Nucl. Instrum. Methods **119**, 9 (1974).

[95] D. Hertzog et al., Nucl. Instrum. Methods **A294**, 446 (1990).

[96] N. Hamann, in *First Biennial Conference on Low Energy Antiproton Physics, Stockholm, Sweden*, edited by P. Carlson, A. Kerek, and S. Szilagyi (World Scientific, Singapore, 1991).

[97] C. Maher, Ph. D. thesis, Carnegie-Mellon University, 1986.

[98] A. Frodesen, O. Skjeggestad, and H. Tøfte, *Probability and Statistics in Particle Physics*, (Universitetsforlaget, Bergen, 1979).

[99] R.K. Bock et al., *Data Analysis Techniques for High-Energy Physics Experiments*, (Cambridge University Press, Cambridge, 1990).

[100] Numerical Algorithms Group, NAG Fortran Library, (NAG Ltd., Oxford, 1991).

[101] Application Software Group, Computing and Networks Division, GEANT Detector Description and Simulation Tool, (CERN, Geneva, Switzerland, 1993).

[102] P. Harris and R. Tayloe, PS185 Internal Note, 1993.

[103] S. Ohlsson, Ph. D. thesis, Uppsala University, 1986.

[104] V.P. Zhigunov, Nucl. Instrum. Methods **216**, 183 (1983).

[105] R. Tayloe, PS185 Internal Note, 1993.

Vita

Rex L. Tayloe was born on March 28, 1964 in Bedford, Indiana. He received a B.S. from Purdue University in 1986 and a M.S. from the University of Illinois in 1987. He worked at the University of Illinois Nuclear Physics Laboratory and received a Ph.D. from the University of Illinois in the spring of 1995.